Formation and Use of Amorphous Silica

Doctoral Thesis

to obtain the doctoral degree of natural sciences (Dr. rer. nat.) of Graz University of Technology

submitted by

Dipl.-Min. Daniel Höllen
Graz, January 2013

Supervisors
Univ.-Prof. Dipl.-Min. Dr. rer. nat. Martin Dietzel
Ao. Univ.-Prof. Dr. phil. Dietmar Klammer
Institute of Applied Geosciences

External Reviewer
Dipl.-Chem. Dr. Albrecht Leis

Statutory Declaration

I declare that I have authored this thesis independently, that I have not used other than the declared sources / resources, and that I have explicitly marked all material which has been quoted either literally or by content from the used sources.

Graz, 2013/01/11

Daniel Höllen

Kurzfassung

Die vorliegende Arbeit beinhaltet drei Studien, die sich mit der Bildung und Nutzung von amorphem Siliziumdioxid beschäftigen. Dieses Material ist sowohl in den Geo- als auch in den Materialwissenschaften von großer Bedeutung, da es einerseits natürlich, z.B. in den Schalen von Kieselalgen oder auch als chemisch gefälltes Sediment (u.a. als „Feuerstein"), vorkommt, andererseits aufgrund seiner oftmals großen spezifischen Oberfläche und damit hohen Reaktivität künstlich erzeugt und technisch eingesetzt wird, z.B. zur dosierten Freisetzung von Arzneimitteln.

Zunächst wurde die Adsorption monomerer und polymerer Kieselsäure an Gibbsit als Funktion des pH-Wertes ($3 \leq pH \leq 8$) und der gelösten Kieselsäurekonzentration ($0.34\ mmol\ L^{-1} \leq [Si] \leq 1.47\ mmol\ L^{-1}$) untersucht, da die Adsorption eine wichtige Vorstufe der Bildung von amorphen und kristallinen kieselsäurehaltigen Festphasen darstellt. Es wurde festgestellt, dass der relative Anteil adsorbierter Kieselsäure mit zunehmendem pH-Wert (für $pH < 9$) und abnehmender initialer Kieselsäurekonzentration steigt. Bei der Adsorption monomerer Kieselsäure wird das leichte Isotop ^{28}Si gegenüber dem schwereren ^{30}Si aufgrund seiner massebedingt höheren Reaktionsgeschwindigkeit bevorzugt fixiert. Die Isotopenfraktionierung ist umso stärker, je höher die initiale Kieselsäurekonzentration ist. Daher kann die Siliziumisotopensignatur von Mineralphasen, die sich durch Adsorptionsprozesse gebildet haben, möglicherweise als Proxy für die Adsorptionsrate verwendet werden. Polymere Kieselsäure wird rascher adsorbiert als monomere Kieselsäure und zerfällt an der Mineraloberfläche und in der Lösung, so dass am Ende der Versuche nur noch monomere Kieselsäure in der Lösung vorliegt.

Darauf aufbauend wurde amorphes Siliziumdioxid durch zyklisches Gefrieren wässriger Lösungen ausgefällt. Es wurde gezeigt, dass mehr Silizium aus der Lösung entfernt wird, wenn gelöstes Aluminium oder Germanium oder suspendierter Kaolinit vorhanden sind, während die Zugabe von Natriumchlorid die Ausfällung hemmt. Der Anteil an ausgefällter Kieselsäure erreicht für pH-Werte zwischen 5 und 7 ein Maximum und nimmt im sauren und alkalischen Bereich ab. Die Ausfällung von amorphem „Siliziumdioxid" wird im sauren Milieu von einer Polymerisation der gelösten Kieselsäure begleitet, insbesondere in Gegenwart von Bor, nicht aber in Gegenwart von Germanium. Eine Fraktionierung der Siliziumisotope erfolgt nur in Gegenwart ausreichender Aluminiumkonzentrationen ($Al \geq 1\ mmol\ L^{-1}$) bei Übersättigung bzgl. amorphem Aluminiumhydroxid. In den letzteren Fällen wird ^{28}Si gegenüber ^{30}Si bevorzugt im Festkörper fixiert, was durch eine Adsorption an primär gebildeten Aluminiumhydroxid-Präzipitaten oder eine Kopräzipitation einer Si-Al-O-OH-Phase erklärt werden kann. Für eine steigende Anzahl von Gefrierzyklen strebt die Isotopenfraktionierung zwischen gelöster und gefällter Kieselsäure gegen 0 ‰. Daher kann die Siliziumisotopenfraktionierung zwischen amorphen kieselsäurehaltigen Festphasen und möglicherweise daraus entstandenen Mineralphasen einerseits und der koexistierenden Lösung andererseits potentiell als Proxy verwendet werden. Auf diese Weise könnte zwischen gerichteten Prozessen wie der Adsorption und zyklischen Prozessen, die mit einer Reorganisation des Präzipitats einhergehen, unterschieden werden.

In der dritten Studie wurde die Anwendung von amorphem Siliziumdioxid am Beispiel seiner hydrothermalen Umwandlung in Zeolithe im alkalischen Milieu untersucht. Dafür wurde biogenes Siliziumdioxid in Form von Kieselerde (Diatomeen) verwendet. Die Umwandlung erfolgt über eine kaliumhaltige Hydroxyaluminosilikat-Übergangsphase, die aus kugelförmigen Partikeln in der Größe von ca. 100 nm besteht und daher durch eine hohe spezifische Oberfläche gekennzeichnet ist. Alterationsprodukte, welche diese Übergangsphase

enthalten, sind besonders effizient im Hinblick auf die Entfernung von gelösten Kupfer-, Blei- und Zinkionen aus wässrigen Lösungen. Die schließlich entstehenden Zeolithminerale (insb. Merlinoit) sind zwar weniger effizient, aber sehr selektiv für Bleiionen. Dies kann durch entsprechend große Käfige in ihrer Kristallstruktur erklärt werden. Durch die Wahl geeigneter Versuchsparameter (0,1 M KOH, 100 °C) ist es gelungen, ein hierarchisch strukturiertes Material zu synthetisieren, bei dem nanokristalliner Merlinoit mit seinen strukturellen Mikroporen in den Makroporen der Kieselalgen wächst. Dieses Material birgt enormes Potential im Hinblick auf die simultane Entfernung partikulärer und gelöster Schadstoffe aus wässrigen Lösungen.

Abstract

This doctoral thesis includes three distinct studies which deal with the formation and use of amorphous silica. This material is of great importance in both Earth and materials sciences, as it occurs on the one hand naturally, e.g. in the shells of diatoms or as chemically precipitated sediment (e.g. as chert), and on the other hand is synthesised and applied industrially due to its specific reactivity and often large specific surface area, e.g. for a controlled release of medicals.

Firstly, the adsorption of monomeric and polymeric silicic acid on gibbsite was investigated as a function of pH ($3 \leq pH \leq 8$) and of the dissolved silica concentration ($0.34\ mmol\ L^{-1} \leq [Si] \leq 1.47\ mmol\ L^{-1}$). Adsorption is an important step during the formation of amorphous and crystalline silica-containing phases. It was found that the relative percentage of adsorbed silicic acid increases with increasing pH (for $pH \leq 9$) and decreasing initial concentration of dissolved silica. During adsorption of monosilicic acid the light isotope ^{28}Si is fixed preferentially versus the heavy isotope ^{30}Si due to its mass-induced higher reactivity. The isotope fractionation is stronger at higher initial concentration of dissolved silica. Hence the signature of silicon isotopes of mineral phases which have formed by Si adsorption processes might be used as a proxy for the adsorption rate. Polymeric silicic acid is adsorbed faster than monomeric silicic acid and depolymerises on the mineral surface and in the solution. Finally there is only monomeric silicic acid in the solution.

Subsequently, amorphous silica was precipitated by cyclic freezing of aqueous solutions. It was shown that more silica is removed from the solution when dissolved aluminium or germanium or suspended kaolinite are present, whereas the presence of sodium chloride inhibits the precipitation. The percentage of precipitated silica reaches a maximum for pH values between 5 and 7 and decreases in the acidic and alkaline range. The precipitation of amorphous silica is accompanied in the acidic range by a polymerisation of dissolved silicic acid, especially in presence of boron, but not in presence of germanium. A fractionation of silicon isotopes occurs only in presence of high concentrations of Al, thus at elevated supersaturation with respect to amorphous aluminium hydroxide. In these cases ^{28}Si is fixed preferentially versus ^{30}Si in the precipitates which can be explained by adsorption of Si onto primarily formed aluminium hydroxide precipitates or coprecipitation of a Si-Al-O-OH solid phase. For an increasing number of freezing cycles the Si isotopic fractionation between dissolved and precipitated silica approaches 0 ‰. Hence the Si isotopic fractionation between amorphous silica-containing solids and possibly subsequently formed mineral phases on the one hand and the coexisting solution on the other hand might be used as a proxy. Thereby unidirectional processes like adsorption and cyclic processes, which are associated with a reorganization of silica within the precipitate, might be distinguished.

In the third study the application of amorphous silica is investigated using the example of its hydrothermal alteration into zeolites under alkaline conditions. Therefore biogenic silica in terms of diatomite was used. The zeolitisation occurred via a potassium-containing hydroxyaluminosilicate intermediate phase (IP) which consists of spherical particles with a size of about 100 nm and is therefore characterised by a high specific surface area. Alteration products containing this intermediate phase are very efficient with respect to the removal of copper, lead and zinc ions from aqueous solutions. The finally formed zeolite minerals (especially merlinoite) are less efficient for ion removal in comparison to the IP, but more selective with respect to lead ions, which can be explained by correspondingly large cages in the crystal structure of merlinoite. By using appropriate experimental parameters (0.1 M KOH, 100 °C) a hierarchically structured material was synthesised, in which nano-crystalline

merlinoite with its structural micropores grows within the macropores of the diatoms. This material has a high potential with respect to simultaneous removal of particulate and dissolved contaminants from aqueous solutions.

Table of Contents

1 Introduction

1.1 Overall Aims of the Thesis

Amorphous silica is a fascinating material which can be formed with or without the help of animals and plants in nature, but is also synthesised and applied in various industries mostly due to its high specific surface area and chemical reactivity. This long path from Earth to materials science is a wonderful example for modern mineralogy.

The aims of this study are to precipitate amorphous silica and hydroxyaluminosilicates by cyclic freezing of aqueous solutions to image processes occurring in cryosols and to use amorphous silica in the form of bio-opal as a substrate for hydrothermal synthesis of zeolites which and whose precursor phases shall be used to remove heavy metals from aqueous solutions. These general ideas are concretised in the following questions:

- Can the Si isotopic composition of amorphous silica phases in cryosols be used to infer whether they have been formed by cyclic freezing?
- How does the presence of Al influence the chemical, mineralogical and isotopic character of the solid phases formed by cyclic freezing?
- Do hydroxyaluminosilicates form by coprecipitation of Si and Al or by subsequent precipitation and adsorption and can this be shown by Si isotopic ratios in phases formed by pure adsorption and precipitation processes?
- Does cyclic freezing lead to a chemical and/or mineralogical and/or isotopic steady state in which dissolution during the thawing period and precipitation during the freezing period are balancing each other out?
- How does the zeolitisation process of diatoms happen in detail?
- Can diatomite be used to produce hierarchically structured materials consisting of macroporous diatoms and microporous zeolites?
- Does the heavy metal removal capacity increase linearly for materials synthesised at different reaction times throughout the conversion of diatomite to zeolites?

1.2 The SiO_2-H_2O system

1.2.1 Dissolution of SiO_2 and Si Hydrogeochemistry

And advanced knowledge about the interaction between rocks and aqueous solutions close to the Earth´s surface is crucial for the understanding of weathering and neoformation of minerals. Distinct reaction kinetics and mechanisms have a large impact on the evaluation of the overall transformation of minerals and rocks, climate change and agriculture issues. SiO_2, also called silica, is the most abundant components of the Earth's crust [1]. As a lithophilic element it occurs predominantly in silicate minerals in the lithosphere, but weathering processes release silicic acid, H_4SiO_4, into the hydrosphere. For example, the concentration of silicic acid in soil solution accounts normally for 0.12 to 1.2 mmol L^{-1} [2]. For a deeper understanding of silicate weathering the solubility of SiO_2 has to be considered. The solubility of quartz at 25 °C accounts for 100 µmol L^{-1} of SiO_2 at 25 °C [3]. However, in Earth surface environments in particular amorphous silica is of great importance. Anhydrous and hydrous

amorphous SiO_2 have a pH-independent solubility of about 1150 µmol L^{-1} and 1700 µmol L^{-1}, respectively, for pH < 8 which increases with temperature to about 7500 µmol L^{-1} SiO_2 at 90 °C [4, 5]. Also an increase in pressure increases silica solubility [5]. When pH is increased to 10.5 the solubility increases strongly to 15000 µmol L^{-1} SiO_2 at 22 °C [4]. The solubility of amorphous silica depends not only on pH, but also on the solution chemistry: For example, in the tropics during allitic weathering tannins and other catechol-like substances are present in the soils which increase silica solubility significantly. This leads to a silicon flow in tropical rainforests of 58 to 76 kg (ha•yr)$^{-1}$ with the contribution of the dissolution of amorphous SiO_2 accounting for about two third of the overall dissolved Si [5]. In a colder climate Al might be dissolved preferentially compared to Si because the amount of biomass is smaller and the larger amount of dissolved carbon dioxide might decrease the pH and increase the solubility of aluminium [5]. Interestingly, also inorganic components of the solution effect silica solubility: On the one hand there are silica dissolution inhibitors like aqueous alumina which decreases the solubility to less than 170 µmol L^{-1} SiO_2 due to the formation of an monolayer of negatively charged aluminosilicate ions on the silica surface [6]. The same effect was observed for metal chlorides in the order of increasing effect 1) Na^+, K^+, 2) Mn^{2+}, Mg^{2+}, Ca^{2+}, Sr^{2+}, 3) Zn^{2+}, Ni^{2+}, Ce^{3+}, Cu^{2+} [7] and by Be^{2+} [5], Al^{3+}, PO_4^{3-} and especially Fe^{2+} [8]. On the other hand there are dissolution catalysts like HCO_3^- [8] or OH^- and F^- which are chemisorbed on the silica surface and increases the coordination number of the silicon atoms which leads to a weakening of their bonds to the underlying oxygen atoms [5]. The rate of dissolution is decreased by the adsorption of monosilicic acid on the surfaces of crystalline and amorphous [5]. Dissolution of amorphous silica is related to its morphology: The solubility is higher when the silica surface is convex and lower when it is concave. This leads to the conversion of silica structures with many convex surfaces like sponges to structures with concave surfaces like flints by dissolution and deposition at another site [5].

Furthermore, it has to be considered that the most abundant mineral group, the feldspars, which make up almost 60 wt.-% of the Earth´s crust [9] contains between 43 and 69 wt.-% SiO_2 and hence contribute about half of the overall SiO_2 content of the crust which is 64 wt.-%. Equilibrium dissolved SiO_2 concentrations resulting from albite weathering account for 394 µmol L^{-1} at pH 7 according to PhreeqC modelling [10] which is higher than for quartz, but lower than for amorphous silica. In the first step of feldspar weathering the potassium ions are exchanged against protons:

$$2\ KAlSi_3O_8 + 2\ H^+ \rightarrow 2\ HAlSi_3O_8 + 2K^+ \qquad (1)$$

In a second step an activated silica complex forms:

$$2\ HAlSi_3O_8 + 5\ H^+ \rightarrow Si_6O_{12}(OH)^- + 2\ Al^{3+} + 3\ H_2O \qquad (2)$$

Finally the silica complexes decompose to monosilicic acid whose properties have been discussed above [11]:

$$Si_6O_{12}(OH)^- + H^+ + 11\ H_2O \rightarrow 6\ Si(OH)_4 \qquad (3)$$

In summary, it can be said that dissolution of quartz and feldspar is the main source of silicic acid which results in worldwide average dissolved Si concentrations of 466 mmol L^{-1} in rivers and 107 mmol L^{-1} in oceans [1]. These concentrations are controlled by the solubility of colloidal aluminosilicates and adsorption processes [5]. Dissolved Si can be enriched in alkaline and hydrothermal solutions by up to two orders of magnitude or even higher [12, 13].

Orthosilicic acid, H_4SiO_4, also written as $Si(OH)_4$, is the main species under acidic and neutral conditions which dominate in soils [14]. It is a non-charged compound and weak acid with a pK value of 9.81 at 25 °C [15]. Above this pH not only negatively charged $SiO(OH)_3^-$ ions become dominant, but also dimers and larger oligomers of several SiO_4 tetrahedra exist. In particular, at pH 10.5, polymeric silicic acids which have molecular weights between 3000 and 10000 g mol^{-1} which correspond to diameters of 1.3 and 1.5 nm, respectively, become dominant [8] and account for already half of the overall dissolved Si (depending on total dissolved silica content). Polysilicic acids in diluted aqueous solutions mainly consist of rings of three to six silicon atoms which are linked by oxygen (siloxane) bridges and are the main cause for the increase of silica solubility at high pH [5]. Polysilicic acids are anhydrous inside and bear OH groups on their surfaces [5]. Since the depolymerisation rate decreases with pH and temperature, polysilicic acid can remain metastable at pH 2 to 5 – with a stability maximum at pH 2.5 [16] - which was also observed in natural systems like forest soils [17]. Their stabilisation is favoured by sulphuric acid and bivalent – and to a smaller degree monovalent – cations (e.g. heavy metal ions) [16]. Additionally, the stability of polysilicic acid is also influenced by the temperature and the salinity of the solution [11]. For example, sodium salts of different acids increase the rate of depolymerisation in the order NO_3^-, HCO_3^-, Cl^-, SO_4^{2-} whereas HPO_4^{2-} decreases it. The more silicic acid is already dissolved the smaller is the depolymerisation rate [18]. From these facts it can be concluded that polysilicic acid can form directly from the decomposition of minerals and its stability depends on the chemical composition of the environment. For example, in river and ground water 50 % of the primarily present polysilicic acid decomposes within 30 minutes [16].

The depolymerisation reaction is in fact an interference of several reactions with different kinetic order. However, considering the overall reaction, the quotient of the total concentration of silicic acid and of the concentration of monosilicic acid at a certain time increases linearly with time. The overall reaction rate constant of this depolymerisation reaction increases slightly underlinearly with increasing pH due to the catalytic effect of the hydroxyl ion and decreases with a decreasing slope with increasing initial silica concentration [7]. Furthermore, the depolymerisation rate is decreased by iron hydroxides on whose positively charged surfaces dissolved silica can be absorbed. Interestingly, despite the general trend of depolymerisation over time some low molecular silicic acids are attached to high molecular silicic acids which increases their molar weight [8].

1.2.2 Neoformation of Silicates

The inverse process of the dissolution or depolymerisation is the polymerisation of monosilicic acid which can be understood as a nucleation for the precipitation of amorphous silica and newly formed silicates. Monosilicic acid can polymerise if the Si concentration exceeds 2 mmol L^{-1} [19]. Increasing polymerisation with increasing Si concentration and K_2O:SiO_2 ratio was also observed by very recent studies [20]. Sometimes no polymerisation takes place although the Si concentration exceeds the solubility of amorphous silica because monosilicic acid can form stable complexes with organic compounds. Another explanation for this phenomenon is that membrane bounded vesicles might adsorb monosilicic acid molecules [5]. In other cases precipitation of silica takes place without previous polymerisation. Amorphous silica can precipitate, for example, directly from monomers and oligomers between pH 5 and 11 in the presence of Al^{3+} ions [5]. However, in the case of insufficient heterogeneous nucleation sites compared with the supersaturation of the solution with respect to amorphous silica, polymerisation is a necessary precursor process for precipitation [5]. This

means that polysilicic acids can be seen as precursors for the formation of pedogenic Al-silicates [17]. In this case several polymers agglomerate and form a network, so that the whole system is converted from a sol into a gel. Sols are aqueous solutions with discrete or separate particles whereas gels contain three-dimensional aggregates which possess siloxane bonds at the points of contacts in the case of silica gels [5]. Silica sols are extraordinarily stable at pH 2, but decompose at higher pH values. In a sol-gel-system small silica particles or polysilicic acid molecules aggregate into chains which are connected to a network. Then water is removed stepwise from the caves of the structure, but layers of several molecules are left behind on the silanol surfaces. Hence a hydrated silica gel forms. Finally, also these layers are removed and the silanol surfaces come into contact when 2.75 mol water per mol SiO_2 are left. Therefore energy is needed to remove both the adsorbed water molecules and the OH groups which are chemically bound to the particles from their surfaces. On the other hand energy is released because the surface area per volume is decreased. This results only in a very small net energy gain which becomes even smaller when the particles have reached a certain size. The formation of solid silica from a hydrous solution depends on the concentration of dissolved silica. If the concentration is high, amorphous silica forms, if it is intermediate, microcrystalline chalcedony may precipitate, and in the case of very low concentrations macrocrystalline quartz crystallises [5]. However, formation of quartz and chalcedony at low temperature conditions is a very slow process. Hence at experimental conditions normally only the formation of amorphous silica is observed.

Dissolved Si is re-fixed in secondary mineral phases. The simplest form of these phases is hydrous amorphous silica which forms by pedogenic processes including evaporation and pH changes in warm climate and seasonal rainfall as so-called silcrete [21]. This type of amorphous silica can either form a complete sedimentary rock or act as a cement in a breccia or conglomerate [21]. When the rainfall is permanent and a mighty soil cover has developed, precipitation of amorphous silica takes place at the base of the soil profile [2]. Another formation environment for hydrous amorphous silica are cryosols where it is precipitated by cyclic freezing which is favoured by the presence of mono- and divalent metal ions [22]. Another example for precipitation of silica, but at higher temperatures, is the formation of agate, microcrystalline quartz, which is still discussed controversially [23]. In marine environments the banded iron formation (BIF´s) are the most fascinating occurrences of silica. These are layered rocks mainly formed during the Archaic and Proterozoic which consist of alternating layers of iron oxides and microcrystalline quartz, so-called chert [24]. Also microorganisms like diatoms and radiolarians participate in the formation of silica and use it as exoskeletons which is called biomineralisation [25]. This process occurs also in plant during the formation of phytholiths. Hydrous amorphous silica can also form by a replacement reaction from apatite via Mg-calcite and a gel in fossil bones [26].

The mentioned examples exhibit a wide range of crystallographic order which is expressed in terms like “amorphous” or “microcrystalline” and the corresponding silica denominations “opal” or “agate”. Despite the fact that crystallography became a modern science with the first X-ray diffraction of crystals already 100 years ago [27] denomination of non-crystalline is still highly disputed. Flörke et al. [28] call materials without sharp X-ray diffraction peaks “non-crystalline” and regards the term “amorphous” as outdated. Contrary, Heide [29] divides non-crystalline solids into amorphous and glassy solids. The distinction is done by the introduction of the term “comparable state”. The comparable state of an amorphous solid is the crystalline state whereas the comparable state of a glassy solid is the undercooled melt. Heating of glasses transfers them into an undercooled melt (and not directly into a crystalline solid) whereas amorphous solids can crystallize over time. In contrast to glassy solids amorphous solids do not show a glass transition which means that they are not converted from

a brittle into a rubber-like state at a certain temperature during heating [18]. In this thesis hydrous non-crystalline silica is precipitated from aqueous solution and the biogenic analogue, opal-A, which is characterised by a water content of 5 – 14 wt.-% [5], in terms of diatomite is used for zeolite synthesis. Applying the classification of Heide [29], opal-A is an amorphous solid because it is transformed within geologic times via disordered opal with interstratified cristobalite and tridymite domains (opal-CT, Lussatite) and a α-cristobalite-like phase (Opal-C, Lussatine) [30] to microcrystalline quartz (chalcedony) [5]. The increase in structural order from opal-CT to opal-C is associated with a decrease in water content. "Water" in this case does not include only molecular water but also silanol groups Si-OH. Molecular water occurs in type A as isolated molecules in structural cages and type B as "liquid water" adsorbed on internal and external surfaces [28]. Heating opal-A leads to a complete water loss at 1000 °C and a phase transition into cristobalite at 1050 °C [30] which melts at 1734 °C [31]. Contrary, to opal, Lechâtelierite, a fusion-derived non-crystalline silica phase found in meteorites, is a glass showing a glass transition at about 1743 °C [32]. Interestingly, glassy silica can be transformed into opal-A in pyroclastic rocks by hydrothermal alteration and devitrification [33].

Re-fixation of dissolved occurs also by the intake of Si by plants which plays an important role in the biogeochemical cycle of Si in two aspects. On the one hand, for marine plants (phytoplankton) Si is a main nutrient [34], on the other hand dissolved silica is absorbed also by terrestrial plants which increases the weathering rate in the surrounding soil [2]. Plant uptake of silicon increases the weathering rate [2]. In marine ecosystems diatoms play the main role in the silicon cycle because they possess opal skeletons. Since diatoms are responsible for the transport of carbon from the sea surface to the deep sea, they connect the silicon with the carbon cycle which is quite important for climate change [35]. In such biomineralisation processes certain proteins, so-called silicateins and silaffins, increase the polymerisation rates of silica in the solution. Also the transport of silicon into organisms happens by organic molecules. They consist of a hydrophobic and a hydrophilic part formed by amino acid sequences and carboxyl groups, respectively [19]. The filaments which consist of these proteins also act as templates for the formation of silica particles [5]. Due to these catalytic effects, biogenic silica can form from a solution undersaturated with respect to amorphous silica at temperatures between 4 and 40 °C [19]. The short-range order in biogenic silica is limited to a range of about three Si-O bond lengths; hence it is amorphous to X-rays. However all objects of biosilica are composed of regularly shaped particles like spheres with a diameter of about 3 – 5 nm [19] and hydroxyl groups on their surfaces [5]. These structures can have a broad variety of shapes and may also contain holes. Sometimes these particles coalesce and form a dense solid. Since the formation of biosilica involves organic tissue this tissue interpenetrates the particles. Furthermore there are often biopolymers like cellulose which strengthen the structure. During long periods of time biosilica can crystallize and forms microcrystalline quartz (chalcedony) [5]. Silica produced by organisms has different properties than silica produced in the laboratory, for example, it is more stable against electron beams [19].

Besides pure or hydrous silica phases also silicates are formed in weathering environments. Weathering reactions of primary silicates like feldspars, micas and mafic minerals with aqueous solutions lead to the release of cations. Firstly, earth alkali metals like Ca^{2+} and Mg^{2+} are released, followed by alkali metals like K^{+} and Na^{+}. More intense weathering at lower pH and higher water supply finally mobilises silica. From the resulting aqueous solution both amorphous and crystalline siliceous phases, so-called secondary minerals, can form. In these systems besides silicon also aluminium (and besides other also Fe) plays an important role. In weakly acid solutions polymeric Al complexes may be stable besides solid gibbsite

($Al(OH)_3$). At a neutral pH $Al(OH)_3^0$ is present besides $[Al(H_2O)_6]^{3+}$ and in an alkaline solution $Al(OH_4)^-$ is dominant. This means that Al is an amphoteric element because it can act as a cation or as an anion, depending on the pH [11]. Interesting is the interaction between dissolved Si and Al species, since above pH 4 colloids of hydroxo-aluminium-silicates (HAS) are formed. This is ecotoxicologically beneficial because free dissolved Al has a toxic effect on the human brain and inhibits important enzymes in animals and the growth of plants [11]. Furthermore, solid $Al(OH)_3$ can react with dissolved $Si(OH)_4$ to form HAS as well which is accompanied by a release of water. This reaction inhibits the depolymerisation of polysilicic acids. There are two types of HAS: HAS_A or proto-imogolite is characterised by a Si-Al relation of 1:1 whereas HAS_B is formed by continuous condensation of monosilicic acid on a HAS_A complex. In contrast to aluminium hydroxides Al can occur in HAS complexes in a tetrahedral coordination. HAS complexes are amorphous to X-rays and have a spherical shape with a diameter between 0.1 and 0.8 µm. Increasing pH values support the formation of HAS phases whereas at low pH values the SiO_4 tetrahedra within the HAS structure become isolated [11]. A similar process is the direct precipitation of allophane from solution in speleothems [36], as cement in pan horizons of andisols [37], as cell-textured material on the surface of potash feldspars [38] and its formation from amorphous (alumo)silica. Subsequently, allophane might be the precursor for the formation of other aluminosilicates [39]. The role of a precursor can also be possessed by glassy silica from volcanic rocks in the formation of zeolites, e.g. heulandite and later mordenite, and clay minerals [40]. During the formation of the latter often amorphous intermediate phases are formed. These precursors were found with respect to smectite on the surface of plagioclase [38] and with respect to glauconite in marine environments [41, 42]. In some cases the process is the other way around: In certain cherts the silicates magadiite and kenyaite are precursor minerals for the formation of silica:

$$NaSi_7O_{13}(OH)_3 \bullet 3\,H_2O + H_3O^+ \rightarrow 7\,SiO_2(s) + Na^+ + 6\,H_2O \qquad (4)$$ (modified after [43]).

The formation of secondary minerals in aqueous (weathering) environments is often a coupled dissolution and precipitation process. For instances when halloysite is precipitated from solution, it subsequently partly dissolves and kaolinite can be formed [44]. Generally, the formation of metastable intermediate phases by precipitation from aqueous solution can be explained by their lower interfacial tension compared to the corresponding stable phase [44]. Even widespread and frequent silicates in sediments and sedimentary rocks like smectites are not necessarily thermodynamically stable and their occurrence can only be understood by considering reaction kinetics [38]. However, finally stable secondary minerals should form.

1.3 Application of Amorphous Silica

It has been shown in the previous chapter that amorphous silica plays a crucial role in Earth sciences. Interestingly, the importance of this material exceeds this field and reaches far into material sciences where it has a wide range of applications including the storage and release of pharmaceuticals [45], industrial coating systems [46], raw material for the production of silicate glasses [47] and as a carrier of quantum dots and nanocatalysts [48] or antibodies [49]. These two fields, Earth and materials sciences, conflate in mineralogy, when amorphous silica is used for the sorption of radioactive nuclides in waste disposal [50] or formed on feldspar surfaces in nature explaining not only feldspar survival in some weathered granites, but enhancing also application of feldspars and feldspar-containing rocks for building purposes and in ceramic industry [51]. Another silica-containing material, water glass – water-soluble sodium silicate glass - , is added to drinking water to avoid corrosion because the water glass

molecules are adsorbed on the corrosion products and form a protection layer which stops the corrosion. The problem is that the dilution of the water glass in the water tube leads to depolymerisation and monomeric silicic acid has in contrast to water glass no anti-corrosive effect [8]. On the other hand, precipitation of amorphous silica has also a negative effect in several technical applications, for example in steam power stations, where it decreases the efficiency of the machine by scaling. Hence dissolved Si has to be removed by using hydroxides of Al or Mg which adsorb the silica on their surfaces [5].

In this thesis previous research where amorphous mesoporous aluminosilicates with large pores compared to e.g. zeolites were synthesised in a sol-gel process [52] [53] is used as an inspiration to tailor hierarchically structured materials for heavy metal removal from aqueous solutions!

1.4 Si Isotope Geochemistry

1.4.1 Introduction into Isotope Geochemistry

Isotopes are atoms of a chemical element which possess a different number of neutrons resulting in a different mass. Chemical processes affect mainly the electron shells of atoms and not their nuclei where the protons and neutrons are located. Hence different isotopes of the same element behave very similarly in chemical reactions. However, slight differences occur due to their different masses which are called mass dependent isotope effects [54]. For example, a heavier isotope is less mobile which decreases the reaction rate which is the key for so-called kinetic fractionation of isotopes. On the other hand, heavier isotopes form stronger bonds due to their lower vibrational frequency, especially for high field strength elements, which explains so-called equilibrium fractionation [54]. The pressure-dependency of this process is mostly low which makes the isotope geochemistry of phases in equilibrium a good proxy for temperatures at their formation which is called geothermometry [54]. Equilibrium fractionation is reached via isotope exchange according to a reaction

$$aA_1 + bB_2 \leftrightarrow aA_2 + bB_1 \tag{5}$$

which is characterised by an equilibrium constant K:

$$K = \frac{\left(\frac{A_2}{A_1}\right)^a}{\left(\frac{B_2}{B_1}\right)^b} = \frac{R_A^a}{R_B^b} \tag{6}$$

A and B are species or phases which contain either the light or heavy isotope 1 or 2, respectively [54]. The equilibrium constant is a function of temperature resulting in a decrease of fractionation with increasing temperature. Isotope fractionation is often also expressed by the fractionation factor α which is defined as the isotope ratio in phase A divided by the corresponding ratio in phase B:

$$\alpha_{A-B} = \frac{R_A}{R_B} \tag{7}$$

The equilibrium constant and the fractionation factor are connected by the number of exchanged atoms n:

$$\alpha = K^{\frac{1}{n}} \tag{8}$$

The isotopic composition of a phase A is commonly referred to the isotopic composition of a standard reference material and expressed as δ-value:

$$\delta^x y_A = \left(\frac{R_A}{R_{St}} - 1 \right) \cdot 10^3 \ (‰) \tag{9}$$

where R_A and R_{St} are the isotope ratios of the phase A and the standard, respectively, and x is the mass of the heavier isotope of the chemical element y [54]. The δ-values of two phases A and B and the fractionation factor between them are related via

$$\delta^x y_A - \delta^x y_B = \Delta^x y_{A-B} \approx 10^3 \ln \alpha_{a-b} \tag{10}$$

and

$$\alpha_b^a = \frac{\delta_a + 10^3}{\delta_b + 10^3} \tag{11} [55]$$

The approximation is quite good for δ-values less than 10 ‰ and for small Δ values. The temperature dependency of isotopic fractionation in equilibrium is expressed by

$$1000 \ln \alpha = \frac{A}{T^2} + B \tag{12}$$

with the temperature T (in Kelvin) and the factors A and B as constants for a certain isotope system [54].

However, in this thesis kinetic isotope fractionation plays a more important role since equilibrium is generally not reached in Earth surface systems. Kinetic isotope fractionation has been studied since the 1950´s [56]. It was found that unidirectional chemical processes can lead to an enrichment of the lighter isotope in the reaction product [54]. As described above the different masses resulting in a different mobility of different isotopes are the reason for this behaviour in most cases. This is called mass-dependent fractionation and results in the observation that in isotope systems with three isotopes, e.g. oxygen with ^{16}O, ^{17}O and ^{18}O, the enrichment of ^{16}O to ^{18}O is about twice as large as that of ^{17}O to ^{18}O [54]. There are also some cases for mass-independent fractionation where this ratio is not valid. Examples include mainly extra-terrestrial processes and are mostly not yet completely understood [54].

1.4.2 Si Isotopes

Silicon possesses three stable isotopes, ^{28}Si, ^{29}Si and ^{30}Si with relative abundances of 92.23, 4.68 and 3.09 %, respectively [57]. Silicon isotope ratios are mostly – and also in this thesis - referred to the standard reference material NBS28, a quartz sand which is characterised by $^{29}Si/^{28}Si$ of 0.0508 and $^{30}Si/^{28}Si$ of 0.0335. This corresponds to abundances of 92.22 % ^{28}Si, 4,69 % ^{29}Si and 3,09 % ^{30}Si which is very close to the overall abundances [58]. The corresponding $\delta^{29}Si$ and $\delta^{30}Si$ values are related by an equilibrium mass-dependent fractionation law: $\delta^{30}Si = 1.93 \bullet \delta^{29}Si$ [59]. There are different numbers concerning the variation of the $\delta^{30}Si$ value: One study estimates an overall variation of 6.2 ‰ [60] whereas another found even only in terrestrial samples a variation from -5.7 to +3.4 ‰ [61]. The heavier isotope occurs especially in Si-rich rocks and minerals. It does not seem to be possible to distinguish between biological processes and abiotically derived silicon by means of isotope geochemistry [60]. The $\delta^{30}Si$ values in water samples range from -0.8 top +3.4 ‰, those in soil solutions from -0.8 ‰ to +1.7 ‰ [61] and the variation within igneous rocks is only 1.1 ‰ [60]. This means that there is an enrichment of ^{30}Si in solution due to the formation of isotopically lighter secondary silicates [61]. These results confirm data for marine water of $\delta^{30}Si = 1.1 \pm 0.3$ ‰ [35]. Analogously the precipitation within aqueous solutions with a $\delta^{30}Si$ around zero leads to the formation of non-crystalline solids with a $\delta^{30}Si$ around -1.4 ‰ [60]. For this process a fractionation index $\alpha^{30}Si_{Opal\text{-}Si(aq)}$ of 0.9963 to 0.9969 was observed [60] whereas another study calculated 0.9989 [62]. Logically, this enrichment of ^{29}Si in the solid phases is accompanied by an increase of the $\delta^{30}Si$ in the sea water [35]. In deep sea waters there is a correlation between the silicon concentration and the $\delta^{30}Si$ value [63]. In surface waters the $\delta^{30}Si$ is higher than in deep sea waters because ^{28}Si is preferentially incorporated into amorphous silica which precipitated from these wasters [35]. Riverine waters have a higher $\delta^{30}Si$ (0.8 ± 0.3) [35] than igneous rocks (-0.3 ± 0.3) [60]. This might be explained by the preferred uptake of ^{29}Si by plants and its deposition as phytoliths therein. Clays are depleted in ^{29}Si compared to igneous rocks. The reaction of feldspars, micas or pyroxenes to clay minerals is related with the release of Si. Biogeneous silica in sponges is also enriched in the light isotope. An isotopic fractionation in the same range occurs during the formation of disordered phyllosilicates, but not during the precipitation of quartz from an aqueous solution (at least above 50 °C). This means that a fractionation of silicon isotopes happens preferentially in amorphous or poorly ordered solids at earth surface temperatures. From this fact it can be concluded that the fractionation might be due to kinetic factors. One of these factors was found by Goldstein [64]: The lighter isotope has a higher reactivity. The reason why this effect can only be seen in a sedimentary system is its openness with respect to the supply of dissolved silica. Hence the number of dissolved ions is much higher than the number of precipitating ions. The transformation of amorphous silica to chalcedony during the diagenesis of siliceous sediments is associated with solution and re-deposition leading to a re-establishment of the equilibrium between the Si isotopes [60]. Figure 1 summarises the fractionation process of Si isotopes in the geochemical cycle:

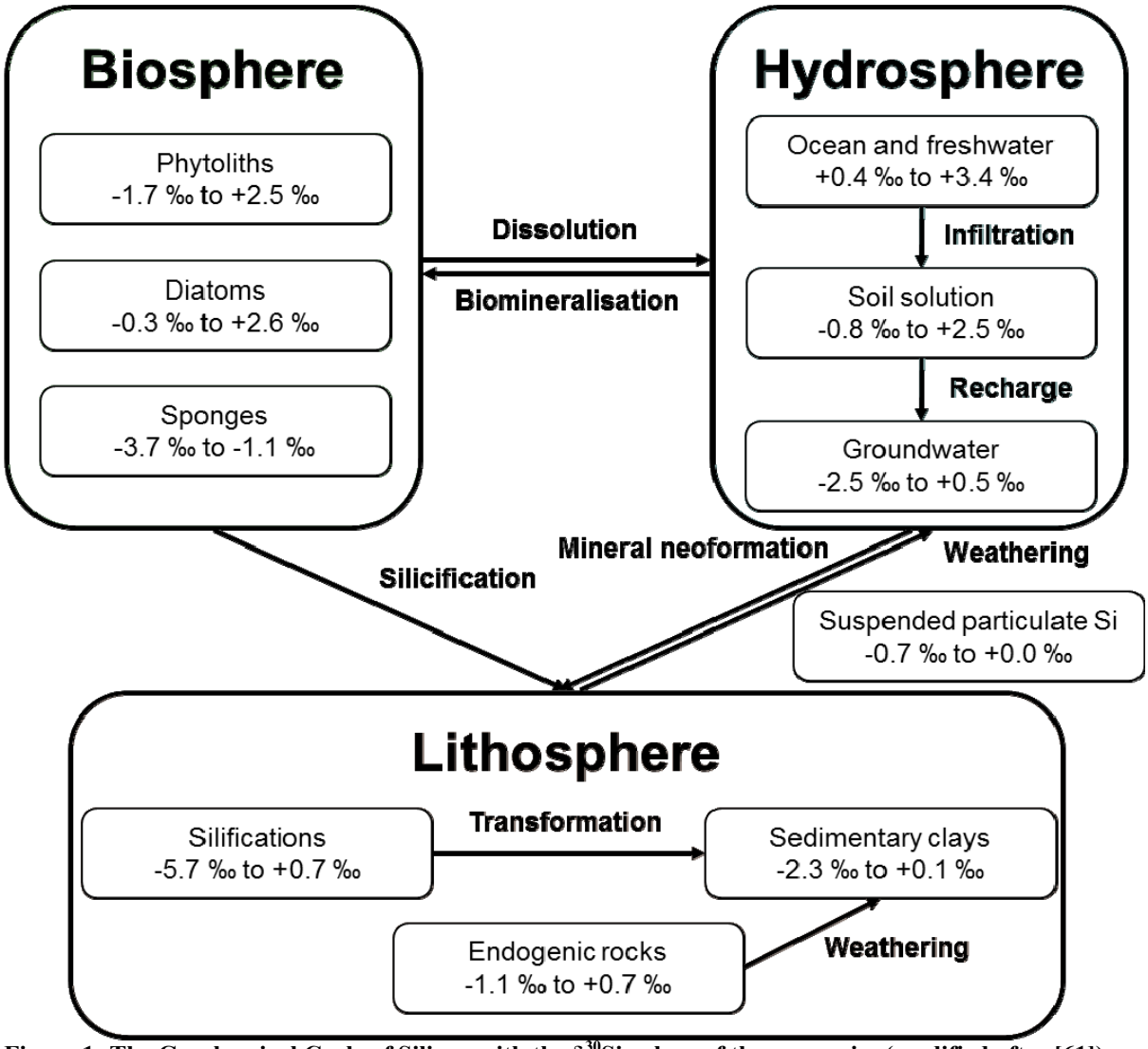

Figure 1: The Geochemical Cycle of Silicon with the δ^{30}Si values of the reservoirs (modified after [61])

There are two different explanation models for the fractionation of silicon isotopes: The Rayleigh model [65] assumes a closed system in which ^{30}Si is enriched exponentially with time in the residual $Si(OH)_4$ solution when a solid phase which discriminates versus ^{30}Si is precipitated from it. This model explains well the fractionation of silicon isotopes in several continental environments. Contrary, in oceans a steady state model considering the continuous supply of $Si(OH)_4$ to the system is more applicable. A part of the monosilicic acid entering the system is transferred to the liquid phase, another part to the solid phase [61]. However, also the Rayleigh model has been applied successfully as a proxy for the role of marine diatoms in the carbon cycle [63].

2 Adsorption of Silicic Acids onto Gibbsite

2.1 Introduction

Adsorption plays an important role in Earth surface processes. Al-hydroxides like gibbsite are common minerals formed in sedimentary environments. Silicic acid is a main species in aqueous solutions. As SiO_2 and Al_2O_3 are the main components of clay minerals the interaction between silicic acid and gibbsite is suggested to be relevant in respect to neoformation of clay minerals in weathering environments.

Adsorption at Solid Surfaces

Adsorption is the accumulation of a chemical substance on a phase boundary [66]. In cases where a dissolved species is adsorbed on a solid surface, the former is called the adsorbate, the latter the adsorbens. The connection, i.e. the chemical or physical bound, between both at a certain solid site is called the adsorption complex [66]. The proportion between adsorbed and dissolved species on a given solid surface depends on pH and concentration where individual adsorption behaviour can be displayed by so-called adsorption edge and adsorption isotherm, respectively [66]. The dependency of adsorption on pH can be explained by the structural surface charge of a solid and by a change in distribution of dissolved species. Especially phases which contain functional groups like OH, which are subjected to protonation and deprotonation, show a pH-dependent adsorption behaviour. These surface groups can carry a surface charge and are responsible for the net charge changes through pH caused by variation in their individual concentration at the solid surfaces. A lot of $(H_3O)^+$ ions occur in solution at acidic pH. These ions protonate the surface and create a positive surface charge. Vice versa at alkaline pH the surface is deprotonated. For every phase there is a characteristic point of zero charge, abbreviated p.z.c., where the surface charge is zero. The pH at which this p.z.c is reached is called pH_{PZC}. Negatively charged species are preferentially adsorbed at acidic and slightly alkaline pH, whereas positively charged species occur at alkaline pH. At longer adsorption times and higher adsorbate concentrations clusters, so-called multinuclear surface complexes, can be formed as precursors for surface precipitates [66]. The bond between adsorbate and adsorbens can be of different strength: If the former is hydrated and therefore loosely bounded to the surface, it is called an outer-sphere complex, whereas a direct chemical bound at the surface is called inner-sphere complex [66].

Adsorption processes play an important role in Earth surface systems. For example, chemisorption of K onto amorphous precursor silica phases is suggested to play an important role for illite formation [67]. In these experiments amorphous aluminium hydroxide was precipitated and Si, K and Mg were fixed on its surface by chemisorption resulting in an x-ray amorphous gel. Ageing of this gel lead to the formation of illite [67]. Other experimental studies showed the formation of authigenic chamosite-like minerals by adsorption of silicic acid on aluminium and iron hydroxide in estuarine and marine environments [68] and the formation of hydroxyapatite by adsorption of Ca and P on boehmite [69]. In further cases the effect of adsorption processes on mineral formation is more complex, e.g. the adsorption of sugars onto ferrihydrite which can inhibit its transformation into hematite and goethite, but also change the crystal habit of the newly formed minerals [70]. The reaction of brucite-gibbsite layers with silica layers during the formation of silicates [67], the intercalation of hydroxyaluminosilicate and hydroxyl-Al ions into montmorillonite [71] and the exchange of K^+ against H_3O^+ during the formation of illite from muscovite [38] can be also treated as

adsorption processes. In the SiO_2-Al_2O_3-H_2O system, especially the adsorption of aluminium ions onto amorphous silica has been studied intensively [72]. In this study, the reverse process, the adsorption of silicic acid onto Al hydroxides, shall be investigated and previous studies are summarised below.

Adsorption of Silicic Acids onto Mineral Surfaces

Adsorption of monosilicic acid onto α-Al_2O_3 has already been studied since the 1970s [73]. It was shown that adsorption from dilute solutions (0.1 to 1 mmol L^{-1} Si) is characterised by an S-type isotherm [73]. Within the first one or two hours adsorption is fast with a rate constant proportional to $[Si]^{1.5}$, whereas later on adsorption slows down to a first order reaction [73]. In later studies also aluminium hydroxide was used for adsorption of monosilicic acid which polymerised on the surface (especially at pH 9 to 9.5) and transferred the aluminium hydroxide into a allophane-like aluminosilicate [74]. Different adsorption reactions could be distinguished, i.e. reactions between monosilicic acids (adsorbed or dissolved), reaction between dissolved monosilicic and newly formed adsorbed polysilicic acids and reactions between polysilicic acids [74]. Furthermore, it was suggested that with increasing initial Si concentration the relative amount of dissolved monosilicic acid after the adsorption experiment decreases [74]. In a further study the adsorption of silicic acid onto crystalline aluminium hydroxide (the modification was not mentioned) was studied [75]. It was demonstrated that during adsorption of silicic acid a part of the octahedrally coordinated aluminium in the solid is transferred into a tetrahedral position which was accompanied by the formation of an amorphous aluminosilicate and an increase of the specific surface area [75]. Also the adsorption of mono- and polysilicic acids on gibbsite has already been studied [76]. Monosilicic acids can be adsorbed onto surfaces of Fe and Al hydroxides even from solutions which are strongly undersaturated in respect to amorphous silica and also in respect to quartz (down to about 50 μmol L^{-1} SiO_2) [77]. The adsorption of monosilicic acid onto ferrihydrite and goethite was also studied by other authors [78] [79]. These adsorption processes result in an x-ray amorphous phase containing up to 90 wt. % SiO_2 [77]. Reaction of this phase with a solution containing silicic acids, but undersaturated with respect to amorphous silica may finally lead to the formation of quartz, e.g. by alteration [77]. Also the adsorption of silicic acids onto gibbsite has been studied in a 0.01 M NaCl solution within a pH range from 4 to 11 [80]. Furthermore it has been shown that silicic acids form weaker surface complexes on gibbsite than on ferrihydrite [81]. Polysilicic and monosilicic acids were adsorbed onto various iron oxides and hydroxides and also onto gibbsite [14]. It was found that polysilicic acids are adsorbed more easily to hematite surfaces than monosilicic acid and that after some time the polymer depolymerises and is desorbed from the hematite surfaces [76]. Despite all these studies some open questions remained, especially the effect of adsorption on Si isotope fractionation which is discussed below.

Si Isotopes as a Proxy in Low-T Environments

The application of Si isotopes in earth sciences reaches back to the 1950s [82]. Almost 30 years later kinetic fractionation of -3.5 ‰ considering ^{30}Si and ^{28}Si by precipitation of opal from aqueous solutions with light isotopes favouring incorporation in the solid could be shown [60]. This effect can be explained by the higher reactivity of lighter isotopes [64]. As a result of precipitation of isotopically lighter secondary minerals in weathering environments, both marine and fluviolacustrine waters are isotopically heavier than igneous rocks [35]. Since silica is used by various organisms as shell material, biotic effects on Si isotope fractionation were also investigated, e.g. a fractionation of -1.1 ‰ by diatoms was observed also with a preference to incorporate lighter isotopes in the solid [62]. This preference is

suggested to be independent from temperature [62]. The application of Si isotopes as a proxy in low-T environments was first tested to reconstruct diatom population and growth in the last glacial period [83]. The oceans are an open system where new silicon is provided by upwelling of water from the depths. Thus opal precipitation in the diatoms, which discriminates against ^{30}Si, leads to a heavier and heavier isotopic signature in the diatoms with more intense diatom growth. The idea behind this scenario is that few diatoms can select the light isotopes better than many diatoms. Hence when diatom growth flourishes isotopic fractionation decreases and diatoms become isotopically heavier. This is in agreement with the observation that during the last glacial maximum, when diatom productivity was minimal, δ^{30} Si values of diatomite were very light, whereas post-glacial temperature increase made diatomite isotopically heavier [83]. The knowledge of fractionation of Si isotopes by diatoms was also used to analyse mixing between surface and deep-sea waters in oceans [84]. Interestingly, Precambrian cherts are enriched in heavy Si isotopes versus the recent global average. This can be explained as follows: In the Precambrian the oceans were very warm. Hence silica precipitation was less intense than today because the solubility of amorphous silica increases with temperature. The less silica precipitates, the higher is its $\delta^{30}Si$ value, which can be explained by a rate effect. Therefore $\delta^{30}Si$ can be used as a paleothermometer: The higher the $\delta^{30}Si$ the warmer is the seawater [85].

Silicon isotope fractionation by adsorption processes has already been studied: During the adsorption of monosilicic acid onto iron oxides light isotopes are favoured. The initial isotopic signature of $\delta^{30}Si = 0.02 \pm 0.07$ ‰ of the dissolved silica shifted during adsorption on iron oxides to values between 0.16 and 0.95 ‰ after 72 h [79]. This explains why river water is depleted in light isotopes [35]. The corresponding heavy reservoirs might be related to precipitated quartz or opal [86], siliceous parts of plants [87] and clay minerals [88], although a comparative study showed that these reservoirs show an isotopically lighter composition than sea water [61]. Also during adsorption of monosilicic acid onto ferrihydrite and goethite the initial isotopic composition of the solution of $\delta^{30}Si = 0.01 \pm 0.04$ ‰ shifted to 0.70 ± 0.07 ‰ for ferrihydrite and 0.50 ± 0.08 ‰ for goethite [78]. The progressive change of the isotopic composition of the solution can be fitted by a Rayleigh process. It seems reasonable to describe an adsorption process by this model which was initially used to describe a condensation process [54]. In this case the initial isotope ratio of a vapour, R_{V0}, develops towards lighter values for the fraction, f, of residual vapour, R_V, due to the condensation of heavier isotopes according to

(13:

$$\frac{R_V}{R_{V0}} = f^{(\alpha-1)} \qquad (13)$$

Aim of this study

In this study the adsorption kinetics of monosilicic and polysilicic acids onto gibbsite is investigated. Differences between both silica species and the effects of pH, solid: liquid ratio and Si concentration in the adsorption behaviour of silicic acid shall be discovered. Silicon isotope fractionation is used as a proxy to distinguish between adsorption processes and silica precipitation induced by cyclic freezing (Chapter 3). Differences between adsorption kinetics of monosilicic and polysilicic acids might fractionate both species in natural systems and the competition between depolymerisation and adsorption is discussed.

2.2 Methodology

2.2.1. Materials

Monosilicic acid was obtained by dissolving Tetraethylorthosilicate (TEOS, Merck, p.a.) in MilliQ water. A stock solution was prepared by dissolving 5.9 g TEOS in 20 L MilliQ water (18.2 MΩ) resulting in a Si concentration of 1472 µmol L^{-1} (~ 40 ppm) and in a pH of 5.4 ± 0.1. Polysilicic acid was used in the form of a sodium water glass (37/40, cognis, 26.93 wt.-% SiO_2, 7.99 wt.-% Na_2O). For experiments with polysilicic acid the suspended gibbsite (γ-$Al(OH)_3$, Merck) was pre-treated for 10 min in an ultrasonic bath (Kudos, 35 kHz) to separate very fine particles with an extraordinarily high adsorption capacity. 30 min after the treatment the supernatant solution was decanted. The sediment was washed with MilliQ water into a porcelain dish and dried at 40 °C. However, for experiments with monosilicic acid pre-treatment was not performed because the fine fraction of Al-hydroxides is thought to play an important role in sedimentary systems as well.

2.2.2 Experimental setup

Experiments with Monosilicic Acid

Adsorption experiments were conducted following the approach of Dietzel & Böhme [76]. In this thesis experimental results are discussed from the point of view of mineral-forming processes whereas in a separate manuscript [89] selected experiments are discussed in the scope of isotope fractionation. Three sets of experiments were conducted for which the Si stock solution was either used undiluted or diluted with MilliQ water to about 20 and 10 ppm (749 and 342 µmol L^{-1}), respectively. The Si concentration is in all experimental solutions below the solubility of amorphous silica [90]. It was checked by the silico-molybdate method [16] that all Si occurs in the monomeric form. 385 mmol (30 g) gibbsite were suspended and 100 mmol NaCl were dissolved in PE bottles containing 1 L of the Si solution and mixed with a stirrer resulting in a pH of 7.3 ± 0.2. pH was adjusted to distinct values ($4.5 \leq pH \leq 8$) and kept constant by titration with 0.1 M NaOH or HCl. After the initial period of frequent sampling the bottle was closed with parafilm to prevent evaporation. During the first six hours of the experiment, the suspension was stirred at 500 rpm using a IKA RW 20 DZM rotor with a Teflon stirrer. Later the bottles were closed and placed in an overhead shaker. Samples of 15 mL were taken with a syringe and solutions were separated from the solid by cellulose acetate filters (0.45 µm). Experimental runtimes accounted for up to 64 days.

Experiments with Polysilicic Acid

In experiments with polysilicic acids 0.1 mol NaCl were dissolved in 1 L MilliQ water to provide a high and constant ionic strength. HCl was used to adjust pH 2.9 ± 0.2 where polysilicic acids are metastable. Then various amounts polysilicic acid were added resulting in total Si concentrations between 0.6 and 1.3 mmol L^{-1} and a pH increase to 3.3 ± 0.1. A sample of this solution was taken to measure the total Si content. In this solution NaOH was added to increase the pH to 9.1, where polysilicic acid in the form of water glass depolymerises within a short time. After two hours this sample was analysed by UV-Vis spectroscopy to determine the total Si concentration which has now been transferred to the monomeric form. Additionally, the depolymerisation kinetics was investigated at pH 3, where polysilicic acids are metastable.

A gibbsite suspension was made by adding various amounts of gibbsite (128 mmol ≤ n ≤ 385 mmol) to 500 mL MilliQ water. For the gibbsite suspension a constant and high ionic strength was adjusted by dissolving 0.05 mol NaCl in 0.5 L MilliQ water resulting in the same ionic strength of 0.1 molL^{-1} like for the Si solution. 500 g of the polymeric Si solution were used for the experiment and mixed with a gibbsite suspension in a 1:1 ratio. Consequently, the determined initial Si concentration of the stock solution and the gibbsite concentration of the suspension were divided by a factor of 2 which is considered in all experimental results. The Si solution was poured into the gibbsite suspension resulting in a pH between 3.1 and 3.8 depending on Si concentration. The pH was kept constant afterwards by addition of HCl. Samples were taken by a syringe and filtered (0.45 µm) after various durations (0.13 h ≤ t ≤ 46 h).

The experiments with polysilicic acid are further on labelled as follows:
a: 385 mmol L^{-1} gibbsite, 651 µmol L^{-1} Si, pH 3.4
b: 385 mmol L^{-1} gibbsite, 587 µmol L^{-1} Si, pH 3.6
c: 769 mmol L^{-1} gibbsite, 249 µmol L^{-1} Si, pH 3.7
d: 385 mmol L^{-1} gibbsite, 304 µmol L^{-1} Si, pH 3.6
e: 385 mmol L^{-1} gibbsite, 618 µmol L^{-1} Si, pH 3.8
f: 192 mmol L^{-1} gibbsite, 653 µmol L^{-1} Si, pH 3.1
g: 128 mmol L^{-1} gibbsite, 655 µmol L^{-1} Si, pH 3.6

2.2.3 Analytics

Attenuated total reflexion Fourier-transformed infrared spectroscopy (ATR-FTIR, Perkin Elmer 100**)** was used in this thesis to characterise the gibbsite. FTIR spectroscopy detects vibrations of molecules. There are two types of molecule vibrations. A vibration where two atoms swing back and forth along the chemical bond is called stretching vibration. A molecule with three atoms can perform bending vibrations where the bonding angle changes but the bond lengths remain constant. Those vibrations which change the dipole momentum of the molecule are IR-active, the others are IR-inactive. Sometimes there are less vibration bands than expected because some vibration levels are degenerate. Sometimes there are additional vibration bands due to the combination of vibrations or due to the harmonics. An IR spectrometer consists of an IR radiation source, a sample chamber, a monochromator, a receiver and an analysing unit. The radiation source can be a Nernst glower of Y_2O_3 or ZrO_2. There are two different detector types. A thermocouple converts the IR radiation into caloric energy; a bolometer converts the radiation energy into electric energy, for example with a semiconductor. A special form of IR spectroscopy is the Fourier transformed infrared spectroscopy (FTIR). The measured pattern in this technique is called interferogram. In this type of FTIR the infrared radiation hits a ray splitter which reflects half of the light and transmits half of it. Each of these partial rays is reflected by a mirror and both rays interfere afterwards. If the two mirrors are arranged symmetrically the partial rays interfere constructively, a relative movement of the mirrors leads to a pathway difference or even to a destructive interference.

X-ray diffraction (XRD, Panalytical X´Pert Pro) was also used to characterize gibbsite. The angle of incidence, 2 Θ, was varied from 4 to 85 °, the step size accounted for 0.017 °2Θ, the measuring time accounted for 20.7 s, the divergence slit was set fix to 0.5 ° 2Θ and the anti-scattering slit to 1 ° 2Θ.

The total specific surface area was measured by BET analyses [91] using an ASAP 2010 V3.02 equipment. Si concentration and speciation were analysed by UV-VIS spectrometry (Varian 100). Calibration was performed with a one-point calibration using a 10 mgL^{-1} standard diluted from a Merck single element ICP standard. Calculation of the polymeric and monomeric percentage of Si was done according to [8]. Monomeric and polymeric silica can be distinguished by UV-Vis spectroscopy where a yellow complex of β-silicomolybdic acid is formed from both polymeric and monomeric silica [8]:

$$7\ Si(OH)_4 + 12\ H_6Mo_7O_{24} \bullet 4\ H_2O + 126\ H_2O \rightarrow 7\ \beta - H_8Si(Mo_2O_7)_6 \bullet 28\ H_2O \qquad (14)$$

Both monomeric and polymeric silica react with the molybdate in a pseudo first-order reaction according to the overall equation

$$X_r = \frac{[M]}{[M]+[P]} \bullet (1 - e^{-k_M \bullet t}) + \frac{[P]}{[M]+[P]} \bullet (1 - e^{-k_P \bullet t}) \qquad (15)$$

to form the above yellow coloured Si-molybdate complex. X_r is the already reacted Si versus initial total Si content [16], t is the elapsed time of measurement, k_M and k_P are reaction rate constants and [M] and [P] are the concentrations of monomeric and polymeric silica at the beginning of a measurement, respectively [8]. The reaction rate of monosilicic acid is about two orders of magnitude higher than that of typical polysilicic acid gained from water glass. The reason for this is that only monosilicic acid reacts directly with the molybdate complex whereas polysilicic acid depolymerises first and the monomers delivered from polymerisation react afterwards. The β-complex shows a characteristic absorption at a wavelength of 390 nm. Hence the concentrations of monomeric and polymeric silicic acid can be measured with a photometer due to their chronologically displaced colour increases. The monomer reacts completely to the β-complex within five minutes. After this period only the formation of the β-complex from the polymer is important for β-complex formation. In a diagram which shows the unreacted percentage of the total silica as a function of time, the slope of the curve beyond 5 min can be prolonged to the ordinate axis. This section approximates the polymeric percentage of the total silica after a certain depolymerisation time [8]. k_M is close to 2 min^{-1} whereas k_P decreases for dimeric, tetrameric, hexameric and octameric silica from 0.9 via 0.7 and 0.6 to 0.4 min^{-1} and for even larger molecules down to 0.001 min^{-1}. k_P is also related to an average diameter d (nm) of the silica species ($\log(d) = -0.284 \bullet \log(k_P)$) from which the polymerisation degree, the number of silicon atoms per molecule, can be calculated ($N = 11{,}5\ d^3$) [5]. After a couple of hours the β-Si-Mo-complex is converted above pH 3 into an α-complex [8], thus analytical data are recorded for a measuring time about 10 min where this conversion can be neglected.

ICP-OES (Perkin Elmer Optima 4300 & Varian Vista Pro) was used to determine total Si and Al concentrations. Calibration of ICP-OES for the Perkin Elmer Optima 4300 was done using three standards containing 0.1, 1 and 10 mgL^{-1} of both Si and Al which were prepared from Merck ICP standards.

Determination of Si isotopic composition was performed at the German Research Centre for Geosciences (GFZ) like described in [92] in the high resolution mode on a Thermo Neptune multi-collector inductively coupled mass spectrometer (MC-ICP-MS) equipped with an H-skimmer cone and the newly developed ThermoR Jet-interface. A detailed description of sample preparation is given in the separate manuscript [89]. Reported errors on delta values are the 95% confidence interval (CI) calculated according to

(16 where $\overline{\delta^{30}Si}$ is the mean of the measured delta values for the sample or standard (at least n=4), t_{n-1} is a critical value from tables of the students-t law and SE is the standard error of the mean.

$$CI = \overline{^{30/28}Si_{NBS28}} \pm t_{n-1} \cdot SE \quad (16)$$

The well-defined Si isotope reference material BHVO-2g, a basalt standard (measured in the last 12 months; includes several individual chemical separations as well as several digestion procedures; $\delta^{30/28}Si_{NBS28}$ = -0.27 ± 0.02; n=73) was usually measured as control standard.

2.3 Results

2.3.1 Experiments with Monosilicic Acid

Characterisation of Gibbsite

ATR-FTIR analyses (Figure 2) show the typical characteristics of gibbsite. The vibrations at 732 and 1014 cm^{-1} are Fe-OH bending vibrations, those at 3370, 3437, 3522 and 3619 cm^{-1} Fe-OH stretching vibrations.

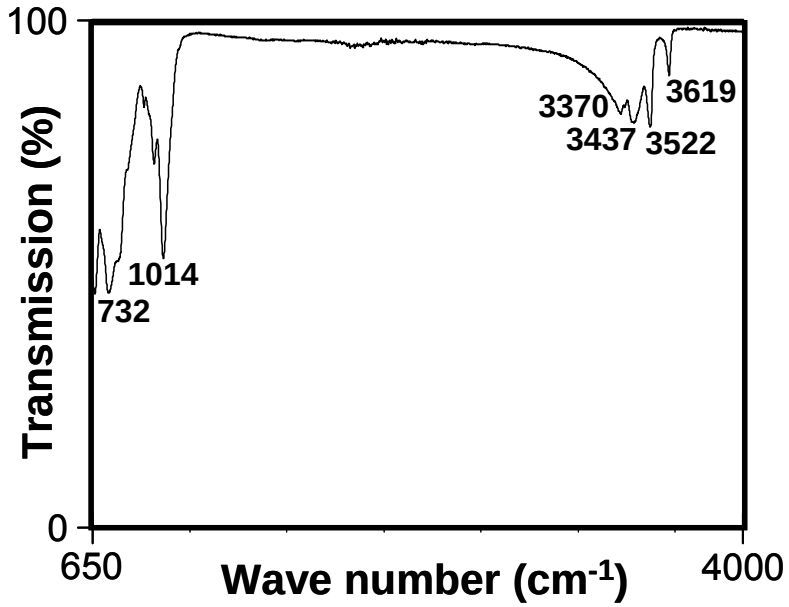

Figure 2: ATR-FTIR spectrum of gibbsite used for adsorption experiments.

The XRD pattern (Figure 3) confirms ATR-FTIR results and reveals the dominant (002), (110), (-112) and (311) lattice planes:

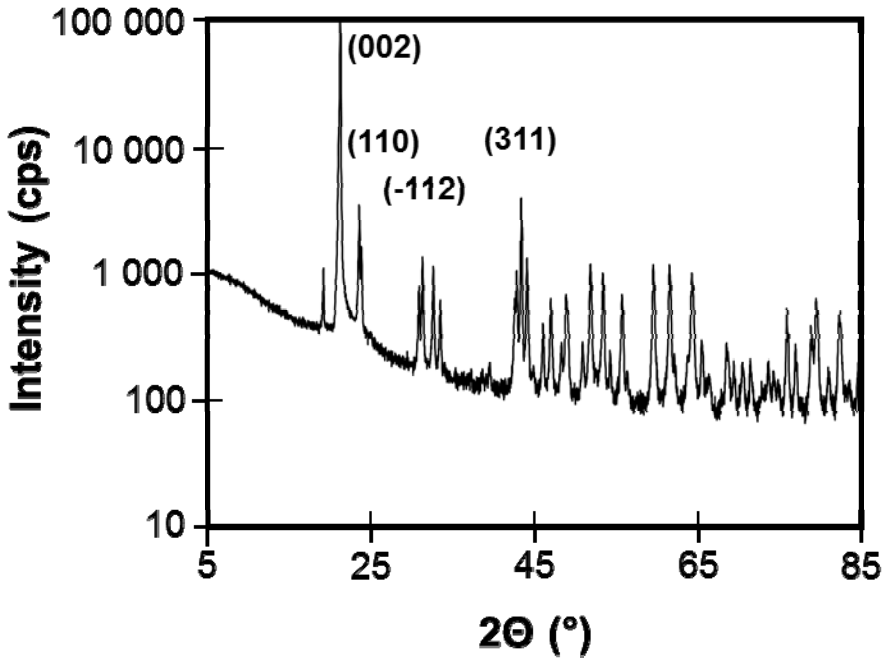

Figure 3: XRD pattern (Co Kα) of gibbsite used for adsorption experiments.

Untreated gibbsite used for experiments with monosilicic acid is characterised by a specific BET surface area of 1.18 ± 0.02 m^2g^{-1}.

Adsorption kinetics

Effect of pH

In a first set of experiments the effect of pH in the range from 5 to 8 on adsorption kinetics of monosilicic acid onto gibbsite was investigated. All other experimental parameters were kept constant: The initial Si concentration accounted for 342 µmol L^{-1} and the gibbsite concentration for 385 mmol L^{-1} which corresponds to 30 g L^{-1} or a surface area of 35.4 m^2 L^{-1}. The experimental results are displayed in Figure 4. Si concentrations were used from UV-Vis analyses. No polymeric silicic acids were detected adsorption experiments carried out with monosilicic acid. However, this does not exclude a potential polymerisation of silicic acids at the gibbsite surface.

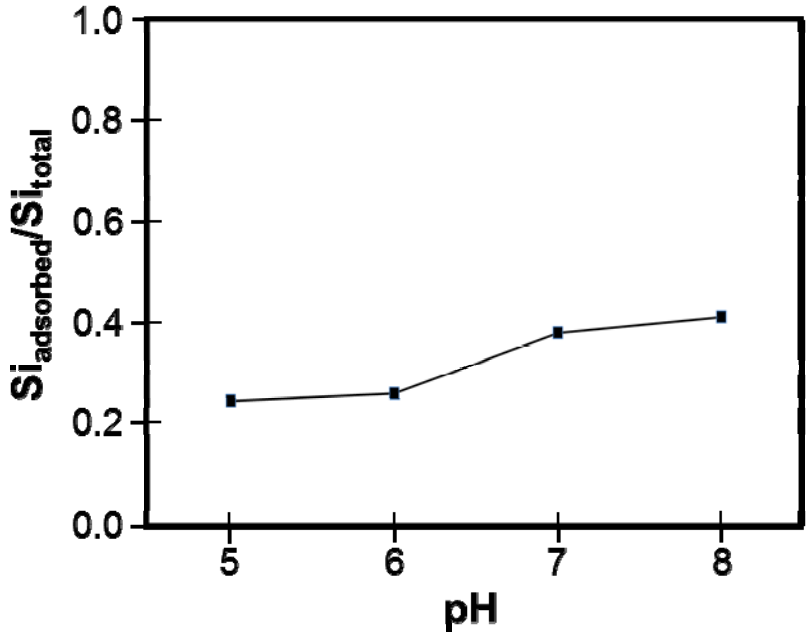

Figure 4: Relative final adsorbed Si concentrations after 72 h adsorption onto gibbsite as a function of pH

The adsorption of monosilicic acid onto Gibbsite is a fast process that is completed within the first hour. Afterwards the concentration of dissolved Si remains constant for several days. A variation of pH shows that at acidic pH (5 or 6) only about 25 % of Si are adsorbed but at neutral and slightly alkaline pH (7 or 8) even 40 to 50 % are adsorbed. Two additional experiments performed at pH 4.5 at different conditions (416 µmol L^{-1} and 1365 µmol L^{-1} Si, respectively) showed no significant adsorption at all.

Effect of Si concentration

Since Si adsorption onto Gibbsite was shown to be more intense at neutral (or slightly alkaline) pH, for further experiments a pH of 7 was chosen. In these experiments the initial Si concentration was varied (355 µmol $L^{-1} \leq c \leq$ 1472 µmol L^{-1}) and the sampling intervals were shortened to increase the temporal resolution for the calculation of adsorption rates. Experimental results from ICP-OES analyses (Varian Vista Pro) show a continuous decrease over time (Figure 5):

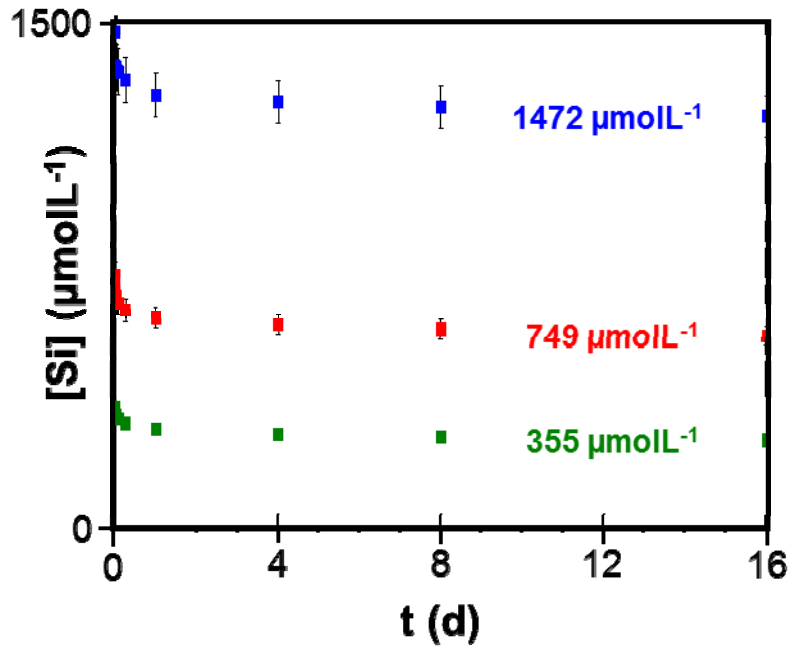

Figure 5: Si concentration in solution as a function of time during adsorption onto gibbsite at various Si concentrations (Table 1)

Between 17 and 29 % of the available Si was adsorbed (Table 1). The lower the initial Si concentration was, the higher was the relative amount of adsorbed Si. For example, after 384 h, 17 % of the initially dissolved silica was adsorbed at an initial Si concentration of 1472 µmol L^{-1}, 24 % at 749 µmol L^{-1} and 29 % at 355 µmol L^{-1}. Concerning the absolute amounts of adsorbed Si after 384 hours, 250 µmol were adsorbed at high, 181 µmol at intermediate and 96 µmol at low Si concentrations which is the inverse order of relative adsorption.

It was shown that adsorption of monosilicic acid onto gibbsite occurs in two or three periods. During the first period which lasts for between 0.5 and 6 hours the adsorption rate constant accounts for 0.05 to 0.17 h^{-1}. For an initial Si concentration of 1472 µmol L^{-1} (40 ppm) this period lasts for 6 h but the corresponding adsorption rate of 0.06 h^{-1} is in a similar range as those for the second period in the experiments at 749 or 355 µmol L^{-1} Si (20 and 10 ppm, respectively) which lasts from 0.45 or 1 h to 6 h, respectively. Combining this fact with the lack of samples taken within the first 0.5 h at an initial Si concentration of 1472 µmol L^{-1} this means that the real first adsorption phase which is characterised by a rate constant > 0.1 h^{-1} was not time-resolved in the experiment with an initial Si concentration of 1472 µmol L^{-1} and the value of 0.06 h^{-1} represents the second adsorption period. The adsorption slows down between 6 and 24 h to a third period which lasts until equilibrium is reached with a rate constant of about 0.005 h^{-1}. The values for the rate constant of a certain period are in the same range for all initial Si concentrations. The transition from one period to another occurs at about the same duration independent from the initial Si concentration. The relative amount of adsorbed Si at the beginning of the second period accounts for 10 %. The corresponding value for the transition to the third period increases from 13 to 20 % when the initial Si concentration is decreased from 1472 via 749 to 355 µmol L^{-1}. The absolute amount of adsorbed Si at the beginning of the second period decreases from 72 to 30 µmol for initial Si concentrations of 749 and 355 µmol L^{-1}, respectively. For the transition to the third period the corresponding values are 186, 125 and 62 µmol for 1472, 749 and 355 µmol L^{-1} initial Si concentration, respectively.

In most experimental solutions the gibbsite dissolution is insignificant. However, some samples taken from experiments with 749 µmol L^{-1} initial Si concentration contain several hundreds of µmol L^{-1} dissolved Al:

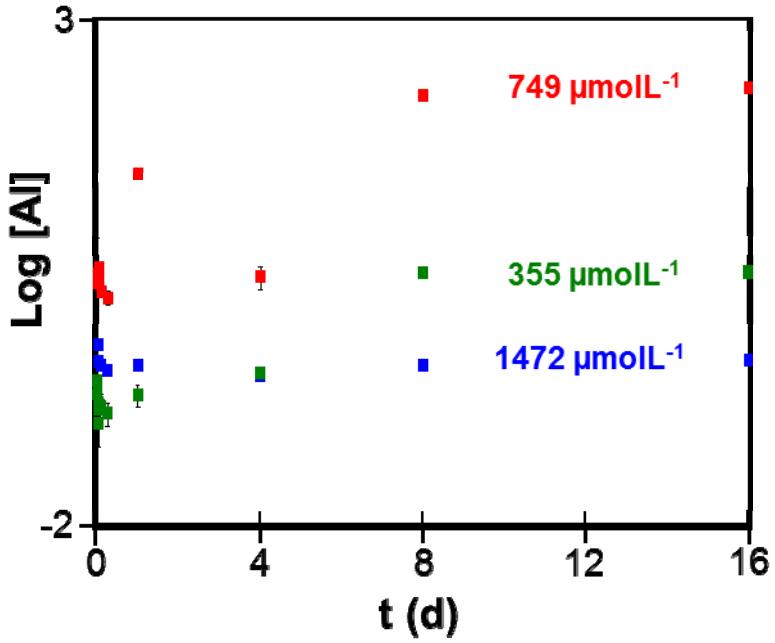

Figure 6: Al concentration in solution as a function of adsorption time onto gibbsite at various initial Si concentrations.

Si isotope fractionation

Si isotope fractionation is discussed for selected experiments with monosilicic acid (pH 7, 385 mmol L^{-1} gibbsite, 100 mmol L^{-1} NaCl) within the model of de Paolo [93] in [89]. Generally, results show that the residual dissolved Si gets isotopically heavier versus the initially dissolved Si due to isotopically lighter adsorbed Si. The initial isotopic composition of the dissolved Si is $\delta^{30}Si$ = -0.08 ± 0.15 ‰ and $\delta^{29}Si$ = -0.04 ± 0.07 ‰. The longer the experimental time is, the isotopically heavier is the dissolved Si. A final $\delta^{30}Si$ value of about 0.5 ± 0.1 ‰ and $\delta^{29}Si$ value of about 0.25 ± 0.05 ‰ is reached. An isotopic steady state at adsorption equilibrium is reached after 32 d. There are no significant differences between isotope ratios after a certain experimental duration for experiments with different initial Si concentration. The isotopic composition of the solution is shown in Figure 7. It is clearly indicated that fractionation of Si isotopes during adsorption of monosilicic acid of gibbsite is a mass-dependent process since the difference between the initial and final isotope ratio is about twice as large for $\delta^{30}Si$ as for $\delta^{29}Si$.

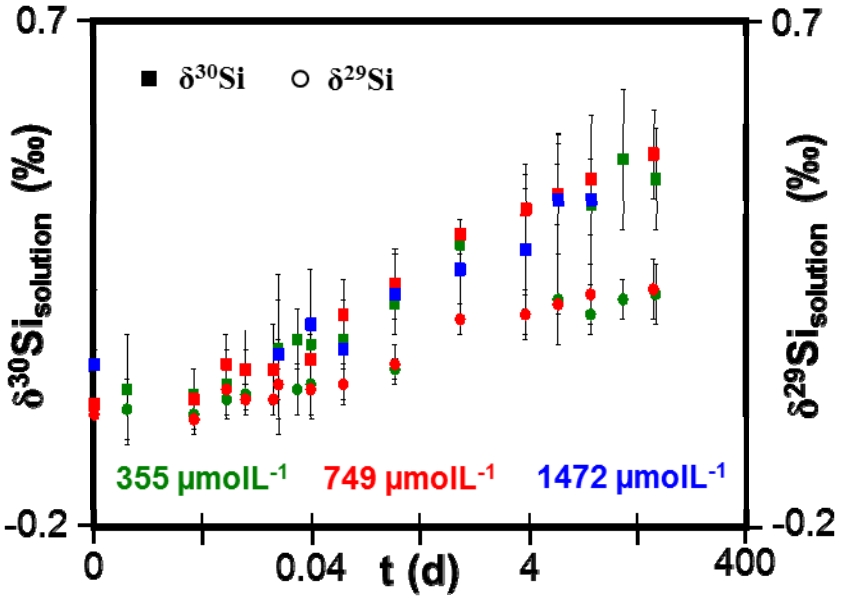

Figure 7: Evolution of $\delta^{30}Si$ (squares) and $\delta^{29}Si$ (circles) of the solution during adsorption of monosilicic acid onto gibbsite at pH 7, 385 mmol L^{-1} gibbsite and 100 mmol L^{-1} NaCl as a function of experimental duration for initial Si concentrations of 355 µmol L^{-1} (green), 749 µmol L^{-1} (red) and 40 µmol L^{-1} (blue)

Isotopic signature of the solution (here always normalised to the initial isotopic composition: $\Delta^{30}Si = \delta^{30}Si_{final} - \delta^{30}Si_{initial}$) can also be plotted against the fraction of Si remaining in solution (Figure 8). Contrary to Figure 7 this plot shows a difference for different initial Si concentrations. At higher initial Si concentrations after a certain experimental runtime a higher fraction of Si is remaining in solution. At a certain fraction of still dissolved Si a higher fractionation of Si isotopes is observed for higher initial Si concentrations. Quantitative evaluation of isotope data was performed in a separate paper [89].

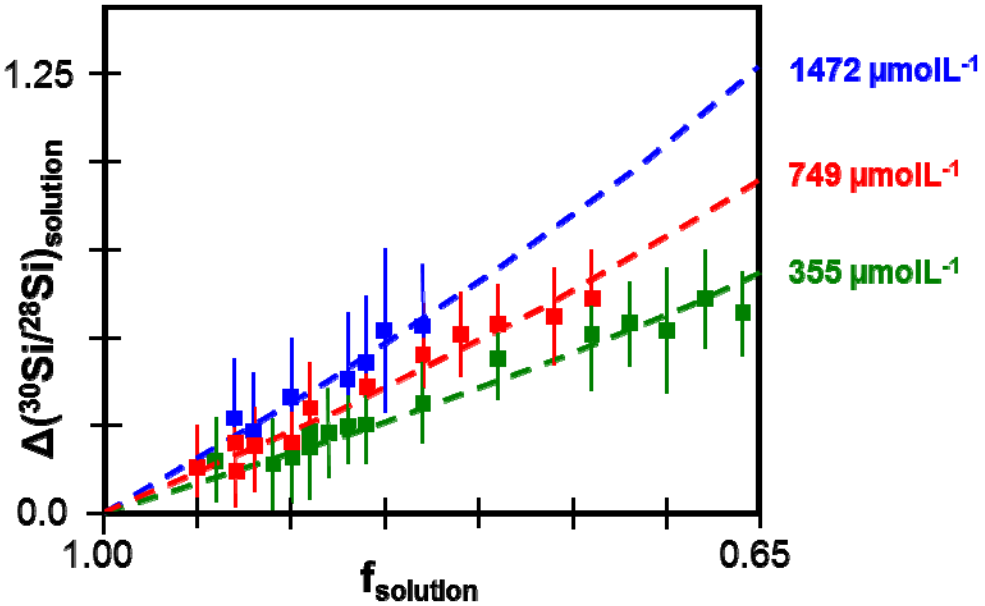

Figure 8: The evolution of $\Delta(^{30}Si/^{28}Si)_{solution}$ during adsorption onto gibbsite, as a function of the fraction of Si remaining in solution ($f_{solution}$). Green, red and blue squares depict experiments with an initial Si concentration of 10, 20 and 40 ppm, respectively. Regression lines for the experimental data are plotted according to the Rayleigh mass balance approach (modified after [89])

2.3.2 Experiments with Polysilicic Acid

Depolymerisation of polysilicic acid in pure Si solutions

Water glass is diluted to a Si concentration of 1513 µmol L^{-1}. At pH of about 3 it consists of 1460 µmol L^{-1} Si bound in polymeric structures and only 54 µmol L^{-1} monomeric silicic acid which corresponds to 96 and 4 % in respect to total dissolved silica, respectively. The reaction rate constants with molybdic acid account for 0.025 and 1.0 min^{-1}, respectively, which suggests the presence of oligomers like dimers besides monomers [5]. However depolymerisation of polysilicic acid occurs which depend strongly on pH. At low pH of about 3 depolymerisation is very slow (with a half-life time of about 8 hours), but at higher pH depolymerisation is much faster. The half life time of polysilicic acid at pH 9 is only about 15 minutes as after 1 h no significant amounts of polysilicic acid could be detected any more. The reaction curves of the initial polysilicic acid and the depolymerised sample (1 h at pH 9) with molybdic acid are displayed in Figure 9. Interestingly, the reaction rate constants for polymeric and monomeric silicic acid change to 0.016 and 1.1 min^{-1}, respectively, throughout the depolymerisation time of 60 min at pH 3. This means that large polymers remain metastable whereas oligomers start to decompose into monomers.

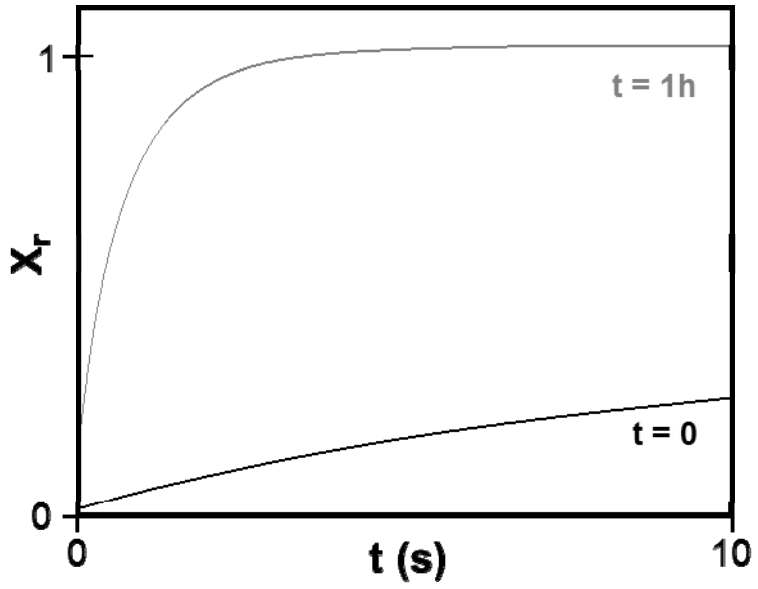

Figure 9: Silica which has already reacted with molybdic acid, X_r, as a function of time for the polymeric stock solution (t = 0, 1513 µmol L^{-1} Si) and the same solution depolymerised at pH 9 for t = 1h according to (15

Adsorption kinetics

Adsorption of polysilicic acid takes place in all experiments (Figure 10 and Table 2 & 3). The maximal relative amount of adsorbed Si ranges from 35 to 93 % in respect to the initially dissolved Si. The relative amount of adsorbed Si reaches a minimum for experiment “b” (385 mmol L^{-1} gibbsite, 587 µmol L^{-1} Si, pH 3.6) and a maximum for the experiment “e” (385 mmol L^{-1} gibbsite, 618 µmol L^{-1} Si, pH 3.8) although the conditions were quite similar. Contrary, at different conditions, e.g. different gibbsite:Si ratios, intermediate relative amounts of Si were adsorbed.

Experiments “c”, “d”, “e” and “f” show a minimum concentration (maximum of adsorption) of total dissolved silica at a certain period after 1 to 40 min, whereas experiments “a”, “b” and

"g" show a continuous decrease in the concentration of dissolved silica. The reaction mechanisms and rates depend on parameters like pH, T, SI and gibbsite concentration. As combined effects are highly complex no significant and systematic correlation with pH, initial Si or gibbsite concentration or the ratio of the two latter factors was found (Figure 10).

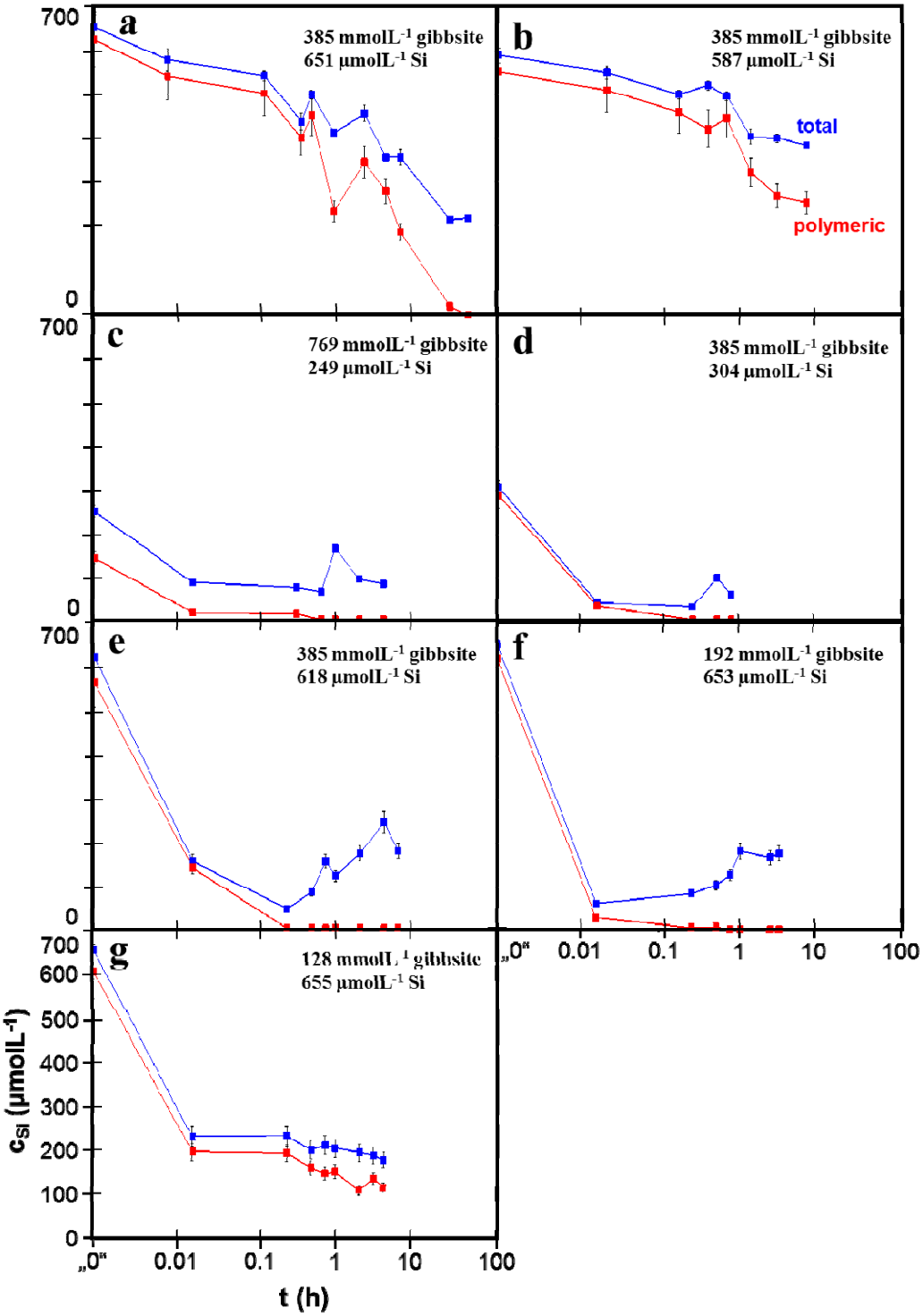

Figure 10: Si concentration in solution during adsorption of a polysilicic and monosilicic acid onto gibbsite. Red symbols indicate the concentration of polysilicic acids, blue symbols the total concentration of dissolved silica. All experiments were performed with 100 mmol L^{-1} NaCl. a: 385 mmol L^{-1} gibbsite, 651 µmol L^{-1} Si, pH 3.4; b: 385 mmol L^{-1} gibbsite, 587 µmol L^{-1} Si, pH 3.6; c: 769 mmol L^{-1} gibbsite, 249 µmol L^{-1} Si, pH 3.7; d: 385 mmol L^{-1} gibbsite, 304 µmol L^{-1} Si, pH 3.6; e: 385 mmol L^{-1} gibbsite, 618 µmol L^{-1} Si, pH 3.8; f: 192 mmol L^{-1} gibbsite, 653 µmol L^{-1} Si, pH 3.1; g: 128 mmol L^{-1} gibbsite, 655 µmol L^{-1} Si, pH 3.6

Adsorption rates constants are largest for the first minute of adsorption where they vary between 9 and 231 h^{-1}. The maximum value is reached in experiments ‴c" which is characterised by the highest gibbsite:Si ratio (769 mmol L^{-1} gibbsite, 249 µmol L^{-1} Si, pH 3.7). Later on adsorption rates are below 8 h^{-1} and sometimes reach negative values down to less than -12 h^{-1} which indicates desorption. The adsorption process is accompanied by a depolymerisation process (Figure 10). The time after which all dissolved silica occurs varies between 0.25 and 46 h. The simultaneousness of depolymerisation and adsorption makes a separate calculation of adsorption rates for mono- and polysilicic acids impossible: The concentration of monosilicic acid decreases due to adsorption, but increases due to depolymerisation of silica in the solution and at the mineral surface. Accordingly, the concentration of polysilicic acid decreases not only due to adsorption, but also due to depolymerisation.

Changes of oligomer and polymer sizes

The reaction rate constants for polysilicic acid with molybdic acid show a similar behaviour in three selected experiments (Figure 11). During the first period they decrease which corresponds to an increase in the size of polysilicic acids. Later on the constants increase again which means a decrease in polymer size before the polymers depolymerise completely.

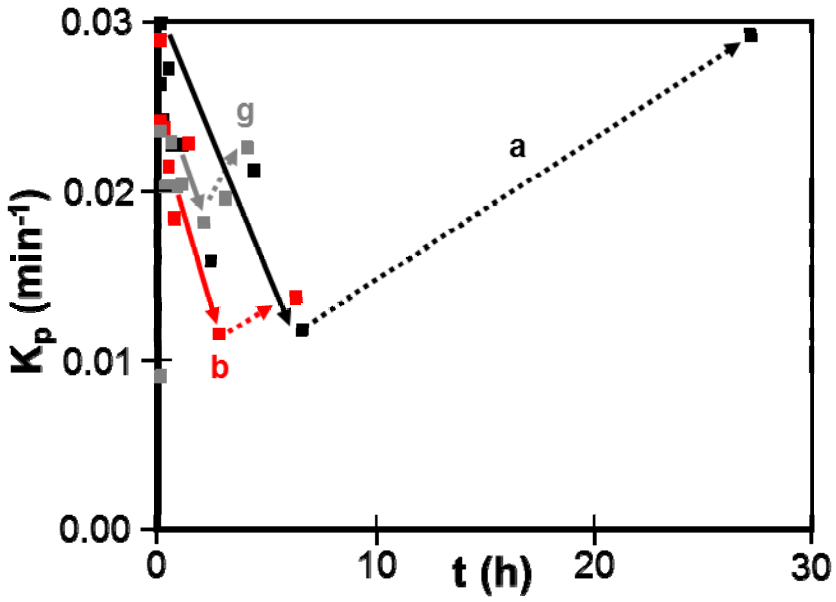

Figure 11: Reaction rate constants of polysilicic acid with molybdic acid, k_p, as a function of adsorption time, t, onto gibbsite for three selected experiments. Letters for individual experiments correspond to Figure 10. a = 385 mmol L^{-1} gibbsite, 651 µmol L^{-1} Si, pH 3.4; b = 385 mmol L^{-1} gibbsite, 587 µmol L^{-1} Si, pH 3.6; g = 128 mmol L^{-1} gibbsite, 655 µmol L^{-1} Si, pH 3.6.

Some experiments show an initial increase in the reaction rate constants of monosilicic acid with molybdic acid, which is followed by a decrease. This indicates the decomposition and subsequent neoformation of oligomers (Figure 12):

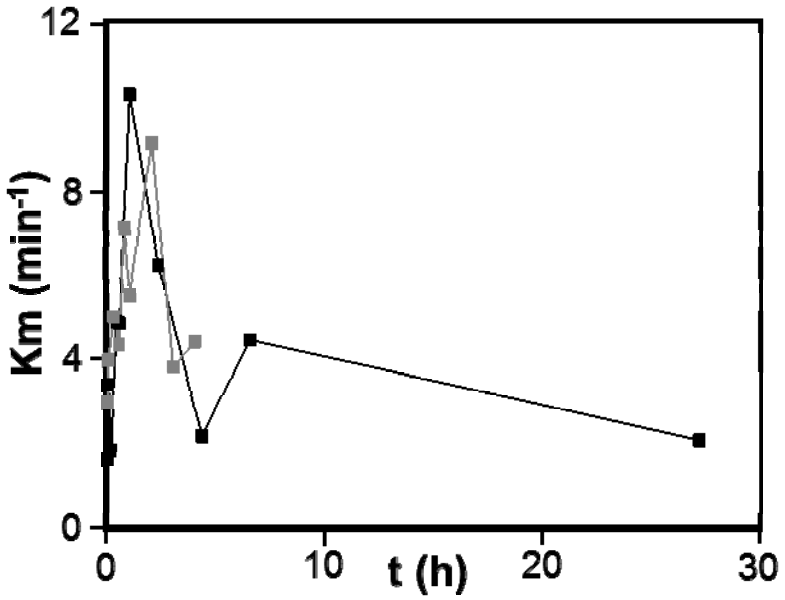

Figure 12: Reaction rate constants of monosilicic acid with molybdic acid, k_m, as a function of adsorption time, t, onto gibbsite for two selected experiments. Letters for individual experiments correspond to Figure 10. a = 385 mmol L^{-1} gibbsite, 651 µmol L^{-1} Si, pH 3.4; g = 128 mmol L^{-1} gibbsite, 655 µmol L^{-1} Si, pH 3.6.

Gibbsite dissolution

Besides adsorption of silicic acid onto gibbsite, also a notable gibbsite dissolution was observed, of course. The equilibrium concentrations of dissolved Al increase with decreasing pH. In some experiments concentrations of up to 200 µmol L^{-1} Al (about 0.05 % of the initially present gibbsite) were found (Figure 13). Interestingly, the resulting solution is oversaturated in respect to gibbsite according to PhreeqC modelling as the equilibrium Al concentration in solution is only 81 and 136 µmol L^{-1} for the respective experiments [10]. Dissolution kinetics follow generally previously observed trends [94]

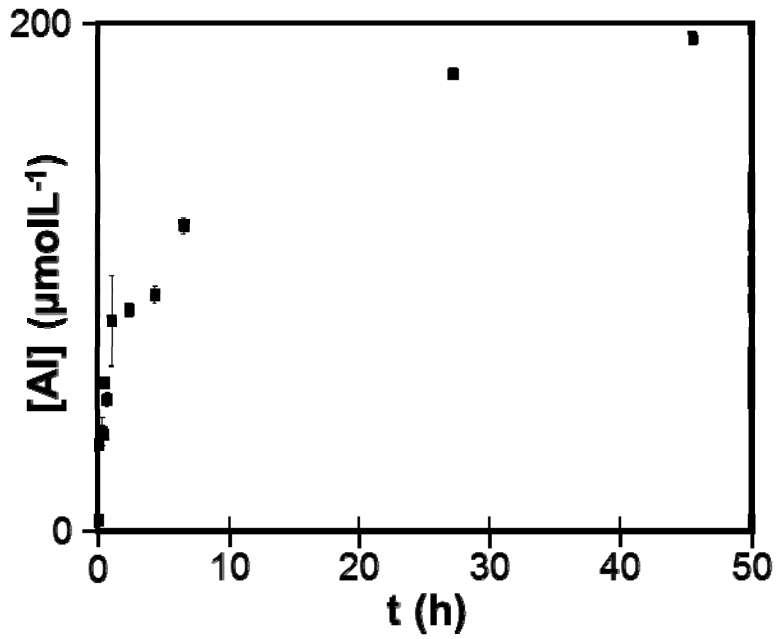

Figure 13: Al concentration in solution due to gibbsite dissolution as a function of experimental runtime in experiment "a" (385 mmol L^{-1} gibbsite, 651 µmol L^{-1} Si, pH 3.4)

2.4 Discussion

2.4.1 Adsorption kinetics

To check if my adsorption data for monosilicic acid fit the general overall approach (

(17)

$$\frac{d[Si]}{dt} = k \cdot [Si] \qquad (17)$$

a semi-logarithmic plot of the concentration of dissolved Si against the duration of adsorption (Figure 14) should result in a linearly falling correlation [95]. The rapid decrease of the curves in the initial period (Figure 14) is in agreement with previous data [96]. This trend can be explained by a multilayer adsorption mechanism followed by a linear behaviour for longer durations [96].

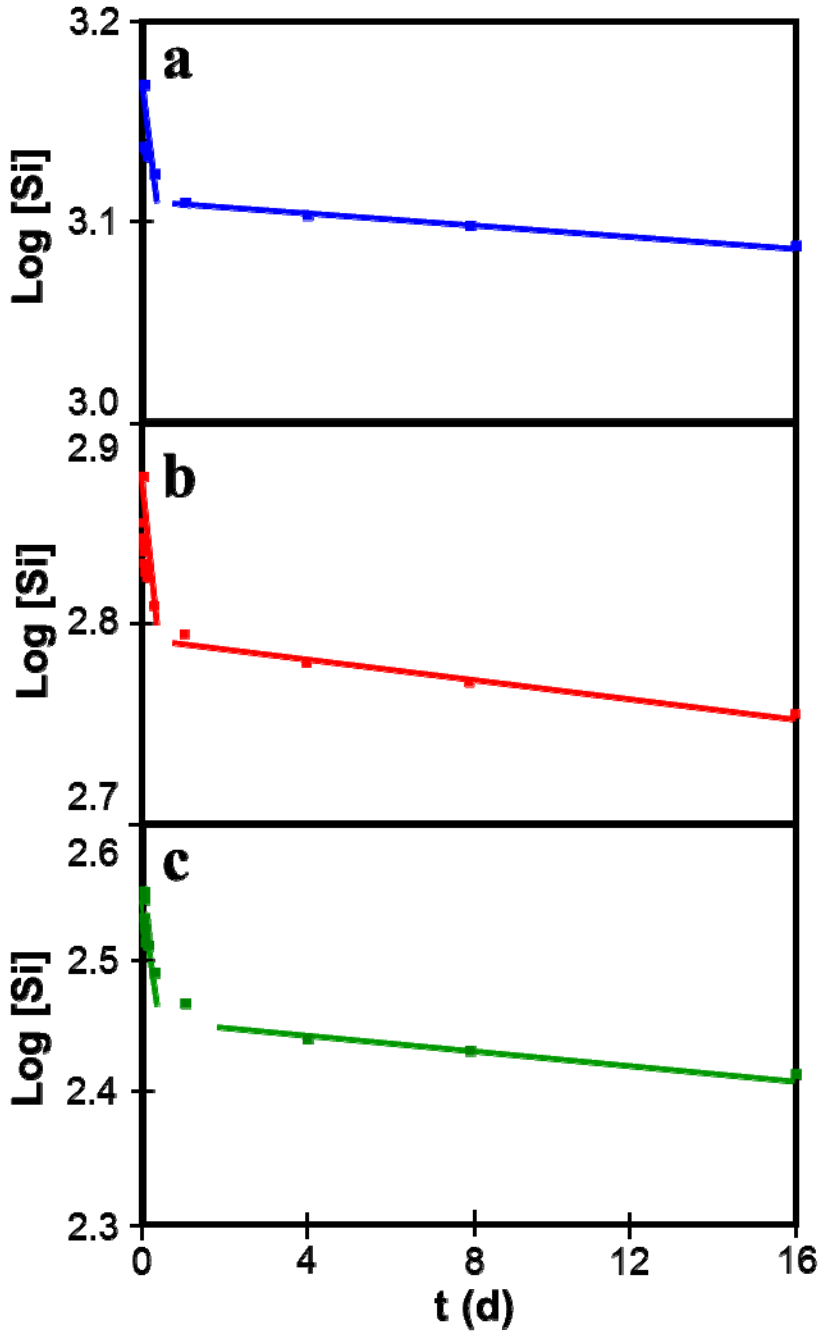

Figure 14: Semi-logarithmic plot of the concentration of dissolved Si for selected experiments (a: 355 µmol L^{-1}; b: 749 µmol L^{-1}; c: 1472 µmol L^{-1} Si_{mono}, 385 mmol L^{-1} $Al(OH)_3$, 100 mmol L^{-1} NaCl, pH 7

Another study [14] suggests that absorption of silicic acid onto gibbsite occurs in two steps: Firstly, Si forms O-$Si(OH)_3$ groups on the gibbsite surface. This process can also be considered as surface complexation [14]. Secondly, further Si units react with the primarily adsorbed groups to form a kind of gel structure at the gibbsite surface [80]. At a first glance this seems to contradict the idea of initial multilayer and later monolayer adsorption [96]. But combining those ideas it can be suggested that monosilicic acids are adsorbed forming multilayer clusters. These adsorbed clusters might possess O-$Si(OH)_3$ groups on their surface.

In the above cited study [14] 298 µmol L^{-1} Si of monosilicic acid reacted with 54 m^2 L^{-1} gibbsite which is in the same range as one experiment from my series (355 µmol L^{-1} Si, 35

$m^2\,L^{-1}$ gibbsite). However, the equilibrium concentration measured after 20 d accounted only for 105 µmol L^{-1} compared to 246 µmol L^{-1} after 64 d in my study. The difference is suggested to be due to the lower provided gibbsite surface area in my study.

Depolymerisation of polysilicic acid at pH 9 and a relative maximum of metastability at pH 2.5 is in agreement with previous work [16]. Experiments with polysilicic acids might result in the formation of Si-Al copolymers. Their formation has been shown in a previous study of the adsorption of silicic acid from sodium metasilicate on gibbsite [80]. If Si-Al copolymers are formed, they cause an inhibition of ongoing depolymerisation [8].

Effect of pH on adsorption kinetics and equilibria

The effect of pH on the kinetics and equilibria of adsorption of silicic acids onto gibbsite was only studied for monosilicic acids as experiments with polysilicic acid were only performed in the pH range of their metastability of about 3.5. The increase of adsorption of monosilicic acid onto gibbsite with increasing pH from 5 to 8 is in agreement with previous data [80] showing an increase up to pH 9 and a decrease at even higher pH. In the latter study 1 g gibbsite was suspended in 100 g solution, which corresponds to a concentration of gibbsite of 128 mmol L^{-1}, whereas in the present study various but higher gibbsite concentrations between 355 and 1472 mmol L^{-1} were used. Experimental times are in the same range in both studies. In the study of Jepson et al. [80] the adsorbed amount of SiO_2 in µmol per m^2 gibbsite was displayed: At pH 5 about 11.5 µmol m^{-2} and at pH 7 about 14 µmol m^{-2} were fixed and an equilibrium was reached after about 300 h. In the present study 96 µmol L^{-1} Si were fixed at pH 7 at initial concentrations of 355 µmol L^{-1} Si and 385 mmol L^{-1} gibbsite with a specific surface area of 1.18 $m^2\,g^{-1}$ equivalent to 92.0 $m^2\,mol^{-1}$. Hence 35.4 $m^2\,L^{-1}$ gibbsite adsorbed 96 µmol L^{-1} Si which corresponds to 2.71 µmol Si per m^2 gibbsite. This is only about 20 % of the adsorbed silica in my study in comparison to Jepson et al. [80]. To understand this difference it is necessary to compare experimental conditions. First of all in the present study significantly higher gibbsite concentration of 385 mmol L^{-1} were used compared to 128 mmol L^{-1} in the previous study, secondly in the present study 355 µmol L^{-1} Si were dissolved whereas in the previous work 160 ppm Si were used which corresponds to 2666 µmol L^{-1} Si. It is obvious that higher Si concentrations lead to a higher amount of adsorbed Si at a constant distribution coefficient between dissolved and adsorbed Si. This can explain the difference between the studies.

Final Si concentrations in solution in the experiments of this study were below that of a previous study [14]. The differences can be explained by the different pH considering the decreasing trend of the equilibrium concentration when pH was decreased from 8.0 to 4.6 [14].

Effect of Si concentration and Si:gibbsite ratio on adsorption kinetics and equilibria

In experiments with monosilicic acid the absolute amount of adsorbed Si after a certain time increased with increasing Si concentration which is in agreement with a previous study [14]. Additionally to existing data [14] the new experiments show that this effect is also valid for polysilicic acid whose concentration was always 363 µmol L^{-1} in the previous study. Considering the experiments with monosilicic acid the results of both studies can be compared quite well. Elevated Si adsorption onto gibbsite surfaces in a previous study can be explained by the higher provided gibbsite surface area (54 compared to 35 $m^2\,L^{-1}$) (Figure 15):

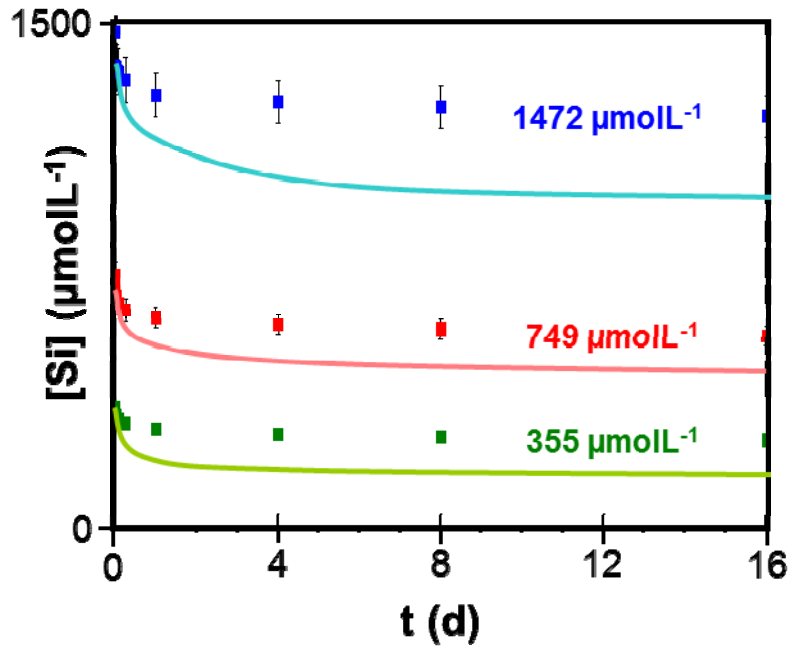

Figure 15: Comparison between adsorption experiments in this study (Figure 5) and a previous study ([14], see given lines) with a higher provided surface area (35 compared to 54 $m^2 L^{-1}$, respectively).

Adsorption kinetics in experiments with polysilicic acid are more complex [14]. The previous observation that the total concentration of dissolved Si passes through a minimum was confirmed for experiments "c", "d", "e" and "f", but not for the experiments "a", "b" and "g" of my study. This shows that the silica system is very sensitive to slight differences in the experimental procedure. However, the time after which the minimum was reached is in the same range as in the previous study. Finally, geometrical approximations suggest that about half of the gibbsite surface is finally covered with silicic acid and the other half with Al-OH groups.

2.4.2 Isotope fractionation

Isotope fractionation is discussed in more detail in a separate paper [89]. Herein only the basic results and interpretations are given. Si isotopic fractionation through Si adsorption onto gibbsite can be explained by mass dependent kinetic isotope fractionation [54]. Adsorption of silicic acid onto solid surfaces is clearly a kinetic process that includes migration of the dissolved Si species along the surface to a free adsorption site where inner-sphere complexes are finally formed. Lighter isotopes are faster in this process which leads to isotopic fractionation. The fact that the kinetic Si isotopic fractionation factor increases with increasing initial Si concentration as shown in Figure 8 can be explained by the DePaolo model [93]. This suggests a competition between kinetic and equilibrium fractionation.

For a geologic interpretation of the results it is most interesting that Si adsorption processes highly fractionate Si isotopes, but not at a constant value for a given substance. An extraordinarily light isotope signature of certain pedogenic minerals can consequently be explained by a Si adsorption process during their formation, especially at elevated Si concentration of the solution during adsorption of Si onto e.g. AL-OH, Mg-OH or Fe-OH surface sites. However, it has to be considered that also other processes like precipitation may fractionate Si isotopes, which is still a matter of debate.

2.4.3 Depolymerisation

The adsorption of one part of the polysilicic acids and the depolymerisation of the other is in agreement with a previous study dealing with the adsorption of polysilicic acids onto several iron oxides and hydroxides and onto gibbsite [14]. Contrary to [14] the concentration of polysilicic acid decreased monotonously in the present study and did not show a minimum after few minutes. The difference might be explained by the different pH of about 3.5 in my study and 6.2 in the previous study. In the more acidic pH metastability of polymeric silica should be more significant, especially as Al is present through incomplete dissolution of gibbsite [17]. Additionally, individual experimental parameters like stirring velocity or buffering might have an additional effect on Si polymerisation behaviour.

2.5 Conclusion

The adsorption of monosilicic and polysilicic acid onto gibbsite was performed at various pH ($3 \leq pH \leq 8$) and Si concentrations in solution ($0.34\ mmol\ L^{-1} \leq [Si] \leq 1.47\ mmol\ L^{-1}$). The relative adsorbed amount of monosilicic acid increases with increasing pH up to 8, increasing available surface area and decreasing initial Si concentration. The adsorption of monosilicic acid onto gibbsite traverses at least two periods which can be explained by multilayer and monolayer adsorption, respectively. During adsorption of monosilicic acid the lighter ^{28}Si isotope is adsorbed onto Gibbsite preferentially compared to the heavier ^{30}Si isotope. The kinetically driven Si isotope fractionation is less valid at lower initial Si concentrations in the solution due to a competition between kinetic and equilibrium fractionation [93]. Hence silicon isotope composition of pedogenic minerals might be used as a proxy for adsorption rates during formation or for ongoing isotopic equilibration of the dissolved Si with the adsorbed Si. When polysilicic acid is used for adsorption experiments, total Si adsorption is faster, but accompanied by Si depolymerisation in the solution and at the mineral surface.

3 Cyclic Freezing of Aqueous Siliceous Solutions

3.1 Introduction

Weathering of silicates is intense at humid and warmer climate conditions, but also present in permafrost and Polar Regions. Frost-induced processes can lead to a very special weathering regime, which cannot be found in warm areas, and are therefore highly interesting in the aspects of weathering and neoformation of silicates. For instance, cyclic freezing is a process which occurs in the top horizon of permafrost-affected soils. It leads to oversaturation and precipitation of minerals during the freezing period and to undersaturation and dissolution during the thawing period. Silicic acid is a main species in soil solutions. Hence the consequences of cyclic freezing for precipitation and dissolution of silica and related phases yield amazing weathering features, which are preserved at the low weathering rates at colder climate conditions, whereas high weathering rates in the tropics often lead to the disappearance of traces of weathering. Thus Earth scientists can use such features in archives for the reconstruction of past climate. In the general mineralogical context this study shall provide new insights into mineral formation in the SiO_2-Al_2O_3-H_2O system at low-temperature conditions.

Freezing of Siliceous Solutions

Precipitation of silica during freezing is generally understood: Firstly, when a siliceous solution is cooled down, the solubility of amorphous silica decreases between 20 and 0 °C from 1.74 to 1.12 mmol L^{-1} [22]. Secondly, freezing of the solution increases supersaturation with respect to amorphous silica because Si is enriched in the liquid phase as it is excluded by the growing ice crystals [22]. Also the kinetics of silica precipitation have already been investigated: Firstly, an activated silica complex is formed wherefore a thermodynamic barrier, the activation energy, has to be overcome. If the system can provide this energy, amorphous silica can form and fix about 90 mol-% of the dissolved silicic acid [22].

The effect of cyclic freezing is less explored: It is known that after re-melting of the ice irregular flakes of amorphous silica are obtained, which have grown at the grain boundaries of the ice crystals. If the initial $Si(OH)_4$ concentration is below 2 mmol L^{-1}, these flakes have a quartz core, which is subsequently overgrown by surface-hydroxylated amorphous silica [5]. Furthermore it is obvious that dissolution of the ice crystals decreases the concentration of dissolved Si, which leads to undersaturation and dissolution of the silica precipitate formed during freezing. However, after a freezing cycle a fraction of the precipitate remains. This percentage increases with decreasing initial $Si(OH)_4$ concentrations and an increasing number of freeze-thaw-cycles. This is the case because the re-dissolution of the amorphous phases during the subsequent thawing period is incomplete. The resulting surviving precipitates can act as precursors for the formation of zeolites if the necessary cations are available in the right proportion and if the colloids of the precipitated silica are small and therefore reactive. This is the case for high initial $Si(OH)_4$ concentrations [22]. Thus cyclic freezing can significantly reduce the geochemical and ecological availability of silica [22]. On the other hand, the resulting decrease of dissolved silica increases undersaturation with respect to silicates, which stimulates their dissolution [22].

The effect of alkali and earth alkali metals on the formation of amorphous silica by cyclic freezing has also been studied and a stimulating effect in the sequence of $Na^+ < Mg^{2+} < Ca^{2+} < K^+$

$<Li^+<Sr^{2+}<Ba^{2+}$ has been found. The resulting precipitates incorporate the respective metals yielding Me/Si ratios between 1 and 4 [22]. However, other additives like Al^{3+}, $Ge(OH)_4$ and $B(OH)_3$ and the effect of other minerals like kaolinite have not yet been investigated. These additives are interesting due to their geochemical similarity to Si and shall therefore be presented briefly (apart from Al which is presented in chapter 1.2.2).

Boron is an element which is incorporated into minerals either in trigonal-planar or tetrahedral coordination. The latter allows substitution of Si by B in silicates like muscovite and also in biogenic silica [97-99]. There are several factors making B an interesting additive in experimental low-temperature geochemistry and mineralogy: (i) B isotopes are used to trace diagenetic processes because ancient marine siliceous oozes have lower $\delta^{11}B$ values than modern ones [100]. (ii) freezing in permafrost regions increases $\delta^{11}B$ values in relictic water [101, 102]. Thus newly formed silicates from groundwater or soil solutions may be traced by B isotopes. (iii) B is an essential element for plant growth but can be toxic at elevated concentrations [103]. This is not only important for agriculture issues, but also for forestry in cold climates since conifers like the Norway spruce suffer from decreasing winter hardiness by B deficiency [104]. Contrary, excess of B aggravated needle necrosis in salt-effected mycorrhizal jack pines [105].

Germanium is a tetravalent element which is predominantly present in the Earth´s crust in silicates where it substitutes for Si and reaches concentrations of up to 100 ppm with a preference for less polymerised silicates [106]. Interestingly, when cryptocrystalline agate is associated with macrocrystalline quartz, Ge is enriched in agate [107]. This leads to the question if Ge incorporation into silica phases occurs only during alteration of volcanic rocks at 60 to 200 °C, when agate is formed [108], or also by cyclic freezing. Probably, at low temperatures vital effects favour incorporation of Ge versus Si into opal [109]. Concerning vital effects it also has to be mentioned that plants discriminate against Ge compared to Si during phytolith formation [110]. It is not yet clear if discrimination against Ge is a protective mechanism since high amounts of inorganic Ge are toxic. Interestingly, lower concentrations of Ge are used in cancer treatment [111].

Kaolinite is a common clay mineral which occurs abundantly in various soil types. Whereas the other experiments provide simple and rather easily understandable systems, the addition of kaolinite to cyclic freezing experiments shall approach a natural soil, but is of course more complex. When kaolinite is present it can act as a substrate for silica precipitation and as adsorbens for dissolved Si and Al species due to cyclic freezing. Furthermore kaolinite can dissolve and release Al and also Si into the solution. The question arises if the presence of kaolinite leads to the formation of new phases besides amorphous silica. Furthermore, interactions between the kaolinite and the newly formed silica might yield a kaolinite-silica nanocomposite since the freezing experiments mimic a technological process called freeze-casting [112]. It has been shown that such a nanocomposite possesses highly interesting properties concerning microstructure and surface area and that its flexural strength is higher than for pure freeze-cast kaolinite or silica ceramics [113]. Adsorption tests indicate that during gel formation, the silica nanoparticles strongly adsorb to the much larger kaolinite platelets, which could be the primary cause for the increased strength of the composites [113]. The manufacturing of ceramics by freeze-casting of silica sols is a highly promising approach of energy-saving low-temperature production of technical devices.

Three more aspects besides the effects of additives have also not been studied yet:

1) Although it has been shown that freezing processes finally lead to the precipitation of amorphous silica [22] and that nucleation of amorphous silica is in fact polymerisation of silicic acids, at least in case of insufficient heterogeneous nuclei [5], polysilicic acids have not yet been found after cyclic freezing [22]. However, varying experimental conditions might yield to polymerisation due to cyclic freezing. The presence of polysilicic acid due to cyclic freezing might explain the enrichment of precipitated amorphous silica with increasing number of freezing cycles since the availability of nuclei would enhance precipitation kinetics.
2) Although silicon isotope fractionation was observed by various geologic processes like adsorption onto iron oxides [79] and formation of diatoms [114] and although it was shown that silicon can be removed from aqueous solution by cyclic freezing [22], it has not yet been verified if Si isotopes fractionate during cyclic freezing of aqueous solutions. Even as Si isotope fractionation was observed in obviously frost-affected regions like Northern Sweden [115] or Iceland [116] the potential effect of freezing on Si isotope fractionation is still not known [117]. Studies focussing on the formation of cryogenic opal-A next to geysers [118] did also not deal with isotope fractionation. The application of Si isotopes in this field is thus a new tool for paleo-environmental studies which have been focused mostly on biogeochemical Si isotope fractionation, e.g. in diatoms [114].
3) Previous experiments dealing with precipitation of amorphous silica by cyclic freezing were conducted at pH 6.5 [22]. Furthermore it has been shown that a decrease in pH enhances flocculation of silica [119]. However, a systematic study on the effect of pH on precipitation of silica by cyclic freezing has not yet been performed.

Cryosols

Frost-affected soils are called cryosols [120]. Such kind of soils is characterised by a lower, permanently frozen C_f horizon (C: loose rock, $_f$: fermented, containing plant relicts) and an upper, cyclically freezing and thawing A_j horizon (A: humic topsoil, $_j$: cryoturbate, from Swedish *tjäle*) [120]. The depth down to which the soil thaws in summer varies between 0.1 and 2 meters depending not only on climate but also on the soil itself, e.g. its thermal conductivity and heat capacity [120]. Cryosols occur in arctic and alpine regions [121]. They are characterized by the presence of ice lenses whose formation can be treated as a special type of desiccation [121]. Freezing and thawing of cryosols lead to frost wedging and crush down the rock basement into fragments [122]. Frost wedging in cryosols increases the surface area and thereby also evokes chemical weathering despite low temperatures [120], [123]. As soon as primary minerals have been dissolved at least partially by chemical weathering, secondary minerals can form in cryosols. Whereas in warmer climate supersaturation with respect to secondary minerals is mostly reached by evaporation, in cryosols freezing-induced supersaturation plays an important role: Since ice does not incorporate most dissolved ions their concentration increases in the soil solution in front of growing ice crystals which is called the transition layer [124]. Supersaturation at this site leads to precipitation of amorphous and crystalline phases. However, even after long frost periods an unfrozen interfacial water layer remains present around ice crystals in soils [125]. After thawing and renewed freezing further stabilisation is reached by renucleation of ice crystals in the pores left by the primary ice crystals [126].

As silicates are the main phases in most cryosols, silicic acids are important components of their interstitial solutions. Therefore, freezing of the A_j horizon in winter can lead to supersaturation of the remaining soil solution with respect to amorphous silica [22]. Although it is known that Si can occur in highly concentrated solutions in polymeric forms [5] and

although polysilicic acids have been found in other soil types [17] they have to my knowledge not yet been found as product of freezing processes in cryosols. The resulting precipitate does not dissolve completely during summer which leads to accumulation of amorphous silica with increasing number of freezing cycles [22]. By this process lamellar opaline silica (LOS) can be formed [127] [128]. A similar mineral is cryogenic opal-A which can be formed by freezing of aqueous solutions in polar and subpolar regions and consists of aggregates of microspheres [119]. Also chalcedony has been found in calcari-regic cryosols [122] but is attributed to weathering processes before glaciation and not to freezing-induced precipitation. Alkali and earth alkali metals favour the formation of amorphous silica [22]. The survival and accumulation of amorphous silica suggests that it plays an important role as precursor phase for the formation of secondary silicates in soils like zeolites [22]. This was reported for chabazite at the boundary of ice-free and ice-cemented horizons in soils developing onto glacial sediments [129]. Observations in nature are supported by experimental studies: Freezing of a 0.1 to 1 mM Si solution resulted in the formation of flakes and fibres (0.5 – 20 µm) consisting of non-crystalline silica [130].

Aim of this study

In the general mineralogical context this study shall provide new insights into mineral formation in the SiO_2-Al_2O_3-H_2O system at low-temperature conditions, e.g. in cryosols. More precisely, the effect of pH, Al, B, Ge and kaolinite on silica precipitation by cyclic freezing shall be studied. The question occurs if the amount of precipitated silica, coprecipitation of other components, distribution of stable Si isotopes, its crystallinity or the concentrations of dissolved Si can be used as a proxy for the number of freezing cycles and/or climate changes.

3.2 Methodology

3.2.1 Materials

Tetraethylorthosilicate (TEOS, Merck, p.a.) and MilliQ water were used to prepare an aqueous stock solution (25 L) containing 1.7 mM Si. Subsets of 1 L were removed for preparing solutions containing additionally 100 µM Al (as $AlNO_3 \cdot 9H_2O$, Merck, p.a.), B (as $NaBO_2 \cdot 4H_2O$, Sigma Aldrich, p.a.) and Ge (as $(NH_4)_2GeF_6$), Merck, ICP standard in 5 % HNO_3). Additional experiments with kaolinite (KGA-1, Clay Mineral Society) were performed by suspending each 2.58 g kaolinite in 0.1 L stock solution. The high crystallisation degree of the used kaolinite was verified by XRD pattern (Figure 23) using a PANanalytical X´Pert Pro X-ray diffractometer with Co Kα radiation:

Constant ion strength was obtained by the addition of 100 mM NaCl in certain experimental series. pH was adjusted to a wide range of values ($3 \leq pH \leq 11$ for experiments with Si, B and Al, pH = 3 and 4.5 for experiments with Ge, pH = 4.5 for experiments with kaolinite) by adding corresponding amounts of 0.1 M NaOH and 0.05 M HCl solutions.

3.2.2 Experimental Setup

The stock solution from chapter 3.2.1 was distributed into 100 mL PE bottles (or 1 L bottles when indicated in results tables). For each experimental series one bottle (t = 0) was filtrated

through a 0.1 μm cellulose acetate membrane and analysed for composition. A second one, the reference sample, was stored at room temperature during the whole experimental runtime. Samples were placed into a computer controlled climate cabinet (Vötsch VC 4033). The temperature was controlled internally by the cabinet and externally by an additional thermometer. The samples were frozen within 6 h from 20 °C to – 20 °C, subsequently the temperature was kept constant for 6 h at – 20 °C before it was raised again to 20 °C and kept constant at 20 °C there for another 6 h. After a completed cycle filtration was performed through a 0.1 μm cellulose acetate membrane. Filter cakes were rinsed into glass tubes with ethanol and dried at 40 °C. Filtrates were stored at room temperature for analyses.

3.2.3 Analytics

Solid Analyses

Secondary electron imaging of solids was carried out by scanning electron microscopy (SEM, Zeiss DSM 982 Gemini) at an accelerating voltage of 5 kV and working distances between 5 and 10 mm. Samples were coated with an Au-Pd alloy using a Scancoat Six sputter apparatus (Edwards Hochvakuum GmbH). Selected samples were analysed with Fourier-transformed infrared spectroscopy (Perkin Elmer FTIR Spectrometer 100) using KBr tablets. TEM-EDX and TEM-STEM analyses (TEM, FEI Tecnai 12) were also performed for a selected sample. X-ray diffraction (XRD, Panalytical X´Pert Pro) was used for selected samples, where sufficient material was available. The angle of incidence, 2 Θ, was varied from 4 to 85 °, the step size accounted for 0.017 °2Θ, the measuring time accounted for 20.7 s, the divergence slit was set fix to 0.5 ° 2Θ and the anti-scattering slit to 1 ° 2Θ. The Si isotopic composition of selected solid was determined by MC-ICP-MS (Thermo Neptune). Calibration and measuring procedures are described in a separate paper [92]. The isotope reference material BHVO-2g was applied which can be backtracked to the Nist NBS28 reference material.

Fourier-transformed infrared spectroscopy (FTIR, Perkin Elmer 100**)** was used in this thesis to characterise the precipitates. In this study the KBr technique was used. One mg of the sample was mixed with 199 mg KBr in an agate mortar and pressed with a hydraulic press at 10 kbar to a tablet, which is similar to a single crystal [131]. Silicates and silica compounds have several characteristic IR-active vibrations: The asymmetric Si-O stretching vibration has an absorption band at 1000 cm^{-1}, the asymmetric Si-O-Si stretching vibration at 1120 cm^{-1}. An increase of the polymerization degree leads to a shift of the peak at 1000 cm^{-1} and to an increasing absorption at 1120 cm^{-1}. A shoulder-like appearance of the latter peak and a weak peak at 1075 cm^{-1} result from a polymeric transition state during the formation of amorphous silica from dissolved silica monomers. The peak at 1100 cm^{-1} gives information about the relative amounts of Si and Na [7].

Liquid Analyses

Si and Al concentration were analysed with inductively coupled plasma mass spectroscopy (ICP-OES) (Perkin Elmer Optima 4300). The calibration for Si was performed by three single-element standards containing 2, 10 and 20 mg L^{-1}, respectively, which were diluted with supra-pure HNO_3 and MilliQ water from a single-element standard (Merck) with a concentration of 1 gL^{-1}. The calibration for Al was conducted with four multi-element standards containing 0.1, 1, 10 and 100 mg L^{-1} of Al, which were obtained by dilution from a corresponding multi-element standard (Merck X). Selected samples (indicated in the results tables) were analysed with another ICP-OES (Spectro Ciros Vision EOP).

Si speciation was determined by UV-VIS spectroscopy (Varian Cary 100 UV-VIS Spectrophotometer) using the β-silico-molybdato method described by Dietzel [8]. The main principle of this method is that only monosilicic acid reacts with molybdate ions according to

$$6\,H_4SiO_4 + 12\,H_2MoO_4 \rightarrow \beta - H_4SiMo_{12}O_{40} + 12\,H_2O, \qquad (18)$$

whereas polymers have to decompose at pH 1.2 during the measurement to intermediate monomers, which then also form the β-silico-molybdate complex. Therefore the absorption at 390 nm, where β-$H_4SiMo_{12}O_{40}$ formation is monitored, increases during the whole measurement when polysilicic acids are present, whereas it reaches a constant value after about one minute when only monomers are present. Quantification of Si in samples containing only monosilicic acid was based on a linear calibration with offset by seven standards (1.0, 3.0, 5.0, 10.0, 20.0, 30.0 and 50.0 mg L^{-1} of Si).

Si isotopic composition of selected solutions was determined by MC-ICP-MS ((Thermo Neptune) as described above and more detailed in a separate paper [92].

3.3 Results

3.3.1 Precipitation and Dissolution Kinetics

General observations:

Already during the first freezing period a precipitate forms which survives the first thawing period. The precipitate is accumulated during further freezing cycles which is indicated by a decrease in the concentration of dissolved Si (Figure 16):

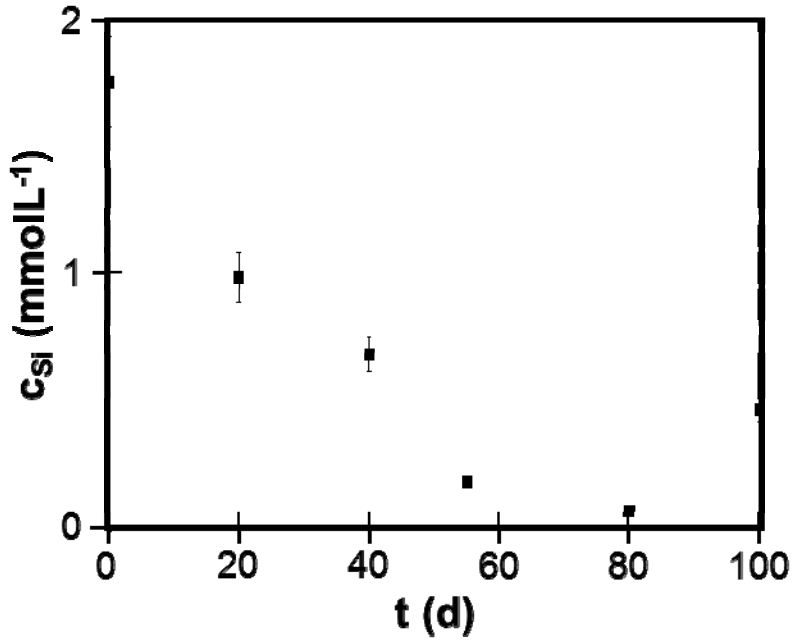

Figure 16: Development of the concentration of dissolved Si as a function of freezing cycles or days, respectively.

Experiments with Si only

Removal of Si from aqueous solution by cyclic freezing is restricted to pH < 11 (Figure 17): At pH 11 the concentration of dissolved Si remains constant over 100 d. This means that all Si that is possibly removed during a freezing period is re-dissolved during the subsequent thawing period. Another explanation is that Si remains dissolved even in the highly concentrated residual solutions due to the high solubility of amorphous SiO_2 at pH > 10.7. For pH < 11 the net precipitation amount increases with decreasing pH until pH 5 and decreases again for pH 3. Maximum removal capacity accounts for about 90 % of the initial Si concentration. Data suggest a maximum fixation of Si after 40 to 50 cycles with subsequent re-dissolution. Without cyclic freezing no precipitation occurs (Table 4).

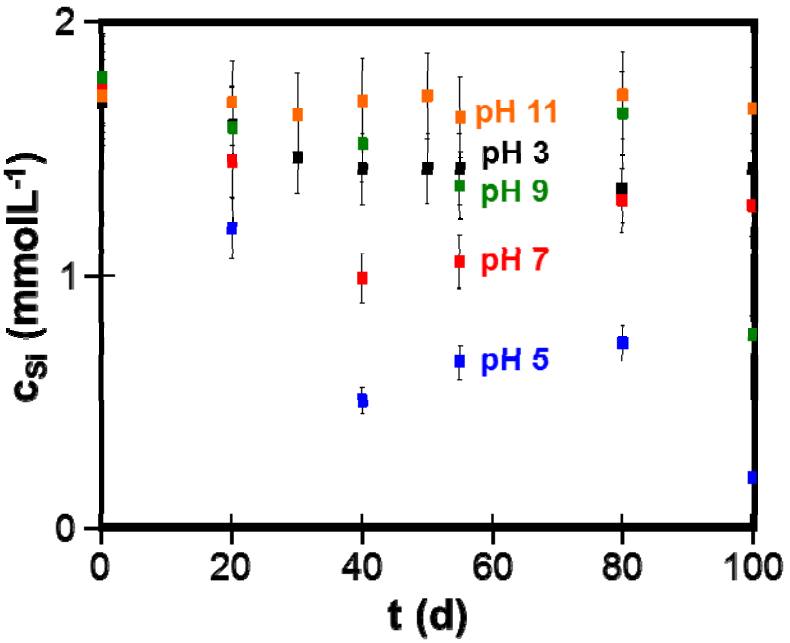

Figure 17: Effect of pH on the dissolved Si concentration in pure Si solutions as a function of freezing cycles or days, respectively

Experiments with Si and Al

Similar to the in experiments with pure Si solutions also in experiments with Al cyclic freezing leads to the removal of Si from the solution and to an accumulation of the precipitate apart from the experiment performed at pH 11 (Figure 18). Additionally at pH 5 or higher also Al is removed from the solution (Table 5). The amount of removed Si in experiments with 0.1 mmol L^{-1} Al depends on pH: It accounts for about 30 % at pH 3, 20 % at pH 5, more than 90 % at pH 7 and about 60 % at pH 9. Thus a maximum decrease of dissolved silica by precipitation of amorphous silica is reached at near neutral pH. These values are partly much higher than for experiments without Al. In those experiments where most Si was removed (pH 7 and 9) a minimal Si concentration was reached after 80 d and afterwards the concentration increased again slightly. The final increase in the concentration of dissolved Si at pH 7 and 9 is correlated with a simultaneous increase in the concentrations of dissolved Al. Al concentrations in the reference samples were constant apart from pH 7 where about 40 % of Al precipitated at room temperature:

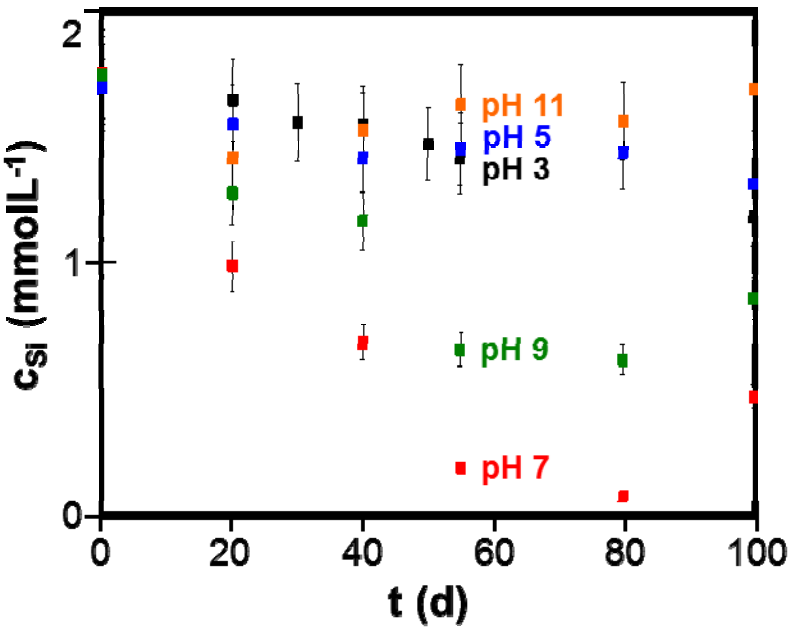

Figure 18: Effect of pH on the concentration of dissolved Si in Si solutions containing 0.1 mmol L^{-1} Al as a function of freezing cycles or days, respectively

Due to the interesting interactions between Si and Al further experiments with 1 mmol L^{-1} Al were conducted. In these experiments also the effect of the addition of 100 mmol L^{-1} NaCl was studied at pH 4.5 and pH 7 (Table 6, Table 7). The first observation is the generally accelerating effect of Al on silica precipitation by cyclic freezing (Figure 19). At pH 7 this accelerating effect is so strong that after the preparation of the solution a Si- and Al-containing precipitate is formed already before the beginning of the experiment ("pre-freezing precipitation"). This initial precipitate enhances Si removal from the solution during cyclic freezing. The presence of an initial precipitate was macroscopically observed and is also reflected in the Si concentrations in the "initial" (not yet frozen) solution of only 0.58 instead of 1.7 mmol L^{-1} for NaCl-containing and of 0.81 mmol L^{-1} for NaCl-free experiments (Table 6, Table 7). After one freezing cycle the concentration of dissolved Si decreased to 0.35 mmol L^{-1} and 0.29 mmol L^{-1} for NaCl-containing and NaCl-free experiments, respectively. Further cyclic freezing resulted in constant concentrations of about 0.12 mmol L^{-1} after 64 and more cycles for NaCl-containing and of 0.06 mmol L^{-1} after 131 d for NaCl-free experiments. When the experimental volume was increased to 1 L already the first freezing cycle decreased the Si concentration to 0.24 mmol L^{-1}.

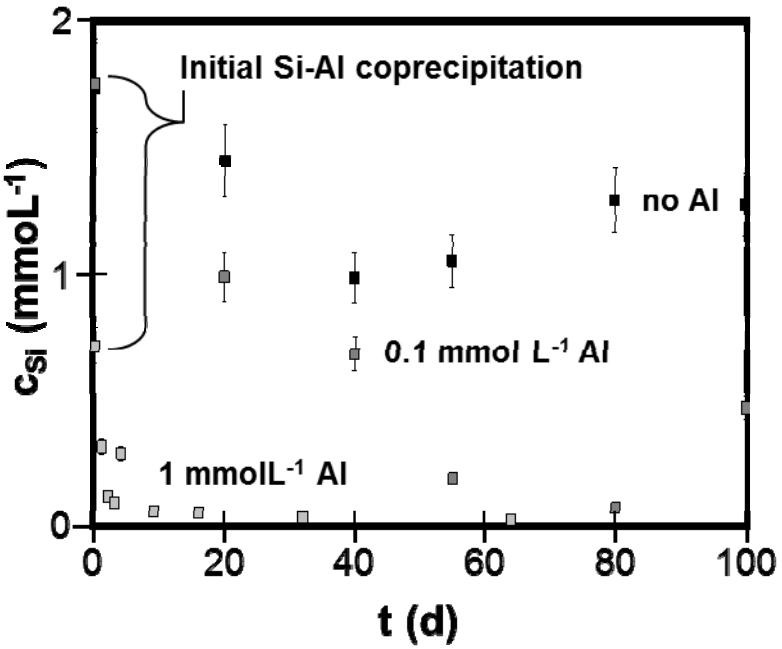

Figure 19: Effect of Al on Si precipitation by cyclic freezing at pH 7

Although at pH 4.5 the pre-freezing precipitation of both Si and Al is less pronounced than at pH 7, it is significant: The "initial" Si concentration decreases by addition of Al only to 1.45 mmol L^{-1} at pH 4.5 instead of 0.58 mmol L^{-1} at pH 7 for NaCl-containing and to 1.13 mmol L^{-1} instead of 0.81 mmol L^{-1} for NaCl-free experiments. Correspondingly, the concentration of dissolved Al drops only to 0.69 mmol L^{-1} at pH 4.5 instead of to almost zero at pH 7 for NaCl-free solutions. When the initial Al concentration accounted only for 0.1 mmol L^{-1}, no pre-freezing precipitation takes place. In the NaCl-containing solution the concentration of dissolved Si is constant during the first freezing cycle, but starts to decrease afterwards (with one outlier for the sample obtained after 16 d) until after 264 d a residual concentration of dissolved Si of 0.52 mmol L^{-1} is reached (Figure 20). Contrary, in the NaCl-free experiment it decreased within the first freezing cycle from 1.13 mmol L^{-1} to 0.63 mmol L^{-1} (for 0.1 L) and from 1.16 mmol L^{-1} to 0.77 mmol L^{-1} (1 L), respectively. Further freezing cycles in the NaCl-free system indicate a slow decrease to 0.34 mmol L^{-1} after 196 d and an increase to 0.54 mmol L^{-1} after 247 d (for 0.1 L). In the experiment with an experimental volume of 1 L a similar concentration of dissolved Si of 0.40 mmol L^{-1} was reached after 132 d (Table 7). A similar evolution with a decrease to 0.33 mmol L^{-1} after 128 d and a possible re-increase to 0.52 mmol L^{-1} after 264 d was observed in the NaCl-containing experiment. Generally, the decrease in Si concentration in the experimental solution is connected with a decrease in Al and Na concentration. The reference sample which was stored at room temperature over the whole experimental period did not show a significant decrease in the concentration of dissolved Si (Table 6). Interestingly, the reference sample of the NaCl-free experiment shows a Si concentration of 1.52 mmol L^{-1} which is higher than that of the initial solution after mixing (Table 7). This behaviour suggests re-dissolution of an initially formed precipitate during storage at room temperature.

The third and important observation is that NaCl suppresses silica precipitation by cyclic freezing: The final concentrations of dissolved Si are twice as high when NaCl is present (Figure 20).

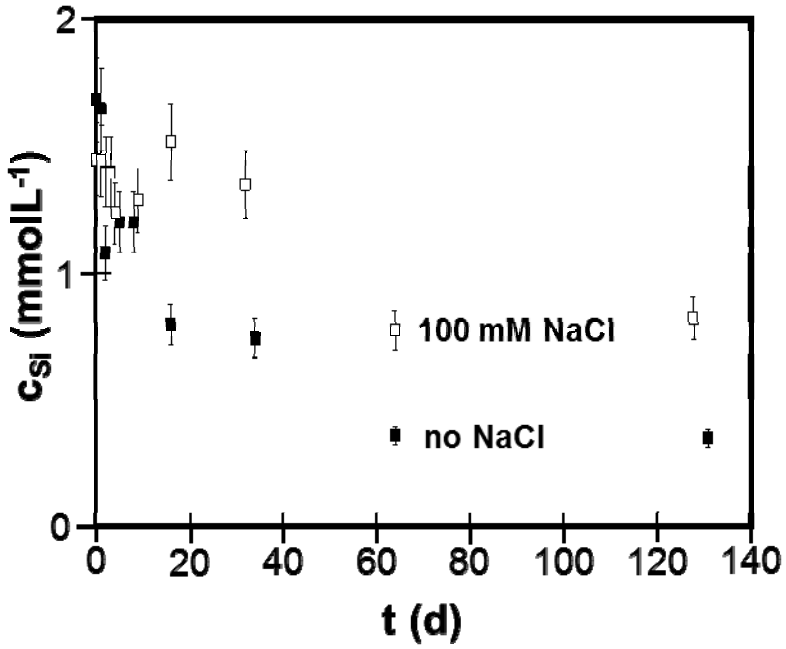

Figure 20: Effect of NaCl addition (100 mmol L^{-1}) on Si precipitation by cyclic freezing at pH 4.5 and 1 mmol L^{-1} Al

Experiments with Si and B

Experimental results show that there was no net removal of B in experiments whereas Si net removal depends on pH (Table 8, Figure 21). At pH 3 only about 20 % of Si was removed which is similar as for experiments with pure Si. At pH 5 conditions were very unstable yielding to net removals from 50 to 90 %. However, considering maximal net Si removal the values are in the same range as for experiments with pure Si solutions. In contrast, at pH 7 the net removal of Si was only about 10 % and concentrations are rather constant whereas in pure Si solutions the percentage of silica precipitation was significantly higher (40 – 50 %). At pH 9 during the first 40 d there was only a slow net removal of about 10 %. However, the net removal rates increase for a larger number of freezing cycles and after 80 d to about 50 % of the initially dissolved Si have precipitated. Without B there was no net removal of Si at pH 7. At pH 11 there was no net removal of Si during the experimental run time which is in agreement with experiments without B. This means that generally B has no significant effect on silica precipitation at acidic and alkaline pH (≤ 5 or 11), but reduces silica precipitation at pH 7 and stimulates silica precipitation at pH 9. In the reference samples no precipitation was observed (Table 8).

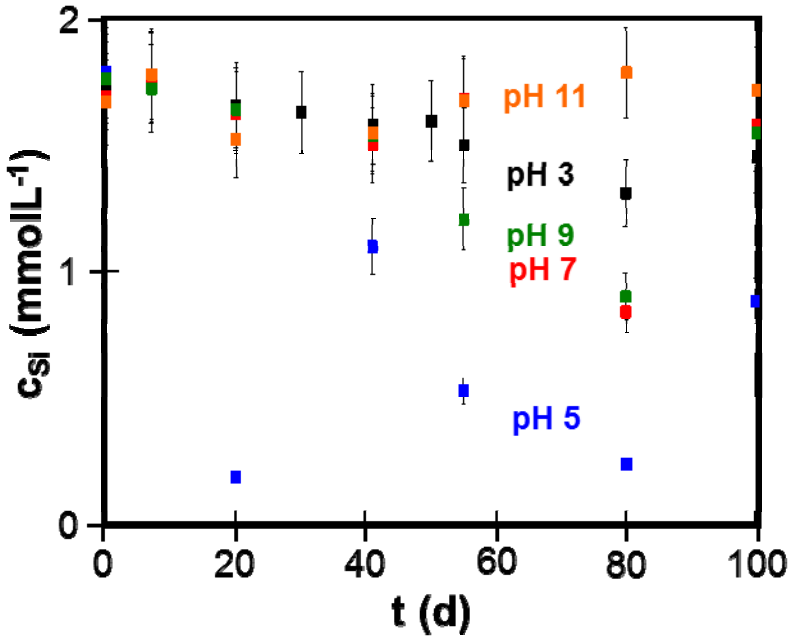

Figure 21: Concentration of dissolved silica as a function of time at various pH in solutions with 0.1 mmol L^{-1} B

Experiments with Si and Ge

In accordance with the above experiments Si was also removed in the presence of Ge from solution by cyclic freezing. Interestingly, in the presence of Ge the net precipitation was much higher than without Ge at pH 3 (Figure 22). Whereas in pure Si solution at pH 3 only about 20 % of dissolved Si were finally fixed, Si fixation accounted for almost 80 % of initially dissolved Si in Ge-containing solutions. Furthermore, in pure Si solutions at pH 3 after 40 d no further net precipitation of Si took place, whereas in Ge-containing solutions net precipitations continued until the end of the experiment. Obviously, Ge concentrations in solution always reached the initial value after each freezing cycle (Table 9). Thus a significant Ge net coprecipitation at the end of each run could not be observed. An increase of pH from 3 to 4.5 decreased concentrations of dissolved Si in Ge-containing experiments (Table 9). This was not the case for pure Si solutions (Table 5). Furthermore a dynamic steady state with cyclically recurring Si concentrations was already reached after two cycles at pH 4.5, but not before 100 cycles at pH 3.

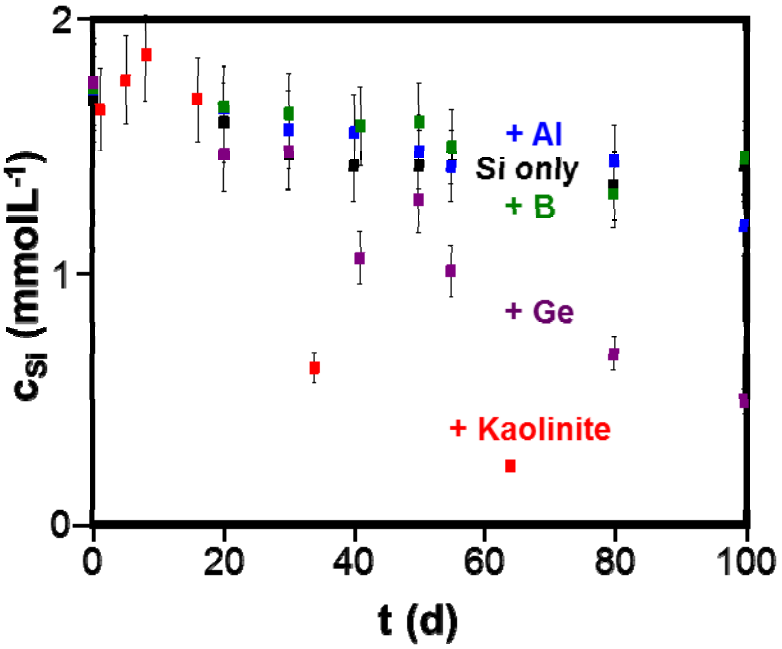

Figure 22: Effect of Al, B, Ge (each 0.1 mmol L^{-1}, pH 3) and kaolinite (10 mmol L^{-1}, pH 4.5) on Si precipitation by cyclic freezing

Experiments with Si and kaolinite

It was checked by XRD that kaolinite is not transformed into other mineral phases after cyclic freezing (Figure 23). In the experiments with kaolinite (pH 4.5, V = 0.1 L, [Si] = 1.7 mmol L^{-1}, [kaolinite] = 2.58 g L^{-1}) the Si concentration remained nearly constant within the first 16 d Table 10). Subsequently, dissolved Si was removed almost quantitatively from solution by silica precipitation until 131 d. Al concentration initially increased to 0.22 mmol L^{-1} and afterwards decreased to the detection limit of 0.0004 mmol L^{-1}.

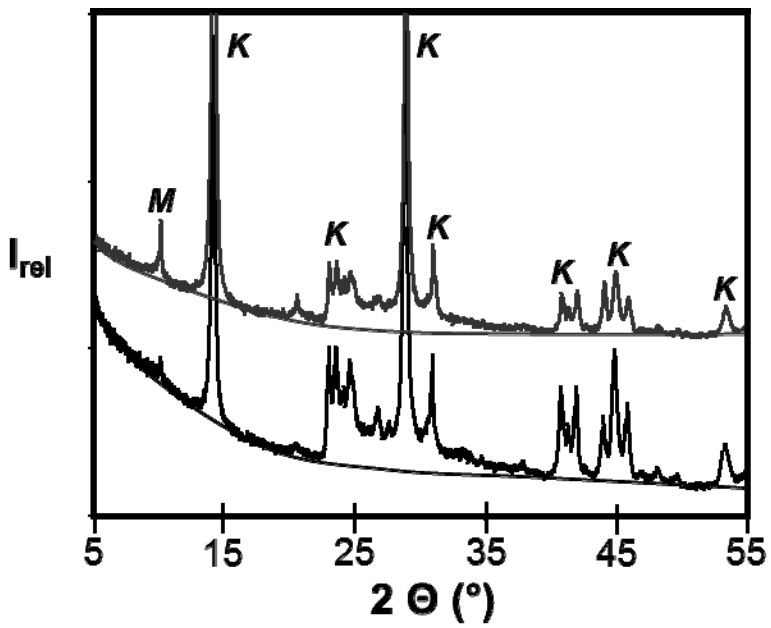

Figure 23: XRD pattern (Co-Kα) of Kaolinite (K) and trace of muscovite (M) before (black) and after (grey) 131 d cyclic freezing with an aqueous solution (pH 4.5) containing 1.7 mmol L^{-1} Si

A slight decrease in full width at half maximum of the (001) peak of kaolinite and the increase in muscovite peak intensity might be due to sample preparation and not due to significant changes of the solid during the experiment.

Summary

Whereas B and Al have only a slight effect on precipitation of Si by cyclic freezing at acidic pH, Ge and especially kaolinite increase silica precipitation significantly (Figure 22). In experiments with dissolved additives the Si concentration decreased linearly, whereas in presence of kaolinite it remained constant during the first 20 d and subsequently decreased rapidly. After 131 d 90 % of dissolved silica has been removed in presence of Ge and even 97 % in presence of kaolinite (Table 10).

3.3.2 Si isotopic fractionation

The behaviour of Si isotopes in the Si-Al experiments is described in detail in a separate manuscript [92]. Briefly, the results show that Si fractionation occurs only at 1 mmol L^{-1} Al but not at 0.1 mmol L^{-1} (Figure 24):

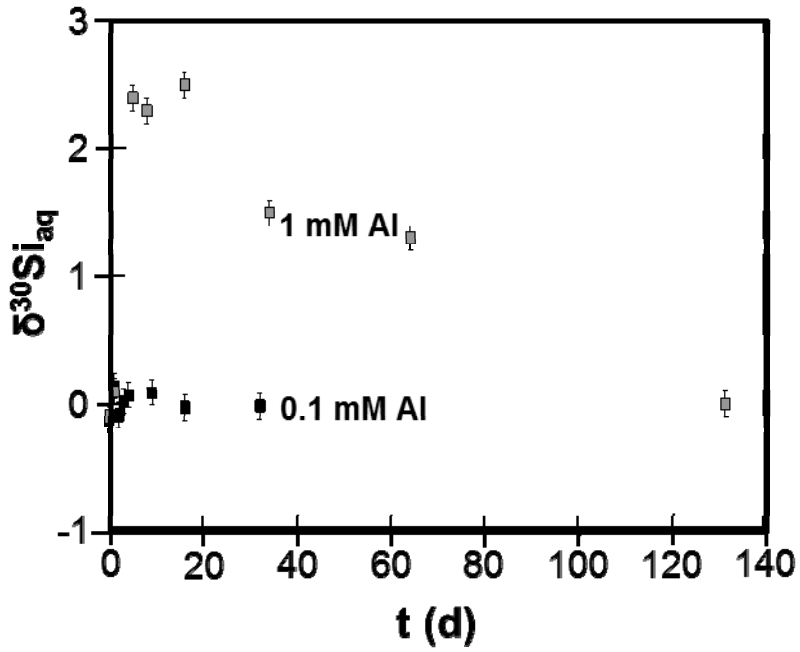

Figure 24: Si isotope fractionation at pH 4.5 at 0.1 mmol L^{-1} and 1 mmol L^{-1} Al

As Si isotopic fractionation takes place, the solution becomes heavier with respect to Si isotopes whereas the precipitate becomes lighter (Figure 25):

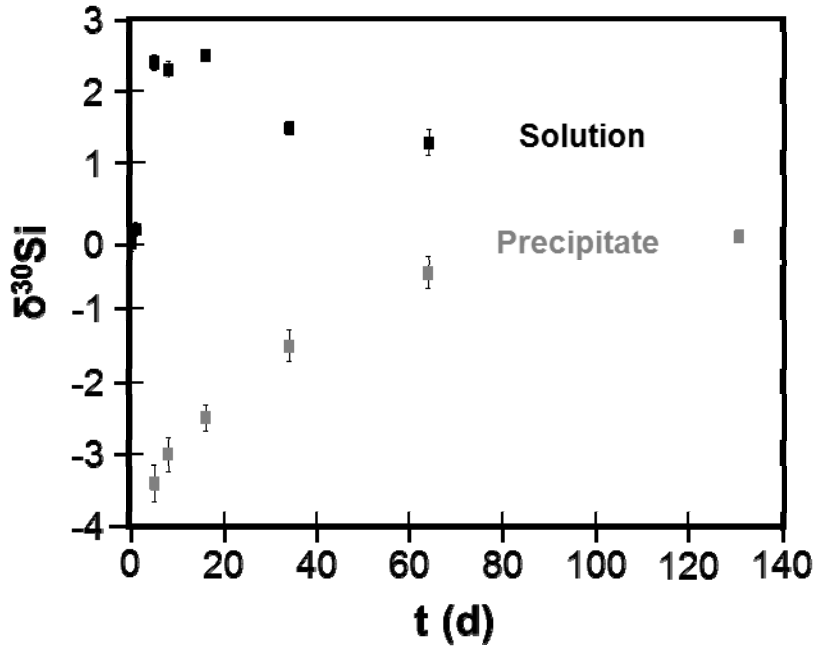

Figure 25: Si isotopic fractionation by cyclic freezing of an aqueous solution (initially 1.7 mmol L^{-1} Si, 1 mmol L^{-1} Al, pH 4.5) as a function of freezing cycles or days, respectively. Black symbols indicate the isotopic composition of the solution and grey symbols that of the precipitate.

The maximum bulk fractionation occurs after five cycles and accounts for $\Delta^{30}Si = \delta^{30}Si_{(aq)}$-$\delta^{30}Si_{(s)}$ = 5.8 ‰. With increasing number of freezing cycles these two values converge again towards a δ-value of about zero (Figure 25). Thus finally there is no significant apparent fractionation of Si isotopes between solution and precipitate due to cyclic freezing for a sufficiently large number of freezing cycles.

3.3.3 Polymerisation

Reaction curves with molybdic acid of characteristic polymeric and monomeric silicic acids [8] from experimental solutions are shown in Figure 26.

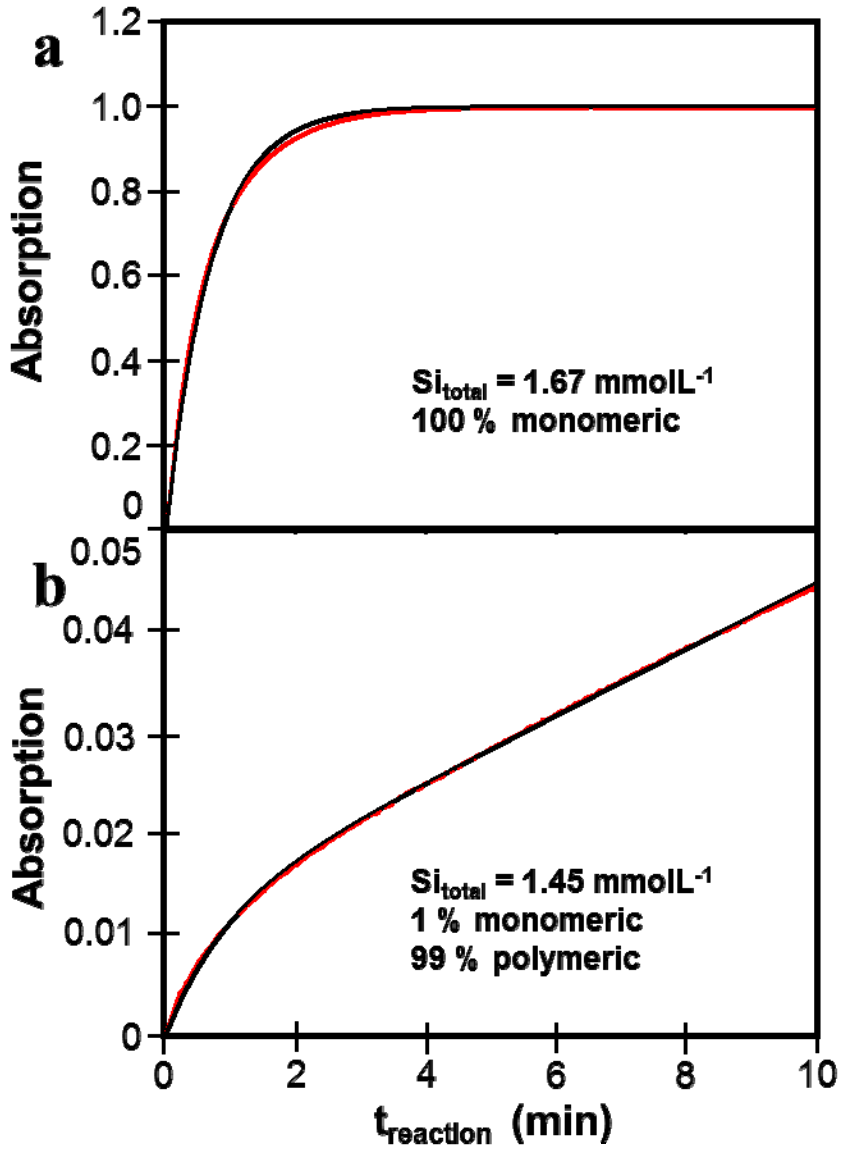

Figure 26: Reaction curves with molybdic acid [8] of a solution initially containing 1.7 mmol L^{-1} Si and 0.1 mmol L^{-1} B after 100 d at room temperature (a) and after 100 d cyclic freezing (b) showing monosilicic and polysilicic acid, respectively, at pH 3. Remark: Ordinate axes are differently scaled. Data are given in Table 8.

After distinct numbers of freezing cycles the experimental solutions were separated from the precipitates and analysed for the total Si concentration and the contribution of monomeric and polymeric silica. Results are shown in Table 8. Obviously, polymerisation occurs already within the first freezing cycle (Figure 27). Afterwards competing processes of depolymerisation and polymerisation of silica lead to a rather complex evolution of the degree of polymerisation. Cyclic freezing leads to polymerisation of silicic acids at pH 3 and 4.5, but not at higher pH (Table 6) and interestingly not in the presence of Ge (Figure 27). The addition of B slightly enhances polymerisation of silica, whereas the addition of Al and kaolinite rather inhibit it or the possibly formed polymers are adsorbed onto an Al-hydroxide or onto kaolinite, respectively.

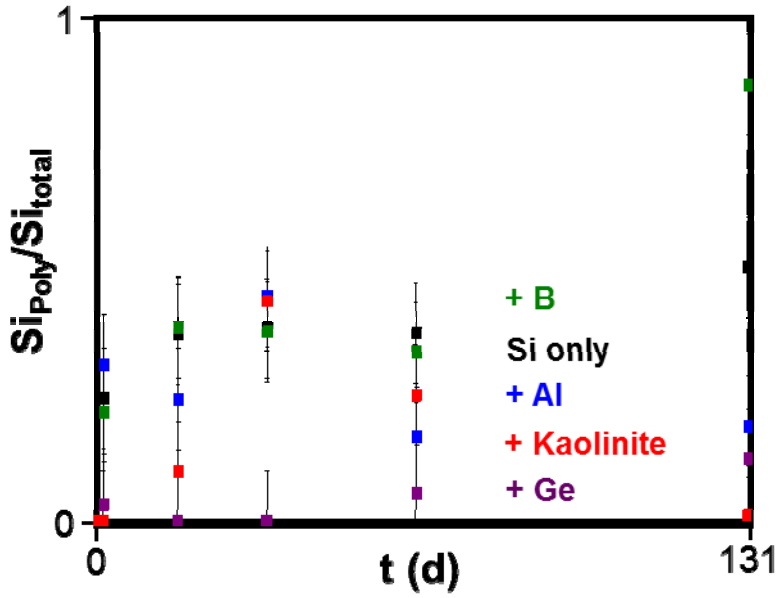

Figure 27: Degree of polymerisation as a function of freezing cycles for various additives at pH 4.5

Polymerisation of silica at pH 3 is more pronounced than at pH 4.5 (Table 4 ff., Figure 28). Besides the degree of polymerisation in terms of the ratio of polymeric versus total dissolved Si, also the size of polymers increases with decreasing pH in case of pure Si and Al-containing solutions, which is indicated by a drop in the reaction rate constant with molybdate ions from 0.02 to 0.003 min^{-1} and from 0.05 to 0.004 min^{-1}, respectively (Table 4 ff.). In case of B-containing solutions no significant difference was observed. However, all these values correspond to macromolecular polysilicic acids [5]. An increase of pH to 5 or more leads to the complete absence of Si polymerisation. Also in the reference samples no polymerisation was observed (Table 8).

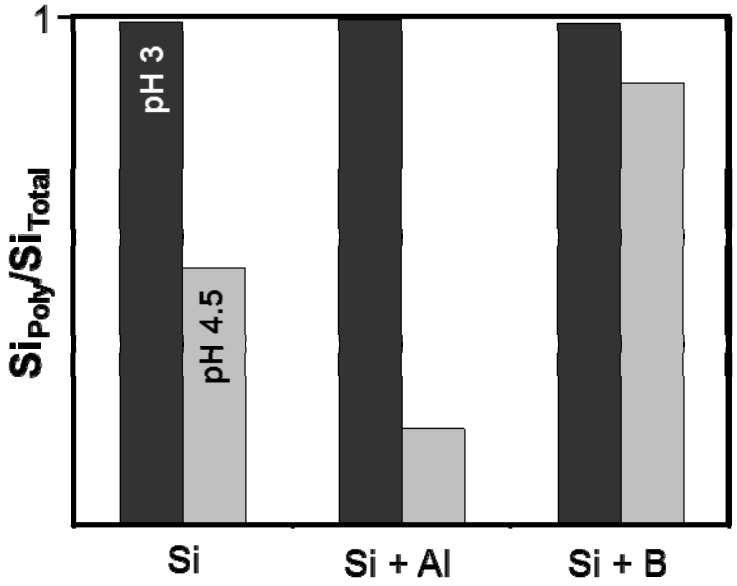

Figure 28: Polymerisation degree (Si_{Poly}/Si_{Total}) of dissolved silicic acid after 100 and 131 d cyclic freezing at pH 3 and pH 4.5, respectively, in experiments with Si only and with 0.1 mmol L^{-1} Al and B, respectively. Values for 64 d at pH 4.5 are in the same range as for 131 d.

3.3.4 Characterisation of Precipitates

The Si-containing precipitates formed by cyclic freezing are in all experiments irregularly shaped particles with a size of 10 to 100 µm (Figure 29). SEM-SE images show that their size and morphology do change neither as a function of the additive (Al or B) (Figure 29a, b, c) nor with reaction time in case of experiments with 1 mmol L^{-1} Al (Figure 29 d, e, f):

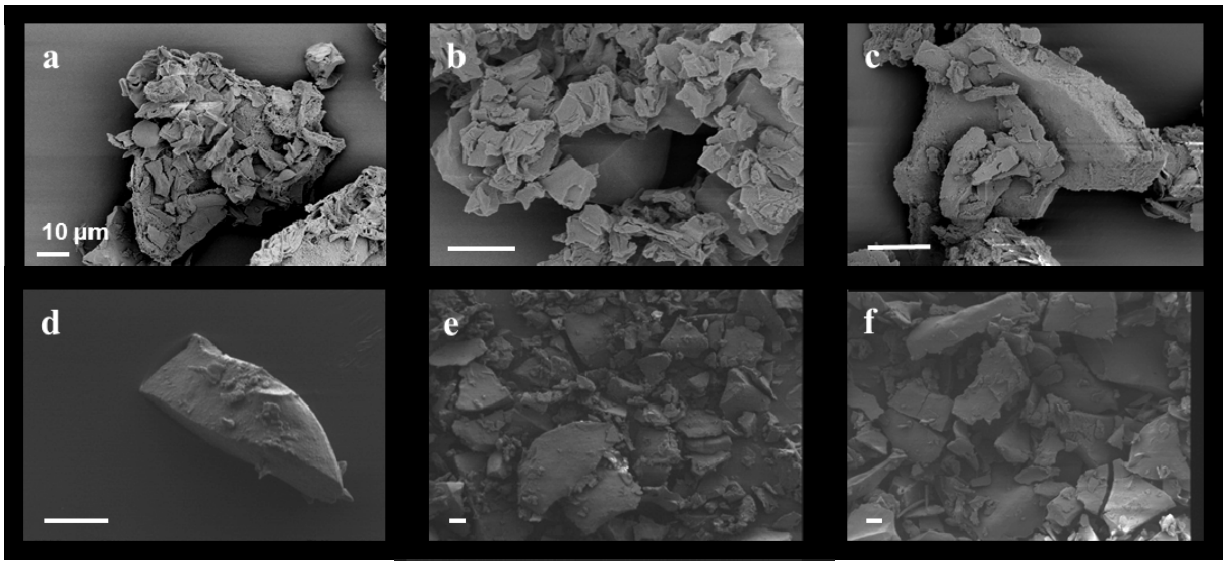

Figure 29: SEM images of different precipitates from freezing experiments: a: Si only (pH 5, 30 d), b: Si + 0.1 mmol L^{-1} B (pH 5, 60 d), c: Si + 0.1 mmol L^{-1} Al (pH 7, 60 d); d: Si + 1 mmol L^{-1} Al, 1 d, e: Si + 1 mmol L^{-1} Al, 2 d, f: Si + 1 mmol L^{-1} Al, 3 d

B and Ge are not incorporated in the solid according to solution chemistry, but Al seems to form a solid compound with Si by cyclic freezing which can also be concluded from solution chemistry. Therefore it is suggested that precipitates from experiments with B and Ge are rather pure amorphous silica whereas precipitates from experiments with Al might represent an alumosilicates phase. In analogy to the experiment with pure Si and with additional B and Ge X-ray diffraction patterns of precipitates obtained from experiments with 1 mmol L^{-1} Al show no distinct peaks which means that they are non-crystalline solids (Figure 30). Furthermore, no significant ripening of the precipitate with increasing number of freezing cycles is suggested by XRD.

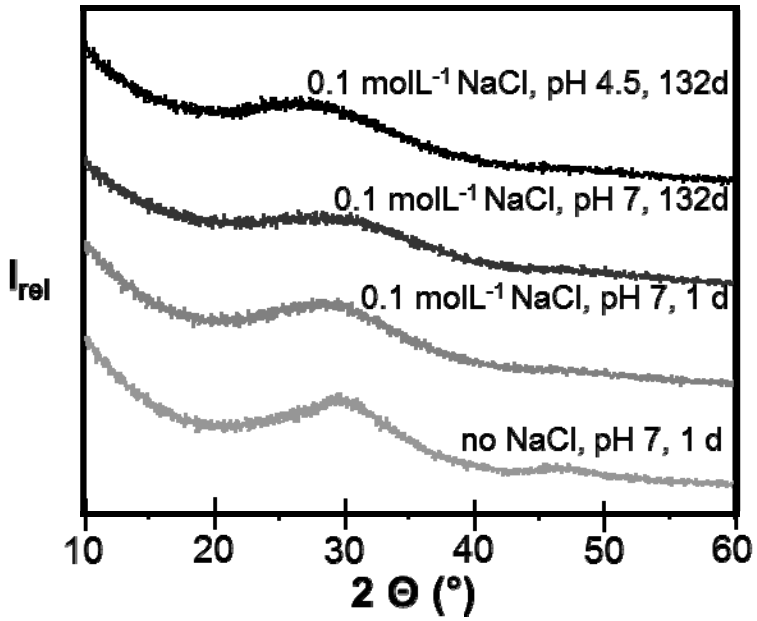

Figure 30: XRD patterns of selected precipitates obtained from cyclic freezing of aqueous solutions containing 1.7 mmol L^{-1} Si and 1 mmol L^{-1} Al (Table 6, Table 7).

Although the lack of discrete peaks is a common feature of all obtained XRD patterns there are some differences: The 2Θ-value of the X-ray scattering bulge shifts from 27 to 29 ° when the pH is increased from 4.5 to 7 and the relative intensity is decreased. Interestingly, the higher the number of freezing cycles is the lower is the relative intensity of the bulge whereas its position remains constant. This loss of intensity indicates rather disordering than ordering. Absence of NaCl increases the bulge intensity and shifts its position to 30 °. Additionally, a second bulge occurs at about 47 °.

For a more detailed characterisation of the amorphous alumosilicate phase a selected sample (three freezing cycles, pH 7, 1.7 mmol L^{-1} $Si_{initial}$, 1 mmol L^{-1} $Al_{initial}$, no NaCl added) was analysed by FTIR spectroscopy and compared to reference spectrum of an allophane-rich sample (60 – 80 % allophane) provided by the Federal Institute for Geosciences and Natural Resources in Hannover, Germany, which is originating from a deposit from the area of Santo Domingo de los Colorados, Ecuador [132]. The two spectra have a good agreement indicating that a allophane-like solid has formed during the experiments (Figure 31).

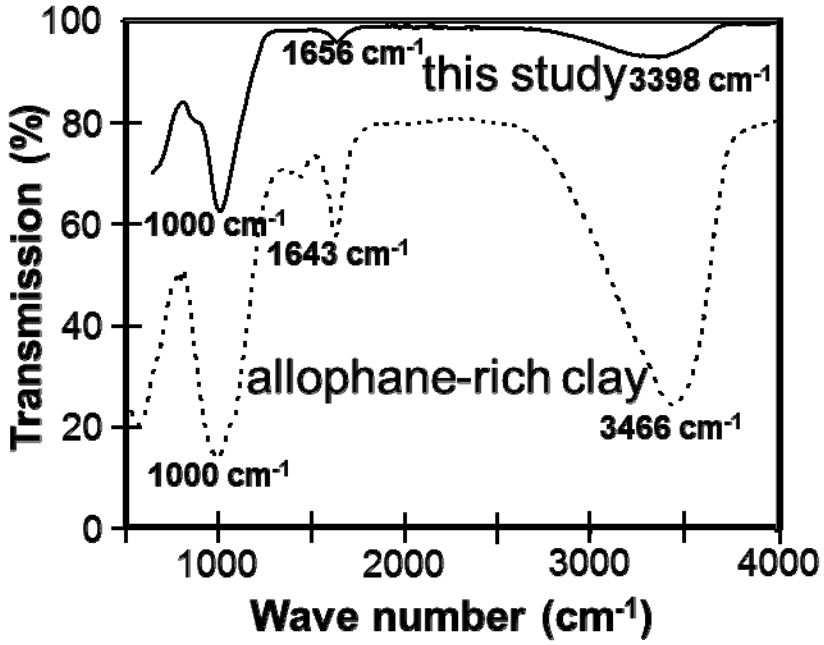

Figure 31: FTIR patterns of a precipitate of cyclic freezing experiments (3 d, pH 7, 1.7 mmol L^{-1} Si, 1 mmol L^{-1} Al) and an allophane-rich reference material described in [132].

TEM-EDX analyses (Figure 32) were performed at different analytical spots in a selected sample (one freezing cycle, 1.7 mmol L^{-1} $Si_{initial}$, 1 mmol L^{-1} $Al_{initial}$, 100 mmol L^{-1} NaCl). Cu peaks in EDX spectra result from the preparation of the sample on a copper net. It can be seen that besides O Si and Al are the main elements present in the precipitate. Si:Al ratios show a wide range from 2:1 to 2:3. Minor amounts of K present in the precipitate result from KOH which was used for pH adjustment.

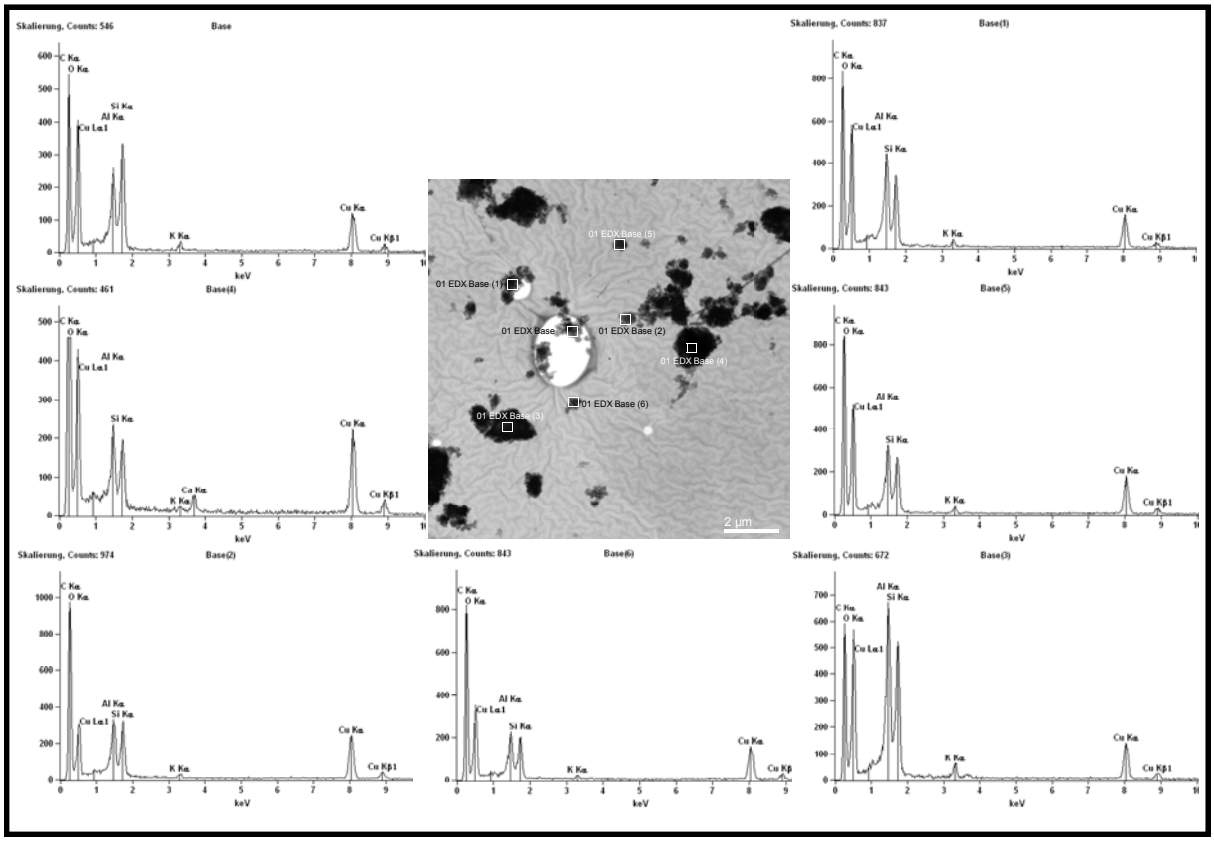

Figure 32: TEM-EDX spectra of different analytical spots on a sample obtained after 1 d from cyclic freezing of a solution containing initially 1.7 mmol L^{-1} Si, 1 mmol L^{-1} Al and 100 mmol L^{-1} Na at pH 7.

At other analytical spots also significant amounts of Na were found which might result from halite crystals precipitated during freezing in the experiment due to added NaCl. However, as stoichiometry of Cl and Na concentrations do not fit together 1:1, a part of Na is bound to an alumosilicate phase. Interestingly, the Si:Al ratio varies even within one particle, but does not show any regular zoning (Figure 33).

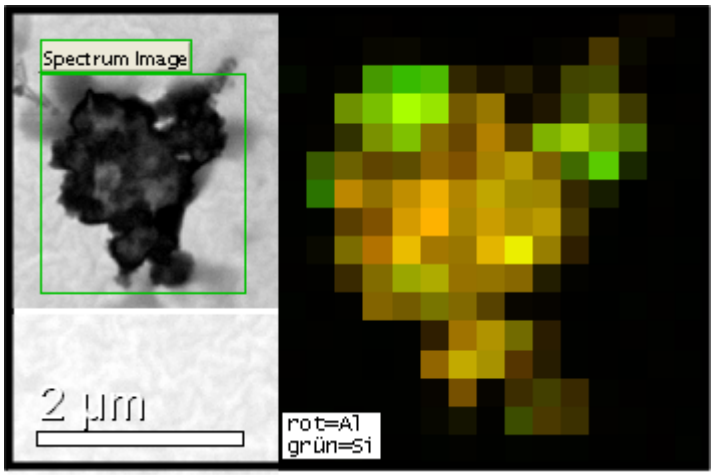

Figure 33: STEM mapping of a selected particle of a precipitate obtained from cyclic freezing (1.7 mmol L^{-1} Si, 1 mmol L^{-1} Al, 100 mmol L^{-1} NaCl, 1 d)

3.4 Discussion

3.4.1 Precipitation of Amorphous Silica

In this study a set of 25 experimental sequences, each consisting of about ten single experiments was conducted to study the effect of pH, foreign elements, suspended matter (kaolinite) and experimental duration on the chemical and isotope composition of silica precipitated by cyclic freezing and of the remaining solution as well as on precipitation kinetics. It was shown that cyclic freezing leads to accumulation of the precipitate and that the composition of this precipitate depends on solution chemistry. In order to understand the ongoing processes during the experiment, it is necessary to discuss several thermodynamic and kinetic effects:

If a solution is cooled down from 20 °C to 0 ° the solubility of amorphous silica decreases from 1.74 to 1.12 mmol L^{-1} [133]. Thus supersaturation with respect to amorphous silica is reached already before freezing. However, supersaturation is a necessary, but not sufficient condition for precipitation since nucleation requires energy. Before freezing occurs in the first cycle homogeneous nucleation is valid for the formation of silica when the bottle wall is neglected. Homogeneous nucleation is energetically less favoured compared to heterogeneous nucleation [95] which is valid in the further freezing sequences. However, freezing of the experimental solution has a double effect on silica precipitation: On the one hand it concentrates the dissolved ions and increases supersaturation with respect to amorphous silica. On the other hand it provides heterogeneous nuclei for precipitation of a silica phase. Hence freezing is considered to be the driving process for silica precipitation. It has to be considered that the macroscopic impression of a completely frozen sample during a freezing cycle is misleading since a previous study [121] showed that there are fluids even in "completely frozen" soils as surface films or microzones.

The general trend of an exponential decrease of concentration of dissolved Si with increasing number of freezing cycles is in agreement with experimental studies [22] and natural observations [118]. The accumulation of amorphous silica obviously indicates that the overall dissolution rate is slower than the overall precipitation rate.

The effect of pH on net precipitation of amorphous silica from pure Si solutions can be explained by its effect on silica solubility: At pH > 10.7 the solubility of amorphous silica is nearly infinite due to the occurrence of polysilicic acids and the dissociation of monosilicic acid at elevated pH [5] [134]. Therefore precipitation even from highly concentrated residual solutions in the freezing period is strongly inhibited and a potential re-dissolution of amorphous silica during the thawing period is enhanced. The effect of pH on Si precipitation is similar for experiments with and without Al or B where additional aqua-complexes might occur, e.g. Al-Si complex formation [135].

During freezing ice crystals are formed which do not incorporate Si or Al. Hence the concentration of these elements – and also of Na, if present – increases in the remaining solution. The solution becomes supersaturated with respect to amorphous $Al(OH)_3$ and amorphous SiO_2. Since the supersaturation with respect to amorphous $Al(OH)_3$ is higher than that with respect to amorphous SiO_2 for pH between 4.5 and 7 at a Si:Al ratio like in these experiments, it is assumed that amorphous $Al(OH)_3$ forms first and Si is adsorbed onto its surface afterwards. This is in agreement with the pre-freezing decrease in Al in case of the

experiments with 1 mM Al. Furthermore, this is supported by the fractionation of Si isotopes as in adsorption experiments it was shown that adsorption processes fractionate Si isotopes and because in freezing experiments with only 0.1 mM Al instead of 1 mM Al Si isotope fractionation is insignificant, which could be explained by direct precipitation of amorphous SiO_2 due to the lack of an $Al(OH)_3$ substrate [92]. Unfortunately, as samples were taken only after a completed cycle, chemical analyses of the solutions could not prove if $Al(OH)_3$ really precipitated before SiO_2. After Si has been adsorbed onto the surface of amorphous $Al(OH)_3$ the bounded Si reacts with Al-OH to allophane which is suggested by FTIR analysis (Figure 31).

The presence of Al enhances Si removal from solution especially at pH 7 and 9 (Figure 18). This might be due to the formation of hydroxyaluminosilicates (HAS) described before [135]. The presence of Al shifts the pH of most intense silica precipitation from 5 to 7 compared to pure Si solutions which can be explained by preferential Si adsorption on Al-OH surfaces at elevated pH (up to about pH 9). This preferential adsorption has a stronger effect on silica or HAS precipitation than the solubility minimum of amorphous $Al(OH)_3$ and HAS close to pH 6.5 [136] and the constant solubility of amorphous silica at acidic and neutral pH [5].

The recurring constant B concentration in the experimental solution is not necessarily constant during every cycle. It is neither known if B is incorporated in the same phase as Si during freezing, nor if B is released from the solid preferentially. Natural diatoms and radiolarians contains about 70 to 80 ppm B [100] and sponges up to 800 ppm [137] which is much less than would be necessary to fix all dissolved B to the precipitated Si in the present experiments. However, a part of the dissolved B might be incorporated in the precipitate and released during the thawing period although B incorporation into amorphous silica is limited by the salinity of the aqueous solution [137]. Possibly B is partly adsorbed during freezing and released during thawing, as the solubility of sassoline, solid H_3BO_3, accounts for about 800 mmol L^{-1} [138] which is orders of magnitude higher than for amorphous silica. However, the constantly recurring concentrations of B after each cycle let B be treated as a conservative element for the net precipitation process. This excludes an effect of cyclic freezing on the biogenic cycle of B in cryosols which precludes climate change in terms of deeper thawing of boreal soils as a reason for B deficiency or excess diseases in conifers. Since B has no effect on silica precipitation rates, Si/B ratios decrease in Si- and B-containing systems as a function for cyclic freezing and could be used as a proxy for cyclic freezing.

Ge behaves very similar as B with respect to its above discussed conservative behaviour. Concerning phytotoxicity of Ge it can be concluded that cryosols do neither act as a source nor as a sink for Ge whereas climate change will increase vegetation and the formation of phytoliths which discriminate against Ge [110]. Trapping in plant roots is obviously less permanent than in phytoliths which should lead to an increase in the concentration of dissolved Ge by global warming.

In the experiments with kaolinite the constant concentration of Si and the increase of the Al concentration can be explained by simultaneous dissolution of kaolinite and adsorption of monosilicic acid onto its surface where Si release and fixation balance each other. After about 8 to 16 d, precipitation becomes dominant compared to dissolution. Thus after some time the dissolution rate of kaolinite is lower than the adsorption rate of monosilicic acid. This might be explained by the inhibition of kaolinite dissolution by a kind of adsorbed monosilicic acid layer. The re-fixation of Al during the second period of the experiment can be explained by co-adsorption with silicic acid. Thus in presence of kaolinite in moderately acidic cryosols a coupled dissolution and precipitation process is assumed.

In the conducted experiments the concentrations of dissolved Si were higher when NaCl was added. NaCl inhibits freezing, it thus also inhibits freezing-induced silica precipitation. It has to be considered that even when the sample seems to be completely frozen macroscopically there are some residual solutions with high concentrations of dissolved Si. When NaCl is present more volume of these solutions is suggested to exist and more Si remains in the dissolved state but at lower concentrations (Figure 20).

3.4.2 Polymerisation of Dissolved Silicic Acids

Throughout freezing the concentration of dissolved silica increases until supersaturation is reached. Supersaturation will induce polymerisation and subsequently nuclei of silica can be formed. The fact that at pH 5 no polymerisation was observed after 100 completed freezing cycles does not mean that no polymers were present within a single freezing cycle when the sample was frozen. Possibly they are even still present after thawing, but adsorbed to the silica surface and therefore not detectable in the filtrated solution anymore. The stabilisation of polysilicic acids at pH up to 7 in the presence of Al can be explained by the formation of Si-Al copolymers which have already been found in acidic soil solutions [17].

Previous cyclic freezing experiments [22] did not lead to polymerisation of silicic acids because they were performed at pH 6.5. This study shows that a decrease in pH to 3 changes polymerisation behaviour of silicic acids during cyclic freezing. Although it has already been known that polysilicic acids form by dissolution of minerals in acidic soils [17], this is to my knowledge the first observation of the formation of polysilicic acids by cyclic freezing.

Enhancement of silica precipitation at pH 3 and pH 4.5 in B-containing solutions compared to pure Si solution is in contrast to previous data at pH 8 [139]. The reasons for this difference might be related to surface charge effects, but are not yet completely understood.

To understand the different effect of Ge and B on polymerisation behaviour the aquatic chemistry of Ge and B have to be compared: Ge occurs in dilute acidic solutions predominantly as $Ge(OH)_2O$ [106] whereas B occurs as $B(OH)_3$ [140]. In both cases the central ion is coordinated trigonally and the bond is polar-covalent as the difference between the electronegativies of O and Ge or B accounts for 1.5 in both cases. However, Ge is a metalloid whereas B is a non-metal. Hence the bond between Ge and O is more ionic whereas that between B and O is more covalent. This might explain differences with respect to catalytic or inhibiting effects on Si polymerisation. Another reason might be that $B(OH)_3$ contains more OH groups than $Ge(OH)_2O$. Considering that silanol groups enhance polymerisation [139], this may explain why B increases polymerisation compared to Ge. Polymerisation can be seen as a first step of precipitation. Thus the formation of "non-leachable solid substances" of boric acid and silicic acid when applied to wood for preservation issues [141] might be seen in the same context as the observed polymerisation of dissolved silicic acid in presence of B.

3.4.3 Isotope Fractionation

The restriction of Si isotopic fractionation to experiments with 1 mM Al in combination with the observation of a rapid drop in Si and Al concentration in those experiments suggests that Si-Al coprecipitation and subsequent adsorption of Si onto this precipitate is the decisive process which fractionates Si isotopes. Si isotopic fractionation is favouring the light Si

isotopes to be adsorbed which is in agreement with previous studies [79] and with adsorption experiments (chapter 2). This suggests furthermore that in freezing experiment Si isotope fractionation occurs by adsorption of Si onto a Si-Al phase during the freezing period and not by desorption and/or dissolution of the precipitate during the thawing period. The adsorption of silicic acid onto gibbsite (chapter 2) or an amorphous (Si-)Al phase (this chapter) can be described by the formation of inner-sphere complexes according to

$$Si(OH)_4 + \equiv AlOH^0 = AlOSiO(OH)_2^- + H_2O + H^+; pK = 3.2. \quad (19)$$ (modified after [14])

The reaction rate constants of this reaction are different for ^{28}Si and ^{30}Si with the lighter isotope reacting faster due to its higher mobility. This results in a maximal kinetic isotopic fractionation of

$$\alpha_{kin} = \left(\frac{k^{30}Si}{k^{30}Si} \right). \quad (20)$$

However, as there is also a backwards reaction, in this case desorption, the observed fractionation is lower than this maximal value [14]. In adsorption experiments adsorption dominates over desorption whereas in freezing experiments this is only valid within the first cycles. Later on desorption during the thawing period becomes more and more important which finally leads to a constantly recurring distribution of total Si and individual Si isotopes between adsorbate/precipitate and solution.

In a separate paper [92] the process leading to isotopically heavier and heavier isotopic composition of the solid with increasing number of freezing cycles is discussed and it is demonstrated that this process finally leads to a fractionation $\Delta_{solid\text{-}solution}$ of about 0 ‰. We suggested that the conditions during the experimental runtime converge towards a steady state which may approach equilibrium conditions. The idea behind that is there is repeatedly recurring isotope exchange between solid and solution within certain periods of each cycle. It can be assumed that this is particularly the case when liquid water forms again around a piece of ice floating in the bottle causing movement of the water and the suspended silica particles. However, the observation that a repeatedly recurring isotopic composition of the solid and the solution is observed and that this composition is in a similar range as the equilibrium between quartz and water [60] does not mean that there is equilibrium because the conditions are not constant, but always changing. Although a thermodynamic equilibrium is never reached in the experiments, the obtained isotopic compositions of precipitate and solution after each cycle for a large number of cycles can be used to calculate a “repeatedly recurring state” isotope fractionation factor. As kinetic effects are more and more ruled out, this factor might approach the equilibrium fractionation factor.

3.4.4 Implications for natural systems

Accumulation of amorphous silica by cyclic freezing which is observed in the experiments might lead in nature finally to the formation of silicates like chabazite which was described for an Antarctic diamictite [129]. The transformation from amorphous silica to zeolites in cryosols is a rather slow process, which is supported by the results of diatomite zeolitisation (chapter 4). These indicate that the time of first zeolitisation decreases with decreasing temperatures and does not occur at room temperature until 64 days. However, when applying amorphous silica and possibly subsequently formed zeolites as a proxy for cyclic freezing in

the geologic past [22] other formation mechanisms of these phases like evaporation or hydrothermal alteration must be ruled out.

Combining the results of adsorption and freezing experiments the initially asked question

"Can the Si isotopic composition of amorphous silica phases in cryosols be used to infer whether they have been formed by cyclic freezing?"

has to be answered in a complex manner: On the one hand cyclic freezing can induce Si isotope fractionation if high concentrations of Al are present. On the other hand it has to be considered that not precipitation itself but adsorption (which might take place nevertheless onto Al-hydroxide precipitates resulting from freezing) is the reason for Si isotope fractionation. For this reason the application of Si isotopes as a proxy for the impact of freezing cycles a certain pedogenic silicate mineral was exposed to is rather limited. However, since experimental data show that for a large number of freezing cycles, which can be assumed for natural permafrost regions, the isotopic fractionation $\Delta_{solid\text{-}solution}$ is close to 0 ‰. Considering that other geologic processes like adsorption on iron hydroxides [79] or basalt weathering [117] lead to an isotopically lighter Si adsorbate or amorphous silica phase, respectively, enables us to distinguish between unidirectional adsorption and precipitation processes on the one hand and cyclic processes on the other hand: Negative $\Delta^{30}Si$ values are a proxy for kinetic isotope fractionation by unidirectional processes whereas $\Delta^{30}Si$ values around zero in kinetically controlled Earth surface environments hint to cyclic processes resulting in a regularly recurring pseudo-steady state.

3.5 Conclusion

Precipitation of amorphous silica by cyclic freezing is favoured by the presence of Al (either at pH 7 or at high Al concentrations), Ge and kaolinite and it is reduced by elevated ionic strength induced by the addition of NaCl. The percentage of Si removal from the solution by precipitation of amorphous silica is maximal for pH between 5 and 7 and decreases for higher and lower pH. Besides precipitation also polymerisation of monosilicic acid to polysilicic acid takes place at acidic pH, especially in the presence of B, but not in the presence of Ge. ^{30}Si is discriminated versus ^{28}Si in the precipitate during the first freezing cycles in presence of 1 mM Al. This is caused by adsorption of Si onto $Al(OH)_3$ surfaces. However the Si isotope fractionation between dissolved and precipitated silica reaches values around 0 ‰ after about 100 cycles. Hence $\Delta^{30}Si$ values of amorphous silica might be used to distinguish between unidirectional adsorption and re-organization of silica through ongoing exchange between solid and solution during cyclic freezing.

4 Zeolitisation of Diatomite for Fixation of Metal Ions

4.1 Introduction

Whereas the chapters 2 and 3 are dealing with the formation of amorphous silica, this chapter treats the application of amorphous silica. For this purpose biogenic silica in terms of diatomite was applied to hydrothermally synthesise zeolites. Zeolitisation of diatomite was used because zeolites are well-known minerals which are applicable for fixation of dissolved metal ions from solutions. This study closes the cycle of this thesis which started from aqueous solutions and leads now via Si adsorption and precipitation to silicate minerals which are used on their part to remove metals from solution again.

Diatoms

Diatoms (*Bacillariophyceae*) are algae 10 to 100 µm in size with opaline cell walls (frustule) occurring in almost all aquatic ecosystems [25]. They are classified into *Centrales* and *Pennales* according to their symmetry. Biomineralisation in diatoms occurs within a silica deposition vesicle "along a proteinaceous template" and is controlled by special proteins (silafins) and silica transporter gens (SITs) [25]. The pore structure results from the cell´s ability to guide silica to certain sites on the cleavage plasmalemma, which is adhered to the silicalemma. The accumulation and compaction of the siliceous parts of dead diatoms lead to the formation of a porous (from 75 to 85 vol.-%), fine-grained rock which is called diatomite. Marine diatomites form preferentially in areas where cold water wells up. This results in high diatom productivity with low terrigenous influx. The opal-A from the diatoms can be transformed via opal-CT into quartz during diagenesis. Like all geological materials, diatomite is not a pure substance, but can be associated with calcium carbonates and terrigenous siliceous minerals. About 60 % of mined diatomite is used in filtration technology. Diatom nanotechnology is a more advanced field of application containing also the coating of diatoms with oxides and hydroxides to obtain ceramic devices with extraordinarily high specific surface areas, e.g. for catalysts [25].

Zeolites

According to the Subcommittee on Zeolites of the International Mineralogical Association **"**a zeolite mineral is a crystalline substance with a structure characterized by a framework of linked tetrahedra, each consisting of four O atoms surrounding a cation. This framework contains open cavities in the form of channels and cages. These are usually occupied by H_2O molecules and extra-framework cations that are commonly exchangeable." [142]. The term "zeolite" is not restricted to silicates. Hence also the beryllophosphates pahasapaite ($Li_8(Ca,Li,K,Na)_{11}Be_{24}(PO_4)_{24} \cdot 38\ H_2O$) and weinebeneite ($CaBe_3(PO_4)_2(OH)_2 \cdot 4\ H_2O$) fulfil the above definition [143]. However, for siliceous zeolites a general formula can be given: $M_{x/n}[(AlO_2)_x(SiO_2)_y] \cdot z\ H_2O$ (where M = Li, Na, K, Cs, NH_4, Mg, Ca, Sr, Ba, Mn, Cu, Pb and n = charge of M, commonly 1 or 2) [143]. The basic unit of the crystal structure of a zeolite is the SiO_4, PO_4, AlO_4, BeO_4 or ZnO_4 tetrahedron. Four, six or eight rings of these tetrahedra form rings. There are three sub-groups of zeolites: Fibrous zeolites consist of parallel chains of rings of four tetrahedrons. Lamellar zeolites consist of sheet-like combinations of rings of four, six and eight tetrahedrons. In cubic zeolites the tetrahedrons are three-dimensionally linked with each other [143]

In nature Zeolites form at temperatures below 250 °C and pressures below 200 MPa in water saturated environments by diagenetic reactions, low-grade metamorphism or hydrothermal alteration and in aqueous high alkaline environments at temperature below 100°C, e.g. in alkaline lakes [144]. Zeolites are present in soils mostly as detrital minerals, which persisted weathering [145], but can also form under the influence of hydrothermal activity in cryosols [127] or by weathering of volcanic ash [146]. In permafrost soils zeolites grow on nuclei of precipitated silica in open pore spaces just above the ice cement.

Zeolites have been synthesised since the 1940s by mixing soluble forms of silica and alumina in alkaline solutions containing alkali metals via the formation of a gel as an intermediate phase [147]. The use of diatoms as a substrate for zeolite synthesis was applied in two other studies [148] [149] where diatoms were coated with zeolite nanoparticles as seeds for further zeolite growth. Similarly, faujasite was synthesised on diatoms by using seed crystals [150]. Mordenite and ZSM-5 were synthesised without additional Al and without seeds but with diethanolamine (DEA) as a template agent [151, 152]. Without the use of seeds Na-P1, analcime, cancrinite and hydroxysodalite [153], but also zeolite P [154] were synthesised from diatomite in NaOH. In another study the diatoms were treated with H_2SO_4 and calcined to remove iron impurities before the reaction with NaOH [155]. Calcination of diatomite was also applied with respect to synthesis of geopolymers where an optimal calcination temperature of 800 °C was found [156]. Another approach is the production of a gel at 30 °C followed by hydrothermal treatment at 90 to 100 °C resulting in the formation of zeolite A [157]. An alternative to a hydrothermal treatment for the zeolitisation of diatomite is vapour-phase transport (VPT) [158]. Some authors used diatomite just as a silica source by completely dissolving a mixture of calcined diatomite and Na_2CO_3 [159] or by producing a gel from them [160] before the synthesis. Others mixed diatomite with paper sludge ash [161]. Addition of NaCl in hydrothermal synthesis of zeolites from diatoms leads to the formation of spherical ZSM-5 crystals [162]. Diatoms cannot only be used as substrate for synthesis of zeolites, but also for $ZnFe_2O_4/SiO_2$ composites [163]. A summary of the application of diatoms as substrates for 3D nanostructured materials has already been composed [164]. Instead of diatoms also rice husk ash [165], fly ash or bottom ash [166], pumice [167], perlite [168], mixed-layer clay minerals [169] or natural clinker [170] can be used for zeolitisation.

Aqueous metal ion fixation by zeolites

A wide range of chemical elements has a negative impact on plants, animals and human beings. In this study two groups of elements are investigated in respect to fixation in the hydrothermally gained reaction product, which are of special interest in environmental geochemistry: heavy metals and elements which possess radioactive isotopes which can be released by nuclear accidents.

Heavy metal ions are abundant water contaminants in mining areas [171]. Zeolites are used to remove these components from aqueous solutions, e.g. [172]. Although natural zeolites are often applied [172], also synthetic zeolites can be used [173]. Zeolites synthesised from fly ash by hydrothermal reaction with 2 M NaOH at 100 °C (NaP1, faujasite, chabazite) removed 100% Pb, 98.9% Cd, 98.8% Zn, 85.6% Cu, 82.8% Fe, 48.3% Ni and 44.8% Ba ions from acid mine drainage [174]. Zeolites are also able to reduce water hardness [175]. The application of zeolites in heavy metal removal from wastewater is limited by pH. Half-life time of zeolite NaP1 synthesised hydrothermally from fly ash was calculated to be 2 years at pH 7 and only 10 days below pH 3 [176]. Natural clinoptilolite was highly metastable for the treatment of acid mine drainage until pH 2 [177]. Besides heavy metal ions also dissolved organic

compounds like anionic indigo carmine can be removed by hydroxyl-sodalite synthesised from fly ash [178]. Living diatoms have been used together with other microorganisms in bioreactors to remove Hg and Cd ions from waste water [179]. Modifying diatomite with polyacrylamide increased Pb removal capacities to about 66 to 69 mgg^{-1}[180]. Natural and MnO_2-modified diatomite was used to adsorb Zn ions from aqueous solutions [181]. Like zeolites also diatomite can remove not only heavy metal ions, but also organic contaminants like dyes [155].

Sr and Cs possess radioactive isotopes (^{90}Sr, ^{134}Cs and ^{137}Cs), which can be released by nuclear accidents, most recently in the Fukushima Daiichi nuclear power plant [182]. The radioactivity released in this case accounted for about 400 $kBqm^{-3}$ for each of these elements [182]. The half-life times of ^{137}Cs and ^{90}Sr account for 30.17 a and 28.78 a, respectively [182]. This means that they maintain in the environment for hundreds of years. Finally, they are enriched in the food chain until they effect also human health which was shown for milk products like cheese [183]. In human beings ^{137}Cs and ^{90}Sr can cause thyroid cancer, especially for children; and even embryos can suffer severe brain damage by an exposure of 100 mSv [184]. That is why a lot of effort is taken to remove these radionuclides from the environment. Zeolites are highly promising materials to solve this task since they can incorporate both Cs and Sr ions into their crystal structure. Zeolite A has already been used to remove ^{90}Sr from Fukushima-like aqueous solutions in laboratory experiments, where 83 % of the initially bound Na were replaced by Sr [185]. In these experiments 10 and 50 mg of zeolite A were mixed with 20 mL aqueous solution for 24 h [185]. In the latter study solutions containing (i) 1.1 mmol L^{-1} of Sr from $Sr(NO_3)_2$ at various pH (1 to 13) using stable Sr isotopes and (ii) 0.14 $nmolL^{-1}$ of ^{90}Sr and (iii) sea water spiked with 0.16 $nmolL^{-1}$ of ^{90}Sr were used [185]. Among all hydrous framework silicates, especially zeolite A was investigated with respect to Sr and Cs ion removal [186]. In another study it was shown that a steady state between a Sr-containing solution and zeolite A is reached within 3 h [187]. Sr ion sorption by zeolite A increases with pH from 2 to 8 [187]. Zeolite A is known to remove Sr ions from simulated contaminated Fukushima seawater [188]. Natural mordenite shows high Cs ion removal capacities comparable with that of synthetic, tailored products, but worse performance in respect to Sr [189]. Indeed, zeolites have really been used to fight radioactive contamination in Fukushima [190]. One example is the construction of permeable reactive barriers from natural clinoptilolite-containing tuffs which possess a high selectivity for Sr and Cs ions [191]. The filters used in Fukushima have been manufactured by the US-American company Kurion and contain either Chabazite-Na ("Herschelite") besides further minerals which are not named [192].

Aims of this Study

Previous studies focussed on the final products of zeolitisation of diatoms. However, the process of zeolitisation itself is less understood. It remains unclear which intermediate phases form and how they are characterised. Their coexistence with unaltered diatomite on the one hand and the final reaction product, zeolites, on the other hand has still to be explored. A potential application of incompletely zeolitised materials has not yet been investigated. Hence in this study the following questions shall be answered:

- How does the zeolitisation process of diatoms proceed in detail?
- Can diatomite be used to produce hierarchically structured materials consisting of macroporous diatoms and microporous zeolites?
- Does the heavy metal removal capacity increase linearly during the conversion of diatomite to zeolites?

4.2 Methodology

4.2.1 Materials

Diatomite

The used diatomite (company "Thiele") originates from a northern African deposit and was not pre-treated, but only gently grinded.

Stock solutions

An aluminium containing stock solution was prepared by placing 1 g of gibbsite (γ-$Al(OH)_3$, Merck p.a.) in 0.5 L of 1 M KOH which had been prepared from solid KOH (Merck p.a.). After a reaction time of 7 d the solution was separated from the partly remaining gibbsite by membrane filtration (0.45 µm). The filtered solution contained 22 mmol L^{-1} Al and the pH accounted for 13.7, which was modelled by PhreeqC.

0.5 L 0.1 M KOH was prepared by dissolving 0.05 mol solid KOH (Merck) in MilliQ water. 1 g gibbsite (γ-$Al(OH)_3$, Merck p.a.) were suspended in the obtained solution and stirred with a magnetic stirrer at 50 °C for one week. After a reaction time of 7 d the solution was separated from the partly remaining gibbsite by membrane filtration (0.45 µm). The resulting Al concentration was 11 mmol L^{-1} and the measured pH accounted for 12.9.

0.1 M KOH was prepared by dissolving 0.05 mol solid KOH (Merck, p.a.) in 0.5 L MilliQ water. The pH of this solution accounted for 12.8.

The synthetic heavy metal stock solution (pH 5.1) contains each 0.5 mmol L^{-1} of Cu^{2+}, Pb^{2+} and Zn^{2+} and was prepared by dissolving $Pb(NO_3)_2$, $Zn(NO_3)_2 \cdot 4\ H_2O$ and $Cu(NO_3)_2 \cdot 3\ H_2O$ (Merck, p.a.) in MilliQ water.

The synthetic Sr and Cs stock solution (pH 7) contains each 0.4 mmol L^{-1} of Sr^{2+} and Cs^{+} and was prepared by dissolving $SrCl_2 \cdot 6\ H_2O$ (Merck, p.a.) and CsCl (Roth, p.a.) in MilliQ water.

A mine drainage solution from a carbonate-hosted lead-zinc deposit (Carinthia, Austria) was filtered through 0.45 µm. The filtrated stock solution contains 1250 µmol L^{-1} of Ca, 0.14 µmol L^{-1} of Cd, 26 µmol L^{-1} of K, 665 µmol L^{-1} of Mg, 153 µmol L^{-1} of Na, 0.48 µmol L^{-1} of Pb, 31 µmol L^{-1} of Si, 0.62 µmol L^{-1} of Sr and 17 µmol L^{-1} of Zn.

4.2.2 Experimental Setup

Diatomite Alteration Experiments

Experiments with 1 M KOH

0.5 g diatomite reacted with 0.025 L of the alkaline solution in a Teflon coated steel autoclave at temperatures of 50 °C (data are from an associated Bachelor Thesis [193]), 75 °C, 100, 125 °C and 150 °C (Figure 34).

Figure 34: Teflon-coated steel autoclave for diatomite alteration experiments

After distinct reaction times from 0.25 up to 64 d the reaction products were separated from the solutions by filtration (0.45 µm). pH of the solution was measured and the filter cake was rinsed with 0.2 L MilliQ water and dried at 40 °C. Both solutions and solids were analysed.

Experiments with 0.1 M KOH

Another set of experiments was performed within the frame of an associated Bachelor Thesis [194] using the same settings as above for 1 M KOH at 100 °C, but only 0.1 M KOH instead of 1 M KOH. Additionally, experiments with pure 0.1 M KOH without dissolution of gibbsite were performed.

Metal Removal Experiments

Selected reaction products from alteration experiments (0.05 g) were suspended in 0.01 L solution of (i) the above Cu^{2+}, Pb^{2+} and Zn^{2+} ions containing synthetic stock solution, (ii) the natural mine drainage stock solution or (iii) within another associated Bachelor thesis [193] the above Sr^{2+} and Cs^{+} ions containing synthetic stock solution and shaken for up to 3 d at 25 °C. Additionally, unaltered diatomite, diatomite altered at room temperature for 64 d (reference sample) and one diatomite sample altered for 1 d at 100 °C were also mixed with the mine drainage solution at pH 8.0 and also shaken for various times ($0.25\ d < t < 3\ d$) at 25 °C . Analogous experiments with unaltered diatomite were carried out to check if alteration significantly changes heavy metal removal capacities.

4.2.3 Analytics

Solids

Solids were analyzed with x-ray diffraction (XRD, Panalytical X´Pert Pro) using Rietveld refinement for quantification. Zincite (Johnson Matthey Chemicals Ltd., spectrographically standardized) was used as an internal standard for the quantification of the amorphous percentage. The background was fitted by granularity and bending factor. Scaling factors of the crystalline phases, zero shifts and the peak-shape parameter W were refined in the mentioned order. The structural models originate from the powder diffraction file. The estimated accuracy of Rietveld refinement accounts for ±10 wt.-% for the main phases and for ±5 wt.-% for accessory phases.

Secondary electron images of solids were obtained by scanning electron microscopy (Zeiss DSM 982 Gemini) at an accelerating voltage of 5 kV and working distances between 5 and 10 mm. Samples were coated with an Au-Pd alloy using a Scancoat Six sputter apparatus (Edwards Hochvakuum GmbH).

Two different transmission electron microscopes (TEM) were used for characterisation of the alteration products. A FEI Tecnai F20 was used for space-resolved chemical analyses by energy-dispersive x-ray spectroscopy (EDX) and selected area electron diffraction (SAED). For more detailed mineralogical investigations the high-resolution SAED patterns obtained from an FEI Tecnai 12 were used. Quantification by TEM-EDX was based on weighing factors for individual elements which were checked for all elements by appropriate standards. K loss was observed during the measurement making accuracy of K quantification with about ±10 wt.-% and for Si and Al about ± 5 wt.-%.

Wavelength-dispersive X-ray fluorescence spectroscopy (XRF, Philips PW 2404) was used to determine bulk chemical composition of unaltered diatomite and diatomite altered at 100 °C for 1 d. The samples were dried over night at 110 °C. Afterwards 1.5 g of the sample were calcined at 1050° C for one hour to release volatiles. The loss on ignition (L.O.I.) was determined by

$$L.O.I.(wt-\%) = 100 \cdot \left(\frac{n_2 - n_3}{n_2 - n_1} \right) \qquad (21)$$

where

n_1 = mass of empty crucible (in g)
n_2 = mass of crucible + sample (in g)
n_3 = mass of crucible + sample (in g) after calcination

The loss on ignition (L.O.I.) is composed of H_2O^+ (crystal water of the sample which has not been released by drying at 110 °C), CO_2, F, Cl and S. The calcined sample was homogenised in an agate mortar and afterwards mixed with a flux ($Li_2B_4O_7$ – dilithium tetraborate) to decrease the fusion temperature. Therefore 6 g $Li_2B_4O_7$ were weighed into a porcelain dish and mixed with 1 g of the calcined sample in an agate mortar. The mixture was transferred into a platinum crucible and molten at 1150 °C in an automatic digestion apparatus (Perl´X,

PANalytical) for 12 min. Data evaluation was performed using the software „Super Q+“ (PANalytical).

The specific surface area and related parameters of diatomite and its alteration products were measured via gas adsorption methods. The total specific surface area was measured by BET analyses [91] using a FlowCash II 2300 equipment and a nitrogen-argon mixture. For selected samples the mesopore radii distribution curve was determined by the BJH method [195] using a Micrometrics TriStar II 3020 V1.03. With this instrument also the micropore volume could be derived from the t-plot [196]. All reported values originate from adsorption (and not desorption) data. Sum parameters like the total specific surface area should be as accurate as ±5 %, but pore-size resolved values like the pore distribution have probably larger errors.

Fourier-transformed infrared spectroscopy (FTIR, Perkin Elmer Spectrum 100) was used to identify short-range order in terms of molecular groups within alteration products. For all but one sample the KBr method was applied: KBr (Merck, for IR spectroscopy) was grinded for about 10 minutes and dried at 90 °C over night whereas the sample was carefully dried at only 40 °C to avoid structural changes during drying. 990 mg KBr and 10 mg sample were mixed in an agate mortar for 10 min. 500 mg of this first dilution were mixed with 500 mg KBr and dried again for 1 h at 40 °C. 200 mg of this second dilution were pressed into tablets at 460 bar for 10 min (Fluxana PR-25A) and immediately measured. An empty sample holder was measured beforehand for automatised background correction. For each analysis 16 spectra between 450 and 4000 cm^{-1} were measured and averaged for better statistics. Evaluation of the spectra was performed using the software Spectrum v5.0. For one sample where XRD patterns suggested the presence of carbonate this was checked by attenuated total reflection (ATR). In this case the spectrum was only obtained for wave numbers above 650 cm^{-1}.

Solutions

Solutions were analysed with inductively coupled plasma mass spectroscopy (ICP-OES) (Perkin Elmer Optima 4300) for Si, Al, K, Ca, Mg, Cd, Cu, Pb and Zn. Calibration for ICP-OES for Si and Al was performed using a two-element standard sequence containing 0.02, 0.87, 4.27 and 10.1 mg L^{-1} Al and 0.04, 2.04, 10.1 and 49.8 mg L^{-1} Si which was prepared from commercial single-element standards for Si and Al (Merck). K, Ca, Mg, Cd, Cu, Pb and Zn were calibrated with a commercial multi-element standards (Merck X) containing 3 mg L^{-1} K, 35 mg L^{-1} K, 15 mg L^{-1} Mg, 20 µg L^{-1} Cd, 20 µg L^{-1} Cu, 25 µg L^{-1} Pb and 50 µg L^{-1} Zn. The accuracy of ICP-OES was about 10 % for K, Ca, Mg, Cd, Cu, Pb and Zn and about 20 % for Si whereas the precision was about 2 % in all cases. ICP-MS (Agilent 7500 cx) was used for quantification of Sr and Cs. Calibration was performed using a standard sequence (10 ng L^{-1}, 10 µg L^{-1}, 10 mg L^{-1}) diluted from a multi-element standard (Inorganic Ventures ICPMS 71-A). The accuracy was about ±20 % and the precision about ±3 %. pH was analysed by using WTW Inolab 740 using a three-point calibration (pH 4, 7 and 10).

4.3 Results: Diatomite Alteration Experiments

4.3.1 General Remarks

The experiments performed at 100 and 125 °C with 1 M KOH are discussed in a separate paper [197]. In this thesis these above experimental results are compared with experiments at 50, 75 and 150 °C with 1 M KOH and at 100 °C with 0.1 M KOH. Experimental results are ordered by the analytical method they were obtained with.

4.3.2 Characterisation of Diatomite

The chemical composition of the diatomite is 93.3 wt.-% SiO_2, 1.7 wt.-% Al_2O_3, 0.8 wt.-% Fe_2O_3, 0.2 wt.-% MgO, 0.3 wt.-% CaO, 0.3 wt.-% K_2O and 3.5 wt.-% L.O.I. Mineralogically the diatomite consists of 97 wt.-% amorphous phase, 2 wt.-% mica and 1 wt.-% quartz. The XRD pattern is displayed together with those of altered diatomite in chapter 4.3.7. SEM-SE images indicate that most diatoms belong to the group of *Centrales* (Figure 35).

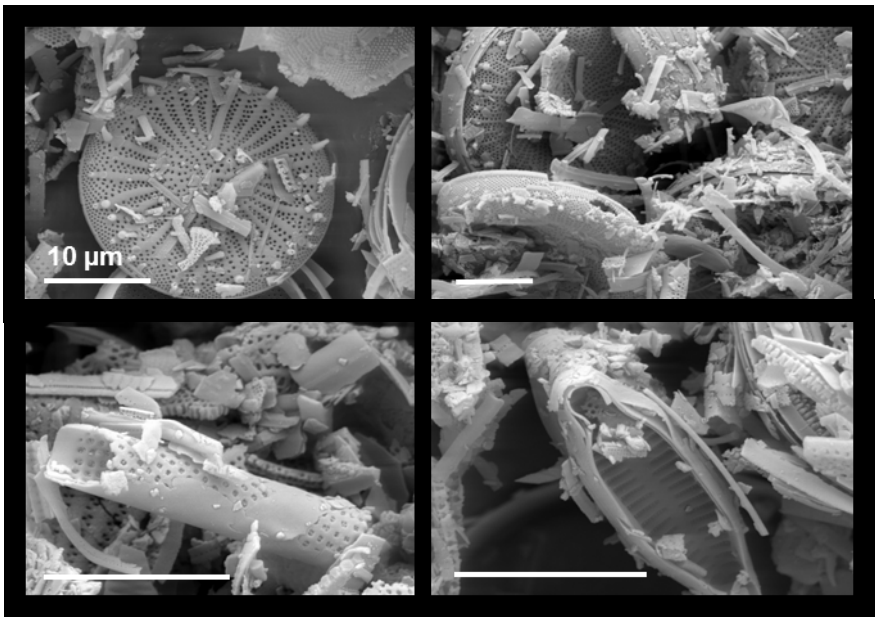

Figure 35: SEM-SE images of unaltered diatomite showing central and minor amounts of pennal diatoms

The specific surface area of the diatomite accounts for 15.5 $m^2 g^{-1}$ according to the BET method and 20.1 m^2g^{-1} according to the Langmuir method (Micromeritics TriStar II 3020 V1.03). Data derived from t-plot analyses indicate that 12.2 $m^2 g^{-1}$ are external surface areas and 3.3 $m^2 g^{-1}$ micropores. According to BJH adsorption data 9.3 $m^2 g^{-1}$ are allotted to a pore diameter range from 1.7 to 300 nm. Values for the average pore diameter range are 13.7 and 20.3 nm for the BET and BJH method, respectively. The molecular cross section is 0.16 nm^2. The whole pore size sum curve is compared with those of alteration products in chapter 4.3.8.

4.3.3 Solution Chemistry

pH

In experiments with 0.1 M KOH pH decreased during experimental runtime from 12.9 in the initial solution via 12.4 after 0.25 d to a constant value of 11.3 ± 0.2 for all durations of 1 d and more (Table 17, Table 18). With 1 M KOH a constant pH of 13.7 ± 0.2 was maintained during the entire experiment (Table 14, Table 15). pH is independent from the initial concentration of dissolved Al (Table 17, Table 18).

Si concentrations

During the first period of the experiment about 70 – 80 wt.-% and 15 wt.-% of the initial diatomite material are dissolved in the highly alkaline solution in case of 1 M and 0.1 M KOH, respectively, which is reflected in a rapid increase of the concentration of dissolved Al (Table 12). The experimental time span after which the Si concentration is constant decreases from 2 d at 50 °C to 0.25 d for all higher temperatures at 1 M KOH and accounts for 1 d and 4 d with 0.1 M KOH and 100 °C with and without Al, respectively. The constant Si concentration at 1 M KOH accounts for 243 ± 11 mmol L^{-1} at 50 °C, for 237 ± 14 mmol L^{-1} at 75 °C, for 261 ± 25 °C at 100 °C, for 261 ± 22 mmol L^{-1} at 125°C and for 249 ± 9 mmol L^{-1} at 150 °C which indicates that dissolution behavior of diatomite in the given alkaline solution does not depend on temperature (Table 12). Interestingly, the reference samples which were stored at room temperature for 64 d showed higher Si concentrations of 557 ± 50 mmol L^{-1} with 1 M KOH. For experiments with 0.1 M KOH the Si concentration increases via 18 mmol L^{-1} after 0.25 d to 52 ± 5 mmol L^{-1} for longer durations where Al was present and via 26 mmol L^{-1} after 0.25 d to 89 mmol L^{-1} after 64 d where Al was absent (Table 17, Table 18). The concentration of dissolved Si in experiments with 0.1 M KOH is about 20 and 30 %, respectively, of the concentration of dissolved Si observed with 1 M KOH.

Al concentrations

The initial Al concentration is only 11 mmol L^{-1} in case of 0.1 M KOH experiments (Table 17) compared to 22 mmol L^{-1} in 1 M KOH experiments (Table 12) because the solubility of gibbsite decreases with decreasing pH. All experiments show a rapid exponential decrease of Al concentration even when no newly formed phases were found by SEM or XRD. The residual Al concentrations are mostly below 3 mmol L^{-1} with 1 M KOH and below 0.03 mmol L^{-1} with 0.1 M KOH and show no clear dependence on temperature, which is confirmed by the observation that also in the reference sample which was stored at room temperature Al concentration was decreased in 1 M KOH to about 3 mmol L^{-1} (Table 11).

K concentrations

For experiments with 0.1 M KOH the initial concentration of K should have been 100 mmol L^{-1} according to the used amount of KOH although analyses indicate a higher value of 150 mmol L^{-1}. During the run of the experiment K concentration a slow decrease from 90 mmol L^{-1} after 0.25 d to 75 mmol L^{-1} after 32 d can be seen. In experiments with 1 M KOH the K concentration does not change significantly over reaction time (Table 12). A similarly constant K concentration was observed for the reference sample (Table 11).

4.3.4 X-ray Fluorescence Analyses

Hydrothermal alteration of diatomite with 1 M KOH solutions containing 22 mmol L^{-1} Al is associated with an enrichment of the solid with Al, K and volatiles. The Al_2O_3 content increased after 1 d at 100 °C from 1.74 to 20.2 wt.-%, the K_2O content from 0.27 to 15.0 wt.-% and the L.O.I. from 3.47 to 11.9 wt.-%, whereas the SiO_2 content decreased from 93.3 to 48.6 wt.-%.

4.3.5 Fourier-Transformed Infrared Spectroscopy

Results from FTIR indicate that the Si-O stretching and bending vibrations of the reaction products show no significant shift as a function of alteration time or temperature, but are constant close to 1000 cm^{-1} and 450 cm^{-1}, respectively (Figure 36). The question arises, if the broader adsorption band in a sample altered at 100 °C for 1 d indicates the presence of two differently polymerised SiO_4 tetrahedra in weakly altered diatomite. Additionally, in the same sample some carbonates are present which disappear afterwards.

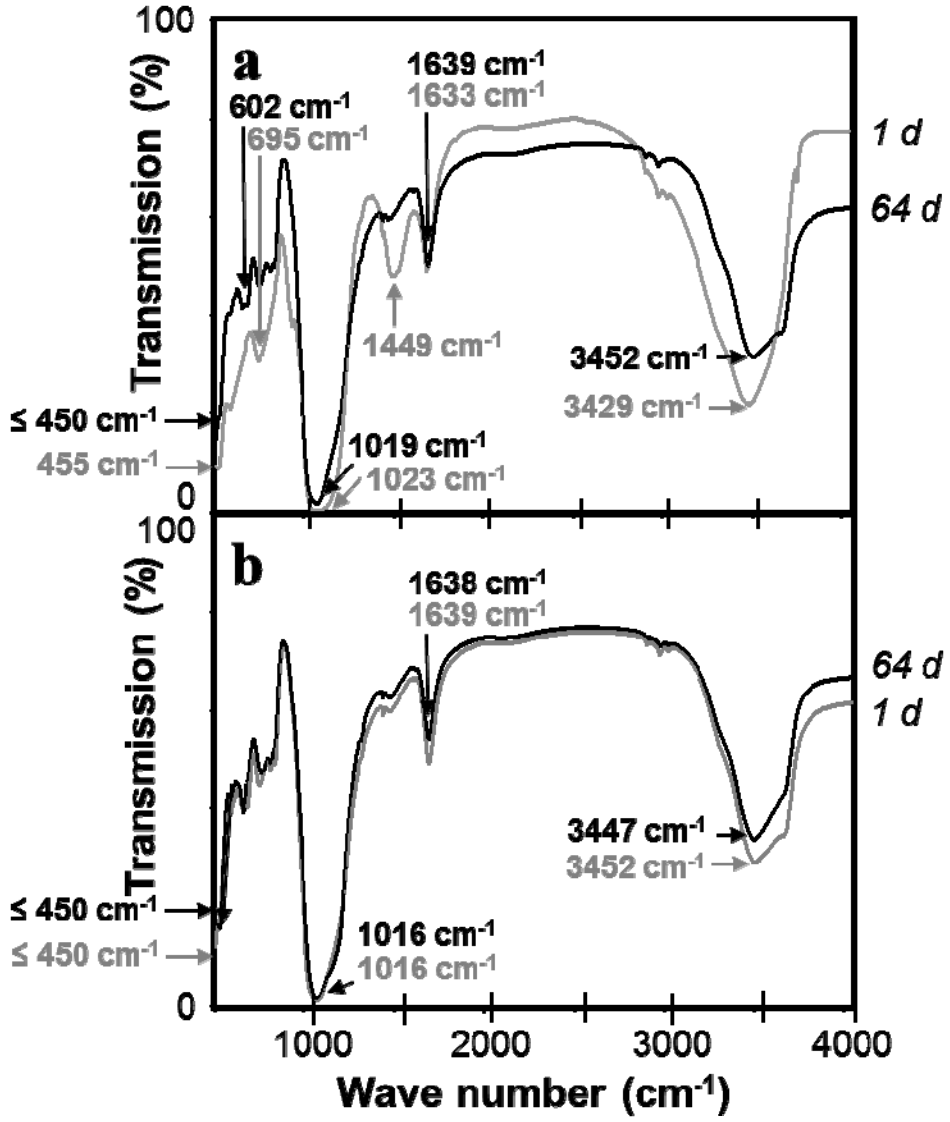

Figure 36: FTIR spectra of weakly (1 d) and intensely (64 d) altered diatomite at 100 °C (a) and 125 °C (b) in 1 M KOH containing 22 mmol L^{-1} Al

4.3.6 Scanning Electron Microscopy

Hydrothermal alteration of diatomite in 1 M KOH leads to the formation of spherical particles, which are revealed by SEM-SE images in samples altered at up to 100 °C, probably also at 125 °C (Figure 37). Interestingly, these particles occur also in the reference sample which was stored at 25 °C for 64 d (Figure 38). The time at which these particles form decreases from 4 d at 50 °C via 2 d at 75 °C to 0.25 d at 100 °C. The size of these particles increases from 100 nm to about 2000 nm between the 2nd and 4th day at 100 °C. They are aggregated and the aggregates are spatially separated from the residual diatoms. The particles dissolve later and are hence called from now on the intermediate phase (IP). In more intensely altered reaction products SEM-SE images indicate the formation of bundle-like aggregates (Figure 37) which can be identified as merlinoite by comparison with previous data [198] and with XRD patterns (chapter 4.3.7). They are present at temperatures of 75 °C and higher and the time of their first occurrence decreases from 8 d at 75 °C via 2 d at 100 °C to 1 d at 125 °C and 150 °C. Rosulate-like aggregates which consist of chabazite [198] occur instead of bundle-like aggregates at 50 °C and coexist with them at 75 °C and 100 °C (Figure 37). This suggests that chabazite is rather a low-temperature phase, whereas merlinoite is the corresponding high-temperature phase in the given chemical system. As both zeolite phases are present chabazite forms a ring around the belt of merlinoite bundles (Figure 37). In the reference sample, which was stored at room temperature, no newly formed phases were observed after 64 d (Figure 38). Interestingly, the intermediate phase remains present after the formation of merlinoite.

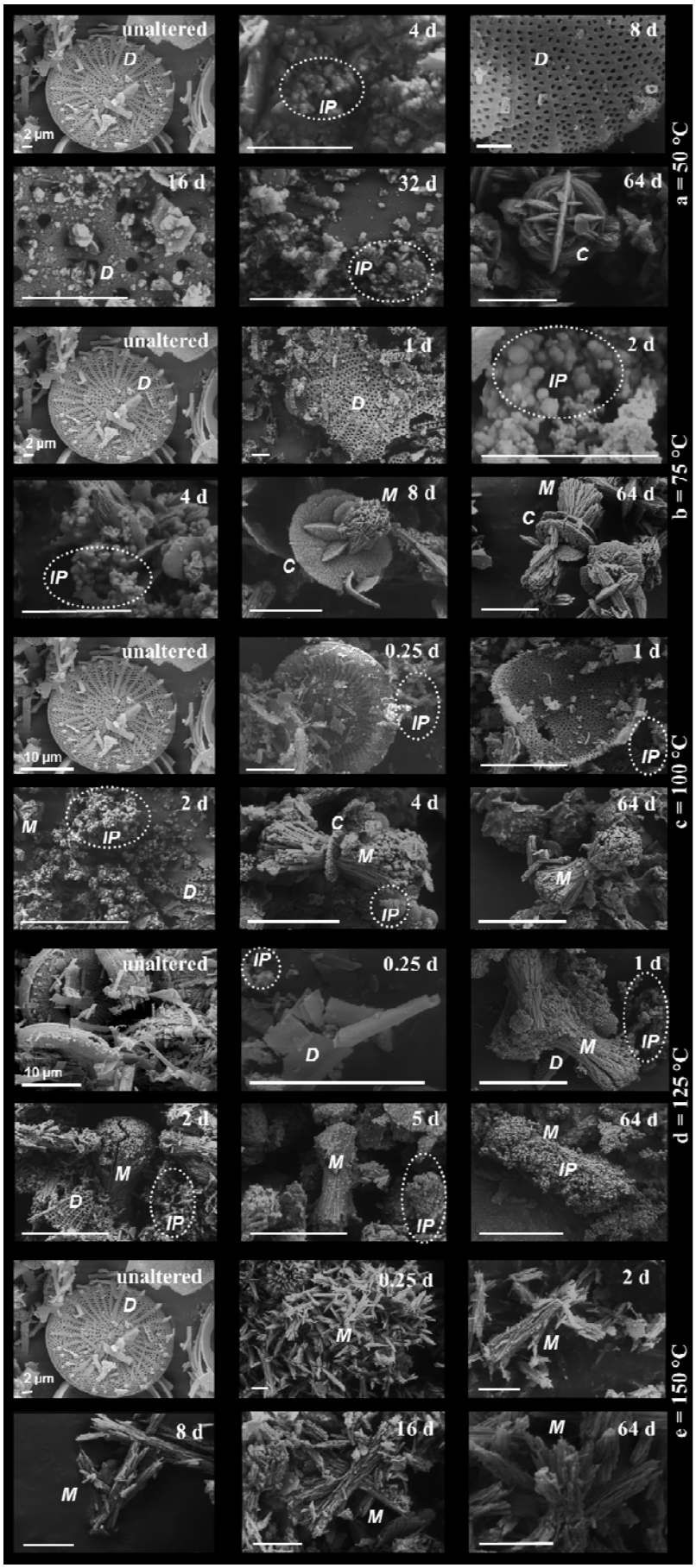

Figure 37: SEM-SE images of unaltered diatomite and diatomite altered in 1 M KOH containing 22 mmol L^{-1} Al at 50 °C (a), 75 °C (b), 100 °C (c), 125 °C (d) and 150 °C (e) for distinct reaction times (0.25 d ≤ t_{syn} ≤ 64 d). D: diatom, IP: intermediate phase, M: merlinoite, C: chabazite

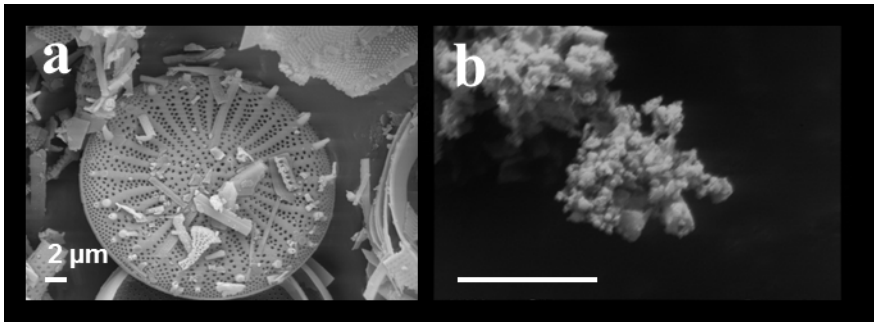

Figure 38: SEM-SE images of unaltered diatomite and the reference sample which was altered in 1 M KOH containing 22 mmol L^{-1} of Al at room temperature for 64 d

In contrast to the experiments with 1 M KOH, SEM-SE images of diatomite altered in 0.1 M KOH, either with or without 11 mmol L^{-1} Al, do not show the formation of bundle-like aggregates, which could be assigned to merlinoite. Even so, alteration processes could also be observed in these experiments: SEM-SE images (Figure 39) indicate already after 0.25 d in experiments with 11 mmol L^{-1} Al bulges around the pores of the diatoms. However, an even more exiting feature arises after 1 d when a hierarchially structured material is formed which is composed of the intermediate phase (IP) in the pores of the diatoms and the diatoms themselves. Later on the IP covers the whole surface of the diatoms, but is not visible within the pores any more. Finally, the surface of the diatoms becomes rougher and remains covered with the IP.

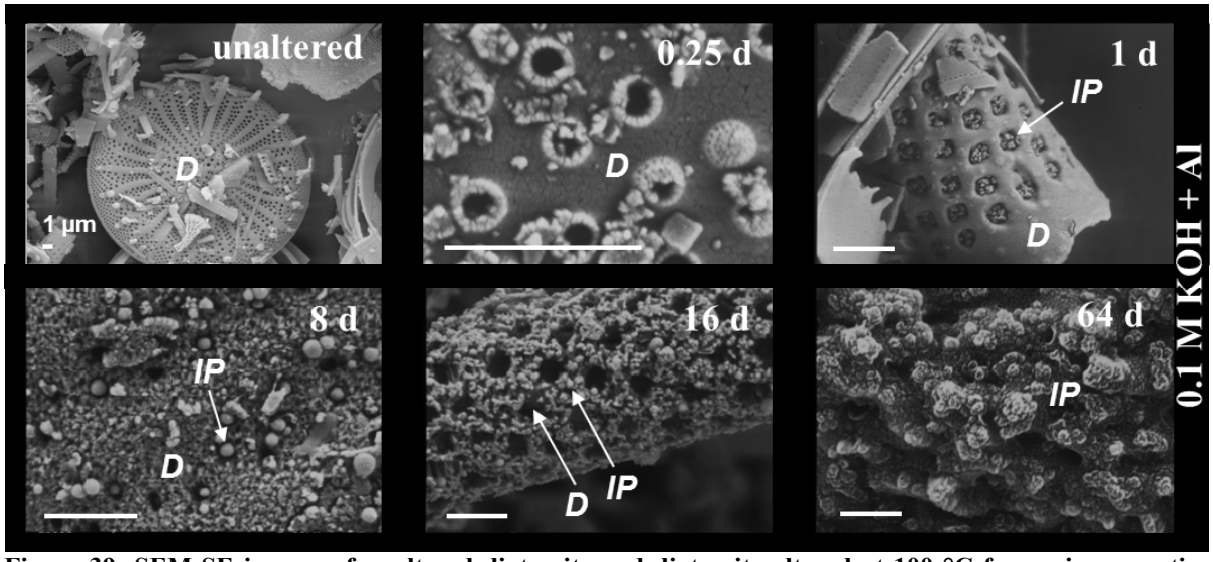

Figure 39: SEM-SE images of unaltered diatomite and diatomite altered at 100 °C for various reaction times in 0.1 M KOH containing 11 mmol L^{-1} of Al. D: diatom, IP: intermediate phase

Without additional Al the IP is formed already after 0.25 d as irregularly shaped isometric particles with a diameter of some hundreds nm (Figure 40). After 1 d the material looks similar as after 64 d in the experiments with Al (Figure 39). This stage might again be described as a hierarchically structured material because it contains both the IP and the diatoms. Surprisingly, the IP starts to disappear afterwards and is completely absent after 32 d.

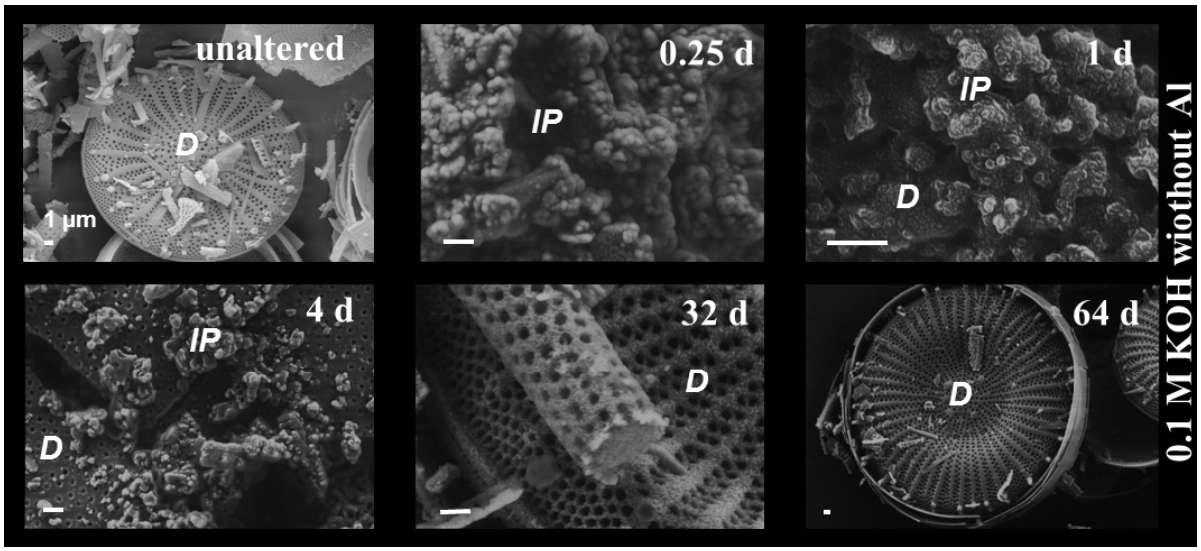

Figure 40: SEM-SE images of unaltered diatomite and diatomite altered at 100 °C for various reaction times in 0.1 M KOH without added Al. D: diatom, IP: intermediate phase

4.3.7 X-ray Diffractions Analyses

Alteration products with 1 M KOH

XRD patterns confirm SEM results suggesting that hydrothermal alteration of diatomite with 1 M KOH solutions containing 22 mmol L^{-1} Al leads to the formation of zeolites, especially merlinoite (Figure 41). Rietveld refinement using ZnO as an internal standard was used to quantify the crystalline phases – the newly formed zeolites merlinoite and chabazite as well as the remnant quartz and illite – versus the amorphous amount which could be attributed qualitatively to diatoms (D) and the intermediate phase (IP) by using SEM-SE images (chapter 4.3.6). The results are displayed in Figure 42 and Table 19ff. During the initial reaction period the remnant phases quartz and illite are more stable than the amorphous diatoms and are subsequently enriched in the solid due to ongoing dissolution of diatoms. After a certain reaction time the zeolite mineral merlinoite is formed. This zeolitisation time decreases with increasing temperature from 64 d at 50 °C via 4 d at 75 °C, 2 d at 100 °C to 1 d at 125 °C. The amorphous amount of the reaction products which is maintained during the alteration of diatomite decreases with increasing temperature from 65 wt.-% at 50 °C via 31 wt.-% at 100 °C to nearly zero at 150 °C after 64 d. Also the remnant phases quartz and mica disappear within the experimental runtime of 64 d. Besides merlinoite traces of other zeolites like zeolite L and chabazite are formed in some cases. Additionally, small amounts of boehmite, an Al-hydroxide, are formed in one sample. This can be explained by the drop in pH during the alteration experiments, which decreases the solubility of Al-hydroxides. However, it has to be considered that the estimation of the amorphous content by Rietveld refinement is rather rough (approximately ± 15 wt.-%). The quality of the Rietveld refinement was checked by the R-values and the goodness of fit [199], which are given in Table 19-23. The reference sample which was stored at room temperature for 64 d did not show any newly formed phases in its XRD pattern besides an increase in the content of quartz and illite due to preferential dissolution of amorphous phases.

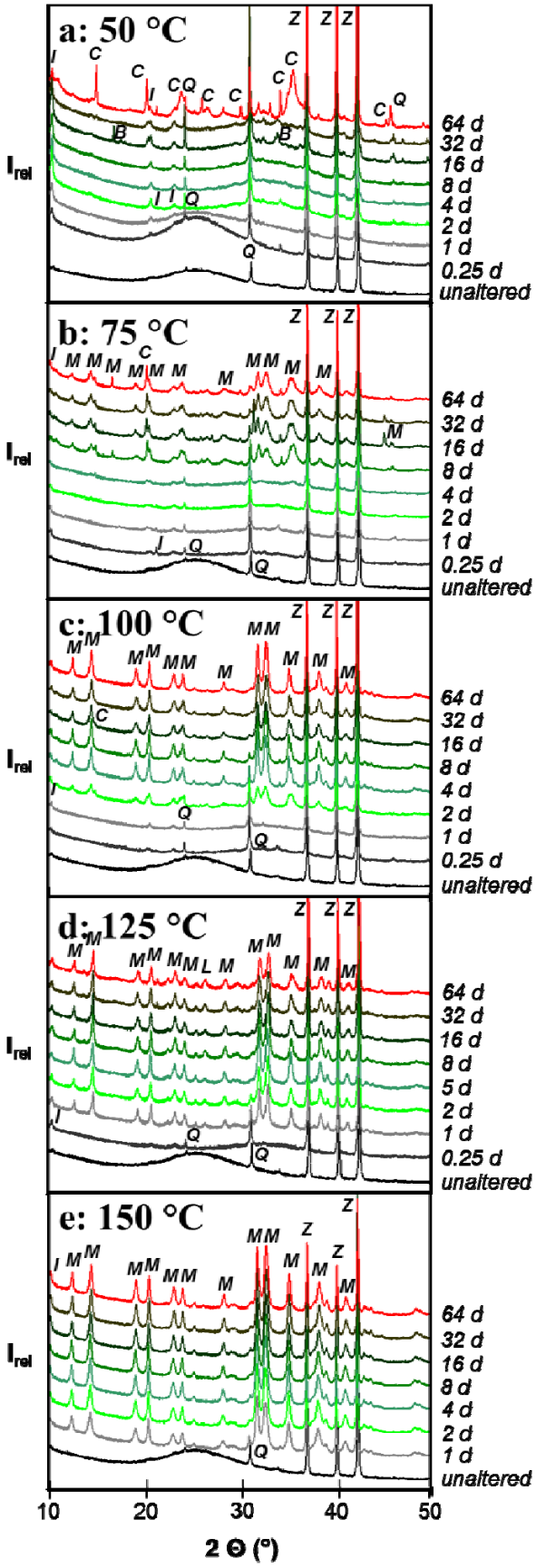

Figure 41: XRD patterns (Co-Kα) of unaltered diatomite and diatomite altered in 1 M KOH containing 22 mmol L^{-1} Al at 50 °C (a), 75°C (b), 100 °C (c), 125 °C (d) and 150 °C (e) for distinct reaction times (0.25 d ≤ t_{syn} ≤ 64 d). M: merlinoite, C: chabazite, L: zeolite L, Q: quartz, I: illite/muscovite, B: boehmite, Z: zincite (added as internal standard). Note: The increase of peak intensities for Q and I (both relicts) through alteration at t_{syn} = 0.25 d may be caused by the preferential dissolution of diatoms.

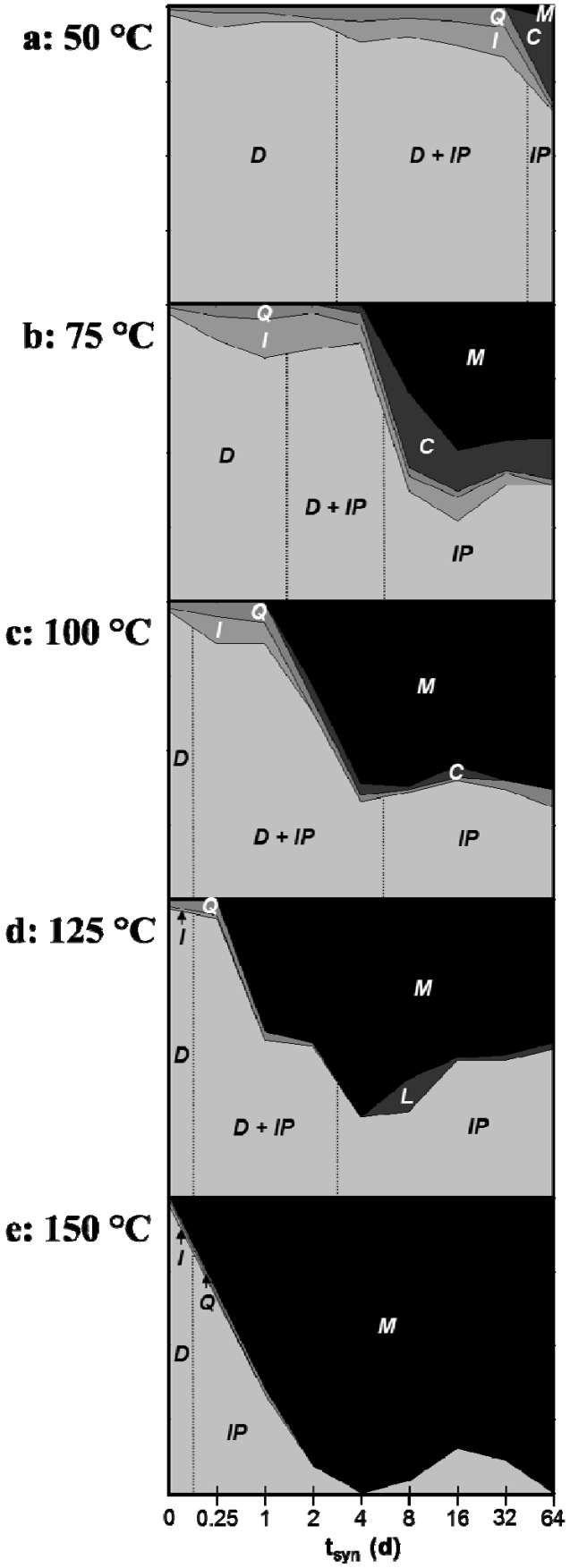

Figure 42: Phase composition of unaltered diatomite and diatomite altered in 1 M KOH containing 22 mmol L^{-1} Al at 50 °C (a), 75 °C (b), 100 °C (c), 125 °C (d) and 150 °C (e) for distinct reaction times (0.25 d ≤ t_{syn} ≤ 64 d). D: diatom, IP: intermediate phase, M: merlinoite, C: chabazite, L: zeolite L, I: illite, Q: quartz

Alteration products with 0.1 M KOH

In contrast to alteration experiments with 1 M KOH no zeolites were formed within the experimental time of 64 d in 0.1 M KOH (Figure 43). There are no significant differences in XRD patterns whether Al was added to the alkaline solution or not. There might be formation of smaller amounts of calcite due to CO_2 absorption – possibly after the hydrothermal alteration during the filtration and rinsing – and the reaction with Ca ions from the used diatomite educt (chemical composition and impurity of the diatomite see chapter 4.3.2). Also traces of diaspore and boehmite are present in some samples. Feldspar was only found once after 64 d in the alteration experiment with an Al-containing solution.

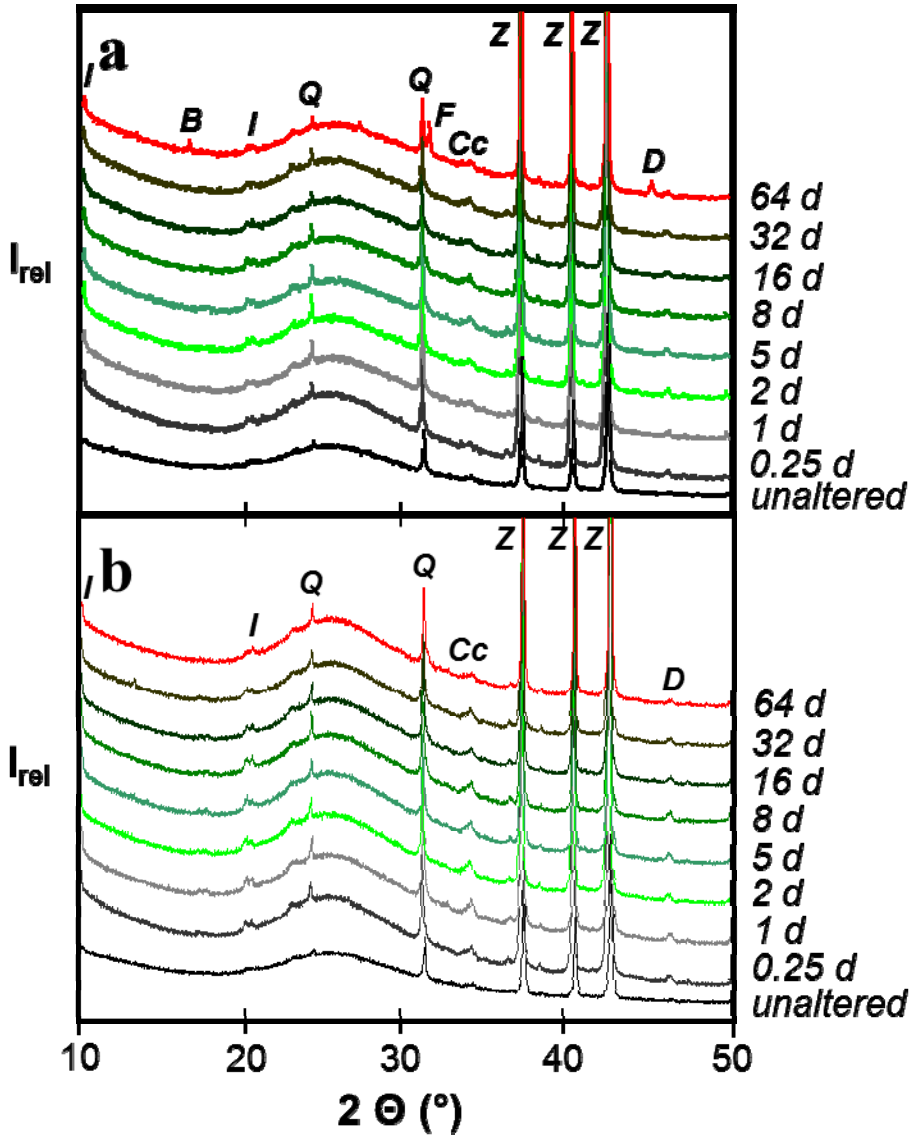

Figure 43: XRD patterns (Co-Kα) of unaltered diatomite and diatomite altered at 100 °C in 0.1 M KOH containing 11 mmol L^{-1} Al (a) or no Al (b) for distinct reaction times (0.25 d ≤ t_{syn} ≤ 64 d). I: illite, Q: quartz, B: boehmite, F: feldspar, Cc: calcite; D: diaspore Z: zincite (added as internal standard).

4.3.8 Specific Surface Area

The evolution of the specific surface area (SSA) during alteration of diatomite traversed two periods which are described below.

Increase of the SSA during the first period

The SSA of diatomite is significantly increased during the first period of hydrothermal alteration. The total BET surface area increased from to 12.6 $m^2 g^{-1}$ to 31.0 and 37.8 $m^2 g^{-1}$ after 6 h alteration in 1 M KOH at 100 and 125 °C, respectively (Table 21 & 22). Also after 8 d alteration at 100 °C in 0.1 M KOH (+ 11 mmol L^{-1} Al) an increase of the total BET surface area to 25.4 $m^2 g^{-1}$ was observed. The increase in specific surface area is especially due to the growth of external surfaces since data derived from t-plot analyses indicate that after 1 d alteration at 100 °C in 1 M KOH the external surface area increased from 12.2 to 25.9 $m^2 g^{-1}$ compared to unaltered diatomite, while the micropore area decreased from 3.3 to 1.1 $m^2 g^{-1}$. The external surface area is suggested to be associated with the surface of the diatoms and closely related to the grain size whereas the micropore area is suggested to be due to vesicles within the diatoms which might be filled during hydrothermal alteration. Interestingly, the BJH mesopore area including all pores between 1.7 nm and 300 nm diameter increased from 9.2 $m^2 g^{-1}$ to 25.0 $m^2 g^{-1}$ during alteration for 1 d at 100 °C in 1 M KOH. This means that a large part of the "external surface area" from the t-plot is better addressed as "mesopore surface are" according to the BJH method.

Decrease of the SSA during the second period

Surprisingly, for longer alteration times, the specific surface area decreased again. After 16 d in 1 M KOH the total BET surface area decreased from 31.0 to 18.3 and from 37.8 to 15.0 $m^2 g^{-1}$ at 100 and 125 °C, respectively, compared to the alteration products obtained after 1 d (Table 22 & 23).

Changes of the pore size distribution

Selected samples were analysed in more detail: The unaltered diatomite "Thiele", a sample where no newly formed phases were found in XRD (1 d at 100 °C in 1 M KOH, Z2) and two merlinoite-rich samples (32 and 64 d at 100 °C in 1 M KOH, Z 13 and Z14, respectively) (Figure 44). The pore size distribution derived from t-plot data indicates that pores become smaller with increasing degree of alteration. Through ongoing alteration at 100 °C in 1 M KOH the mean pore diameter decreased from 9.3 nm for unaltered diatomite via 7.1 nm after 1 d and 5.7 nm after 32 d to 5.1 nm after 64 d. This is suggested to be due to the formation of secondary nanoparticles within the pores of the diatoms which was observed for larger pores by TEM (chapter 4.3.9) but might be also valid for nanopores within the diatoms. The upper quartile is more or less constant during the first alteration period (20.6 nm for unaltered diatomite and 20.0 nm for the alteration product after 1 d at 100 °C). During the second period of alteration, the value of the upper quartile decreased to 12.5 nm after 32 d and even to 10.5 nm after 64 d. In contrast, the first quartile accounts for unaltered diatomite for 2.3 nm and increases to 2.8 nm after 1 d alteration in 1 M KOH. The second period of alteration has little effect on this parameter: The first quartile increases only slightly to 3.2 nm after 32 d and decreases again to 2.9 nm after 64 d alteration in 1 M KOH.

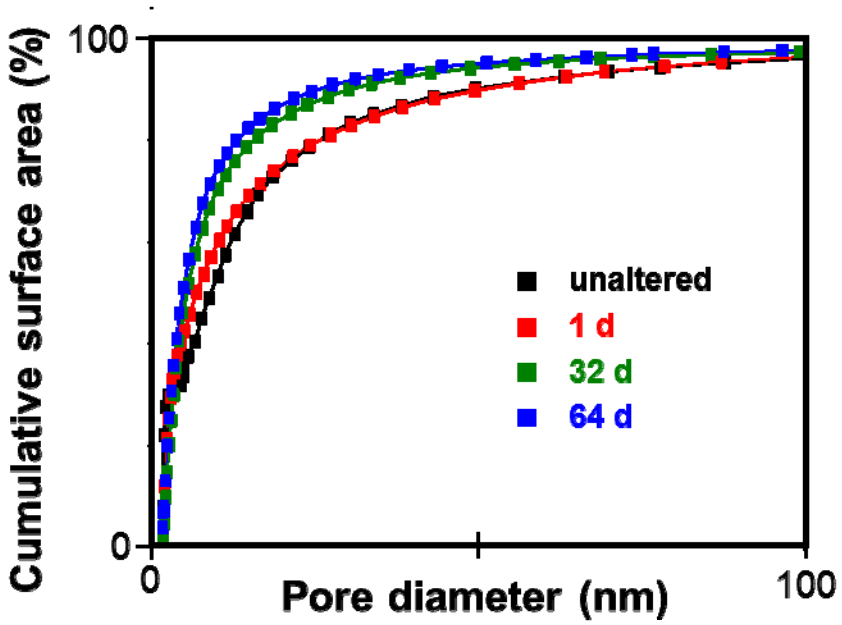

Figure 44: Cumulative surface area (%) of unaltered diatomite and diatomite altered for various reaction times (1, 32, 64 d) in 1 M KOH at 100 °C as a function of pore diameter analysed by the t-plot method by BET

Interestingly, alteration of diatomite in 0.1 M KOH with 11 mmol L^{-1} Al leads to a different the pore size distribution (Figure 45). The pore size distribution sum curve indicates clearly the formation of a hierarchically structured material: On the one hand the relative amount of small pores increased with ongoing alteration in 0.1 M KOH, which can be expressed by a decrease of the median pore diameter from 9 to 4 nm within 8 d. On the other hand the higher relative percentage of larger pores indicates the survival of diatoms. The combination of the macropores (~ 100 nm) from the diatoms and of nanopores (< 5 nm) justifies the classification as hierarchically structured material.

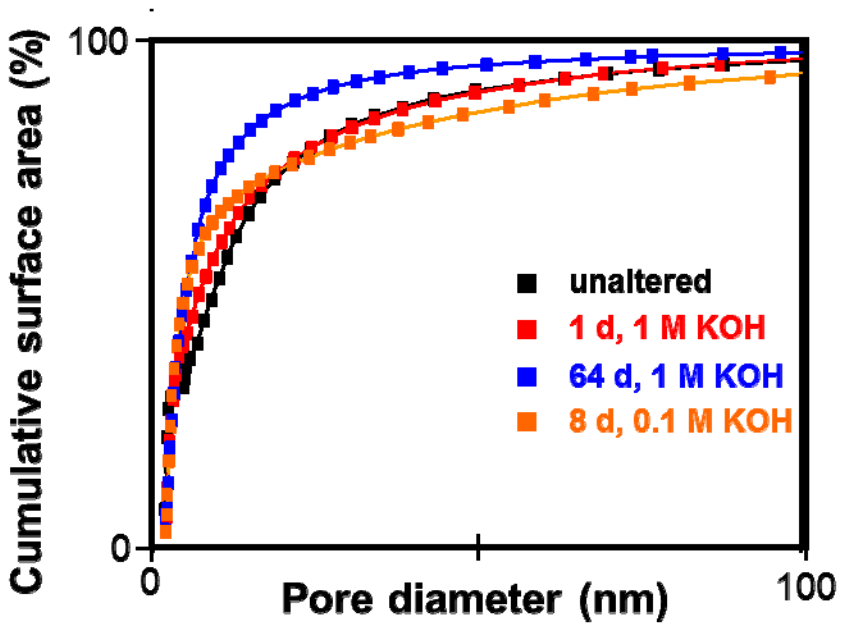

Figure 45: Cumulative surface area (%) of unaltered diatomite and diatomite altered 8 d in 0.1 M KOH with 11 mmol L^{-1} Al and for 1 and 64 d in 1 M KOH with 22 mmol L^{-1} Al at 100 °C as a function of pore diameter analysed by the t-plot method by BET

4.3.9 Transmission Electron Microscopy

TEM analyses were taken from samples altered with 1 M KOH containing 22 mmol L^{-1} Al at 100 °C for 1 d (Z2) and 2 d (Z5) and at 125 °C for 2 d (Z7) to investigate the character of the intermediate phase (IP) in more detail and to confirm the presence of merlinoite. Sample Z2 is composed of diatoms (D) and the IP. The diatoms are amorphous in respect to TEM-SAED patterns (Figure 46):

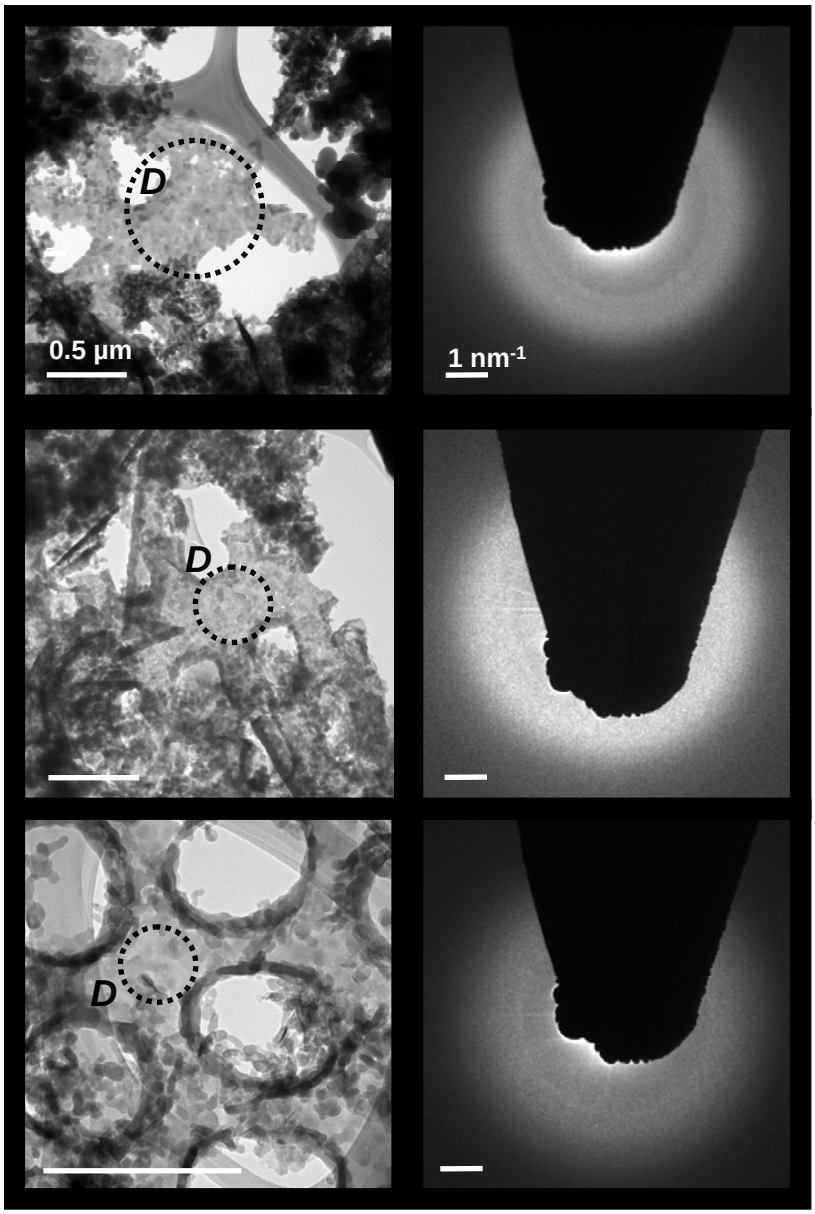

Figure 46: TEM images and corresponding SAED patterns of amorphous diatoms in diatomite altered in 1 M KOH containing 22 mmol L^{-1} Al for 1 d

The chemical composition determined by TEM-EDX at the analytical spots in Figure 46 indicates that the diatoms themselves are enriched in Al and K – which originate from the solution - compared to their composition before the treatment, whereby a large variation can be detected within the diatoms ranging from 23 wt.-% Al_2O_3 at spot "a" via 24 wt.-% spot "b" to 27 wt.-% at spot "c" with a reversed behavior of K_2O from just 4 wt.-% at spot "c" via 8 wt.-% at spot "b" to 16 wt.-% at spot "a".

The IP was identified by its spherical shape in TEM images (Figure 47 a-e). TEM-SAED patterns indicate that the IP is amorphous whereas other particles which grow in the pores of the diatoms are crystalline (Figure 47 & 48). They might be merlinoite although this phase was not detected by XRD in this sample.

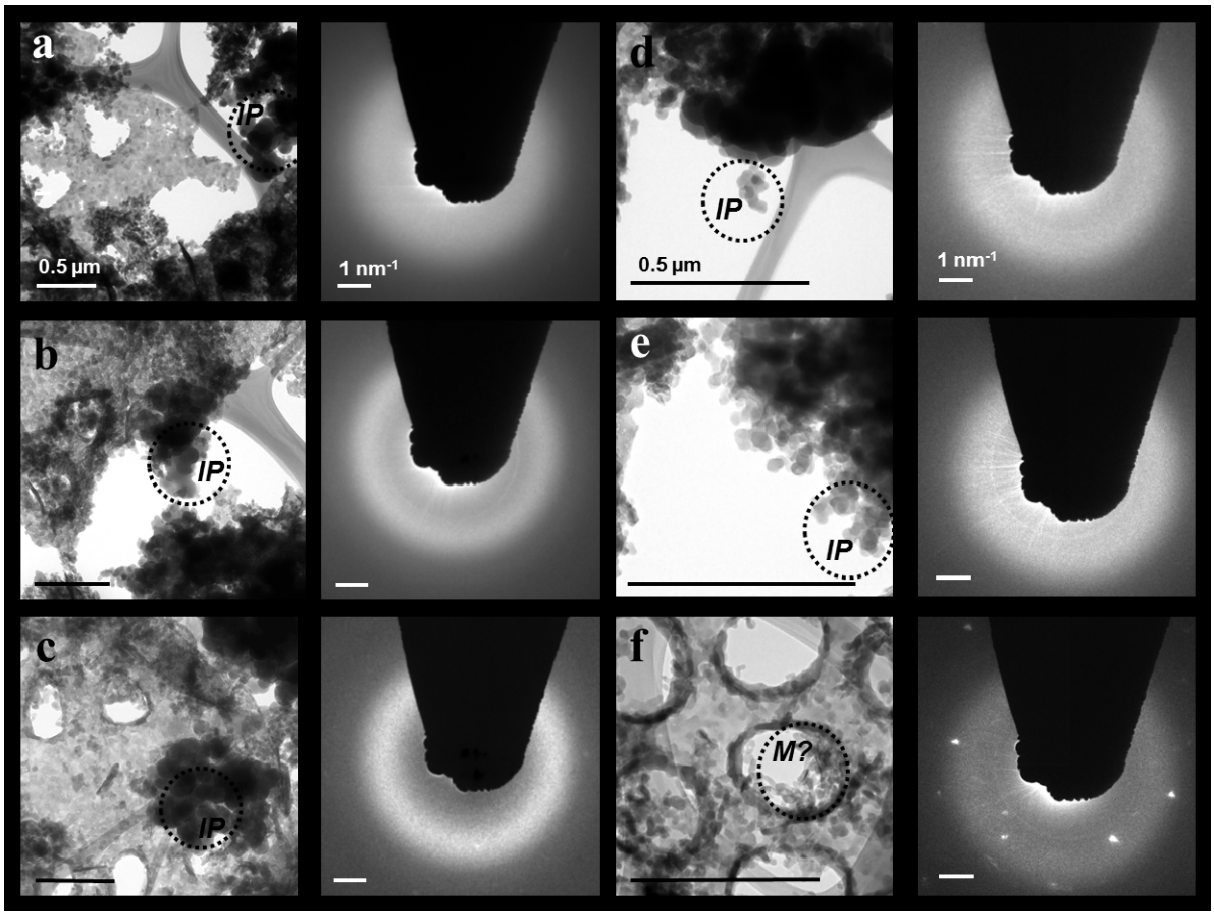

Figure 47: TEM images and corresponding TEM-SAED patterns of the amorphous intermediate phase (IP) (a – e) and some particles of a crystalline phase, maybe merlinoite (M) grown in the pores of a diatom (f) in diatomite altered in 1 M KOH containing 22 mmol L^{-1} Al for 1 d.

TEM-EDX spectra were taken at the spots "a" to "d" and indicate that the particles "a" and "b" consist of 58 and 56 wt.-% SiO_2, 28 and 27 wt.-% Al_2O_3 and 14 and 16 wt.-% K_2O, respectively, whereas the particles "c" and "d" have higher SiO_2 concentrations of 64 wt.-% at a lower K_2O concentration of only 7 to 9 wt.-% and an Al_2O_3 concentration in the same range as the particles "a" and "b" (Table 24). Interestingly, the crystalline phase (Figure 47f) has a similar composition as the IP particles "c" and "d" (67 wt.-% SiO_2, 26 wt.-% Al_2O_3, 5 wt.-% K_2O).

Further investigations on this sample were performed by the Tecnai TF 20 TEM where more precise TEM-SAED patterns can be obtained. On the one hand the amorphous IP was

identified (Figure 48). On the other also the presence of crystalline particles was observed and the Bragg reflexes could be assigned to merlinoite (Figure 49).

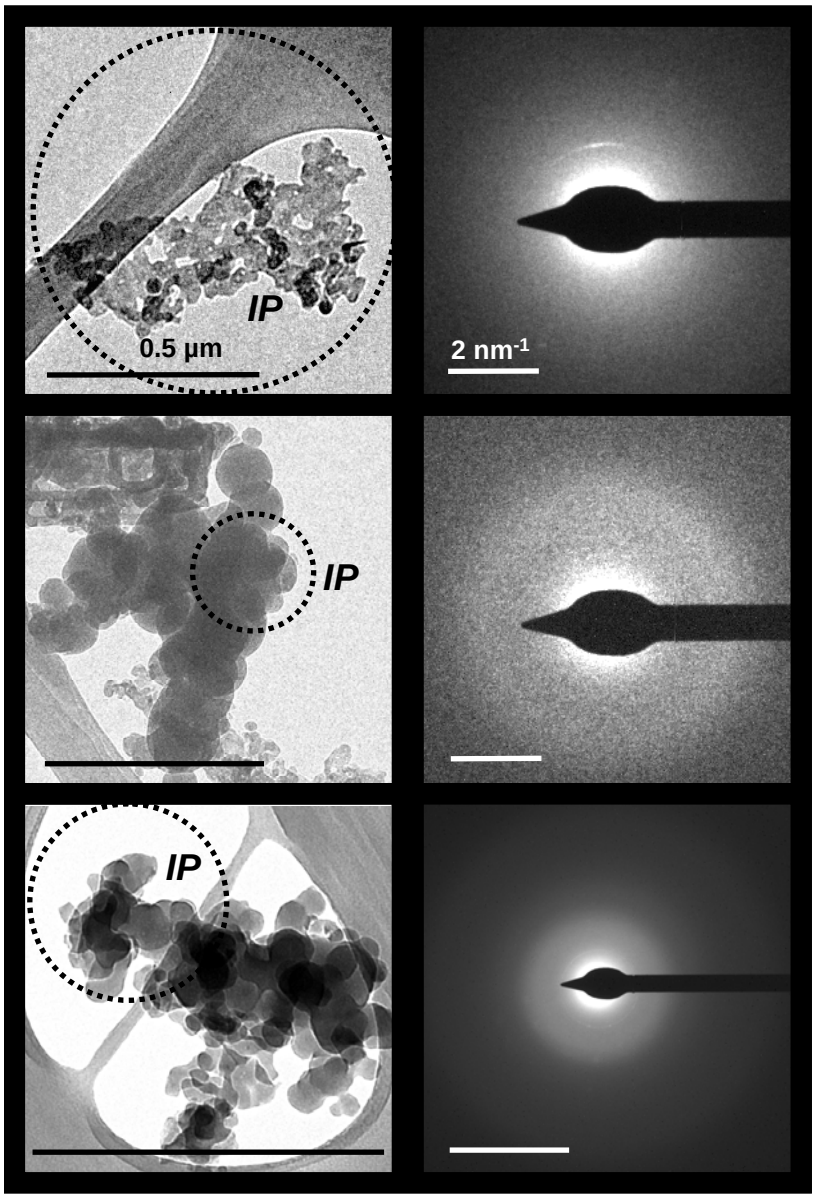

Figure 48: TEM images and corresponding TEM-SAED patterns of the IP in diatomite altered in 1 M KOH containing 22 mmol L^{-1} Al for 1 d

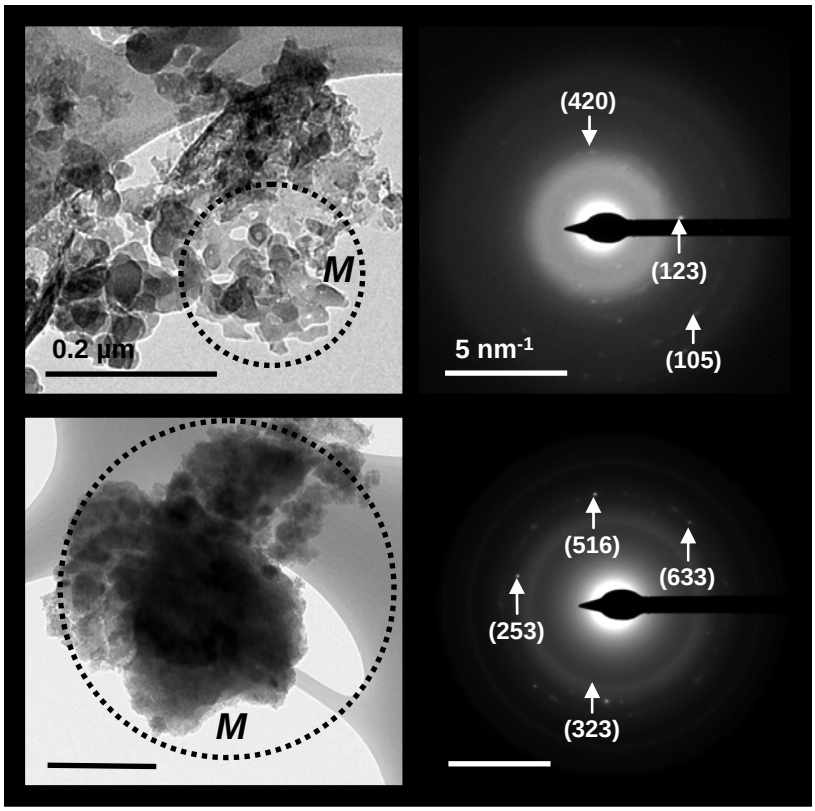

Figure 49: TEM images and corresponding TEM-SAED patterns of merlinoite (M) crystals in diatomite altered in 1 M KOH containing 22 mmol L^{-1} Al for 1 d. Miller indices were calculated from d-values according to the powder diffraction file 01-083-1533 of the PANalytical X´Pert Pro database

After a second day of alteration at 100 °C the structure of the sample has changed. TEM-SAED patterns show now only crystalline phases – merlinoite and also erionite ($K_{10}[Al_{10}Si_{26}O_{72}] \cdot 32H_2O$) (Figure 50), which was not found by XRD - although SEM-SE images still contain the IP and Rietveld refinement of XRD patterns indicate an amorphous amount of 63 wt.-%. The difference is suggested to be due to the small crystal size of the merlinoite crystals (about 10 to 20 nm) which cannot be detected by X-ray diffraction.

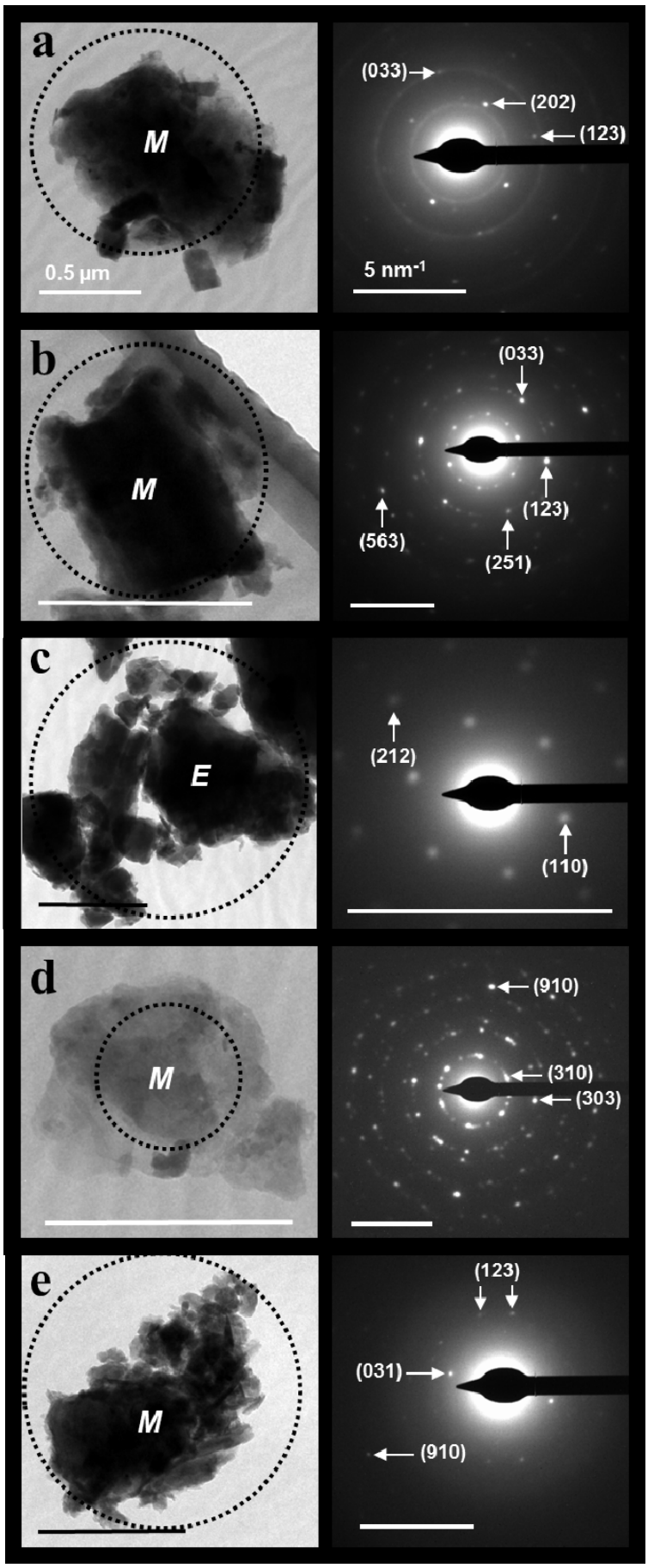

Figure 50: **TEM images and corresponding TEM-SAED patterns of merlinoite (M) (a & b, d & e) and erionite (E) (c) in diatomite altered with 1 M KOH containing 22 mmol L^{-1} Al at 100 °C for 2 d**

The effect of temperature on morphology, chemistry and crystallography was studied by comparing the above described sample Z5 (2 d at 100 °C) with sample Z7 (2 d at 125 °C): Like at 100 °C an amorphous phase is still present after 2 d. It consists of Si, Al and K but in contrast to the particles observed at 100 °C also of Ca. Interestingly, the amorphous particles present here are not isometric, but fibrous. However, investigations with Tecnai TF 20 indicate that some of these fibrous particles are also crystalline merlinoite (Figure 52). Merlinoite does not occur only as fibres, but also as platy particles in diatomite altered for 1 d with 1 M KOH containing 22 mmol L^{-1} Al at 125 °C (Figure 53). Another type of particles was observed in TEM images. It is characterised by its isometric, angular shape and a crystalline order which is destroyed during TEM measurements under loss of potassium (Figure 54).

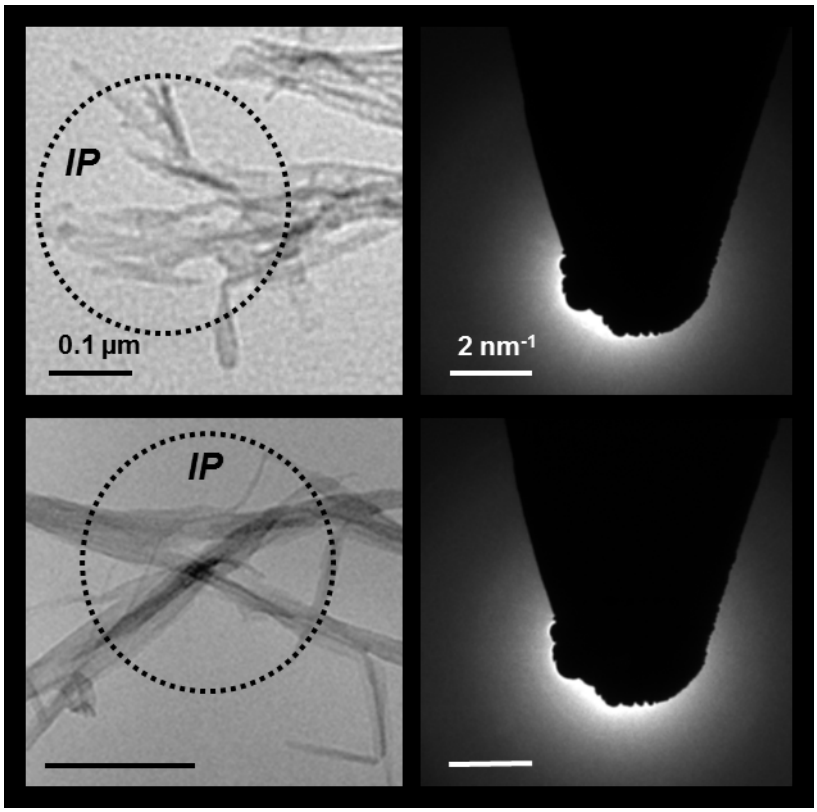

Figure 51: TEM images and TEM-SAED patterns of amorphous fibrous particles in diatomite altered with 1 M KOH containing 22 mmol L^{-1} Al at 125 °C for 2 d

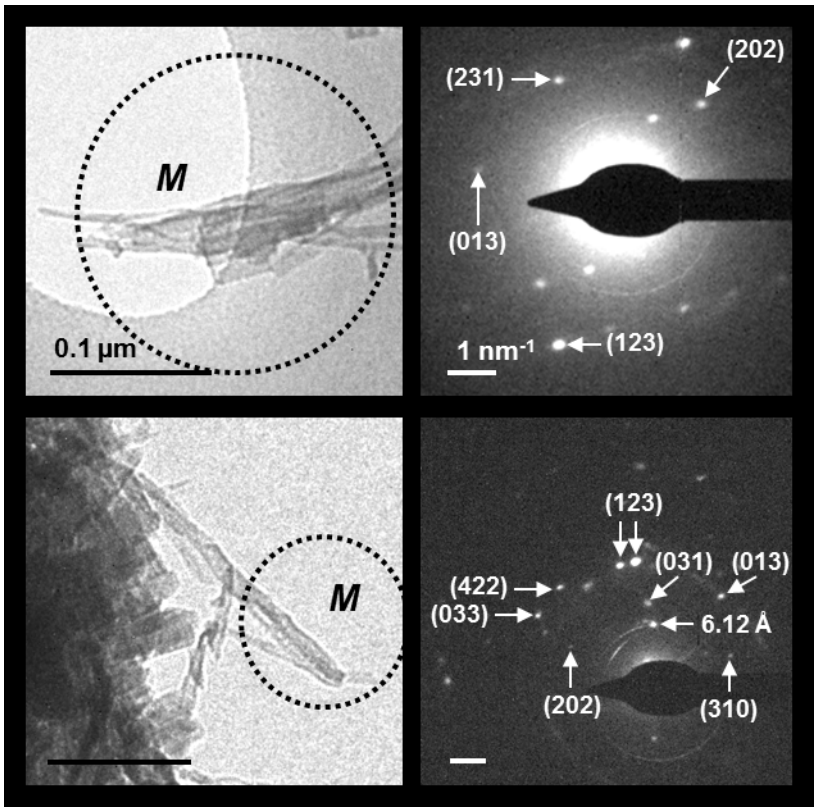

Figure 52: TEM images and corresponding TEM-SAED patterns of fibrous merlinoite particles in diatomite altered with 1 M KOH containing 22 mmol L^{-1} Al at 125 °C for 2 d

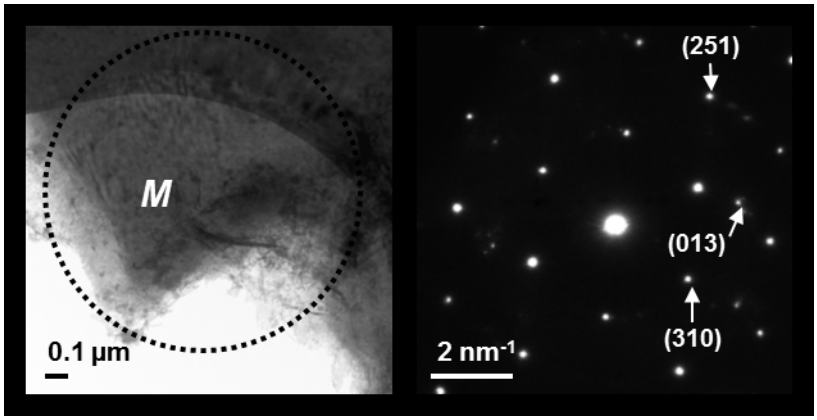

Figure 53: TEM image and corresponding TEM-SAED pattern of platy merlinoite in diatomite altered with 1 M KOH containing 22 mmol L^{-1} Al at 125 °C for 2 d

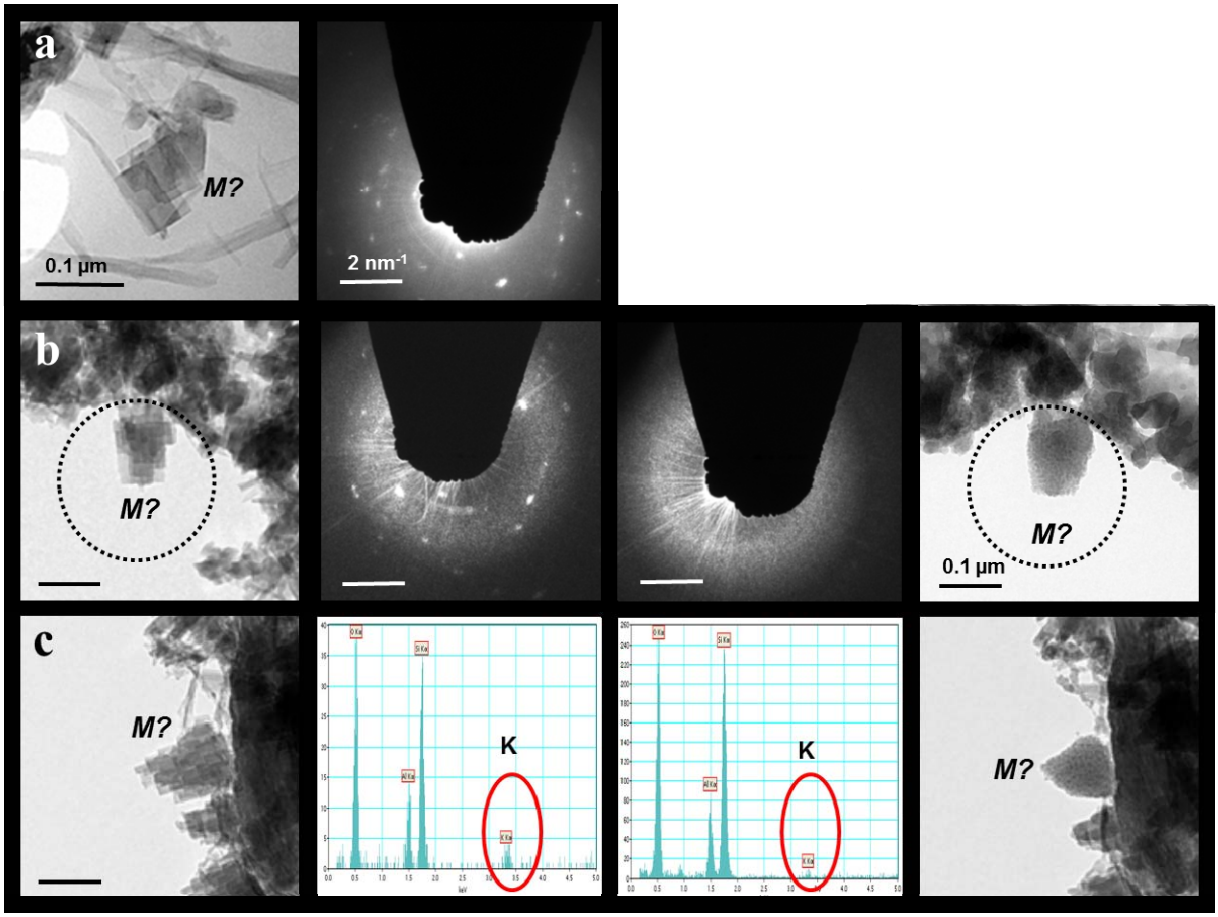

Figure 54: TEM images, TEM-SAED patterns and TEM-EDX spectra of a primarily crystalline phase (a), probably merlinoite (M), which is amorphised (b) and depleted in K (c) during the measurement in diatomite altered with 1 M KOH containing 22 mmol L^{-1} Al at 125 °C for 2 d

The radiation damage is obvious also for particles which are amorphous before radiation as their shape gets rounded and their surface evolves special patterns during electron beam exposure (Figure 55):

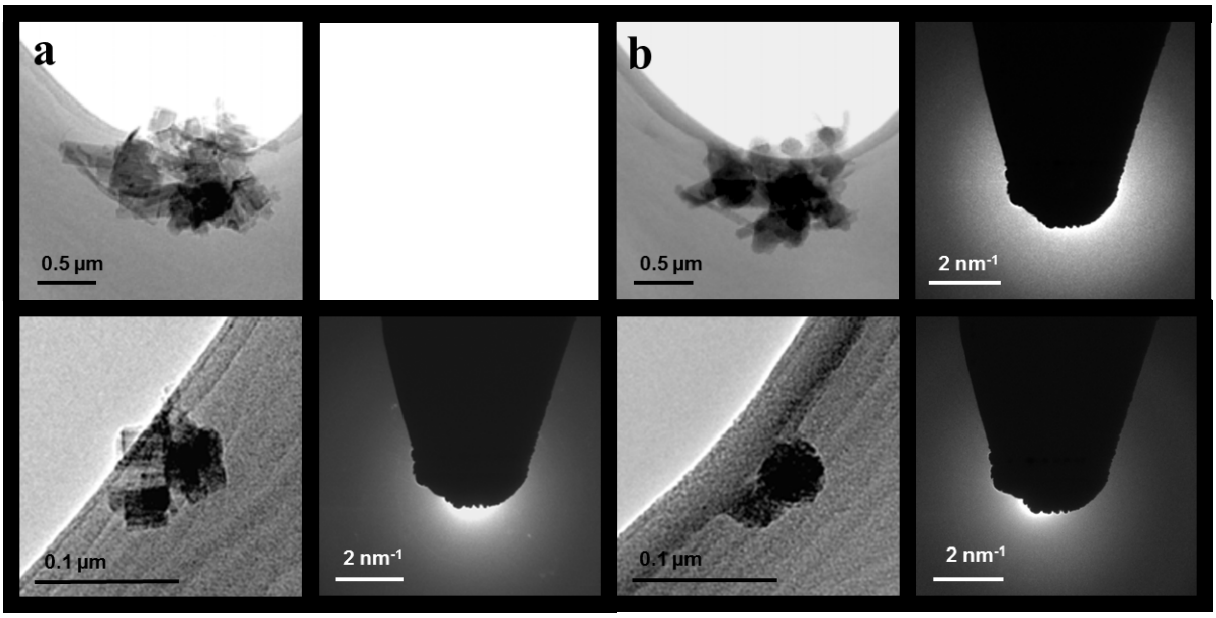

Figure 55: TEM images and TEM-SAED images of isometric particles in diatomite altered with 1 M KOH containing 22 mmol L^{-1} Al at 125 °C for 2 d before and after electron beam exposure (a and b, respectively) showing changes in morphology and in case of the second particle assemblage (bottom) its (almost) amorphous character already before electron beam exposure

If the isometric, angular particles do not have contact to other particles, radiation with an electron beam causes amorphisation, but only little K loss from 20 to 16 wt.-% K_2O in the reaction product. The SiO_2 and Al_2O_3 contents are constant with about 65 to 67 wt.-% and 16 to 17 wt.-%, respectively.

4.3.10 Results overview

Hydrothermal alteration of diatomite in 1 M KOH containing 22 mmol L^{-1} Al leads to the formation of a non-crystalline or nanocrystalline, K-containing intermediate phase (IP) and later to the crystallisation of merlinoite. Contrary, crystallisation of merlinoite is not realised in experiments with 0.1 M KOH. Instead the intermediate phase is formed in the pores of the diatoms resulting in a hierarchically structured material with both micro- and macropores. This material is stabilised in presence of 11 mmol L^{-1} Al.

4.4 Results: Metal Removal Experiments

4.4.1 Synthetic Solution containing Cu, Pb and Zn

Unaltered diatomite

Unaltered diatomite has only a limited capacity to remove heavy metal ions from the synthetic solution containing Cu, Pb and Zn ions. Pb ion removal is insignificant and Cu removal accounts for less than 20 %. However, about 1.5 mmol L^{-1} K ions are released even from unaltered diatomite during reaction with the synthetic solution containing Cu, Pb and Zn (Table 29).

Alteration products from experiments with 1 M KOH

Alteration of diatomite in 1 M KOH containing 22 mmol L^{-1} Al increases significantly its capacity to remove Cu, Pb and Zn ions from the synthetic Cu-Pb-Zn solution. Interestingly, intermediately altered diatomite (reaction time = 2 d, merlinoite present) is less efficient with respect to Cu and Zn ion removal compared to weakly altered diatomite (reaction time 0.25 d, merlinoite absent) (Figure 56, Table 27, Table 28). When alteration becomes more intense (reaction time = 4 and 5 d) the selectivity with respect to Cu, Pb and Zn ions increases: Compared to moderately altered diatomite Pb ions are removed more efficiently (and its concentration decreases below the detection limit for the sample altered at 100 °C for 5 d) and Zn less efficiently by intensely altered diatomite whereas Cu ion removal is similarly efficient. More than 99.9 % of Pb, 98.5 % or 99.6 % of Cu, but only 74 or 92 % of Zn ions in relation to the initially present concentration are removed by materials altered in 1 M KOH containing 22 mmol L^{-1} Al at 100 and 125 °C, respectively (Figure 56). Selectivity of ion removal calculated as molar ratios of the concentrations of a dissolved metal ion x to the sum of Cu, Pb and Zn show the same sequence of elements in respect to ion removal. The increase of ion selectivity correlates with a coupled complete dissolution of diatoms and formation of zeolites between the 2nd and 4th day at 100 °C (Figure 42). Initial increase and later decrease in Zn removal capacity of diatomite as a function of alteration time correlate with the specific surface area (BET) (Table 21 & 22) and with the rise and decline of the intermediate phase (Figure 37). When merlinoite is formed after 2 d alteration at 100 °C and after 1 d at 125 °C, Zn removal capacity decreases significantly (Figure 56). Hence it is suggested that the intermediate phase with its high specific surface area is better capable of removing Zn from aqueous solutions than merlinoite.

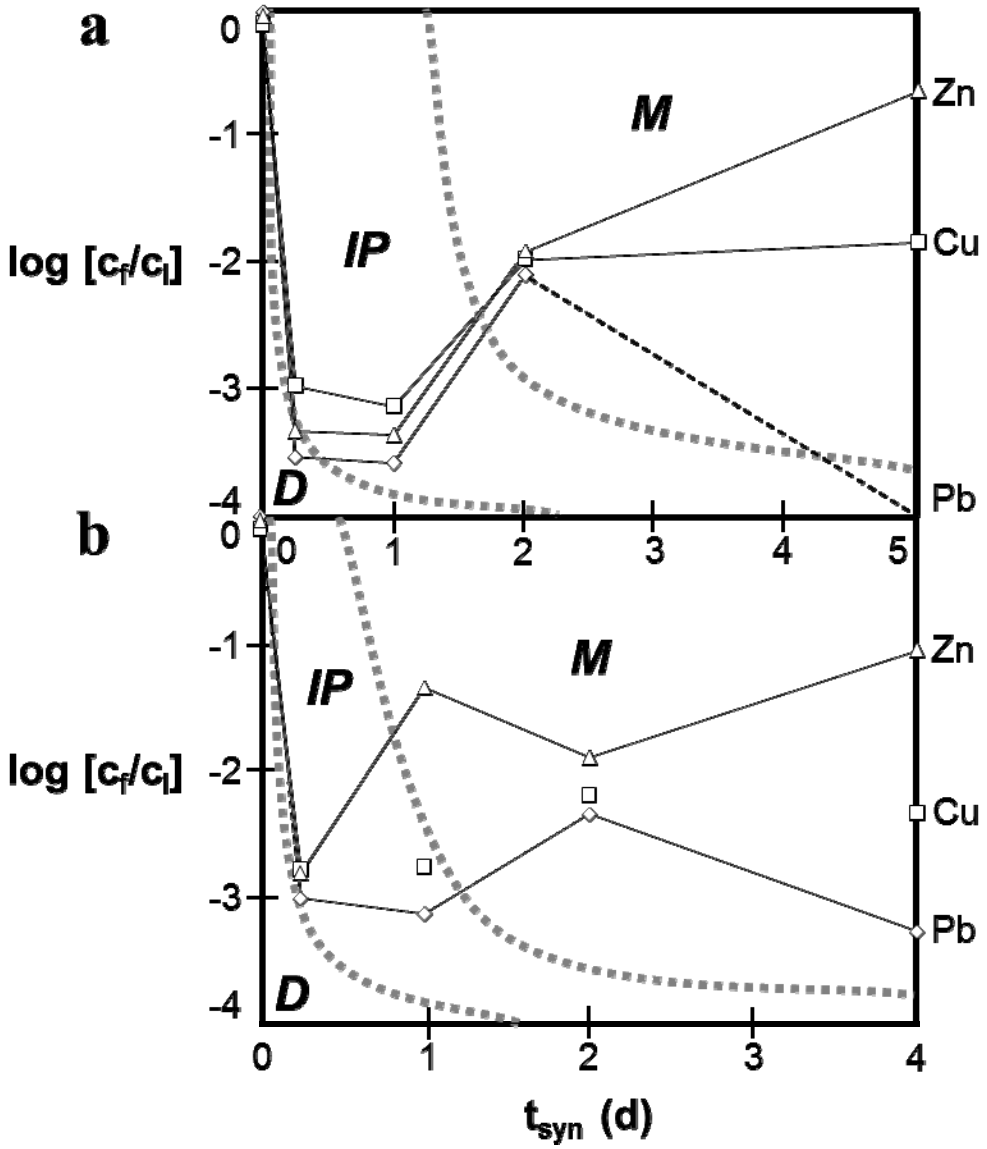

Figure 56: Cation removal capacities of unaltered diatomite (D) and diatomite altered for distinct reaction times (0.25 d ≤ t_{syn} ≤ 5 d) in 1 M KOH containing 22 mmol L^{-1} at 100 °C (a) and 125 °C (b) for Cu^{2+}, Pb^{2+}, and Zn^{2+}. c_i and c_f denote the initial and final molar metal concentrations in the solution. Dashed solid line: value of c_f is below the detection limit. Dotted lines: Schematical view of the predominance of diatoms (D), intermediate phase (IP) and merlinoite (M) within the alteration products.

Alteration products from experiments with 0.1 M KOH

Also alteration of diatomite in 0.1 M KOH creates a capacity to remove Pb ions from the synthetic Cu-Pb-Zn solution. Pb ion removal is more efficient (up to 99 %) when 11 mmol L^{-1} Al are present (Table 29 & 30, Figure 57). In the absence of Al it only accounts for 40 to 70 % with a maximum for diatomite altered for intermediate periods (4 d). Similarly, the capacity for removal of Cu ions increases during alteration of diatomite from 20 % for unaltered diatomite to 40 % during alteration in pure 0.1 M KOH and even to 60 % in the presence of Al. Compared to Cu and Pb, Zn ions are only removed to a very limited degree (10 – 20 %) from the synthetic Cu-Pb-Zn solution even by altered diatomite. The order of selectivity of heavy metal ion removal from the synthetic solution is therefore Pb > Cu > Zn, no matter if Al is present in alteration experiments.

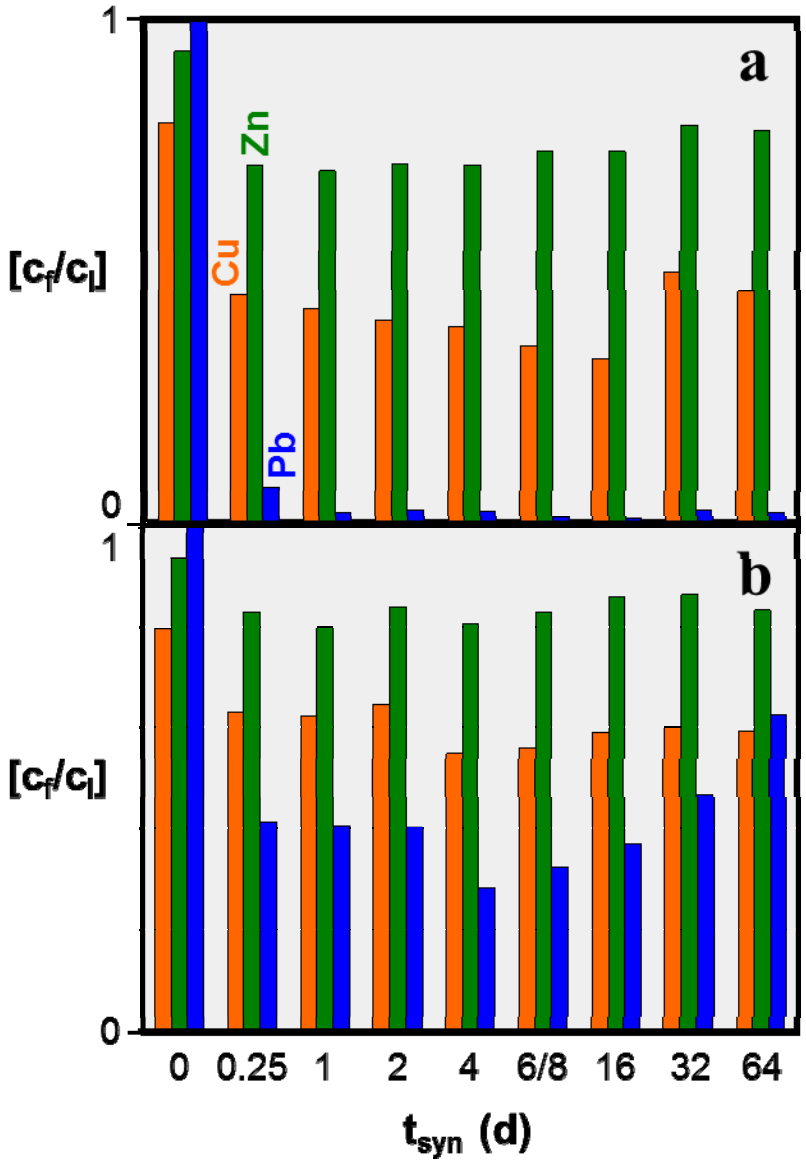

Figure 57: Heavy metal removal from the synthetic Cu-Pb-Zn solution (each 0.5 mM Cu, Pb and Zn, pH 5) after 3 d of reaction with unaltered diatomite (t_{syn} = 0 d) and diatomite altered for various durations (0.25 d ≤ t_{syn} ≤ 64 d) in 0.1 M KOH with or without 11 mmol L^{-1} Al (a and b, respectively). Concentrations of dissolved metal ions are given as ratios between the final concentration, c_f, and the initial concentration, c_i.

Reaction with the reference sample

A reference sample stored at room temperature in 0.1 M KOH with 11 mmol L^{-1} Al removed also 85 % of Cu, 99 % of Pb and 56 % of Zn ions resulting in concentrations of 75, 2 and 222 µmol L^{-1}, respectively. Also in this experiment 1814 µmol L^{-1} K^+ were released for charge compensation and 195 µmol L^{-1} Si were dissolved from diatomite. Alteration at room temperature with pure 0.1 M KOH even creates a material that removes more than 99.9 % of Cu, Pb and Zn ions resulting in respective concentrations of only about 0.1 µ molL^{-1} of the heavy metal ions. This means that alteration of diatomite at room temperature yields in reaction products at even better suitable for heavy metal removal from the synthetic Cu-Pb-Zn solution as hydrothermally altered diatomite which increases economic feasibility.

4.4.2 Synthetic Solution containing Sr and Cs

Unaltered diatomite cannot remove significant amounts of Sr and Cs from an aqueous solution containing 379 µmol L^{-1} Sr and 365 µmol L^{-1} Cs. Alteration of diatomite in 1 M KOH containing 22 mmol L^{-1} Al at 75 °C creates a high capacity of removing those metals from solution. It can be seen that metal removal capacity tends to increase with alteration degree and reaches about 99 % referred to the initial concentrations of dissolved Sr and Cs ions for intensely altered reaction products (Table 10, Figure 58).

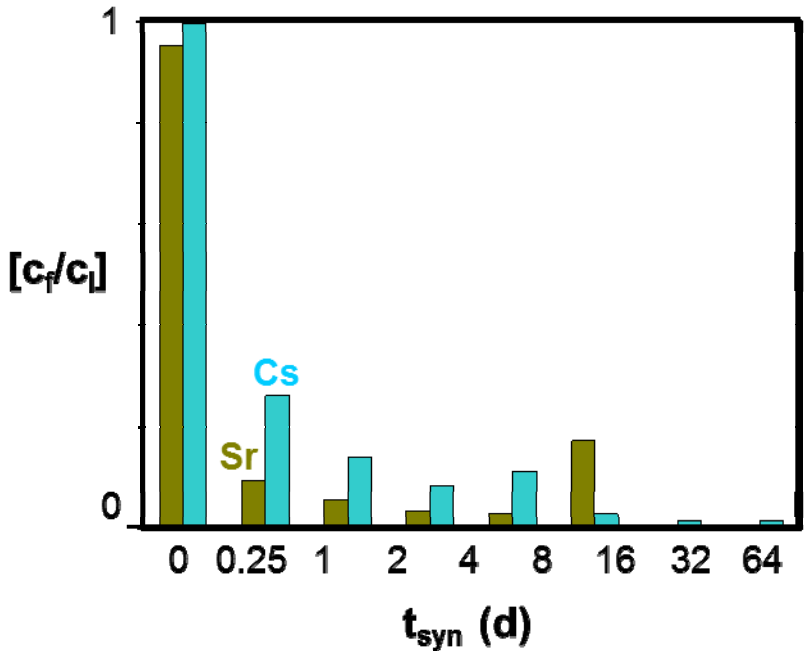

Figure 58: Sr and Cs ion removal from an aqueous solution (379 µmol L^{-1} Sr and 365 µmol L^{-1} Cs) after 3 d of reaction with unaltered diatomite (t_{syn} = 0 d) and with diatomite altered for various durations (0.25 d ≤ t_{syn} ≤ 64 d) in 1 M KOH containing 11 mmol L^{-1} at 75 °C. Concentrations of dissolved metal ions are given as ratios between the final concentration, c_f, and the initial concentration, c_i.

Reaction with the reference sample

The reference sample which was stored at room temperature for 64 d was able to decrease the concentrations of dissolved Sr and Cs ions by 99.5 and 84 % to 1.86 and 58.4 µmol L^{-1}, respectively. This means that Sr ion removal capacity of altered diatomite is independent from alteration temperature and is valid also for alteration at 25 °C whereas Cs ion removal capacity is higher for higher alteration temperatures.

4.4.3 Mine Drainage Solution

Reaction with unaltered diatomite

In contrast to the experiments with the synthetic solution containing Cu, Pb and Zn ions unaltered diatomite removes 94 % of Pb and more than 50 % of Zn from the mine drainage solution (Table 32). Also Cd concentrations could be reduced by 36 % to 0.009 µmol L^{-1}.

Alteration products from experiments with 1 M KOH

Alteration of diatomite at 75 °C in 1 M KOH containing 22 mmol L^{-1} Al increases its capacity to remove heavy metal ions from a mine drainage solution (Figure 59) compared to the untreated diatomite. As Cu concentrations are insignificant and Cd and Sr concentrations are decreased below the detection limit of 0.44 µmol L^{-1} by altered diatomite, Ca is displayed. Interestingly, Zn ions are removed more efficiently from the mine drainage solution than Pb ions, if altered diatomite is used. However, Pb ions are removed more efficiently from the mine drainage solution, if unaltered diatomite is used. Furthermore, Pb ions are also removed preferentially compared to Zn ions, if altered diatomite is suspended in the synthetic Cu-Pb-Zn solution containing higher concentrations of Pb and Zn ions. Besides heavy metal ion removal altered diatomite also reduces water hardness in terms of Ca concentrations (Figure 59). Like for other experiments also in this case metal ion removal is associated with the release of about 3000 µmol L^{-1} K (Table 33). During metal ion removal experiments a minor part of the altered diatomite dissolves resulting in concentrations of dissolved Si of about 200 to 300 µmol L^{-1}.

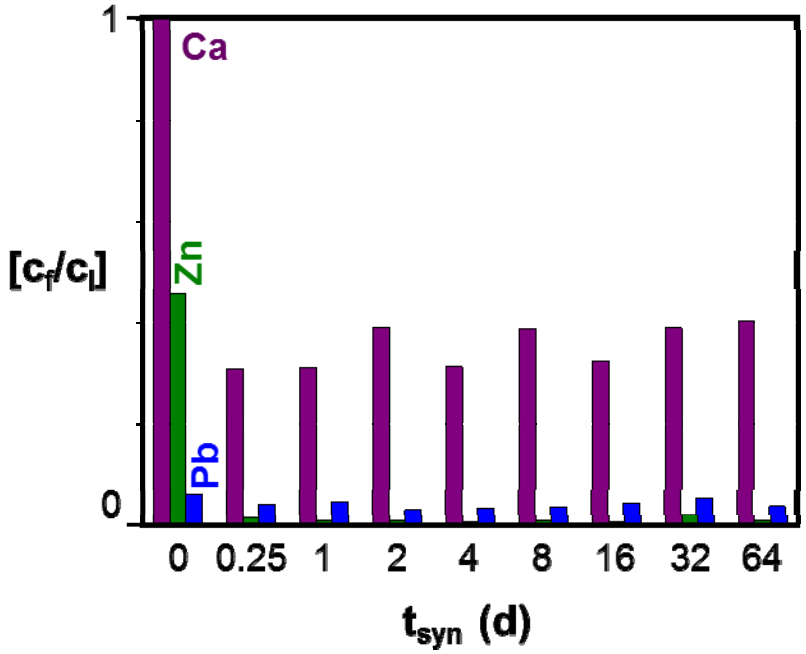

Figure 59: Ca, Zn and Pb removal from a mine drainage solution (0.14 µmol L^{-1} Cd, 0.48 µmol L^{-1} Pb, 17 µmol L^{-1} Zn, pH 8) after 3 d of reaction with unaltered diatomite (t_{syn} = 0 d) and diatomite altered at 75 °C for various durations (0.25 d ≤ t_{syn} ≤ 64 d) in 1 M KOH containing 11 mmol L^{-1} Al. Concentrations of dissolved metal ions are given as ratios between the final concentration, c_f, and the initial concentration, c_i.

Alterations products obtained with 1 M KOH containing 22 mmol L^{-1} Al after 1 d at 100 °C were used to study metal removal kinetics since they show increased Zn removal capacity by almost two orders of magnitude compared to unaltered diatomite (Table 26). It was shown that adsorption takes place within the first day. Ion uptake rates, k, were calculated according to the equation:

$$-\frac{d[M]}{dt} = k \cdot ([M] - [M]_{eq}) \qquad (22)$$

The average metal ion concentration after the 1st and the 3rd day was used as equilibrium and the concentration after 0.25 d as [M] (Table 26). The obtained k values for Ca, Mg, Sr and Zn

account for $2.9 \cdot 10^{-4}$,$1.8 \cdot 10^{-4}$, $1.1 \cdot 10^{-4}$ and $5.8 \cdot 10^{-3}$, respectively. Furthermore, it was calculated that after 4.4, 7.1, 11.2 and 0.2 hrs 99 % of the finally adsorbed amounts of Ca, Mg, Sr and Zn are removed from the solution.

Alteration products from experiments with 0.1 M KOH

Diatomite altered in 0.1 M KOH can also remove heavy metal ions from the mine drainage solution more efficiently than unaltered diatomite (Figure 60, Table 32, Table 34). Like for all other alteration products, heavy metal ion removal is connected with K release. The relative amount of heavy metal ions removed by altered diatomite is higher for the mine drainage solution than for the synthetic solution containing Cu, Pb and Zn which had much higher initial concentrations. Interestingly, diatomite altered in pure 0.1 KOH was more capable of removing heavy metals than diatomite altered in Al-containing KOH (Figure 60). Zn ions are removed more efficiently than Pb ions from the mine drainage solution, although Pb ions are removed more efficiently than Zn ions from the synthetic solution containing Cu, Pb and Zn. The capacity of Cd ion removal is between that of Pb and Zn ions. Generally, the duration of alteration had no impact on the capacity of heavy metal removal. Water hardness in terms of Ca and Mg concentration was also significantly reduced by altered diatomite, especially when Al was present in alteration experiments. Diatomite dissolution during metal removal experiments as expressed by concentrations of dissolved Si is slightly higher when alteration took place in presence of Al (Table 32 & 34).

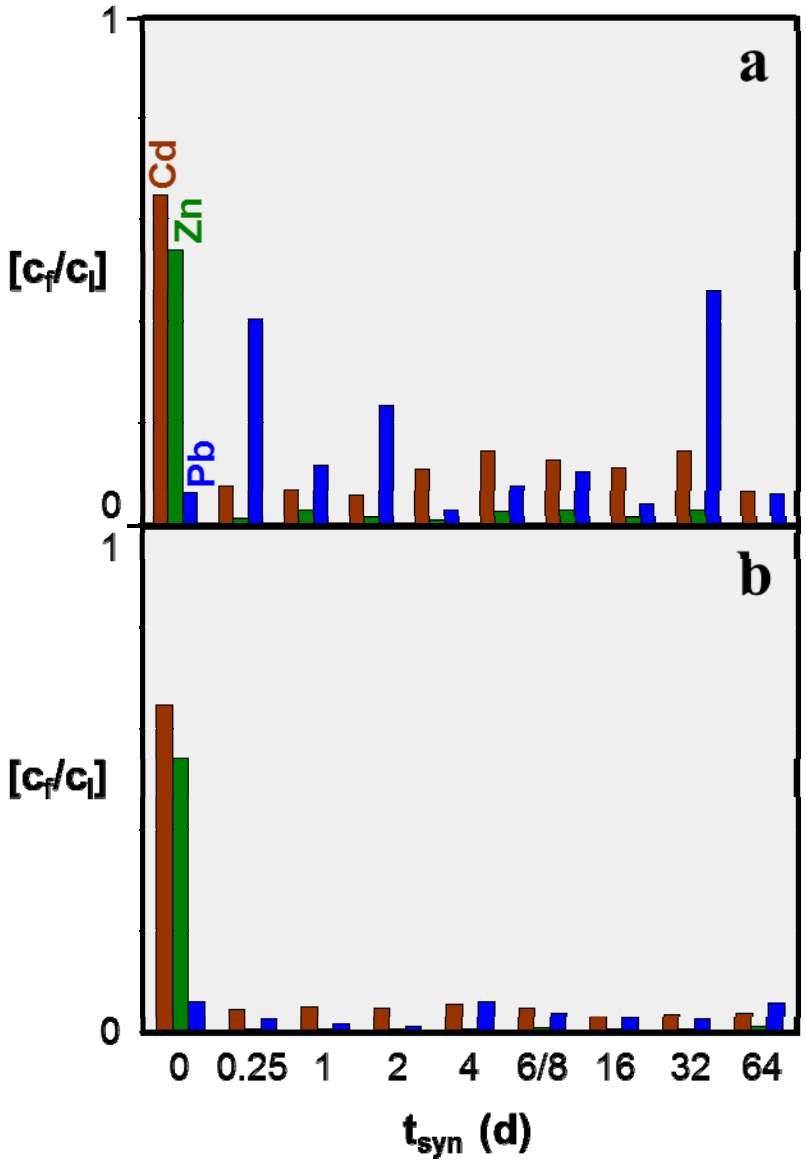

Figure 60: Heavy metal removal from a mine drainage solution (0.14 µmol L^{-1} Cd, 0.48 µmol L^{-1} Pb, 17 µmol L^{-1} Zn, pH 8) after 3 d of reaction with unaltered diatomite (t_{syn} = 0 d) diatomite altered for various durations (0.25 d ≤ t_{syn} ≤ 64 d) in 0.1 M KOH with or without 11 mmol L^{-1} Al (a and b, respectively). Concentrations of dissolved metal ions are given as ratios between the final concentration, c_f, and the initial concentration, c_i.

Reaction with the reference sample

A reference sample which was stored at room temperature in 1 M KOH containing 22 mmol L^{-1} Al showed increased heavy metal ion removal capacities in the same range as for the alteration products obtained at 75 °C with the same solution: Pb concentrations were reduced by at least 97 % below the detection limit of 0.014 µmol L^{-1} and Zn concentrations by 99 % to 0.14 µmol L^{-1}. With respect to Ca and Mg the reference sample yields even better results: 77 % of Ca and 60 % of Mg ions were removed from the solution leading to concentrations of 282 µmol L^{-1} and 252 µmol L^{-1}, respectively.

4.4.4 Results Overview

Experimental results show that alteration of diatomite significantly increases its capacity for removing cations from aqueous solutions (Figure 56 to 58). The cation removal capacity of alteration products accounts for up to 99.9 % with respect to the initial metal concentration. In all cases, the removal of cations is accompanied by a release of K^+ from the solids into the solution. Removal experiments lead to constant cation concentrations at experimental runtimes of 1 d and more (Table 26). K^+ release and kinetics reflect typical ion exchange/adsorption behavior. Besides capacity for ion removal alteration of diatomite also changes selectivity of ion removal: Unaltered diatomite removes rather Mg and Zn ions from the mine drainage and Cu and Zn ions from the synthetic Cu-Pb-Zn-solution, whereas alteration leads to preferential removal of Ca (but also Zn) ions in the former and of Pb ions in the latter case.

Alteration products were analysed after metal ion removal experiments with the synthetic solution containing Cu, Pb and Zn by SEM-SE images and no significant changes were observed. Hence the IP and the merlinoite are at least metastable at pH 5. In contact with the mine drainage solution (pH 8) dissolution of unaltered diatomite was less significant as for altered diatomite resulting in concentrations of dissolved Si of only 129 µmol L^{-1} compared to more than 200 µmol L^{-1}. This suggests that at pH 8 the IP is less stable than the bio-opal of the unaltered diatomite.

4.5 Discussion I: Diatomite Alteration Experiments

4.5.1 Early Stage Diatomite Alteration

Fast and rather complete dissolution of diatomite as obtained in the above discussed diatomite alteration experiments in strongly alkaline environments at elevated temperature is in agreement with literature data for amorphous silica [5]. However, in the presence of Al silica dissolution is retarded [5]. This explains why (i) diatomite does not dissolve completely even in 1 M KOH when 22 mmol L^{-1} Al are present and (ii) more silica is dissolved in the absence of Al in experiments with 0.1 M KOH. Higher pH of a 1 M KOH solution compared to that of a 0.1 M KOH solution results in elevated concentrations of Si and Al in equilibrium with Al-O-OH phases and silica or silicates [5]. The decrease in K concentration throughout the hydrothermal treatment of diatomite in 0.1 M KOH containing 11 mmol L^{-1} Al can be explained by the incorporation of K into the diatoms and the IP which was confirmed by XRF and TEM-EDX analyses. The decrease of K concentration during alteration of diatomite was not observed in experiments with 1 M KOH as the expected mass transfer of K from the solution to the solid is within the analytical error of K analyses (assuming an accuracy of 10 % for ICP-OES analyses in 1 M KOH this corresponds to 100 mmol L^{-1} or 2.5 mmol in the experimental volume of 25 mL which corresponds to 57.5 mg K. When 75 wt-% of the 0.5 g diatomite are dissolved, which is suggested by concentrations of dissolved Si, only 0.125 g remain. 20 wt-% of K_2O hence correspond to 12.5 mg K_2O or 5.3 mg K).

The first observed alteration of the diatoms during hydrothermal treatment is referred to the formation of bulges around their pores (Figure 39) and the enrichment of K and Al in these areas (Figure 46). The mechanism of K and Al uptake has not yet been completely

understood. Natural opal contains only few hundreds mg kg^{-1} K [107]. However, this does not necessarily mean that opal or in general amorphous silica cannot incorporate high amounts of K because the K concentrations in natura are significantly lower than in the experiments. It remains unclear at which stage of alteration of diatoms to zeolites [200] K incorporation into the structure may occur. Since TEM images display also visually undestroyed diatoms with a significant K enrichment simple adsorption or ion exchange might dominate over incorporation during solid re-organisation at this early stage of diatomite alteration.

4.5.2 The Intermediate Phase

Observations suggest the formation of intermediate phases (IP) during the alteration of diatomite at all experimental conditions:

1) SEM-SE images show spherical or irregularly shaped particles attached to the diatom´s surfaces which are not present in unaltered diatomite (Figure 37).
2) TEM-SAED patterns of these particles give no Bragg reflexes (Figure 47).
3) IP particles are present in samples without newly formed crystalline phases observed by XRD (especially in 0.1 M KOH experiments) (Figure 39, Figure 43).
4) Maximum specific surface area of the alteration product is observed for samples which are rich in the IP particles (Table 21).

The IP seems to form homogeneously in 1 M KOH containing 22 mmol L^{-1} Al (Figure 37, Figure 38) and is subsequently attached to the remaining diatoms. In experiments with 0.1 M KOH containing 11 mmol L^{-1} an IP-related hierarchically structured composite material (IP-HSCM) is formed. The discovery of this IP-HSCM is a main outcome of this thesis as this material is highly promising in respect to simulataneous removal of heavy metal ions and suspended matter from aqueous solution (see chapter 4.6). The formation conditions of the IP-HSCM, their properties and their possible applications shall be discussed in this section:

Formation conditions of the IP and the IP-HSCM

The formation of IP-like phases can be compared to that of amorphous hydroxyaluminosilicates (HAS). The latter is suggested to form by adsorption of Al on amorphous silica [201] which might be a valid process also for the formation of the IP. This concept is supported by the decrease of the Al concentration already before the first formation of new phases according to SEM-SE images (Table 12 in combination with Figure 37). Little attention was paid to intermediate phases in studies concerning zeolitisation of diatomite [151] although it is well known that amorphous precursors play a crucial role in zeolite formation [202]. In studies where seed crystals (e.g. silicalite-1) were used zeolites are growing without the formation of an intermediate phase [158]. Interestingly, one study of the zeolitisation of diatoms results in particles of similar size (100 nm like in the present study) and shape (isometric, but less rounded than in the present study) turned out to be crystalline zeolite P [154]. In this thesis particles are referred to as the IP with amorphous TEM-SAED patterns (Figure 48). As far as I know this study is the first description of such an intermediate phase formed during zeolitisation of diatoms.

Intermediate phases during zeolite formation have been described from experiments without diatoms, e.g. an amorphous phase containing four-membered rings was described [203]. One of these phases, imogolite, is characterised by a Si:Al ratio of 1:2, which is not reached in the present experiment, and by an XRD peak at 18.4 Å which was neither observed in the present

case [204]. Considering the Si:Al ratio of about 1:1 after 32 d, the IP can be better described by HAS_b [205]. The formation of the latter phase - richer in Si than imogolite and allophane - has already been observed in case of Si excess – which is also valid in the present study [205]. In contrast to HAS_b higher Al:Si ratios and significant K concentrations were observed. However, the presence of K in HAS-like phases is comparable with the presence of Na in similar concentrations within amorphous hydroxoaluminosilicates precipitated from aqueous solutions where NaOH was added to control pH [206]. It is suggested that a substitution of H^+ by Na^+ or K^+, respectively, occurs in this case. Further investigations of the polymerisation degree and Si-Al ratios in tetrahedral positions might be performed by using ^{29}Si NMR [207].

In a previous study [154] no amorphous intermediate phase, but crystalline zeolite P of similar size (100 nm) and shape (isometric) as the IP in the present study was found. Contrary, the IP in the present study is X-ray amorphous. I suggest that an IP-like phase might have been present also in the previous study [154], but dissolved already within the first 6 h. It might be that pseudomorphic replacement of the IP in a previous study [154] is associated with the different crystal structures of zeolite P and merlinoite. The structure of zeolite P is characterised by "doubly connected 4-rings" of $(Si,Al)O_4$ tetrahedra "linked into chrankshaft chains" which are cross-linked forming 8-ring channels [208]. The difference is that in zeolite P the channels are directed into the a- and b-directions and in merlinoite in the c-direction [144]. The monodirectional character of the merlinoite structure explains the elongated shape of the crystals and this might be the reason why the isometric IP has to dissolve in the present experiments to enable merlinoite formation whereas the isometric zeolite P in [154] can form without dissolution only by long-range ordering processes. In this context it should be mentioned that the tetragonal cross section of the merlinoite crystals (Figure 37) is in agreement with previous observations [209].

It might be that the different crystal structures of merlinoite and zeolite P explain not only the above suggested reaction path but also the survival of the IP. The survival of the IP in the present study might also caused by pH: Du et al. [154] used an 5 M NaOH whereas in this thesis 1 M KOH was applied. Due to the higher solubility of silica-containing solids at stronger alkaline conditions [5] the IP is suggested to be stabilised in the present study. A further reason might be that in the previous study [154] the diatomite was mixed first with pure NaOH and the mixture was subsequently pre-heated for 1 h. Subsequently, the Na-Al solution was added. In this study an alkaline solution containing both K and Al was used and mixed with the diatomite.

A further focus was directed to the contemporaneousness versus subsequence of the observed processes of diatomite dissolution and IP formation: Initial experiments with 1 M KOH (Table 12 to 16) at temperatures between 50 and 150 °C showed that 70 to 80 wt-% of the added diatomite were dissolved. Thus these conditions are not proper for the formation of a hierarchically structured composite material (HSCM) uniting the advantages of diatomite macropores for retention of particulate matter and flowability and of micropores from the IP or later formed zeolites for metal ion removal. Hence the experimental design was tailored by decreasing the KOH concentration from 1 M to 0.1 M to diminish diatomite dissolution. In the latter experiments a hierarchically structured composite material (HSCM) containing the intermediate phase (IP) was observed at 100 °C (Figure 39 & 45). The formation of the IP-HSCM is suggested to occur in the following way: (i) partly dissolution of the diatoms providing the dissolved silica; (ii) fixation of dissolved Al and K by the diatoms. Since TEM-EDX analyses were only carried out for samples obtained with 1 M KOH and 22 mmol L^{-1} only they can be used for further interpretation. TEM-EDX results from experiments with 1 M KOH and 22 mmol L^{-1} suggest that the process (i) and (ii) occur simultaneously and lead to

the formation of the rims around the pores of the diatoms in Figure 39. At the rim of the pores the surface of a diatom is not even, but curved which can be compared to an edge of a crystal which is known to dissolve faster than the even surface [210]. Hence it is suggested that at the rims of the diatoms dissolution of the diatoms and subsequent IP formation is initiated. However, during the first period dissolution dominates over precipitation which is reflected in increasing concentrations of dissolved Si. This leads to higher supersaturation with respect to the IP, which can then grow also in the pores with only loose contact to the diatoms. This finally creates the IP-HSCM.

The IP-HSCM is more conspicuous in experiments with 1 M KOH containing 22 mmol L^{-1} Al than in experiments with 0.1 M KOH containing 11 mmol L^{-1}, as it was detected only by TEM, but not by SEM in the latter alteration products. This might be due to the higher solubility of the diatoms in 0.1 M KOH which results in fewer remaining diatoms, which could act as a substrate for the IP-HSCM, than in 1 M KOH.

Properties of the IP and the IP-HSCM

The metastability of the IP strongly depends on the Al content of the system. If no Al is added to the alkaline solution, the IP can be formed, but is dissolved again rapidly (Figure 40). Hence the IP that forms in those experiments must have a different composition than the highly metastable IP from the experiments where Al was added. Thus it can be concluded that a metastable, Al-containing IP has to be distinguished from a less stable Al-poor IP. The character of the latter IP was not investigated completely in the present study as it is less relevant for the proposed aims. However, the Al-poor IP is amorphous as given by XRD patterns and is suggested to be rather an opal-like (amorphous silica) phase. Amorphous silica dissolves rapidly at highly alkaline conditions [5], whereas the Al-containing IP is highly metastable like e.g. HAS phases [135]. An analogous behavior is given by the Al-containing diatomite which is less soluble than “pure” Si-diatomite [211].

The hierarchical structure of the composite material of diatoms and the IP combines macropores of the diatoms with a diameter of about 100 nm with micropores of the IP in the range of less than 5 nm according to BJH (Figure 45). Such hierarchically structured materials are highly promising for technical applications [148]. The IP already contains nanopores although no zeolites could be found in XRD. This gives new insights into the nanostructure of the IP. Unfortunately, no TEM investigations have been performed on the IP-HSCM yet. However, even in diatomite altered with 1 M KOH at 100 °C after 1 d it was shown by TEM images combined with TEM-SAED patterns and TEM-EDX analyses (Figure 47) that a new phase enriched in K and Al grows in the pores of diatom. This phase was not detected as a crystalline phase by XRD due to its size of only about 10 to 20 nm, but displayed Bragg reflexes in TEM-SAED. Hence it is proposed that hydrothermal alteration of diatomite leads to the crystallisation of nano-merlinoite in the pores of a diatom resulting finally in a hierarchically structured material. These findings are highly promising in particular for the application of the IP-HSCM or the nano-merlinoite containing hierarchically structured material. No matter, if the material is “amorphous” or “nano-crystalline”, it can be used for filtration issues removing suspended matter down to 100 nm by the diatom macropores and dissolved ions in the range of few nm by the nanopores of the IP or the nano-merlinoite.

4.5.3 Formation of Merlinoite

Stability of different zeolites

The above suggested formation of nano-merlinoite is supported by the further evolution of the reaction products throughout hydrothermal treatment: Shortly after the nanocrystals have been found (in alteration products obtained from experiments with 1 M KOH at 100 °C after 1 d), also XRD patterns indicate the formation of merlinoite (in this case after 2 d). The formation of merlinoite was observed in all alteration experiments from 50 to 150 °C in 1 M KOH with 22 mmol L^{-1} Al. Comparable alteration experiments in NaOH at 175 to 200 °C lead to the formation of analcime [212]. The application of Na instead of K in a previous study [154] might decrease merlinoite stability [213] and theoretically philippsite should form instead of zeolite P at high Na:K ratios. Experimental conditions in this study were in good agreement with [209] concerning molar Si:Al ratios but were different with respect to molar K:Na ratios (about 4:1 in [209] and about 76:1 in this study). However, K:Na ratios are in the stability range of merlinoite observed at 25 °C and 1 bar [213]. Contrary, it was suggested that the excess alkalinity, m = (K + Na - Al)/Si, has to be below 2.9 to prevent the formation of other phases, called L-20 and L-23, respectively, the latter phase similar to zeolite M, instead of merlinoite [209]. In the present study the excess alkalinity accounts for 3.3, where merlinoite should not be stable. Hence, it is suggested that merlinoite stability is increased to higher excess alkalinities when K:Na ratios are increased. This idea is supported by the increase in crystallinity of merlinoite by 40 % when the K/(K+Na) ratio is increased from 0.4 to 0.8 [209]. It is assumed that besides its crystallinity also the stability of merlinoite is increased if K/(K+Na) ratios increase even closer to 1.

Effect of zeolitisation on pore size distribution

Interestingly, the decrease in larger pores during hydrothermal alteration of diatomite (Figure 44) is obviously associated with the formation of zeolites: The upper quartile is more or less constant when the IP is formed (20.6 nm for unaltered diatomite and 20.0 nm for the IP-rich reaction product after 1 d at 100 °C with 1 M KOH). When zeolites become dominant, this value decreases to 12.5 nm after 32 d and even to 10.5 nm after 64 d. In contrast to the formation of zeolites, the formation of the IP decreases the contribution of small pores to the overall surface area which is indicated by the first quartile: In unaltered diatomite it accounts for 2.3 nm and increases to 2.8 nm after 1 d. The formation of zeolites has little effect on the first quartile of the pore size distribution which remains constant at 3.0 ± 0.2 nm during zeolite formation.

Effect of temperature and pH on zeolitisation

The increase of zeolitisation time with decreasing alteration temperature and pH can be generally explained by reaction kinetics. At 50 °C chabazite is the dominant zeolite phase whereas chabazite is not present at temperatures of 100 °C and higher. This means that chabazite is more stable at lower temperatures. This observation is in agreement with observations of zeolite formation by bentonite-cement interaction [214] where both chabazite and merlinoite formed at 60 °C and only merlinoite at 90 °C.

4.5.4 Dissolution and Neoformation of Accessory Phases

Formation of calcium carbonates at alkaline conditions can be explained by CO_2 adsorption according to (23 & 24.

$$CO_2 + OH^- \rightarrow HCO_3^- \quad (23)$$

$$HCO_3 + OH^- + Ca^{2+} \rightarrow CaCO_3 + H_2O \quad (24)$$

Formation of boehmite and diaspore (Figure 43) can be explained by the decreasing solubility of Al-hydroxides induced by a decrease in pH during the experimental run. The presence of diaspore in the experiments with 0.1 M KOH and of boehmite with 1 M KOH may be referred to the different concentrations of dissolved Al of 11 and 22 mmol L^{-1}, respectively [66].

4.6 Discussion II: Metal Removal Experiments

4.6.1 Synthetic Cu-Pb-Zn solution

Previous studies show that even unaltered diatomite can remove significant amounts of Pb ions from aqueous solutions [215]. However, in the present study no significant removal of Pb from the synthetic stock solution was observed for unaltered diatomite at pH 5 although the specific surface area and the pore size distributions of the diatomite were similar in [215] and in the present study. But, on the other hand, a decrease of the Pb ion removal capacity for a pH shift from 7 to 4 was observed.

Alteration products containing either the IP or zeolites or mixtures thereof exhibit already a classic ion exchange behavior defined as metal ion removal with simultaneous K release (Table 27ff). The fact that also zeolite-free alteration products release some K during metal removal experiments is in agreement with their K content and with previous studies showing that in hydrothermal syntheses of various zeolites alkali metals are already present in an amorphous precursor phase [202]. Challenging issues are to discover whether the K is adsorbed on the surface or is bound in the bulk of the IP and whether the metal ions are bound at the former or latter site. It was shown that Na^+ species are adsorbed onto silica during the formation of aqueous aluminosilicates by ^{23}Na nuclear magnetic resonance spectroscopy [201]. Hence a combination of adsorption and incorporation might occur with increasing importance of the incorporation for more intensely altered diatomite.

Alteration products from experiments with 0.1 M KOH have a lower metal ion removal capacity than those from experiments with 1 M KOH. This suggests that with 1 M KOH the amount of reaction products (both the IP and merlinoite) is higher and this higher amount is necessary for removal of large amounts of Cu, Pb and Zn (up to 25 µmol heavy metal ions per gram altered diatomite) from highly contaminated solutions.

Alteration products from experiments with 0.1 M KOH show different performances in metal ion removal experiments depending on the presence or absence of Al in alteration experiments (Figure 57). When Al was present in alteration experiments Pb ion removal capacity is much higher than for alteration products from experiments with pure 0.1 M KOH. This is by far not as pronounced for Cu and Zn ions. Considering that the IP is formed more pronounced and is more stable in the presence of Al it can be concluded that the IP is responsible for preferential Pb ion removal. This might be explained by a short range order of the IP which already resembles the cages of the later formed zeolites. Considering the TEM-

SAED results of X-ray amorphous samples in alteration experiments with 1 M KOH, which revealed the presence of nanocrystalline phases, it is reasonable that nano-merlinoite is the real cause for selectivity of the IP for Pb. Cu and Zn ions fit worse into the zeolite cages as discussed below. Hence the fixation of Cu and Zn ions to a limited degree by diatomite altered with 0.1 M KOH can be explained predominantly by ion adsorption. The fact that the more efficient Pb ion fixation by alteration products from experiments with Al correlates with a twice as high release of K (Table 29 & 30) supports the suggestion that ion exchange in a cage-like structure takes place, although no zeolites were found in XRD.

Alteration products containing zeolites can be compared with other zeolites with respect to their heavy metal ion removal capacity: Significant removal of heavy metals from mine waters was observed by using similar solid:liquid ratios (30 g L^{-1} instead of 20 g L^{-1}) and a similar zeolite synthesised from fly ash [216]. Also metal ion concentrations were in the same range. An increase of cation exchange capacity (CEC) even to 3000 mmol kg^{-1} compared to 15 mmol kg^{-1} in the present study during zeolitisation was also observed for fly ash [217], but it has to be considered that in the present study heavy metal ions were removed quantitatively and higher metal ion concentrations were not applied. Correlation between metal removal capacity and specific surface area leading to extraordinarily high efficiencies for weakly altered diatomite are in agreement with previous work in which the adsorbent surface area was increased by impregnation of the diatomite surface by manganese oxides [218]. However, specific surface areas of zeolites, but even of the IP measured in this study (< 38 m^2 g^{-1}) are significantly lower than those of zeolite P synthesised from fly ash (69 m^2 g^{-1}) [219].

The correlation between the increase in sensitivity from the 2nd to the 5th day of alteration at 100 °C and the 2nd ant the 4th day at 125 °C (1 M KOH) on the one hand and the increase of the zeolite:diatomite ratio (originating from the disappearance of diatoms and/or the increase of the merlinoite content, the latter only at 100 °C) suggests the importance of the merlinoite structure for selectivity for Pb ions. From previous data [209] the radius of a merlinoite cage surrounded by eight SiO_4 tetrahedra can be calculated assuming a regular octagon and subtracting the covalent oxygen radius and accounts for 148 pm. Hence, these cages might favour Pb^{2+} (132 pm) incorporation as its size is quite similar to the initially incorporated K^+ (133 pm) compared to Zn^{2+} (82 pm) and Cu^{2+} (73 pm). When the merlinoite:diatom ratio increases the ion-selective contribution of the merlinoite dominates the overall behavior of the reaction product. It was postulated that the hydration energies of the respective metal ions given in [220] do not effect selectivity. However, it was shown that the rate constant for the adsorption of Zn^{2+}, Cu^{2+} and Pb^{2+} ions on hydrous oxide surface increases in the respective order [95] which is the same that was observed in the present study. It was furthermore found out that in the respective order the rate constants for water exchange of the hydration sphere increase as well [95]. This is in agreement with the stronger hydration sphere for Cu^{2+} and Zn^{2+} compared to Pb^{2+} [221]. Hence, it is suggested that both for adsorption on surface sites and for incorporation into zeolites at least a part of the hydration sphere has to be removed, which is more easy for Pb than for Cu and even more for Zn ions. This is supported by the crystal structure of merlinoite which is characterised by spatial separation of water and cation positions in the cages [222]. However, a previous study [223] showed that in zeolite Y the Cu ion occurs with a complete hydration sphere. Preference for Cu^{2+} compared to Zn^{2+} removal by the reaction products which was observed for merlinoite-rich products in this study (Figure 56) was also found for natural clinoptilolite [172]. Interestingly, diatomite altered at room temperature has at least the same heavy metal ion removal capacity as diatomite altered at higher temperatures. This can be explained by the presence of the IP also in the reference sample (Figure 38).

4.6.2 Synthetic Sr-Cs solution

Removal of Sr and Cs ions from aqueous solution by unaltered diatomite is insignificant (Table 31) although a diatomite-based ceramic filter was able to remove ^{90}Sr and ^{137}Cs from radioactively contaminated sludge [224]. The difference is suggested to be due to firing of the ceramic. Alteration of diatomite significantly increases the ion removal capacity for both Sr and Cs already before zeolites become detectable in XRD. However, as zeolite-like cages might be present on the nanoscale and as about 2 to 3 mmol L^{-1} K are released during metal removal experiments, an ion exchange is suggested. Fixation of Sr and Cs is in agreement with previous studies for other zeolites [185, 225]. However, merlinoite has not yet been tested for Sr and Cs removal from waste water. As merlinoite is formed after 2 d, this is the first study dealing with Sr and Cs removal by merlinoite.

Sr ion removal by altered diatomite is independent from the alteration temperature, whereas Cs ion removal is more efficient for hydrothermally altered diatomite compared to diatomite altered at room temperature. Thus it is suggested that Cs ions are rather incorporated into cages of the nano-merlinoite-containing IP which might also form at room temperature whereas Sr is rather adsorbed on the solid surface. Considering the ionic radii of Sr^{2+} and Cs^{+} of 113 pm and 169 pm, respectively, it seems that the larger Cs^{+} ion can somehow be fixed in a distorted cage-like structure although the finally suggested merlinoite cages should be too small (148 pm). Contrary, the Sr^{2+} ion is too small for the cage which might explain the worse performance of the reference sample with respect to Sr.

4.6.3 Mine drainage solution

Unaltered diatomite reduces Pb, Zn and Cd ion concentrations, but not Ca and Mg ion concentrations from the mine drainage solution (Table 30, Table 31). A previous study with raw diatomite [226] showed maximum adsorption capacities for Zn, Cd and Pb ions of 0.311, 0.18 and 0.096 mmolg $^{-1}$, respectively. In this study 0.5 g diatomite removed only 0.2 µmol Zn (= 0.4 µmolg^{-1}), 1.25 nmol Cd (= 2.5 nmolg^{-1}) and 0.01 µmol Pb (= 0.02 µmolg^{-1}) ions which is about one order of magnitude below that value. However, it has to be considered that the obtained final concentrations in the present study are very low and it is obvious that for higher initial concentrations higher amounts of metals could be removed. This is also confirmed by the results with the synthetic solution containing Cu, Pb and Zn ions (Figure 56).

Alteration of diatomite creates a capacity to reduce water hardness (Ca and Mg ions) and increases the ion removal capacity with respect to Cd and Zn ions (Figure 59, Figure 60). As the capacity for Cd and Zn removal is rather independent from the alteration degree and pH and also similar for the reference sample (Table 25, Table 32 to 34), it is suggested that the increase in metal ion removal capacity is mostly due to the increased surface area. Contrary, the presence of Al in alteration experiment has an effect, since diatomite altered in pure 0.1 KOH was more capable of removing Cd, Pb and Zn ions than diatomite altered in Al-containing KOH (Figure 60). Consequently, the IP, which is more “stable” in the presence of Al and which performed very well for highly contaminated solutions like the synthetic solution containing Cu, Pb and Zn ions, has a negative effect at low metal concentrations like for the used mine drainage solution. It is suggested that adsorption sites of the IP favour heavy metal ion removal at high metal concentrations, but act reversely at low concentrations. Contrary, the adsorption sites on the diatoms behave vice versa due to their different ion affinities.

4.7 Conclusion

Hydrothermal alteration of diatomite in alkaline solutions leads to the formation of zeolites. The reaction path is characterised by an intermediate phase (IP) which is more efficient, but less selective than the resulting zeolites for the removal of Cu^{2+}, Pb^{2+} and Zn^{2+} ions from aqueous solutions. Hence a surface-controlled ion-insensitive exchange mechanism and an incorporation-controlled ion-sensitive exchange mechanism can be distinguished. However, also the IP is suggested to contain already some cage-like structures, but the effect of the high specific surface area is postulated to be dominant. Tailoring of a hierarchically structured material consisting of the IP and of diatoms combining the micropores of the former and the macropores of the latter resulted in high metal removal capacities combined with a retention capacity for suspended matter. A challenging issue for the future is the optimisation of KOH concentration to obtain more micropores / cages without complete dissolution of diatoms. The evolution of reaction products and their properties are summarised in Figure 61.

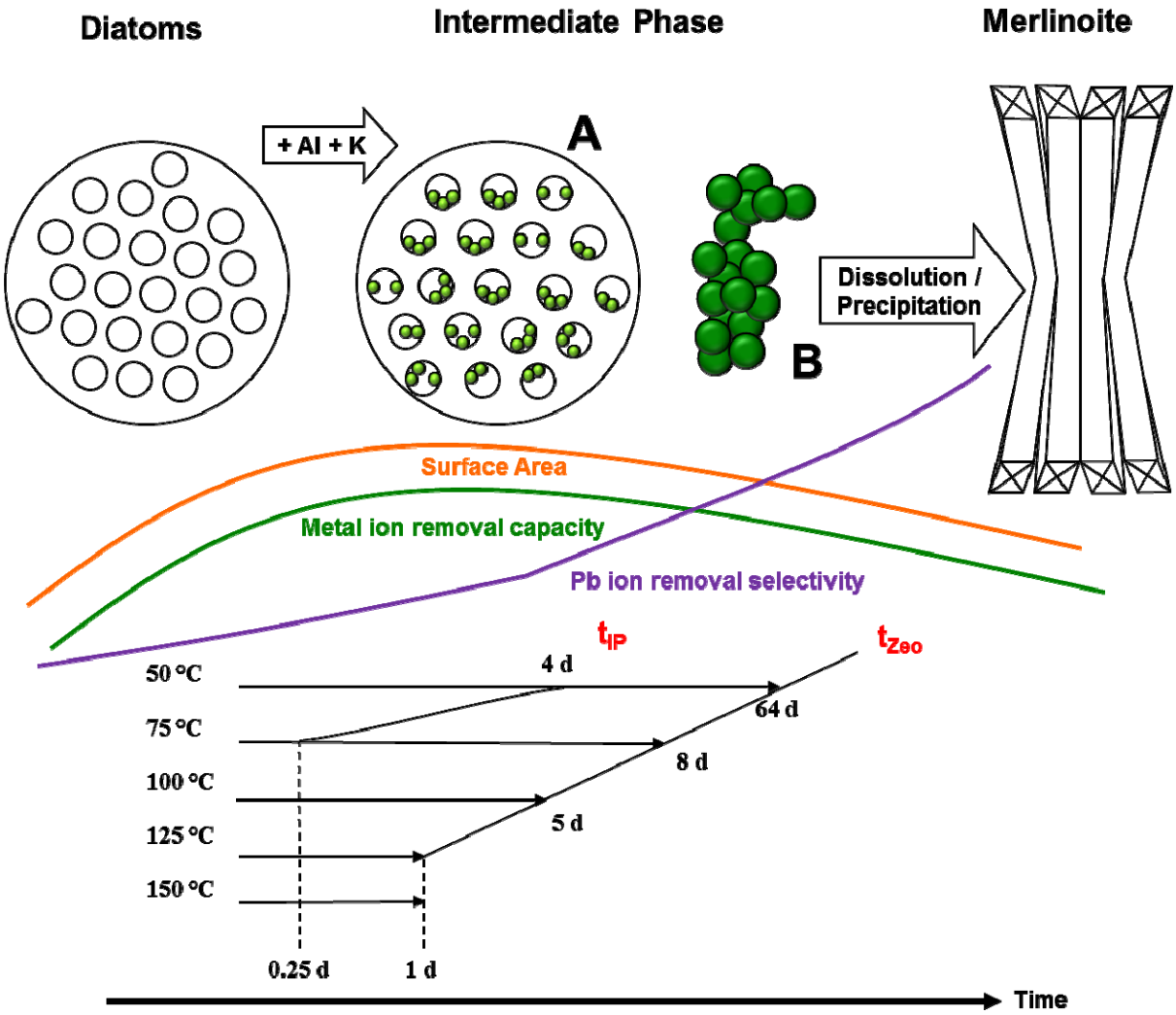

Figure 61: Evolution of diatomite during hydrothermal alteration. In the upper part the morphological changes due to Al and K incorporation and coupled dissolution and precipitation of silica are displayed schematically. The intermediate phase is shown in its two varieties: (A) as hierarchically structured material consisting of nano-merlinoite and amorphous phases growing in the pores of a diatom and (B) as aggregate of spherical particles grown in the solution. The general increase and decrease of metal ion removal capacity is also displayed schematically. The sketch at the bottom shows the dependency of the time of first formation of the intermediate phase, t_{IP}, and the time of first zeolitisaion, t_{Zeo}, at the given alteration temperature.

5 Summary and Conclusions

Amorphous silica is of great importance in both Earth and materials sciences, as it occurs on the one hand naturally, e.g. in the shells of diatoms or as chemically precipitated sediment (e.g. as chert), and is on the other hand synthesised and applied industrially due to its specific reactivity and often large specific surface area, e.g. for a controlled release of medicals. This thesis entitled "Formation and Use of Amorphous Silica" combines three studies dealing with adsorption of silicic acids onto gibbsite, precipitation of silica by cyclic freezing and hydrothermal alteration of biogenic silica for metal ion removal, respectively. Thus it traces the whole pathway of the genesis, existence and transformation of silica in natural and man-made systems.

5.1 Adsorption of Silicic Acids onto Gibbsite

Firstly, the adsorption of monomeric and polymeric silicic acid on gibbsite was investigated as a function of pH ($3 \leq pH \leq 8$) and of the concentration of dissolved silica ($0.34 \text{ mmol } L^{-1} \leq [Si] \leq 1.47 \text{ mmol } L^{-1}$). The adsorption of monosilicic acid onto gibbsite is a fast process that is completed within the first hour. Afterwards the concentration of dissolved Si remains constant for several days. It was found that the relative percentage of adsorbed silicic acid increases with increasing pH (for $pH \leq 9$) and decreasing initial concentration of dissolved silica, i.e. that at acidic pH (5 or 6) only about 25 % of Si are adsorbed but at neutral and slightly alkaline pH (7 or 8) even 40 to 50 % are adsorbed. The lower the initial Si concentration was, the higher was the relative amount of adsorbed Si. For example, after 384 h, 17 % of the initial Si was adsorbed at an initial Si concentration of 1472 μmol L^{-1}, 24 % at 749 μmol L^{-1} and 29 % at 355 μmol L^{-1}. Concerning the absolute amounts of adsorbed Si after 384 hours, 250 μmol were adsorbed at high, 181 μmol at intermediate and 96 μmol at low initial Si concentrations which is the reverse order of relative adsorption. It was shown that adsorption of monosilicic acid onto gibbsite occurs in two or three time periods. During the first period which lasts for between 0.5 and 6 hours the adsorption rate constant accounts for 0.05 to 0.17 h^{-1}. The values for the rate constant of a certain time period are in the same range for all initial Si concentrations. The relative amount of adsorbed Si at the beginning of the second period accounts for 10 %. The corresponding value for the transition to the third period increases from 13 to 20 % when the initial Si concentration is decreased from 1472 via 749 to 355 μmol L^{-1}. The absolute amount of adsorbed Si at the beginning of the second period decreases from 72 to 30 μmol for initial Si concentrations of 749 and 355 μmol L^{-1}, respectively. For the transition to the third period the corresponding values are 186, 125 and 62 μmol for 1472, 749 and 355 μmol L^{-1} initial Si concentration, respectively. The rapid decrease of the concentration of dissolved silica in the initial period which can be explained by a multilayer adsorption mechanism followed by a linear behaviour for longer durations is in agreement with previous data [96].

During adsorption of monosilicic acid the light isotope ^{28}Si is fixed preferentially versus the heavy isotope ^{30}Si due to its mass-induced higher reactivity. Si isotope fractionation is discussed for selected experiments with monosilicic acid (pH 7, 385 mmol L^{-1} gibbsite, 100 mmol L^{-1} NaCl) within the model of de Paolo [93] in [89]. The initial isotopic composition of the dissolved Si is $\delta^{30}Si = -0.08 \pm 0.15$ ‰ and $\delta^{29}Si = -0.04 \pm 0.07$ ‰. The longer the experimental time is, the isotopically heavier is the dissolved Si. A final $\delta^{30}Si$ value of about 0.5 ± 0.1 ‰ and $\delta^{29}Si$ value of about 0.25 ± 0.05 ‰ is reached. An isotopic steady state at adsorption equilibrium is reached after 32 d. Fractionation of Si isotopes during adsorption of

monosilicic acid of gibbsite is a mass-dependent process since the difference between the initial and final isotope ratio is about twice as large for $\delta^{30}Si$ as for $\delta^{29}Si$ [54]. The isotope fractionation is the stronger, the higher the initial concentration of dissolved silica is which can be explained by the DePaolo model [93] suggesting a competition between kinetic and equilibrium fractionation. Hence the signature of silicon isotopes of mineral phases which have formed by Si adsorption processes might be used as a proxy for the adsorption rate. For a geologic interpretation of the results it is most interesting that Si adsorption processes highly fractionate Si isotopes, but not at a constant value for a given substance. An extraordinarily light isotope signature of certain pedogenic minerals can consequently be explained by a Si adsorption process during their formation, especially at elevated Si concentration of the solution during adsorption of Si onto e.g. Al-OH, Mg-OH or Fe-OH surface sites. However, it has to be considered that also other processes like precipitation may fractionate Si isotopes which is still a matter of debate.

Adsorption of polyisilicic acid onto gibbsite was investigated by using *water glass* which was diluted to a Si concentration of 1513 µmol L^{-1}. At a pH of about 3 the obtained diluted solution consists of 1460 µmol L^{-1} Si bound in polymeric structures and only 54 µmol L^{-1} monomeric silicic acid which corresponds to 96 and 4 % in respect to total dissolved silica, respectively. The reaction rate constants with molybdic acid account for 0.025 and 1.0 min^{-1}, respectively, which suggests the presence of oligomers like dimers besides monomers [5]. Adsorption of polysilicic acids on gibbsite is accompanied by depolymerisation of polysilicic acid which depends strongly on pH. At low pH of about 3 depolymerisation is very slow (with a half-life time of about 8 hours), but at higher pH of about 9 depolymerisation is much faster with a half-life time of about 15 minutes. During depolymerisation, large polymers remain metastable whereas oligomers start to decompose into monomers. Polymeric silicic acid is adsorbed faster onto gibbsite than monomeric silicic acid and depolymerises on the mineral surface and in the solution. Finally there is only monomeric silicic acid in the solution. The reaction mechanisms and rates of adsorption of polyisilicic acids onto gibbsite depend on parameters like pH, T, SI and gibbsite concentration. Geometrical approximations suggest that about half of the gibbsite surface is finally covered with silicic acid and the other half with Al-OH groups in adsorption experiments with polysilicic acids. Besides adsorption of silicic acid onto gibbsite, also notable gibbsite dissolution was observed. In some experiments concentrations of up to 200 µmol L^{-1} Al (about 0.05 % of the initially present gibbsite) were found.

5.2 Cyclic Freezing of Aqueous Siliceous Solutions

Aqueous solutions containing 1.7 mmol L^{-1} Si were cyclically frozen and thawed (6 h freezing from +20 °C to -20 °C, 6 h constant at -20 °C, 6 h thawing from -20 °C to +20 °C, 6 h constant at +20 °C). Already during the first freezing period a amorphous silica was precipitated which survives the first thawing period. The precipitate is accumulated during further freezing cycles which is indicated by a decrease in the concentration of dissolved Si. Removal of Si from aqueous solution by cyclic freezing is restricted to pH < 11 where the net precipitation increases with decreasing pH until pH 5 and decreases again for pH 3. The maximal removal capacity accounts for about 90 % of the initial Si concentration. Data suggest a maximum fixation of Si after 40 to 50 cycles with subsequent re-dissolution. Without cyclic freezing no precipitation occurs.

In further experiments the effect of the addition of Al, B, Ge and kaolinite on silica precipitation by cyclic freezing was investigated. Firstly, distinct amounts of Al (0.1 mmol L^{-1}

and 1 mmol L^{-1}) were added to the siliceous aqueous solutions. Compared to experiments with pure Si solutions, the addition of Al enhanced the precipitation of silica by cyclic freezing for pH < 11. Additionally at pH ≥ 5 also Al is removed from the solution. The amount of removed Si in experiments with 0.1 mmol L^{-1} Al accounts for about 30 % at pH 3, 20 % at pH 5, more than 90 % at pH 7 and about 60 % at pH 9. These values are partly much higher than for experiments without Al. In those experiments where most Si was removed (pH 7 and 9) a minimal Si concentration was reached after 80 d and afterwards the concentration increased again slightly. The final increase in the concentration of dissolved Si at pH 7 and 9 is correlated with a simultaneous increase in the concentration of dissolved Al. In experiments with 1 mmol L^{-1} Al immediately after the preparation of the solution a Si- and Al-containing precipitate was formed ("pre-freezing precipitation") which decreased the "initial" concentration of dissolved Si to 1.13 mmol L^{-1} at pH 4.5 and even to 0.81 mmol L^{-1} at pH 7 and the "initial" concentration of dissolved Al to 0.69 mmol L^{-1} at pH 4.5 and even to almost zero at pH 7. This pre-freezing precipitate enhances Si removal from the solution during cyclic freezing. In selected experiments besides Al also 100 mmol L^{-1} NaCl were added which resulted in twice as high residual concentrations of dissolved silica, a retardation of precipitation of silica from the first to subsequent freezing cycles and also a removal of Na ions from the solution.

The addition of 0.1 mmol L^{-1} B to the siliceous aqueous solution also lead to the precipitation of silica for pH < 11, but no net removal of B was observed. B was found to have no significant effect on silica precipitation at acidic and alkaline pH (≤ 5 or 11), but reduces silica precipitation at pH 7 and stimulates silica precipitation at pH 9.

The addition of 0.1 mmol L^{-1} Ge to the siliceous aqueous solution increased the Si removal from the solution by cyclic freezing. Whereas in pure Si solution at pH 3 only about 20 % of dissolved Si were finally removed, Si removal accounted for almost 80 % of initially dissolved Si in Ge-containing solutions. Furthermore, in pure Si solutions at pH 3 after 40 d no further net precipitation of Si took place whereas in Ge-containing solutions net precipitations continued until the end of the experiment. Like for B, also for Ge no significant net coprecipitation could be observed.

The addition of 2.58 g L^{-1} kaolinite to the siliceous aqueous solution inhibited completely net precipitation of silica by cyclic freezing within the first 16 days. However, for experimental runtimes of more than 16 days net precipitation of silica began and dissolved Si was removed almost quantitatively from solution until 131 d. Dissolution of kaolinite increased the concentration of dissolved Al initially to 0.22 mmol L^{-1}, but subsequent coprecipitation with silica decreased the concentration of dissolved Al finally to the detection limit of 0.0004 mmol L^{-1}.

The precipitation of amorphous silica is accompanied by a polymerisation of dissolved silicic acid at pH 3 and 4.5, but not at higher pH. Polymerisation of dissolved silicic acids occurs already within the first freezing cycle. Afterwards competing processes of depolymerisation and polymerisation of silica lead to a rather complex evolution of the degree of polymerisation. The addition of B slightly enhances polymerisation of silica whereas the addition of Al and kaolinite rather inhibit it or the possibly formed polymers are adsorbed onto an Al-hydroxide or onto kaolinite, respectively. Polymerisation of silica at pH 3 is more pronounced than at pH 4.5. Besides the degree of polymerisation in terms of the ratio of polymeric versus total dissolved Si, also the size of polymers increases with decreasing pH in case of pure Si and Al-containing solutions.

A fractionation of Si isotopes occurs only in presence of high Al concentration, thus at elevated supersaturation with respect to amorphous aluminium hydroxide. In these cases ^{28}Si is fixed preferentially versus ^{30}Si in the precipitates which can be explained by Si adsorption onto primarily formed aluminium hydroxide precipitates or coprecipitation of a Si-Al-O-OH solid phase. Thus the solution becomes heavier with respect to Si isotopes whereas the precipitate becomes lighter. The maximum bulk fractionation occurs after five cycles and accounts for $\Delta^{30}Si = \delta^{30}Si_{(aq)}-\delta^{30}Si_{(s)} = 5.8$ ‰. With increasing number of freezing cycles these two values converge again towards a δ-value of about 0 ‰. Thus finally there is no significant apparent fractionation of Si isotopes between solution and precipitate due to cyclic freezing for a sufficiently large number of freezing cycles. Hence the Si isotopic fractionation between amorphous silica-containing solids and possibly subsequently formed mineral phases on the one hand and the coexisting solution on the other hand might be used as a proxy to distinguish between unidirectional processes like adsorption and cyclic processes which are associated with a reorganisation of silica within the precipitate.

The Si-containing precipitates formed by cyclic freezing are in all experiments irregularly shaped particles with a size of 10 to 100 µm. B and Ge are not incorporated in the solid according to solution chemistry, but Al seems to form a solid compound with Si by cyclic freezing which can also be concluded from solution chemistry. Therefore it is suggested that precipitates from experiments with B and Ge are rather pure amorphous silica whereas precipitates from experiments with Al might represent an alumosilicates phase. This is supported by FTIR patterns revealing a good agreement with natural allophane. Furthermore, TEM-EDX analyses give Si:Al ratios ranging from 2:1 to 2:3 which scatter within one particle, but do not show any regular zoning. In analogy to the experiment with pure Si and with additional B and Ge X-ray diffraction patterns of precipitates obtained from experiments with 1 mmol L^{-1} Al show no distinct peaks which means that they are non-crystalline solids.

Finally, the initially asked questions regarding cyclic freezing experiments can be answered:

- Can the Si isotopic composition of amorphous silica phases in cryosols be used to infer whether they have been formed by cyclic freezing?
    - Generally, Si isotope compositions of pedogenic minerals and coexisting fluids should have a $\Delta^{30}Si$ value of about 0 ‰, if they formed during sufficiently long cyclic freezing, and of about 0.1 to 0.5 ‰, if they formed during adsorption. However, several factors like Al concentration, adsorption and freezing kinetics, other minerals which might act as adsorbens in soils and diagenetic processes have to be considered. Thus Si isotopic signals of pedogenic minerals have to be interpreted carefully.
- How does the presence of Al influence the chemical, mineralogical and isotopic character of the solid phases formed by cyclic freezing?
    - Al is incorporated in silica precipitates formed by cyclic freezing. Incorporation of Al does not induce long-range order in the precipitate. Si isotope fractionation by cyclic freezing occurs only in presence of Al.
- Do hydroxyaluminosilicates form by coprecipitation of Si and Al or by subsequent precipitation and adsorption and can this be shown by Si isotopic ratios in phases formed by pure adsorption and precipitation processes?
    - Hydroxyaluminosilicates can form by adsorption of silicic acids onto gibbsite and by coprecipitation due to cyclic freezing of an aqueous solution containing Si and Al. A pure adsorption process leads to $\Delta^{30}Si$ of about 0.1 to 0.5 ‰ depending on the fraction of remaining dissolved Si, whereas in freezing experiments higher values of $\Delta^{30}Si$ of up to 6 ‰ were observed. However, the

fractionation depends on adsorption rates and the number of freezing cycles, respectively, and isotopic signatures of secondary minerals in soils have to be treated carefully.

- Does cyclic freezing lead to a chemical and/or mineralogical and/or isotopic steady state in which dissolution during the thawing period and precipitation during the freezing period are balancing each other out?
    - Yes, after about 100 freezing cycles a regularly recurring state is reached. This state approaches chemical and isotopic equilibrium, since after each cycle the same chemical and isotopic composition of precipitate and solution is reached. However, mineralogical changes have still to be investigated in more detail.

5.3 Zeolitisation of Diatomite for Fixation of Metal Ions

In the third study the application of amorphous silica is investigated using the example of its hydrothermal alteration into zeolites under alkaline conditions (25 °C ≤ T_{syn} ≤ 150 °C, 0.1 M ≤ [KOH] ≤ 1 M, 0 mmol L^{-1} ≤ [Al] ≤ 22 mmol L^{-1}). Therefore 0.5 g of biogenic silica in terms of diatomite was suspended in 25 mL alkaline solution and heated for up to 64 days.

During the first period of the experiment about 70 – 80 wt.-% and 15 wt.-% of the initial diatomite material are dissolved in the highly alkaline solution in case of 1 M and 0.1 M KOH, respectively, which is reflected in a rapid increase of the concentration dissolved Si which depends on pH but not on temperature. All experiments show a rapid exponential decrease of Al ion concentration even before secondary phases formed. The residual Al ion concentrations are mostly below 3 mmol L^{-1} with 1 M KOH and below 0.03 mmol L^{-1} with 0.1 M KOH and show no clear dependence on temperature. The diatoms incorporate or adsorb K and Al ions from the solution which results in contents of about 25 wt.-% Al_2O_3 and about 10 wt.-% K_2O in the diatoms themselves.

Subsequently, a potassium-containing hydroxyaluminosilicate intermediate phase (IP) was formed both in experiments with 1 M and with 0.1 M KOH, but the morphology is slightly different. In experiments with 1 M KOH the IP consists of spherical particles with a size of about 100 nm and is therefore characterised by a high specific surface area. In 1 M KOH the time at which the IP forms decreases from 4 d at 50 °C via 2 d at 75 °C to 0.25 d at 100 °C. In experiments with 1 M KOH the IP particles are aggregated and the aggregates are spatially separated from the residual diatoms. The IP consists of about 60 wt.-% SiO_2, 30 wt.-% Al_2O_3 and 10 wt.-% K_2O. In experiments conducted at 100 °C with 0.1 M KOH with 11 mmol L^{-1} Al the alteration process starts with the formation of bulges around the pores of the diatoms after 0.25 d. Subsequently after 1 d the IP starts to grow in the pores of the diatoms resulting in a hierarchically structured composite material (HSCM-IP). The hierarchical structure of the HSCM-IP is reflected in an increase of nanopores (< 5 nm), but also of larger pores (~ 100 nm). The formation of the IP is associated with an increase in the specific surface area to 25 to 38 m^2 g^{-1}. It is suggested that the IP growing in the pores of the diatoms in experiments with 0.1 M KOH is nanocrystalline because crystalline features of similar X-ray amorphous nanoparticles of the IP were found in experiments with 1 M KOH. If no Al was added to the 0.1 M KOH, the IP is also formed, but disappeared after 32 d.

Hydrothermal alteration of diatomite in 1 M KOH containing 22 mmol L^{-1} Al finally results in the formation of zeolites whereas alteration in 0.1 M KOH did not lead to zeolitisation. At temperatures of 125 and 150 °C merlinoite was the only formed zeolite, at room temperature no growth of zeolites was observed, at 50 °C only chabazite crystallized and at 75 °C and 100

°C a mixture of merlinoite and chabazite was formed. The zeolitisation time decreases in experiments with 1 M KOH with increasing temperature from 64 d at 50 °C via 4 d at 75 °C, 2 d at 100 °C to 1 d at 125 °C. The amorphous amount of the reaction products which is maintained during the alteration of diatomite decreases with increasing temperature from 65 wt.-% at 50 °C via 31 wt.-% at 100 °C to nearly zero at 150 °C after 64 d. The formation of zeolites is associated with a decrease of the specific surface area compared to alteration products rich in the IP. The chemical composition of the synthesised merlinoite was 67 wt.-% SiO_2 26 wt.-% Al_2O_3 and 5 wt.-% K_2O.

Heavy metal ion removal experiments were conducted with two synthetic solutions, one containing about 500 mmol L^{-1} of Cu, Pb and Zn (pH 5), the second one about 400 mmol L^{-1} of Sr and Cs, and with a mine drainage solution from a carbonate-hosted Pb-Zn deposit (pH 7). Alteration of diatomite increases the capacity to remove heavy metal ions from the synthetic solution containing Cu, Pb and Zn ions. Alteration products rich in the IP, even the material obtained at room temperature have a higher capacity with respect to Cu and Zn ion removal than zeolite-rich alteration products. The initial increase and later decrease in Zn ion removal capacity through alteration time correlates with the specific surface area. Contrary, zeolite-rich reaction products exhibit a preference for Pb ion removal due to the merlinoite crystal structre. In contrast to unaltered diatomite, alteration products remove up to 99 % of the initially dissolved Sr and Cs ions. The removal capacity in respect to Sr ions is the same for IP-rich and zeolite-rich reaction products whereas the removal capacity in respect to Cs ions is better for zeolite-rich reaction products. In contrast to the experiments with the synthetic solution containing Cu, Pb and Zn ions unaltered diatomite removes 94 % of Pb and more than 50 % of Zn from the mine drainage solution. But also in respect to the mine drainage solution alteration of diatomite - even at room temperature - increases its capacity to remove heavy metal ions to up to 99.9 % referred to the initial concentrations of dissolved heavy metal ions. The heavy metal ion removal capacity in respect to the mine drainage solution was the same for IP-rich and zeolite-rich reaction products. In all metal ion removal experiments, the removal of cations is accompanied by a release of K^+ from the solids into the solution. It was furthermore confirmed that alteration products were neither changed significantly with respect to phase composition and morphology during metal ion removal experiments nor dissolved significantly during the application for metal ion removal.

Finally the initially asked questions can be answered:

- How does the zeolitisation process of diatoms occur in detail?
    - Zeolitisation of diatoms occurs via an intermediate non-crystalline or nano-crystalline, hydrous, potassium-rich aluminosilicate phase which consists of mostly spherical particles in the range of about 100 nm.
- Can diatomite be used to produce hierarchically structured materials consisting of macroporous diatoms and microporous zeolites?
    - Yes, alteration of diatomite in 0.1 M KOH at 100 °C yields in a hierachically structured material where nanocrystalline merlinoite grows in the pores of the remaining diatoms. This material is highly interesting with respect to the combined removal of particulate matter and dissolved metal ions in wastewater treatment.
- Does the heavy metal ion removal capacity increase linearly during the conversion of diatomite to zeolites?
    - No, the heavy metal ion removal capacity increases rapidly during the first period of alteration and subsequently remains constant of even decreases, depending on the respective metal. Generally, heavy metal ion removal

capacity correlates with specific surface area. The latter increases due to partial dissolution of diatomite and formation of an intermediate phase or nanocrystalline merlinoite. Subsequently the specific surface area decreases slightly due to dissolution of the IP and growth of merlinoite crystals.

6 Acknowledgement

I would like to thank my supervisors Martin Dietzel and Dietmar Klammer for helpful discussions and detailed comments as well as for preparation of the manuscript. I am grateful to Albrecht Leis as external referee for reviewing my thesis. My colleagues Andre Baldermann (helpful discussions) and Andrea Niedermayr (helpful discussions + critical review), Christine Latal (assistance with XRD) as well as Andrea Wolf and Maria Hierz (assistance with adsorption and zeolitisation experiments) and Judith Jernej (assistance with XRF) contributed to the success of this thesis. Furthermore I would like to thank the BSc students Gerald Raab and Dominik Petzold for their support in conducting zeolitisation and metal removal experiments. Special thanks goes to Marcus Oelze and Friedhelm von Blankenburg (German Research Centre for Geosciences) with whom the papers dealing with adsorption and freezing experiments were prepared for publishing and who conducted the isotopic analyses. External collaborators like Patrick Grunert (SEM, Institute of Earth Sciences, KFU Graz), Ilse Letowsky-Papst (TEM, FELMI Graz), Andrea Brunnsteiner (BET, Institute for Material Testing and Building Materials Technology, TU Graz) and Michael Piller (BET, Research Center Pharmaceutical Engineering, Graz) also supported me with analytical work wherefore I would like to thank them.

7 Appendices

Table 1: Concentration of dissolved Si, dissolved Si isotopic signature ($\delta^{30}Si$ and $\delta^{29}Si$), corresponding confidence intervals and concentration of dissolved Al in adsorption experiments with monosilicic acids with three different initial concentrations (a: 1472 µmmol L^{-1}, b: 749 µmol L^{-1}, c: 355 µmol L^{-1})

	t	Si	$\delta^{30}Si$	CI (95 %)	$\delta^{29}Si$	CI (95 %)	Al
	h	µmol L^{-1}	‰	‰	‰	‰	µmol L^{-1}
a	0	1472	-0.08	0.15	-0.05	0.07	bdl
	0.01	1371	0.12	0.16	0.05	0.08	n.a.
	0.5	1370	0.14	0.11	0.05	0.06	0.41
	1	1365	0.20	0.07	0.08	0.02	0.59
	2	1355	0.15	0.08	0.10	0.07	0.37
	6	1329	0.26	0.07	0.11	0.10	0.33
	24	1286	0.31	0.12	0.18	0.06	0.37
	96	1267	0.35	0.11	0.17	0.12	0.30
	192	1252	0.45	0.17	0.17	0.07	0.37
	384	1222	0.45	0.10	0.25	0.05	0.42
b	0	749	-0.08	0.11	-0.04	0.06	bdl
	0.01	697	0.04	0.06	0.02	0.01	n.a.
	0.08	709	0.05	0.06	0.01	0.02	2.42
	0.17	695	0.12	0.04	0.07	0.03	3.03
	0.25	691	0.11	0.03	0.05	0.03	2.59
	0.5	686	0.14	0.09	0.08	0.01	3.41
	0.45	677	0.11	0.06	0.05	0.05	2.69
	1	670	0.13	0.07	0.07	0.03	2.58
	2	666	0.22	0.07	0.08	0.04	1.99
	6	645	0.28	0.03	0.12	0.03	1.72
	24	624	0.38	0.09	0.21	0.04	30.2
	96	604	0.43	0.06	0.22	0.02	2.82
	192	590	0.46	0.04	0.24	0.06	180
	384	568	0.49	0.09	0.26	0.06	216
	1464	551	0.54	0.09	0.27	0.04	203
c	0	355	-0.08	0.11	-0.04	0.06	bdl
	0.02	350	0.07	0.05	0.03	0.04	n.a.
	0.08	339	0.06	0.07	0.02	0.03	n.a.
	0.17	335	0.08	0.08	0.05	0.04	0.26
	0.25	336	0.11	0.10	0.06	0.07	0.19
	0.50	333	0.15	0.06	0.08	0.05	0.16
	0.75	325	0.17	0.02	0.07	0.07	0.14
	1	328	0.16	0.08	0.08	0.04	0.10
	2	323	0.17	0.05	0.08	0.02	0.15
	6	308	0.24	0.02	0.11	0.03	0.13
	24	293	0.36	0.07	0.21	0.05	0.19
	96	275	0.43	0.12	0.22	0.09	0.32
	192	269	0.46	0.06	0.25	0.04	3.06
	384	259	0.44	0.14	0.22	0.04	3.17
	768	254	0.53	0.1	0.25	0.06	n.a.
	1536	246	0.49	0.06	0.26	0.03	n.a.

Table 2: Experimental duration, t, Si concentrations (monomeric and polymeric), Si adsorption rate constants, k, reaction rate constants with molybdic acid, depolymerisation rates and measured and equilibrium Al concentrations during adsorption experiments of polysilic acid onto gibbsite: a = 385 mmol L^{-1} gibbsite, 651 µmol L^{-1} Si, pH 3.4; b = 385 mmol L^{-1} gibbsite, 587 µmol L^{-1} Si, pH 3.6; c = 769 mmol L^{-1} gibbsite, 249 µmol L^{-1} Si, pH 3.7; d = 385 mmol L^{-1} gibbsite, 304 µmol L^{-1} Si, pH 3.6; e = 385 mmol L^{-1} gibbsite, 618 µmol L^{-1} Si, pH 3.8; f = 192 mmol L^{-1} gibbsite, 653 µmol L^{-1} Si, pH 3.1; g = 128 mmol L^{-1} gibbsite, 655 µmol L^{-1} Si, pH 3.6

	t	Si	k	$Si_{Polymeric}$	$K_{Polymeric}$	$Si_{Monomeric}$	$K_{Monomeric}$	$r_{Depolymerisation}$	Al	Al_{eq}
	h	µmol L^{-1}	h^{-1}	µmol L^{-1}	min^{-1}	µmol L-1	min^{-1}	h^{-1}	µmol L^{-1}	µmol L^{-1}
	0.00	651		625	0.030	0.03	1.60		3.30	136
	0.01	579	22	542	0.026	0.03	3.36	2.76	33.3	
	0.13	543	0.84	503	0.024	0.04	1.81	0.08	38.9	
	0.27	468	2.0						38.5	
	0.38	439	1.1	403	0.027	0.04	4.86	0.04	37.4	
	0.52	500	-1.8	454	0.023	0.04	4.83	0.07	57.8	
a	0.65	468	0.92						51.1	
	0.98	414	0.73	235	0.023	0.18	10.30	0.73	82.6	
	2.33	457	-0.15	346	0.016	0.11	6.21	-0.14	87.0	
	4.32	357	0.28	281	0.021	0.07	2.16	-0.02	93.0	
	6.55	357	0.00	189	0.012	0.17	4.43	0.12	120	
	27.22	216		19.4	0.029	0.20	2.06	0.02	181	
	45.65	220		0.00		0.22	2.90	0.00	195	
	0.00	587		552	0.029	0.04	1.60		2.90	81
	0.02	550	9.3	510	0.024	0.04	3.12	0.60	14.1	
	0.04	536	4.5						5.20	
	0.08	511	5.3						6.80	
	0.11	518	-1.6						8.70	
	0.14	518	0.0						10.5	
	0.17	500	5.6	459	0.024	0.04	3.15	0.07	13.1	
	0.25	532	-2.9						14.4	
b	0.30	493	6.1						15.2	
	0.35	486	1.3						16.2	
	0.38	521	-8.9	421	0.022	0.10	6.40	0.51	202	
	0.43	514	1.1						19.6	
	0.50	464	7.1						27.0	
	0.65	496	-2.2	445	0.018	0.05	1.95	-0.34	28.8	
	1.28	404	2.6	322	0.023	0.08	3.34	0.16	48.9	
	2.72	400	0.13	267	0.012	0.13	4.39	0.09	112	
	6.25	382		251	0.014	0.13	3.04	0.00	127	
	0.00	249		142	0.033	0.11	1.50		n.a.	69
	0.02	85	230	16.0	0.035	0.07	1.60	23	n.a.	
	0.33	74		12.6	0.30	0.06	2.30	0.05	n.a.	
c	0.67	64	-2.5	0.00		0.06	1.80	0.51	n.a.	
	1.00	164		0.00		0.16	8.00		n.a.	
	2.00	93	2.0	0.00		0.09	2.60		n.a.	
	4.00	82		0.00		0.08	2.00		n.a.	

Table 3: Experimental duration, t, Si concentrations (monomeric and polymeric), Si adsorption rate constants, k, reaction rate constants with molybdic acid, depolymerisation rates and measured and equilibrium Al concentrations during adsorption experiments of polysilic acid onto gibbsite: a = 385 mmol L^{-1} gibbsite, 651 µmol L^{-1} Si, pH 3.4; b = 385 mmol L^{-1} gibbsite, 587 µmol L^{-1} Si, pH 3.6; c = 769 mmol L^{-1} gibbsite, 249 µmol L^{-1} Si, pH 3.7; d = 385 mmol L^{-1} gibbsite, 304 µmol L^{-1} Si, pH 3.6; e = 385 mmol L^{-1} gibbsite, 618 µmol L^{-1} Si, pH 3.8; f = 192 mmol L^{-1} gibbsite, 653 µmol L^{-1} Si, pH 3.1; g = 128 mmol L^{-1} gibbsite, 655 µmol L^{-1} Si, pH 3.6

	t	Si	k	$Si_{Polymeric}$	$Kp_{Polymeric}$	SiMonomeric	$Kp_{Monomeric}$	$r_{Depolymerisation}$	Al	Al_{eq}
	h	µmol L^{-1}	h^{-1}	µmol L^{-1}	min^{-1}	µmol L-1	min^{-1}	h^{-1}	µmol L^{-1}	µmol L^{-1}
	0.00	304		286	0.020	0.02	2.00		n.a.	81
	0.02	39.0		30.6	0.050	0.01	6.00	9.5	n.a.	
	0.25	29.0	-0.28	0.0		0.03	5.00	0.18	n.a.	
	0.50	96.0	2.3	0.0		0.10	6.00		n.a.	
d	0.75	57.0	-1.5	0.0		0.06	5.00		n.a.	
	1.00	132	3.6						n.a.	
	2.00	161	0.83						14	
	4.00	193							72	
	6.00	184							n.a.	
	0.00	618		561	0.012	0.06	0.32		n.a.	47
	0.02	153		139	0.023	0.01	1.6	0.05	n.a.	
	0.25	46.0	-12	0.00		0.05	2.3	3.9	n.a.	
	0.50	83.0	1.4	0.00		0.08	2.3		n.a.	
e	0.75	153	5.6	0.00		0.15	3.0		n.a.	
	1.00	121	-3.5	0.00		0.12	2.4		n.a.	
	2.00	171	2.3	0.00		0.17	3.2		n.a.	
	4.00	242		0.00		0.24	6.0		n.a.	
	6.00	176		0.00		0.18	2.7		n.a.	
	0.00	653		619	0.020	0.03	4.0		n.a.	286
	0.02	121							n.a.	
	0.02	60.0		26.3	0.25	0.03	0.5	31	n.a.	
	0.25	82.0	0.93	3.60	0.20	0.08	2.8	1.7	n.a.	
f	0.50	101	0.95	5.00	0.30	0.10	3.0	-0.02	n.a.	
	0.75	125	1.6						n.a.	
	1.00	179		0.00		0.18	4.4		n.a.	
	2.33	164		0.00		0.16	2.8		n.a.	
	3	174		0.00		0.17	2.8		n.a.	
	0.00	655		608	0.009	0.03	3.0		1.50	81
	0.02	230	130	197	0.024	0.03	4.0	4.4	4.20	
	0.25	231	-0.09	193	0.020	0.04	5.0	0.15	5.50	
	0.50	200	3.4	160	0.023	0.04	4.3	0.14	32.7	
g	0.75	210	-1.4	148	0.020	0.06	7.1	0.39	10.5	
	1.00	204	0.81	151	0.020	0.05	5.5	-0.15	56.8	
	2.00	194	0.46	109	0.018	0.08	9.2	0.18	6.60	
	3.00	187	0.47	136	0.020	0.05	3.8	-0.17	7.00	
	4.00	177		115	0.023	0.06	4.4	0.08	n.a.	

Table 4: Concentration and speciation (monomeric/polymeric) of dissolved Si and the corresponding reaction constants with molybdic acid, k, for cyclic freezing experiments with pure Si solutions and for the reference sample stored at room temperature, n.a.: not analysed

	pH 3					pH 4.5				
t	Si	Si_{Mono}	k_{Mono}	Si_{Poly}	k_{Poly}	Si	Si_{Mono}	k_{Mono}	Si_{Poly}	k_{Poly}
d	mmol L^{-1}	mmol L^{-1}	min^{-1}	mmol L^{-1}	min^{-1}	mmol L^{-1}	mmol L^{-1}	min^{-1}	mmol L^{-1}	min^{-1}
0	1.69	1.69	n.a.	0.00		1.60	n.a.	n.a.	n.a.	n.a.
1						1.68	1.30	1.19	0.41	0.05
2						1.67	n.a.	n.a.	n.a.	n.a.
5						1.85	n.a.	n.a.	n.a.	n.a.
8						1.87	n.a.	n.a.	n.a.	n.a.
16						1.60	1.01	1.08	0.59	0.04
20	1.60	n.a.	n.a.	n.a.	n.a.					
30	1.47	n.a.	n.a.	n.a.	n.a.					
34						1.60	0.99	0.89	0.61	0.04
40	1.42	n.a.	n.a.	n.a.	n.a.					
50	1.42	n.a.	n.a.	n.a.	n.a.					
55	1.42	n.a.	n.a.	n.a.	n.a.					
64						1.51	0.96	0.93	0.57	0.04
80	1.34	n.a.	n.a.	n.a.	n.a.					
100	1.42	0.02	1.17	1.41	0.003					
131						1.53	0.76	1.31	0.77	0.02
Reference	1.67	1.67	1.39	0.00						

	pH 5					pH 7				
t	Si	Si_{Mono}	k_{Mono}	Si_{Poly}	k_{Poly}	Si	Si_{Mono}	k_{Mono}	Si_{Poly}	k_{Poly}
d	mmol L^{-1}	mmol L^{-1}	min^{-1}	mmol L^{-1}	min^{-1}	mmol L^{-1}	mmol L^{-1}	min^{-1}	mmol L^{-1}	min^{-1}
0	1.77	n.a.	n.a.	n.a.	n.a.	1.75	n.a.	n.a.	n.a.	n.a.
20	1.18	n.a.	n.a.	n.a.	n.a.	1.46	n.a.	n.a.	n.a.	n.a.
40	0.50	n.a.	n.a.	n.a.	n.a.	0.99	n.a.	n.a.	n.a.	n.a.
55	0.65	n.a.	n.a.	n.a.	n.a.	1.05	n.a.	n.a.	n.a.	n.a.
80	0.73	n.a.	n.a.	n.a.	n.a.	1.30	n.a.	n.a.	n.a.	n.a.
100	0.19	0.19	n.a.	0.00	n.a.	1.28	1.28	n.a.	0.00	n.a.
Reference	1.70	n.a.	n.a.	n.a.	n.a.	1.67	n.a.	n.a.	n.a.	n.a.

	pH 9					pH 11				
t	Si	Si_{Mono}	k_{Mono}	Si_{Poly}	k_{Poly}	Si	Si_{Mono}	k_{Mono}	Si_{Poly}	k_{Poly}
d	mmol L^{-1}	mmol L^{-1}	min^{-1}	mmol L^{-1}	min^{-1}	mmol L^{-1}	mmol L^{-1}	min^{-1}	mmol L^{-1}	min^{-1}
0	1.79	n.a.	n.a.	n.a.	n.a.	1.72	n.a.	n.a.	n.a.	n.a.
20	1.59	n.a.	n.a.	n.a.	n.a.	1.69	n.a.	n.a.	n.a.	n.a.
30						1.64	n.a.	n.a.	n.a.	n.a.
40	1.52	n.a.	n.a.	n.a.	n.a.	1.70	n.a.	n.a.	n.a.	n.a.
55	1.36	n.a.	n.a.	n.a.	n.a.	1.63	n.a.	n.a.	n.a.	n.a.
80	1.64	n.a.	n.a.	n.a.	n.a.	1.72	n.a.	n.a.	n.a.	n.a.
100	0.76	0.76	n.a.	0.00	n.a.	1.67	1.67	n.a.	0.00	n.a.
Reference	1.66	n.a.	n.a.	n.a.	n.a.	1.70	n.a.	n.a.	n.a.	n.a.

Table 5: Concentration and speciation (monomeric/polymeric) of dissolved Si and the corresponding reaction constants with molybdic acid, k, isotopic composition ($\delta^{30}Si$) and concentrations of dissolved Al for cyclic freezing experiments with Si solutions containing 0.1 mmol L^{-1} Al and for the reference sample stored at room temperature. Italic numbers indicate that data were obtained by UV-Vis spectroscopy instead of ICP-OES. n.a.: not analysed

				pH 3		
t	Si	Si_{Mono}	k_{Mono}	Si_{Poly}	k_{Poly}	Al
d	mmol L^{-1}	mmol L^{-1}	min^{-1}	mmol L^{-1}	min^{-1}	mmol L^{-1}
0	1.73	n.a.	n.a.	n.a.	n.a.	0.11
20	1.65	n.a.	n.a.	n.a.	n.a.	0.10
30	1.57	n.a.	n.a.	n.a.	n.a.	0.09
40	1.55	n.a.	n.a.	n.a.	n.a.	0.10
50	1.48	n.a.	n.a.	n.a.	n.a.	0.09
55	1.42	n.a.	n.a.	n.a.	n.a.	0.10
80	1.44	n.a.	n.a.	n.a.	n.a.	0.10
100	1.18	0.01	0.62	1.18	0.004	0.10
Reference	1.68	n.a.	n.a.	n.a.	n.a.	0.10

					pH 4.5			
t	Si	$\delta^{30}Si_{(aq)}$	Si_{Mono}	k_{Mono}	Si_{Poly}	k_{Poly}	Al
d	mmol L^{-1}	‰	mmol L^{-1}	min^{-1}	mmol L^{-1}	min^{-1}	mmol L^{-1}
0	1.43	-0.12	n.a.	n.a.	n.a.	n.a.	0.09
1	*1.65*	0.14	1.13	1.16	0.51	0.06	0.09
2	1.42	-0.09	n.a.	n.a.	n.a.	n.a.	0.09
3	1.41	0.02	n.a.	n.a.	n.a.	n.a.	0.09
4	1.40	0.07	n.a.	n.a.	n.a.	n.a.	0.09
9	1.29	0.09	n.a.	n.a.	n.a.	n.a.	0.09
16	*0.79*	-0.03	0.60	0.94	0.19	0.05	0.09
34	*0.74*	-0.02	0.41	0.89	0.33	0.02	0.10
64	*0.36*	n.a.	0.30	0.98	0.06	0.10	0.09
131	*0.35*	n.a.	0.28	1.48	0.07	0.05	0.07
Reference	1.85	n.a.	n.a.	n.a.	n.a.	n.a.	0.08

	pH 5		pH 7			pH 9		pH 11	
t	Si	Al	Si	$\delta^{30}Si_{(aq)}$	Al	Si	Al	Si	Al
d	mmol L^{-1}	mmol L^{-1}	mmol L^{-1}	‰	mmol L^{-1}	mmol L^{-1}	mmol L^{-1}	mmol L^{-1}	mmol L^{-1}
0	1.70	0.09	1.76	0	0.10	1.76	0.10	2.02	0.21
20	1.56	0.08	0.99	-0.1	0.06	1.28	0.08	1.42	0.01
40	1.42	0.08	0.68	-0.1	0.08	1.17	0.08	1.54	0.08
55	1.46	0.02	0.18	-0.2	0.03	0.66	0.00	1.64	0.08
80	1.44	0.02	0.07	-0.2	0.02	0.61	0.01	1.57	0.02
100	1.32	0.08	0.47	0.5	0.09	0.86	0.10	1.70	0.10
Reference	1.75	0.09	1.74	n.a.	0.06	1.76	0.09	1.64	0.09

Table 6: Concentration and speciation (monomeric/polymeric) of dissolved Si and the corresponding reaction constants with molybdic acid, k, isotopic composition (δ^{30}Si) and concentrations of dissolved Al and Na for cyclic freezing experiments with Si solutions containing 1 mmol L^{-1} Al with 100 mmol L^{-1} NaCl and for the reference sample stored at room temperature. Italic numbers indicate that data were obtained by UV-Vis spectroscopy instead of ICP-OES, bold numbers indicate that data were obtained at the GFZ Potsdam by ICP-OES, * indicate an experiment with 1 L sample volume, n.a.: not analysed, bdl: below detection limit

	pH 4.5			pH 7					
t	Si	Al	Na	Si	Si_{Mono}	k_{Mono}	Si_{Poly}	k_{Poly}	Al
d	mmol L^{-1}	mmol L^{-1}	mmol L^{-1}	mmol L^{-1}	mmol L^{-1}	min^{-1}	mmol L^{-1}	min^{-1}	mmol L^{-1}
0	**1.42**	0.99	85.9	0.72/*0.58*	n.a.	n.a.	n.a.	n.a.	0.628
1	**1.42**	1.00	81.8	0.31/*0.35/0.24**	n.a.	n.a.	n.a.	n.a.	0.015
2	**1.42**	0.96	79.7	0.12/*0.24*	n.a.	n.a.	n.a.	n.a.	0.002
3	**1.40**	n.a.	n.a.	0.09	n.a.	n.a.	n.a.	n.a.	0.001
4	**1.39**	0.85	70.9	0.36/*0.38*	0.33	1.15	0.03	0.10	0.280
9	**1.29**	n.a.	n.a.	0.05	n.a.	n.a.	n.a.	n.a.	bdl
16	**1.36**	n.a.	n.a.	0.05/*0.30*	n.a.	n.a.	n.a.	n.a.	0.030
32	**1.35**	n.a.	n.a.	0.03	0.03	3.43	0.00	0.02	0.093
64	*0.77*	n.a.	n.a.	0.02/*0.11*	n.a.	n.a.	n.a.	n.a.	bdl
128	**0.33**	n.a.	n.a.	*0.13*	n.a.	n.a.	n.a.	n.a.	bdl
196	*0.88*	n.a.	n.a.						
264	*0.52*	n.a.	n.a.						
Reference	*1.57*	n.a.	n.a.	0.72	n.a.	n.a.	n.a.	n.a.	0.006

Table 7: Concentration and speciation (monomeric/polymeric) of dissolved Si and the corresponding reaction constants with molybdic acid, k, isotopic composition (δ^{30}Si) and concentrations of dissolved Al and Na for cyclic freezing experiments with Si solutions containing 1 mmol L^{-1} Al and for the reference sample stored at room temperature. Italic numbers indicate that data were obtained by UV-Vis spectroscopy instead of ICP-OES, bold numbers indicate that data were obtained at the GFZ Potsdam by ICP-OES, * indicate an experiment with 1 L sample volumen, n.a.: not analysed

	pH 4.5				pH 7	
t	Si	δ^{30}Si(aq)	δ^{30}Si(s)	Al	Si	Al
d	mmol L^{-1}	‰	‰	mmol L^{-1}	mmol L^{-1}	mmol L^{-1}
0	**1.69/**1.16*	-0.1		0.69/0.66*	**0.72/**0.57*	n.a.
1	**1.65/**0.77*	0.1		0.17/0.32*	**0.31/***0.44**	0.01*
2	**1.08**			0.17	**0.11**	n.a.
3					**0.09/***0.22**	n.a.
4					**0.29**	n.a.
5	0.57	2.4	-3.4	0.18		
8	1.20	2.3	-3.0	0.68		
9					**0.05**	n.a.
16	0.80	2.5	-2.5	0.39	**0.05**	n.a.
32					**0.03**	n.a.
34	0.74	1.5	-1.5	0.48		n.a.
64	0.36	1.3	-0.5		**0.02**	n.a.
131	0.35/*0.40**	0.0	0.0	0.49	*0.06/0.09**	n.a.
196	*0.34*					n.a.
247	*0.54*					n.a.
264						n.a.
Reference	*1.52*/1.51*				**0.72/**0.62	n.a.

Table 8: Concentration and speciation (monomeric/polymeric) of dissolved Si and the corresponding reaction constants with molybdic acid, k, and concentrations of dissolved B for cyclic freezing experiments with Si solutions containing 0.1 mmol L^{-1} B and for the reference sample stored at room temperature.

				pH 3		
t	Si	Si_{Mono}	k_{Mono}	Si_{Poly}	k_{Poly}	B
d	mmol L^{-1}	mmol L^{-1}	min^{-1}	mmol L^{-1}	min^{-1}	mmol L^{-1}
0	1.74					0.10
20	1.66					0.10
30	1.63					0.10
41	1.58					0.10
50	1.60					0.10
55	1.50					0.10
80	1.31					0.09
100	1.45	0.02	1.12	1.44	0.003	0.10
Reference	1.67	1.67	1.44	0.00		0.10

				pH 4.5		
t	Si	Si_{Mono}	k_{Mono}	Si_{Poly}	k_{Poly}	B
d	mmol L^{-1}	mmol L^{-1}	min^{-1}	mmol L^{-1}	min^{-1}	mmol L^{-1}
0	1.65					0.11
1	1.68	1.31	1.25	0.36	0.06	0.11
2	1.74					0.11
5	1.89					0.12
8	1.84					0.12
16	1.66	1.03	1.04	0.64	0.04	0.11
34	1.61	1.00	1.04	0.61	0.04	0.10
64	1.51	0.99	1.05	0.51	0.06	0.21
131	0.56	0.09	4.38	0.48	0.001	0.37
Reference						

	pH 5		pH 7		pH 9		pH 11	
t	Si	B	Si	B	Si	B	Si	B
d	mmol L^{-1}	mmol L^{-1}	mmol L^{-1}	mmol L^{-1}	mmol L^{-1}	mmol L^{-1}	mmol L^{-1}	mmol L^{-1}
0	1.79	0.11	1.69	0.10	1.76	0.12	1.67	0.10
20	0.18	0.09	1.63	0.10	1.64	0.10	1.52	0.09
30								0.10
41	1.10	0.10	1.50	0.10	1.54	0.10	1.55	0.10
50								0.11
55	0.53	0.11	1.68	0.11	1.21	0.11	1.68	0.11
64								
80	0.24	0.10	0.84	0.10	0.90	0.11	1.79	0.11
100	0.88	0.10	1.58	0.10	1.55	0.10	1.72	0.10
Reference	1.77	0.11	1.77	0.11	1.72	0.10	1.78	0.11

Table 9: Concentration and speciation (monomeric/polymeric) of dissolved Si and the corresponding reaction constants with molybdic acid, k, and concentrations of dissolved Ge for cyclic freezing experiments with Si solutions containing 0.1 mmol L^{-1} Ge and for the reference sample stored at room temperature.

			pH 3		
t	Si	Si_{Mono}	k_{Mono}	Si_{Poly}	Ge
d	mmol L^{-1}	mmol L^{-1}	min^{-1}	mmol L^{-1}	mmol L^{-1}
0	1.76				0.09
16					0.77
20	1.47				0.08
30	1.48				0.09
34					0.79
41	1.06				0.09
50	1.29				0.10
55	1.00				0.08
80	0.67				0.09
100	0.49	0.49	1.48	0.00	0.08
Reference	1.74	1.74	1.53	0.00	0.08
			pH 4.5		
Si	Si_{Mono}	k_{Mono}	Si_{Poly}	k_{Poly}	Ge
t	mmol L^{-1}	min^{-1}	mmol L^{-1}	min^{-1}	mmol L^{-1}
d	1.53	1.81	0.00	0.02	0.12
0	0.26	3.73	0.01	0.00	0.11
1					0.12
2					0.13
5					0.12
8	0.16	5.02	0.00	0.10	0.11
30	0.16	5.00	0.00	0.10	0.11
55	0.14	5.48	0.01	0.00	
100	0.17	7.72	0.02	0.00	

Table 10: Concentration and speciation (monomeric/polymeric) of dissolved Si and the corresponding reaction constants with molybdic acid, k, and concentrations of dissolved Al for cyclic freezing experiments with Si solutions containing 10 mmol L^{-1} kaolinite

t	Si	Si_{Mono}	k_{Mono}	Si_{Poly}	k_{Poly}	Al
d	mmol L^{-1}	mmol L^{-1}	min^{-1}	mmol L^{-1}	min^{-1}	mmol L^{-1}
1	1.65	1.65	1.65	0.00		0.01
5	1.77					0.00
8	1.87					0.22
16	1.69	1.52	1.70	0.17	0.10	0.06
34	0.62	0.35	1.96	0.27	0.00	bdl
64	0.23	0.17	2.56	0.06	0.00	0.04
131	0.06	0.06	4.05	0.00	0.10	0.00

Table 11: Chemical composition of the alkaline solution during hydrothermal alteration of diatomite at room temperature ("reference sample") for 64 d

Sample	t	Si	Al	K	pH
	d	mmol L^{-1}	mmol L^{-1}	mmol L^{-1}	
R50 = Z35	64	159			
R75	64	516	1.92	1100	
R150	64	543	1.86	892	
R100/125	64	612	5.07	895	13.9

Table 12: Chemical composition of the alkaline solution during hydrothermal alteration of diatomite in 1 M KOH containing 22 mmol L^{-1} Al at 50 °C after various durations

Sample	t	Si	Al	K
	d	mmol L^{-1}	mmol L^{-1}	mmol L^{-1}
Z0	0	0.00	22.0	n.a.
Z27	0.25	6.00	0.24	829
Z28	1	117	0.03	839
Z29	2	242	0.02	805
Z30	4	246	0.02	811
Z31	8	236	0.02	793
Z32	16	228	1.58	772
Z33	32	259	1.73	792
Z34	64	250	1.72	774

Table 13: Chemical composition of the alkaline solution during hydrothermal alteration of diatomite at in 1 M KOH containing 22 mmol L^{-1} Al 75 °C after various durations

Sample	t	Si	Al	K
	d	mmol L^{-1}	mmol L^{-1}	mmol L^{-1}
Z0II	0	0.00	22.1	685
Z18	0.25	220	5.74	672
Z19	1	223	4.19	654
Z20	2	240	2.09	692
Z21	4	236	1.71	687
Z22	8	228	0.27	672
Z23	16	248	0.25	715
Z24	32	263	0.08	744
Z25	64	238	0.41	1100

Table 14: Chemical composition of the alkaline solution during hydrothermal alteration of diatomite in 1 M KOH containing 22 mmol L^{-1} Al at 100 °C after various durations

Sample	t	Si	Al	K	pH
	d	mmol L^{-1}	mmol L^{-1}	mmol L^{-1}	
DH Z0	0	n.a.	22.0	n.a.	n.a.
DH Z1	0.25	236	5.56	857	13.4
DH Z2	1	241	3.37	823	13.5
DH Z5	2	240	1.04	850	13.5
DH Z6	5	240	0.37	818	13.6
DH Z9	8	277	2.93	895	13.4
DH Z10	16	287	2.96	947	13.5
DH Z13	32	298	2.81	979	13.7
DH Z14	64	269	2.70	855	13.8

Table 15: Chemical composition of the alkaline solution during hydrothermal alteration of diatomite in 1 M KOH containing 22 mmol L^{-1} Al at 125 °C after various durations

Sample	t	Si	Al	K	pH
	d	mmol L^{-1}	mmol L^{-1}	mmol L^{-1}	
Z0	0	0	22.0	n.a.	n.a.
Z3	0.25	235	4.15	815	13.3
Z4	1	228	1.78	847	13.5
Z7	2	279	0.48	958	13.5
Z8	4	n.a.	n.a.	n.a.	n.a.
Z11	8	276	3.05	916	13.6
Z12	16	270	2.65	891	13.5
Z15	32	259	3.14	839	13.8
Z16	64	282	2.97	918	13.8

Table 16: Chemical composition of the alkaline solution during hydrothermal alteration of diatomite in 1 M KOH containing 22 mmol L^{-1} Al at 150 °C after various durations

Sample	t	Si	Al	K
	d	mmol L^{-1}	mmol L^{-1}	mmol L^{-1}
150°C_0d	0	n.a.	n.a.	n.a.
150°C_1d	1	230	0.23	831
150°C_2d	2	249	0.45	943
150°C_5d	5	260	8.62	893
150°C_8d	8	251	0.20	910
150°C_16d	16	254	0.20	968
150°C_35d	35	253	0.18	929
150°C_64d	64	247	0.19	889

Table 17: Chemical composition of an Al-containing alkaline solution (initially 0.1 M KOH, 11 mmol L^{-1} Al) during hydrothermal alteration of diatomite at 100 °C

Sample	t	Si	Al	K	pH
	d	mmol L^{-1}	mmol L^{-1}	mmol L^{-1}	
with Al	0	0	10.9	*153*	12.9
Z 36	0.25	18	1.12	90	12.4
Z 37	1	59	0.19	89	11.4
Z 38	2	56	0.31	86	11.5
Z 39	4	55	0.33	84	11.1
Z 40	8	49	0.03	78	11.3
Z 41	16	50	0.02	79	11.5
Z 42	32	45	0.01	75	11.2
Z 43	64	n.a.	n.a.	n.a.	11.4

Table 18: Chemical composition of an Al-free alkaline solution (initially 0.1 M KOH) during hydrothermal alteration of diatomite at 100 °Cm, bdl: below detection limit

Sample	t	Si	Al	K	pH
	d	mmol L^{-1}	mmol L^{-1}	mmol L^{-1}	
without Al	0	0	bdl	n.a.	12.8
Z 45	0.25	26	bdl	86	12.5
Z 46	1	56	bdl	81	11.5
Z 47	2	51	bdl	73	11.3
Z 48	4	87	bdl	77	11.3
Z 49	6	89	bdl	140	11.3
Z 50	16	n.a.	n.a.	n.a.	11.4
Z 51	32	n.a.	n.a.	n.a.	11.4
Z 52	64	n.a.	n.a.	n.a.	n.a.

Table 19: Phase composition of unaltered diatomite and diatomite altered for various durations at 50 °C, also given are the weights of ZnO and the sample for XRD and the Rietveld quality paramters

Sample	t	ZnO	Sample	Solid phase composition (wt-%)					Rietveld quality parameters		
	d	g	g	amorphous	illite	quartz	chabazite	merlinoite	R profile	weighted R profile	Goodness of fit
Z0	0	0.011	0.089	97	2	1	0	0	4.70	7.60	5.92
Z27	0.25	0.011	0.070	93	5	2	0	0	4.09	6.12	10.1
Z28	1	0.013	0.073	95	3	2	0	0	3.38	5.18	6.36
Z29	2	0.011	0.071	95	1	4	0	0	3.63	5.57	7.18
Z30	4	0.010	0.071	88	7	5	0	0	3.76	5.77	7.73
Z31	8	0.011	0.070	90	6	4	0	0	3.26	5.09	6.21
Z32	16	0.011	0.060	87	8	5	0	0	4.09	6.64	12.3
Z33	32	0.009	0.059	83	10	7	0	0	3.15	4.70	5.69
Z34	64	0.016	0.066	65	1	2	28	4	6.29	8.95	20.1

Table 20: Phase composition of unaltered diatomite and diatomite altered for various durations in 1 M KOH containing 22 mmol L^{-1} Al at 75 °C, also given are the weights of ZnO and the sample for XRD and the Rietveld quality paramters

Sample	t	ZnO	Sample	Solid phase composition (wt-%)					Rietveld quality parameters		
	d	g	g	amorphous	illite	quartz	chabazite	merlinoite	R profile	weighted R profile	Goodness of fit
Z0II	0	0.011	0.089	97	2	1	0	0	4.70	7.60	5.92
Z18	0.25	0.069	0.012	88	8	4	0	0	4.29	7.53	6.67
Z19	1	0.059	0.010	82	13	5	0	0	3.74	5.67	3.91
Z20	2	0.060	0.010	85	12	3	0	0	3.53	5.58	3.69
Z21	4	0.059	0.009	87	6	4	3	0	3.36	4.82	2.81
Z22	8	0.062	0.010	37	5	3	25	30	5.47	7.81	7.27
Z23	16	0.060	0.010	27	8	2	14	49	6.68	9.72	11.3
Z24	32	0.060	0.015	39	4	1	10	46	5.86	8.28	8.51
Z25	64	0.061	0.016	39	0	2	14	45	6.32	8.92	9.37

Table 21: Phase composition of unaltered diatomite and diatomite altered for various durations in 1 M KOH containing 22 mmol L^{-1} Al at 100 °C, also given are the weights of ZnO and the sample for XRD and the Rietveld quality paramters and the BET surface area

Sample	t	BET	ZnO	Sample	Solid phase composition (wt-%)					Rietveld quality parameters		
	d	m^2g^{-1}	g	g	Amor-phous	illite	quartz	chabazite	merlinoite	R profile	Weighted R profile	Good-ness of fit
Z0	0	12.6	0.089	0.089	97	1	2	0	0	4.70	7.60	5.92
Z1	0.25	37.8	0.076	0.076	86	9	5	0	0	4.49	7.93	7.87
Z2	1	n.a.	0.079	0.079	86	7	7	0	0	3.38	5.12	3.79
Z5	2	n.a.	0.088	0.088	63	0	4	5	28	4.33	5.89	4.45
Z6	5	n.a.	0.067	0.067	33	0	2	4	61	6.40	9.21	10.9
Z9	8	19.9	0.087	0.087	36	0	1	1	62	6.52	9.12	10.5
Z10	16	18.3	0.070	0.070	40	0	1	4	55	5.75	8.30	8.85
Z13	32	n.a.	0.069	0.069	37	0	3	0	60	6.27	9.25	10.9
Z14	64	22.3	0.069	0.069	31	0	6	0	63	6.52	9.42	11.2

Table 22: Phase composition of unaltered diatomite and diatomite altered for various durations in 1 M KOH containing 22 mmol L^{-1} Al at 125 °C, also given are the weights of ZnO and the sample for XRD and the Rietveld quality paramters and the BET surface area, n.a.: not analysed

Sample	t	BET	ZnO	Sample	Solid phase composition (wt-%)					Rietveld quality parameters		
	d	m^2g^{-1}	g	g	Amor-phous	illite	quartz	zeolite L	merlinoite	R profile	weighted R profile	Good-ness of fit
Z0	0	12.6	0.011	0.089	97	1	2	0	0	4.70	7.60	5.92
Z3	0.25	31.0	0.015	0.071	94	1	5	0	0	3.16	4.99	3.61
Z4	1	n.a.	0.015	0.090	53	0	3	0	44	5.19	7.43	6.92
Z7	2	n.a.	0.013	0.064	51	0	1	0	48	5.91	8.58	9.35
Z8	4	n.a.	0.010	0.077	27	0	0	0	73	6.27	8.97	9.51
Z11	8	n.a.	0.010	0.098	29	0	0	11	60	5.84	8.76	10.3
Z12	16	15.0	0.020	0.070	46	0	0	1	53	6.16	8.87	9.74
Z15	32	n.a.	0.020	0.070	46	0	0	2	52	5.56	8.31	9.62
Z16	64	n.a.	0.020	0.069	50	0	0	2	48	5.74	8.32	8.49

Table 23: Phase composition of unaltered diatomite and diatomite altered for various durations in 1 M KOH containing 22 mmol L^{-1} Al at 150 °C, also given are the weights of ZnO and the sample for XRD and the Rietveld quality paramters

Sample	t	ZnO	Sample	Solid phase composition (wt-%)					Rietveld quality parameters		
	d	g	g	amorphous	illite	quartz	chabazite	merlinoite	R profile	weighted R profile	Good-ness of fit
150°C_0d	0	0.011	0.089	97	2	1	0	0	4.70	7.60	5.92
150°C_1d	1	0.006	0.051	33	0	2	0	65	7.22	11.0	14.9
150°C_2d	2	0.005	0.051	9	0	0	0	91	4.96	6.81	5.71
150°C_5d	5	0.006	0.050	0	0	0	0	100	5.43	7.44	6.81
150°C_8d	8	0.005	0.053	4	0	0	0	96	5.48	7.62	7.01
150°C_16d	16	0.018	0.090	15	0	0	0	85	6.04	8.44	8.92
150°C_35d	35	0.012	0.088	11	0	0	0	89	6.06	8.93	9.75
150°C_64d	64	0.012	0.091	0	0	0	0	100	5.81	8.28	8.32

Table 24: Chemical composition at selected analytical spots within particles of the intermediate phase (IP) derived after alteration of diatomite in 1 M KOH containing 22 mmol L^{-1} Al for 1 d

Spot	SiO_2	Al_2O_3	K_2O
	wt.-%	wt.-%	wt.-%
a	58	28	14
b	56	27	16
c	64	29	7
d	64	27	9

Table 25: Chemical composition of the reference sample (64 d in 1 M KOH containing 22 mmol L^{-1} Al at 25 °C) after 3 d reaction with the natural mine drainage solution „Bleiberg“

Ca	K	Mg	Na	Si	Cd	Fe	Pb	Sr	Zn
µmol L^{-1}	µmol L^{-1}	µmol L^{-1}	µmol L^{-1}	µmol L^{-1}	µmol L^{-1}	µmol L^{-1}	µmol L^{-1}	µmol L^{-1}	µmol L^{-1}
282	4586	255	122	165	< 0.007	0.30	< 0.014	< 0.09	0.14

Table 26: Chemical composition of a mine drainage solution (initially 1205 µmol Lol L^{-1} Ca, 18 µmol L^{-1} K, 642 µmol L^{-1} Mg, 31 µmol L^{-1} Si, 0.014 µmol L^{-1} Cd, 0.48 µmol L^{-1} Pb, 1.56 µmol L^{-1} Sr and 14 µmol L^{-1} Zn, pH 8) after various exchange times, t_{ex}, with diatomite altered in 1 M KOH containing 22 mmol L^{-1} Al at 100 °C for 1 d

Sample	t_{ex} d	Ca µmol L^{-1}	Cd µmol L^{-1}	K µmol L^{-1}	Mg µmol L^{-1}	Na µmol L^{-1}	Pb µmol L^{-1}	Si µmol L^{-1}	Sr µmol L^{-1}	Zn µmol L^{-1}
Z2	0.25	235	< 0.006	2609	664	249	< 0.048	687	0.220	0.29
Z2	1	62	< 0.006	2813	415	142	< 0.048	213	0.045	0.12
Z2	3	84	< 0.006	3171	343	184	< 0.048	296	0.070	0.19

Table 27: Chemical composition of an an aqueous solution (initially about 500 µM Cu, Pb and Zn, pH 5) after 3 d reaction with diatomite altered for various durations (0.25 d ≤ t_{syn} ≤ 64 d) at 100 °C in an alkaline solution (1 M KOH, 22 mmol L^{-1} Al), n.a.: not analysed

Sample	t_{syn} d	Cu µmol L^{-1}	Pb µmol L^{-1}	Zn µmol L^{-1}	Si µmol L^{-1}	Al µmol L^{-1}	K µmol L^{-1}
Z0	0	416.9	1067.1	484.3	n.a.	n.a.	1517
Z1	0.25	0.6	0.1	0.2	248	204	4808
Z2	1	0.4	0.1	0.2	216	99	3811
Z5	2	5.7	4.1	6.4	673	266	4783
Z6	5	7.8	bdl	122.3	172	99	3325

Table 28: Chemical composition of an an aqueous solution (initially about 500 µM Cu, Pb and Zn, pH 5) after 3 d reaction with diatomite altered for various durations (0.25 d ≤ t_{syn} ≤ 64 d) at 125 °C in an alkaline solution (1 M KOH, 22 mmol L^{-1} Al), n.a.: not analysed

Sample	t_{syn} d	Cu µmol L^{-1}	Pb µmol L^{-1}	Zn µmol L^{-1}	Si µmol L^{-1}	Al µmol L^{-1}	K µmol L^{-1}
Z0	0	417.2	1067.1	484.3	n.a.	n.a.	1517
Z3	0.25	0.8	0.5	0.8	205	103	4399
Z4	1	0.9	0.4	22.8	367	99	3913
Z7	2	3.3	2.2	6.4	649	103	5166
Z8	4	2.4	0.3	45.4	386	110	4425

Table 29: Chemical composition of an aqueous solution (initially about 500 µM Cu, Pb and Zn, pH 5) after 3 d reaction with diatomite altered for various durations (0.25 d ≤ t_{syn} ≤ 64 d) in an alkaline solution (0.1 M KOH, 11 mmol L^{-1} Al), n.a.: not analysed

Sample	t_{syn} d	Cu µmol L^{-1}	Pb µmol L^{-1}	Zn µmol L^{-1}	Si µmol L^{-1}	Al µmol L^{-1}	K µmol L^{-1}
unaltered	0	417	510	485	n.a.	n.a.	n.a.
Z 36	0.25	238	36	368	132	2.48	1241
Z 37	1	223	8	362	133	3.57	1336
Z 38	2	210	11	369	138	14.91	1421
Z 39	4	203	9	368	140	1.10	1422
Z 40	8	183	4	382	149	0.72	1519
Z 41	16	170	3	382	128	0.91	1533
Z 42	32	260	10	409	119	1.60	1285
Z 43	64	241	8	404	125	5.64	1290

Table 30: Chemical composition of an aqueous solution (initially about 500 µM Cu, Pb and Zn, pH 5) after 3 d reaction with diatomite altered for various durations (0.25 d ≤ t_{syn} ≤ 64 d) in an alkaline solution (0.1 M KOH, no Al), n.a.: not analysed

Sample	t_{syn}	Cu	Pb	Zn	Si	Al	K
	d	µmol L^{-1}	µmol L^{-1}	µmol L^{-1}	µmol L^{-1}	µmol L^{-1}	µmol L^{-1}
unaltered	0	417	510	485	n.a.	n.a.	n.a.
Z 45	0.25	331	209	429	159	19.49	525
Z 46	1	326	206	413	189	17.35	500
Z 47	2	339	205	435	146	2.35	548
Z 48	4	288	144	418	182	0.83	729
Z 49	6	292	164	428	156	1.17	743
Z 50	16	309	188	444	161	0.40	733
Z 51	32	315	237	447	155	1.16	592
Z 52	64	311	318	431	177	3.27	497

Table 31: Chemical composition of an aqueous solution (initially 379 µmol L^{-1} Sr and 365 µmol L^{-1} Cs, pH 7) after 3 d reaction with diatomite altered for various durations (0.25 d ≤ t_{syn} ≤ 64 d) in an alkaline solution (1 M KOH, 22 mmol L^{-1} Al), n.a.: not analysed

Sample	t_{syn}	Sr	Cs	K
	d	µmol L^{-1}	µmol L^{-1}	µmol L^{-1}
Z0II	0	360	363	34.1
Z18	0.25	36	96	n.a.
Z19	1	21	52	2460
Z20	2	12	31	1650
Z21	4	10	41	1860
Z22	8	65	10	2780
Z23	16	1	5	3430
Z24	32	2	5	2230
Z25	64	2	58	2370

Table 32: Chemical composition of a mine drainage solution (initially 1205 µmol L^{-1} Ca, 18 µmol L^{-1} K, 642 µmol L^{-1} Mg, 31 µmol L^{-1} Si, 0.014 µmol L^{-1} Cd, 0.48 µmol L^{-1} Pb, 1.56 µmol L^{-1} Sr and 14 µmol L^{-1} Zn, pH 8) after 3 d reaction with diatomite altered for various durations (0.25 d ≤ t_{syn} ≤ 64 d) in an alkaline solution (0.1 M KOH, 11 mmol L^{-1} Al)

Sample	t_{syn}	Ca	K	Mg	Si	Cd	Pb	Sr	Zn
	d	µmol L^{-1}	µmol L^{-1}	µmol L^{-1}	µmol L^{-1}	µmol L^{-1}	µmol L^{-1}	µmol L^{-1}	µmol L^{-1}
unaltered	0	1406	92	742	129	0.009	0.029	< 0.009	7.67
Z 36	0.25	779	848	515	100	0.001	0.192	0.49	0.14
Z 37	1	612	930	475	241	0.001	0.055	0.40	0.34
Z 38	2	616	874	492	198	0.001	0.112	0.36	0.19
Z 39	4	628	894	491	236	0.002	0.013	0.42	0.09
Z 40	8	601	924	467	279	0.002	0.036	0.47	0.33
Z 41	16	597	1008	495	318	0.002	0.049	0.53	0.35
Z 42	32	659	696	504	230	0.002	0.018	0.46	0.17
Z 43	64	676	812	481	263	0.002	0.218	0.46	0.36

Table 33: Chemical composition of a mine drainage solution (initially 1205 µmol L^{-1} Ca, 18 µmol L^{-1} K, 642 µmol L^{-1} Mg, 31 µmol L^{-1} Si, 153 µmol L^{-1} Na, 0.014 µmol L^{-1} Cd, 0.48 µmol L^{-1} Pb, 1.56 µmol L^{-1} Sr and 14 µmol L^{-1} Zn, pH 8) after 3 d reaction with diatomite altered for various durations (0.25 d ≤ t_{syn} ≤ 64 d) in an alkaline solution (1 M KOH, 22 mmol L^{-1} Al) at 75 °C

Sample	t_{syn}	Ca	K	Mg	Na	Si	Cd	Fe	Pb	Zn
	d	µmol L^{-1}	µmol L^{-1}	µmol L^{-1}	µmol L^{-1}	µmol L^{-1}	µmol L^{-1}	µmol L^{-1}	µmol L^{-1}	µmol L^{-1}
Z0II	0	1409	92	751	216	129	0.0086	0.18	0.029	7.67
Z18	0.25	386	3321	375	149	266	< 0.0006	0.29	0.020	0.25
Z19	1	388	2968	467	112	238	< 0.0006	0.26	0.022	0.15
Z20	2	486	2926	472	105	197	< 0.0006	0.24	< 0.014	0.16
Z21	4	391	2892	463	100	197	< 0.0006	0.26	0.016	0.15
Z22	8	484	3780	504	119	356	< 0.0006	0.71	0.017	0.19
Z23	16	405	4035	502	116	387	< 0.0006	0.33	0.021	0.12
Z24	32	486	2864	512	129	297	< 0.0006	2.20	0.026	0.33
Z25	64	506	2809	509	101	253	< 0.0006	0.23	0.018	0.16

Table 34: Chemical composition of a mine drainage solution (initially 1205 µmol L^{-1} Ca, 18 µmol L^{-1} K, 642 µmol L^{-1} Mg, 31 µmol L^{-1} Si, 0.014 µmol L^{-1} Cd, 0.48 µmol L^{-1} Pb, 1.56 µmol L^{-1} Sr and 14 µmol L^{-1} Zn, pH 8) after 3 d reaction with diatomite altered for various durations (0.25 d ≤ t_{syn} ≤ 64 d) in an alkaline solution (0.1 M KOH, no Al) at 100 °C

Sample	t_{syn}	Ca	K	Mg	Si	Cd	Pb	Sr	Zn
	d	µmol L^{-1}	µmol L^{-1}	µmol L^{-1}	µmol L^{-1}	µmol L^{-1}	µmol L^{-1}	µmol L^{-1}	µmol L^{-1}
unaltered	0	1406	92	742	129	0.0090	0.029	< 0.009	7.67
Z 45	0.25	784	413	531	177	0.0006	0.012	1.31	0.08
Z 46	1	811	318	533	174	0.0007	0.007	1.28	0.08
Z 47	2	775	326	524	201	0.0007	0.005	1.11	0.07
Z 48	4	724	419	495	217	0.0008	0.029	0.96	0.09
Z 49	6	703	481	520	214	0.0007	0.018	1.01	0.10
Z 50	16	732	479	527	212	0.0004	0.013	1.05	0.06
Z 51	32	740	400	519	209	0.0005	0.013	1.09	0.08
Z 52	64	800	298	508	237	0.0005	0.028	1.27	0.14

References

[1] B. Mason, C. Moore, Grundzüge der Geochemie, Ferdinand Enke Verlag, Stuttgart, 1985.
[2] A. Alexandre, J.-D. Meunier, F. Colin, J.-M. Koud, Plant impact on the biogeochemical cycle of silicon and related weathering processes, Geochimica et Cosmochimica Acta, 61 (1997) 677-682.
[3] G.W. Morey, R.O. Fournier, J.J. Rowe, The solubility of quartz in water in the temperature interval from 25°C to 300° C, Geochimica et Cosmochimica Acta, 26 (1962) 1029-1043.
[4] G. Okamoto, T. Okura, K. Goto, Properties of silica in water, Geochimica et Cosmochimica Acta, 12 (1957) 123-132.
[5] R.K. Iler, The Chemistry of Silica, John Wiley & Sons, 1979.
[6] R.K. Iler, Effect of adsorbed alumina on the solubility of amorphous silica in water, Journal of Colloid And Interface Science, 43 (1973) 399-408.
[7] M. Dietzel, E. Usdowski, Depolymerization of soluble silicate in dilute aqueous solutions, Colloid and Polymer Science, 273 (1995) 590-597.
[8] M. Dietzel, Depolymerisation von hochpolymerer Kieselsäure in wässriger Lösung (Dissertation), Georg-August-Universität Göttingen, 1993.
[9] H.-J. Rösler, Lehrbuch der Mineralogie, Deutscher Verlag für Grundstoffindustrie, Leipzig, 1991.
[10] D.L. Parkhurst, C.A.J. Apello, User's guide to PHREEQC, U.S. Geological Survey, 1999.
[11] A. Möller, Bildung und Stabilität von hochpolymeren Al-Si-Komplexen und –Kolloiden (Diplomarbeit), Georg-August-Universität Göttingen, 2002.
[12] D.E. White, W.W. Brannock, K.J. Murata, Silica in hot-spring waters, Geochimica et Cosmochimica Acta, 10 (1956) 27-59.
[13] B.F. Jones, S.L. Rettig, H.P. Eugster, Silica in Alkaline Brines, in, 1967, pp. 1310-1314.
[14] M. Dietzel, Interaction of polysilicic and monosilicic acid with mineral surfaces, in: I. Stober, K. Bucher (Eds.) Water-Rock Interaction, Kluwer Academic Publishers, 2002, pp. 207 - 235.
[15] I. Grenthe, J. Fuger, R.J. Lemire, J.F. Muller, C.N.-T. Cregu, H. Wanner, Chemical Thermodynamics of Uranium, Berichte der Bunsengesellschaft für physikalische Chemie, 96 (1992) 1326-1326.
[16] M. Dietzel, Dissolution of silicates and the stability of polysilicic acid, Geochimica et Cosmochimica Acta, 64 (2000) 3275-3281.
[17] H. Wonisch, F. Gérard, M. Dietzel, J. Jaffrain, O. Nestroy, J.P. Boudot, Occurrence of polymerized silicic acid and aluminum species in two forest soil solutions with different acidity, Geoderma, 144 (2008) 435-445.
[18] ISO, ISO11357-2: Plastics - Differential scanning calorimetry (DSC) - Part 2: Determination of glass transition temperature 1999.
[19] C.C. Perry, Silification: The Processes by Which Organisms Capture and Mineralize Silica, Reviews in Mineralogy & Geochemistry, 54 (2003) 291 - 327.
[20] J. Martínez-Martínez, D. Benavente, M. Gomez-Heras, L. Marco-Castaño, M.Á. García-del-Cura, Non-linear decay of building stones during freeze-thaw weathering processes, Construction and Building Materials, 38 (2013) 443-454.
[21] K. Grant, G.D. Aitchison, The engineering significance of silcretes and ferricretes in Australia, Engineering Geology, 4 (1970) 93-120.
[22] M. Dietzel, Impact of cyclic freezing on precipitation of silica in Me-SiO_2-H_2O systems and geochemical implications for cryosoils and -sediments, Chemical Geology, 216 (2005) 79-88.

[23] J. Götze, W. Schrön, R. Möckel, K. Heide, The role of fluids in the formation of agates, Chemie der Erde - Geochemistry, 72 (2012) 283-286.
[24] K.O. Konhauser, D.K. Newman, A. Kappler, The potential significance of microbial Fe(III) reduction during deposition of Precambrian banded iron formations, Geobiology, 3 (2005) 167-177.
[25] J.P.S. Smol, Eugene F., The Diatoms: Applications for the Environmental and Earth Sciences, Cambridge University Press, 2010.
[26] B. Pewkliang, A. Pring, J. Brugger, The formation of precious opal: Clues from the opalization of bone, Canadian Mineralogist, 46 (2008) 139-149.
[27] W. Friedrich, P. Knipping, M. Laue, Interferenzerscheinungen bei Röntgenstrahlen, Annalen der Physik, 346 (1913) 971-988.
[28] O.W.G. Flörke, H.; Martin, B.; Röller, K.; Wirth, R., Nomenclature of Micro- and Non-Crystalline Silica Minerals, Based on Structure and Microstructure, Neues Jahrbuch Miner. Abh., 163 (1991) 19 - 42.
[29] G. Heide, Zur Systematik nichtkristalliner Materialien, Dr. habil., Technischen Universität Clausthal, 2002.
[30] J.B. Jones, E.R. Segnit, The nature of opal I. nomenclature and constituent phases, Journal of the Geological Society of Australia, 18 (1971) 57-68.
[31] F.E. Wagstaff, Crystallization and Melting Kinetics of Cristobalite, Journal of the American Ceramic Society, 52 (1969) 650-654.
[32] P. Richet, Y. Bottinga, Glass transitions and thermodynamic properties of amorphous SiO_2, $NaAlSi_nO_{2n+2}$ and $KAlSi_3O_8$, Geochimica et Cosmochimica Acta, 48 (1984) 453-470.
[33] A.M. Ilieva, Boriana; Tsintsov; Zdravko; Petrov, Ognyan, Structural State of Microcrystalline Opals: A Raman Spectroscopic Study, American Mineralogist, 92 (2007) 1325 - 1333.
[34] O. Ragueneau, P. Tréguer, A. Leynaert, R.F. Anderson, M.A. Brzezinski, D.J. DeMaster, R.C. Dugdale, J. Dymond, G. Fischer, R. François, C. Heinze, E. Maier-Reimer, V. Martin-Jézéquel, D.M. Nelson, B. Quéguiner, A review of the Si cycle in the modern ocean: recent progress and missing gaps in the application of biogenic opal as a paleoproductivity proxy, Global and Planetary Change, 26 (2000) 317-365.
[35] C.L. De La Rocha, M.A. Brzezinski, M.J. Deniro, A first look at the distribution of the stable isotopes of silicon in natural waters, Geochimica et Cosmochimica Acta, 64 (2000) 2467-2477.
[36] J.A. Webb, B.L. Finlayson, Allophane and opal speleothems from granite caves in south-east Queensland, Australian Journal of Earth Sciences, 31 (1984) 341-349.
[37] M.A. Wilson, R. Burt, T.M. Sobecki, R.J. Engel, K. Hipple, Soil properties and genesis of pans in till-derived Andisols, Olympic Peninsula, Washington, Soil Science Society of America Journal, 60 (1996) 206-218.
[38] K. Jasmund, G. Lagaly, Tone und Tonminerale, Dietrich Steinkopff Verlag GmbH & Co. KG, Darmstadt, 1993.
[39] N. Wells, C.W. Childs, C.J. Downes, Silica Springs, Tongariro National Park, New Zealand-analyses of the spring water and characterisation of the alumino-silicate deposit, Geochimica et Cosmochimica Acta, 41 (1977) 1497-1499,1501-1506.
[40] K.P. Kitsopoulos, The genesis of a mordenite deposit by hydrothermal alteration of pyroclastics on Polyegos Island, Greece, Clays and Clay Minerals, 45 (1997) 632-648.
[41] C. Jeans, The Neoformation of Clay Minerals in Brackish and Marine Environments, Clay Minerals, 9 (1971) 209 - 217.
[42] E. Kohler, H. Köster, Zur Mineralogie, Kristallchemie und Geochemie kretazischer Glaukonite, Clay Minerals, 11 (1976) 273 - 302.
[43] J. Götze, W. Zimmerle, Quartz and silica as guide to provenance in sediments and sedimentary rocks, in: T. Aigner, T. Cross, V.P. Wright (Eds.) Contributions to Sedimentary

Geology, E. Schweizerbart´sche Verlagsbuchhandlung (Nägele u. Obermiller), Tübingen, Golden, Cardiff, 2000, pp. 91.
[44] C.I. Steefel, P. Van Capellen, K.L. Nagy, A.C. Lasaga, Modeling water-rock interaction in the surficial environment: The role of precursors, nucleation, and Ostwald ripening, Chemical Geology, 84 (1990) 322-325.
[45] E. Verraedt, G. van den Mooter, J.A. Martens, Novel amorphous microporous silica spheres for controlled release applications, Journal of Pharmaceutical Sciences, 100 (2011) 4295-4301.
[46] L. Kutik, Structure and Properties of Amorphous Silica Gel in Coatings Applications, Journal of Coatings Technology, 58 (1986) 91-95.
[47] A.K. Sinevich, Application of synthetic amorphous silica for making silicate glasses, Glass and Ceramics, 44 (1987) 78-79.
[48] Y. Jin, A. Li, S.G. Hazelton, S. Liang, C.L. John, P.D. Selid, D.T. Pierce, J.X. Zhao, Amorphous silica nanohybrids: Synthesis, properties and applications, Coordination Chemistry Reviews, 253 (2009) 2998-3014.
[49] R. Collino, J. Therasse, P. Binder, F. Chaput, J.P. Boilot, Y. Levy, Thin films of functionalized amorphous silica for immunosensors application - Code: GP3, Journal of Sol-Gel Science and Technology, 2 (1994) 823-826.
[50] V. Moulin, D. Stammosf, G. Ouzounian, Actinide sorption at oxide-water interfaces. Application to α-alumina and amorphous silica, Applied Geochemistry, (1992) 163-166.
[51] J.V. Smith, Atmospheric weathering and silica-coated feldspar: Analogy with zeolite molecular sieves, granite weathering, soil formation, ornamental slabs, and ceramics, Proceedings of the National Academy of Sciences of the United States of America, 95 (1998) 3366-3369.
[52] C. Rizzo, A. Carati, C. Barabino, C. Perego, G. Bellussi, Silica-aluminas: Sol-gel synthesis and characterization, in: Studies in Surface Science and Catalysis, 2001, pp. 401-411.
[53] N. Yao, G. Xiong, M. He, S. Sheng, W. Yang, X. Bao, A novel method to synthesize amorphous silica-alumina materials with mesoporous distribution without using templates and pore-regulating agents, Chemistry of Materials, 14 (2002) 122-129.
[54] J. Hoefs, Stable Isotope Geochemistry, 3 ed., Springer-Verlag, New York, Berlin, Heidelberg, 1987.
[55] G. Faure, T.M. Mensing, Isotopes. Principles and Applications., John Wiley & Sons, Inc., Hoboken, New Jersey, USA, 2005.
[56] J. Bigeleisen, M. Wolfsberg, Theoretical and Experimental Aspects of Isotope Effects in Chemical Kinetics, in: Advances in Chemical Physics, John Wiley & Sons, Inc., 2007, pp. 15-76.
[57] Rosman, R. K. J, Taylor, P. P. D, Isotopic Compositions of the Elements 1997, Pure and applied chemistry, Research Triangle Park, NC, USA, 1998.
[58] S. Valkiers, K. Ruße, P. Taylor, T. Ding, M. Inkret, Silicon isotope amount ratios and molar masses for two silicon isotope reference materials: IRMM-018a and NBS28, International Journal of Mass Spectrometry, 242 (2005) 321-323.
[59] J. Chmeleff, I. Horn, G. Steinhoefel, F. von Blanckenburg, In situ determination of precise stable Si isotope ratios by UV-femtosecond laser ablation high-resolution multi-collector ICP-MS, Chemical Geology, 249 (2008) 155-166.
[60] C.B. Douthitt, The geochemistry of the stable isotopes of silicon, Geochimica et Cosmochimica Acta, 46 (1982) 1449-1458.
[61] I. Basile-Doelsch, Si stable isotopes in the Earth's surface: A review, Journal of Geochemical Exploration, 88 (2006) 252-256.

[62] C.L. de la Rocha, M.A. Brzezinski, M.J. DeNiro, Fractionation of silicon isotopes by marine diatoms during biogenic silica formation, Geochimica et Cosmochimica Acta, 61 (1997) 5051-5056.
[63] C.P. Beucher, M.A. Brzezinski, J.L. Jones, Sources and Biological Fractionation of Silicon Isotopes in the Eastern Equatorial Pacific, Geochimica et Cosmochimica Acta, 72 (2008) 3063-3073.
[64] M.J. Goldstein, Kinetic isotope effects and organic reaction mechanisms, Science, 154 (1966) 1616-1621.
[65] L. Rayleigh, L. Theoretical considerations respecting the separation of gases by diffusion and similar processes, Philosophical Magazine Series 5, 42 (1896) 493-498.
[66] G. Sposito, The Surface Chemistry of Natural Particles, Oxford University Press, New York, 2004.
[67] H. Harder, Illite mineral synthesis at surface temperatures, Chemical Geology, 14 (1974) 241-253.
[68] L. Guo, J. Guo, F. Li, Physicochemical processes of silicates in the estuarine region: (V). A simulation experiment on the formation of authigenic silicate minerals by adsorption, Acta Oceanologica Sinica, 5 (1986) 70-75, 148.
[69] W. Li, W. Xu, J.B. Parise, B.L. Phillips, Formation of hydroxylapatite from co-sorption of phosphate and calcium by boehmite, Geochimica et Cosmochimica Acta, 85 (2012) 289-301.
[70] R.M. Cornell, Effect of simple sugars on the alkaline transformation of ferrihydrite into goethite and hematite, Clays and Clay Minerals, 33 (1985) 219-227.
[71] K. Sakurai, P.M. Huang, Intercalation of hydroxy-aluminosilicate and hydroxy-aluminum in montmorillonite and resultant physicochemical properties, Soil Science Society of America Journal, 62 (1998) 362-368.
[72] Y.G. Frolov, E.K. Dragalova, V.V. Nazarov, Adsorption Modification of Colloidal Silica by Aluminium Oxide, Colloid Journal of the USSR (English Translation of Kolloidnyi Zhurnal), 44 (1982) 545-548.
[73] C.P. Huang, The removal of aqueous silica from dilute aqueous solution, Earth and Planetary Science Letters, 27 (1975) 265-274.
[74] T. Yokoyama, O. Nakamura, T. Tarutani, Polymerization of Silicic Acid Adsorbed on Aluminium Hydroxide, Bull. Chem. Soc. Jpn., 55 (1982) 975-978.
[75] T. Yokoyama, A. Ueda, K. Kato, K. Mogi, S. Matsuo, A study of the alumina-silica gel adsorbent for the removal of silicic acid from geothermal water: Increase in adsorption capacity of the adsorbent due to formation of amorphous aluminosilicate by adsorption of silicic acid, Journal of Colloid and Interface Science, 252 (2002) 1-5.
[76] M. Dietzel, G. Böhme, Adsorption and stability of polymeric silica, Chemie der Erde - Geochemistry, 57 (1997) 189-203.
[77] H. Harder, W. Flehmig, Quarzsynthese bei tiefen Temperaturen, Geochimica et Cosmochimica Acta, 34 (1970) 295-305.
[78] S. Delstanche, S. Opfergelt, D. Cardinal, F. Elsass, L. André, B. Delvaux, Silicon isotopic fractionation during adsorption of aqueous monosilicic acid onto iron oxide, Geochimica et Cosmochimica Acta, 73 (2009) 923-934.
[79] S. Opfergelt, G. de Bournonville, D. Cardinal, L. André, S. Delstanche, B. Delvaux, Impact of soil weathering degree on silicon isotopic fractionation during adsorption onto iron oxides in basaltic ash soils, Cameroon, Geochimica et Cosmochimica Acta, 73 (2009) 7226-7240.
[80] W.B. Jepson, D.G. Jeffs, A.P. Ferris, The adsorption of silica on gibbsite and its relevance to the kaolinite surface, Journal of Colloid And Interface Science, 55 (1976) 454-461.

[81] J.P. Gustafsson, Modelling competitive anion adsorption on oxide minerals and an allophane-containing soil, European Journal of Soil Science, 52 (2001) 639-653.
[82] F.S. Grant, The geological significance of variations in the abundances of the isotopes of silicon in rocks, Geochimica et Cosmochimica Acta, 5 (1954) 225-242.
[83] C.L. De La Rocha, M.A. Brzezinski, M.J. DeNiro, A. Shemesh, Silicon-isotope composition of diatoms as an indicator of past oceanic change, Nature, 395 (1998) 680-683.
[84] B.C. Reynolds, M. Frank, A.N. Halliday, Silicon isotope fractionation during nutrient utilization in the North Pacific, Earth and Planetary Science Letters, 244 (2006) 431-443.
[85] F. Robert, M. Chaussidon, A palaeotemperature curve for the Precambrian oceans based on silicon isotopes in cherts, Nature, 443 (2006) 969-972.
[86] I. Basile-Doelsch, J.D. Meunier, C. Parron, Another continental pool in the terrestrial silicon cycle, Nature, 433 (2005) 399-402.
[87] K. Ziegler, O.A. Chadwick, M.A. Brzezinski, E.F. Kelly, Natural variations of $\delta^{30}Si$ ratios during progressive basalt weathering, Hawaiian Islands, Geochimica et Cosmochimica Acta, 69 (2005) 4597-4610.
[88] R.B. Georg, B.C. Reynolds, M. Frank, A.N. Halliday, Mechanisms controlling the silicon isotopic compositions of river waters, Earth and Planetary Science Letters, 249 (2006) 290-306.
[89] M. Oelze, F. Von Blanckenburg, D. Höllen, M. Dietzel, J. Bouchez, The competition between kinetic and equilibrium Si stable isotope fraction II: Silica adsorption and implications for weathering systems, Geochimica et Cosmochimica Acta, (submitted).
[90] I. Gunnarsson, S. Arnórsson, Amorphous silica solubility and the thermodynamic properties of H_4SiO_4 in the range of 0 ° to 350 °C at Psat, Geochimica et Cosmochimica Acta, 64 (2000) 2295-2307.
[91] S. Brunauer, P.H. Emmett, E. Teller, Adsorption of Gases in Multimolecular Layers, Journal of the American Chemical Society, 60 (1938) 309-319.
[92] M. Oelze, F. von Blanckenburg, D. Höllen, M. Dietzel, J. Bouchez, The competition between kinetic and equilibrium Si stable fractionation I: Silica precipitation by cyclic Si and Al removal, Geochimica et Cosmochimica Acta, (submitted).
[93] D.J. DePaolo, Surface kinetic model for isotopic and trace element fractionation during precipitation of calcite from aqueous solutions, Geochimica et Cosmochimica Acta, 75 (2011) 1039-1056.
[94] M. Dietzel, G. Böhme, The dissolution rates of gibbsite in the presence of chloride, nitrate, silica, sulfate, and citrate in open and closed systems at 20°C, Geochimica et Cosmochimica Acta, 69 (2005) 1199-1211.
[95] W. Stumm, Chemistry of the Solid-Water Interface, John Wiley & Sons, 1992.
[96] Y.S.R. Chen, J.N. Butler, W. Stumm, Kinetic study of phosphate reaction with aluminum oxide and kaolinite, Environmental Science & Technology, 7 (1973) 327-332.
[97] L.M. Anovitz, E.S. Grew, Mineralogy, Petrology and Geochemistry of Boron: An Introduction, in: L.M. Anovitz, E.S. Grew (Eds.) Boron. Mineralogy, Petrology and Geochemistry. , Mineralogical Society of America, Washington D.C., 1996.
[98] E.S. Grew, Borosilicates (exclusive of tourmaline) and Boron in Rock-forming Minerals in Metamorphic Environments, in: E.S. Grew, L.M. Anovitz (Eds.) Boron. Mineralogy, Petrology and Geochemistry, Reviews in Mineralogy, Washington D.C., 1996.
[99] M.R. Palmer, G.H. Swihart, Boron Isotope Geochemistry: An Overview, in: E.S. Grew, L.M. Anovitz (Eds.) Boron: Mineralogy, Petrology and Geochemistry, Mineralogical Society of America, Washington, D.C., 1996.
[100] T. Ishikawa, E. Nakamura, Boron isotope systematics of marine sediments, Earth and Planetary Science Letters, 117 (1993) 567-580.

[101] J. Casanova, P. Négrel, R. Blomqvist, P. Wikberg, Boron Isotope Fractionation in Groundwaters as an Indicator of Permafrost Past Conditions in the Fractured Crystalline Bedrock of the Fennoscandian Shield, in: Goldschmidt, Oxford, 2000.
[102] J. Casanova, P. Négrel, R. Blomqvist, Boron isotope fractionation in groundwaters as an indicator of past permafrost conditions in the fractured crystalline bedrock of the fennoscandian shield, Water Research, 39 (2005) 362-370.
[103] S.V. Eaton, Effects of Boron Deficiency and Excess on Plants, Plant Physiol., 15 (1940) 95–107.
[104] A. Rummukainen, R. Julkunen-Tiitto, M. Räisänen, T. Lehto, Phenolic compounds in Norway spruce as affected by boron nutrition at the end of the growing season, Plant and Soil, 292 (2007) 13-23.
[105] M. Calvo Polanco, J. Zwiazek, M. Jones, M. MacKinnon, Responses of mycorrhizal jack pine (*Pinus banksiana*) seedlings to NaCl and boron, Trees - Structure and Function, 22 (2008) 825-834.
[106] L.R. Bernstein, Germanium geochemistry and mineralogy, Geochimica et Cosmochimica Acta, 49 (1985) 2409-2422.
[107] H.J. Blankenburg, W. Schron, Zum spurenelementchemismus der Vulkanitachate, Chemie der Erde - Geochemistry, 41 (1982) 121-135.
[108] J. Götze, M. Plötze, M. Tichomirowa, H. Fuchs, J. Pilot, Aluminium in quartz as an indicator of the temperature of formation of agate, Mineralogical Magazine, 65 (2001) 407-413.
[109] B. Shen, C.T.A. Lee, S. Xiao, Germanium/silica ratios in diagenetic chert nodules from the Ediacaran Doushantuo Formation, South China, Chemical Geology, 280 (2011) 323-335.
[110] S.W. Blecker, S.L. King, L.A. Derry, O.A. Chadwick, J.A. Ippolito, E.F. Kelly, The ratio of germanium to silicon in plant phytoliths: Quantification of biological discrimination under controlled experimental conditions, Biogeochemistry, 86 (2007) 189-199.
[111] E. Rosenberg, Germanium: Environmental occurrence, importance and speciation, Reviews in Environmental Science and Biotechnology, 8 (2009) 29-57.
[112] A. Lottermoser, Über das Ausfrieren von Hydrosolen, Berichte der deutschen chemischen Gesellschaft, 41 (1908) 3976-3979.
[113] W. Li, K. Lu, J.Y. Walz, Formation, structure and properties of freeze-cast kaolinite-silica nanocomposites, Journal of the American Ceramic Society, 94 (2011) 1256-1264.
[114] M.J. Leng, G.E.A. Swann, M.J. Hodson, J.J. Tyler, S.V. Patwardhan, H.J. Sloane, The potential use of silicon isotope composition of biogenic silica as a proxy for environmental change, Silicon, 1 (2009) 65-77.
[115] E. Engström, I. Rodushkin, B. Öhlander, J. Ingri, D.C. Baxter, Silicon isotopic composition of boreal forest vegetation in Northern Sweden, Chemical Geology, 257 (2008) 250-259.
[116] P.A.E. Pogge von Strandmann, S. Opfergelt, Y.J. Lai, B. Sigfússon, S.R. Gislason, K.W. Burton, Lithium, magnesium and silicon isotope behaviour accompanying weathering in a basaltic soil and pore water profile in Iceland, Earth and Planetary Science Letters, 339 (2012) 11-23.
[117] S. Opfergelt, R.B. Georg, K.W. Burton, R. Guicharnaud, C. Siebert, S.R. Gislason, A.N. Halliday, Silicon isotopes in allophane as a proxy for mineral formation in volcanic soils, Applied Geochemistry, 26 (2011) S115-S118.
[118] B. Jones, R.W. Renaut, Impact of seasonal changes on the formation and accumulation of soft siliceous sediments on the discharge apron of geysir, Iceland, Journal of Sedimentary Research, 80 (2010) 17-35.
[119] A. Channing, I.B. Butler, Cryogenic opal-A deposition from Yellowstone hot springs, Earth and Planetary Science Letters, 257 (2007) 121-131.

[120] W. Scheffer, P. Schachtschabel, Lehrbuch der Bodenkunde, 16 ed., Spektrum Akademischer Verlag, Heidelberg, 2010.
[121] B. van Vliet-Lanoë, Properties and Processes of Cryosols, in: J.M. Kimble (Ed.) Cryosols, Springer, Berlin, Heidelberg, 2004, pp. 726.
[122] H.P. Blume, J. Chen, E. Kalk, D. Kuhn, Mineralogy and Weathering of Antarctic Cryosols, in: J.M. Kimble (Ed.) Cryosols. Permafrost affected soils, Springer, Berlin, Heidelberg, 2004.
[123] D. Kopp, A. Kowalkowski, Cryogenic and pedogenic perstruction in Tertiary and Quarternary deposits, as exemplified in the outcrop of Sternebeck, Quarternary Stud. in Poland, 9 (1990) 51-71.
[124] P. Hoekstra, R.D. Miller, On the mobility of water molecules in the transition layer between ice and a solid surface, Journal of Colloid and Interface Science, 25 (1967) 166-173.
[125] D.M. Anderson, A.R. Tice, Thawing of Frozen Clays, American Society of Civil Engineers, 1985.
[126] V. Ostroumov, O. Makeev, Winter drainage of frozen fissuring soils, Soil Sci., (1980) 80-87.
[127] C.L. Ping, S. Shoji, T. Ito, Properties and Classification of Three Volcanic Ash-derived Pedons from Aleutian Islands and Alaska Peninsula, Alaska, Soil Science Society of America Journal, 52 (1988) 455-462.
[128] T. Henmi, R.L. Parfitt, Laminar opaline silica from some volcanic ash soils in New Zealand, Clays and Clay Minerals, 28 (1980) 57-60.
[129] W.W. Dickinson, R.H. Grapes, Authigenic chabazite and implications for weathering in Sirius Group diamictite, Table Mountain, Dry Valleys, Antarctica, Journal of Sedimentary Research, 67 (1997) 815-820.
[130] A. Nagasato, S. Wada, Formation of silica microplates by freezing dilute silicic acid solutions, Soil Science and Plant Nutrition, 29 (1983) 93-95.
[131] M. Otto, Analytische Chemie, Wiley-VCH Verlag GmbH & Co. KGaA, Weinheim, 2006.
[132] S. Kaufhold, A. Kaufhold, R. Jahn, S. Brito, R. Dohrmann, R. Hoffmann, H. Gliemann, P. Weidler, A new massive deposit of allophane raw material in Ecuador, Clays and Clay Minerals, 57 (2009) 72 - 81.
[133] J.D. Rimstidt, H.L. Barnes, The kinetics of silica- water reactions, Geochimica et Cosmochimica Acta, 44 (1980) 1683-1699.
[134] G.B. Alexander, W.M. Heston, R.K. Iler, The Solubility of Amorphous Silica in Water, The Journal of Physical Chemistry, 58 (1954) 453-455.
[135] F.J. Doucet, C. Schneider, S.J. Bones, A. Kretchmer, I. Moss, P. Tekely, C. Exley, The formation of hydroxyaluminosilicates of geochemical and biological significance, Geochimica et Cosmochimica Acta, 65 (2001) 2461-2467.
[136] C. Exley, Reflections upon and recent insight into the mechanism of formation of hydroxyaluminosilicates and the therapeutic potential of silicic acid, Coordination Chemistry Reviews, 256 (2012) 82-88.
[137] M.J. Furst, Boron in siliceous materials as a paleosalinity indicator, Geochimica et Cosmochimica Acta, 45 (1981) 1-13.
[138] Merck, Data Sheet Boric Acid, in: Merck (Ed.), Merck, 2012.
[139] O. Weres, A. Yee, L. Tsao, Kinetics of silica polymerization, Journal of Colloid And Interface Science, 84 (1981) 379-402.
[140] D.I. Foustoukos, I.P. Savov, D.R. Janecky, Chemical and isotopic constraints on water/rock interactions at the Lost City hydrothermal field, 30 °N Mid-Atlantic Ridge, Geochimica et Cosmochimica Acta, 72 (2008) 5457-5474.
[141] H. Yamaguchi, Silicic acid/boric acid complexes as ecologically friendly wood preservatives, Forest Products Journal, 55 (2005) 88-92.

[142] D.S. Coombs, A. Alberti, T. Armbruster, G. Artioli, C. Colella, E. Galli, J.D. Grice, F. Liebau, J.A. Mandarino, H. Minato, E.H. Nickel, E. Passaglia, D.R. Peacor, S. Quartieri, R. Rinaldi, M. Ross, R.A. Sheppard, E. Tillmanns, G. Vezzalini, Recommended nomenclature for zeolite minerals; report of the Subcommittee on Zeolites of the International Mineralogical Association, Commission on New Minerals and Mineral Names, Canadian Mineralogist, 35 (1997) 533-571
[143] D.S. Coombs, A. Alberti, T. Armbruster, G. Artioli, C. Colella, E. Galli, J.D. Grice, F. Liebau, J.A. Mandarino, H. Minato, E.H. Nickel, E. Passaglia, D.R. Peacor, S. Quartieri, R. Rinaldi, M. Ross, R.A. Sheppard, E. Tillmanns, G. Vezzalini, Recommended nomenclature for zeolite minerals; report of the Subcommittee on Zeolites of the International Mineralogical Association, Commission on New Minerals and Mineral Names, Mineralogical Magazine, 62 (1998) 533-571.
[144] W.A.H. Deer, R.A.; Zussman, J., Framework Silicates: Silica Minerals, Feldspathoids and the Zeolites, The Geological Society, 2004.
[145] D.W. Ming, J.B. Dixon, Occurrence and weathering of zeolites in soil environments, Occurrence, properties and utilization of natural zeolites. 2nd international conference, 1985, Budapest, (1988) 699-715.
[146] G.O. Linkletter, Authigenic phillipsite in lacustrine sediments, Taylor Valley, Antarctica, New Zealand Journal of Geology and Geophysics, 17 (1973) 603-610.
[147] R.M. Milton, Molecular Sieve Science and Technology. A Historical Perspective, in: M.L.R. Occeli, Harry E. (Ed.) Zeolite Synthesis, American Chemical Society, 1989.
[148] M.W. Anderson, S.M. Holmes, R. Mann, P. Foran, C.S. Cundy, Zeolitisation of diatoms, Journal of Nanoscience and Nanotechnology, 5 (2005) 92-95.
[149] M.W. Anderson, S.M. Holmes, N. Hanif, C.S. Cundy, Hierarchical pore structures through diatom zeolitization, Angewandte Chemie - International Edition, 39 (2000) 2707-2710.
[150] O. Hernández-Ramírez, P.I. Hill, D.J. Doocey, S.M. Holmes, Removal and immobilisation of cobalt ions by a novel, hierarchically structured, diatomite/zeolite Y composite, Journal of Materials Chemistry, 17 (2007) 1804-1808.
[151] V. Sanhueza, U. Kelm, R. Cid, Synthesis of mordenite from diatomite: A case of zeolite synthesis from natural material, Journal of Chemical Technology and Biotechnology, 78 (2003) 485-488.
[152] V. Sanhueza, U. Kelm, R. Cid, L. López-Escobar, Synthesis of ZSM-5 from diatomite: A case of zeolite synthesis from a natural material, Journal of Chemical Technology and Biotechnology, 79 (2004) 686-690.
[153] A. Chaisena, K. Rangsriwatananon, Synthesis of sodium zeolites from natural and modified diatomite, Materials Letters, 59 (2005) 1474-1479.
[154] Y. Du, S. Shi, H. Dai, Water-bathing synthesis of high-surface-area zeolite P from diatomite, Particuology, 9 (2011) 174-178.
[155] K. Rangsriwatananon, A. Chaisena, C. Thongkasam, Thermal and acid treatment on natural raw diatomite influencing in synthesis of sodium zeolites, Journal of Porous Materials, 15 (2008) 499-505.
[156] K. Pimraksa, P. Chindaprasirt, A. Rungchet, K. Sagoe-Crentsil, T. Sato, Lightweight geopolymer made of highly porous siliceous materials with various Na_2O/Al_2O_3 and SiO_2/Al_2O_3 ratios, Materials Science and Engineering A, 528 (2011) 6616-6623.
[157] B. Ghosh, D.C. Agrawal, S. Bhatia, Synthesis of zeolite A from calcined diatomaceous clay: Optimization studies, Industrial and Engineering Chemistry Research, 33 (1994) 2107-2110.
[158] Y.J. Wang, Y. Tang, X.D. Wang, A.G. Dong, W. Shan, Z. Gao, Fabrication of hierarchically structured zeolites through layer-by-layer assembly of zeolite nanocrystals on diatom templates, Chemistry Letters, (2001) 1118-1119.

[159] J.H. Li, Z.Q. Chi, H.F. Chen, Synthesis of NaY zeolite molecular sieves from calcined diatomite, Advanced Materials Research, 236-238 (2011) 362-368.
[160] V. Sanhueza, U. Kelm, G. Alfaro, Synthesis of zeolites Nap-GIS, with different morphologies, from two diatomites, Revista Mexicana de Ingeniera Qumica, 10 (2011) 117-123.
[161] T. Wajima, M. Haga, K. Kuzawa, H. Ishimoto, O. Tamada, K. Ito, T. Nishiyama, R.T. Downs, J.F. Rakovan, Zeolite synthesis from paper sludge ash at low temperature (90 °C) with addition of diatomite, Journal of Hazardous Materials, 132 (2006) 244-252.
[162] W. Shan, Y. Zhang, Y. Wang, J. Xia, Y. Tang, Synthesis of meso-/macroporous zeolite (Fe,Al)-ZSM-5 microspheres from diatomite, Chemistry Letters, 33 (2004) 270-271.
[163] Z. Liu, T. Fan, H. Zhou, D. Zhang, X. Gong, Q. Guo, O. Hiroshi, Synthesis of $ZnFe_2O_4$ /SiO_2 composites derived from a diatomite template, Bioinspiration and Biomimetics, 2 (2007) 30-35.
[164] D. Losic, J.G. Mitchell, N.H. Voelcker, Diatomaceous lessons in nanotechnology and advanced materials, Advanced Materials, 21 (2009) 2947-2958.
[165] T. Wajima, O. Kiguchi, K. Sugawara, T. Sugawara, Synthesis of zeolite-A using silica from rice husk ash, Journal of Chemical Engineering of Japan, 42 (2009) 61-66.
[166] K. Pimraksa, P. Chindaprasirt, N. Setthaya, Synthesis of zeolite phases from combustion by-products, Waste Management and Research, 28 (2010) 1122-1132.
[167] C.D. Johnson, F. Worrall, Zeolitisation of pumice - Microporous materials on macroporous support structures derived from natural materials, Journal of Materials Chemistry, 17 (2007) 476-484.
[168] U. Barth-Wirsching, H. Höller, D. Klammer, B. Konrad, Synthetic zeolites formed from expanded perlite: Type, formation conditions and properties, Mineralogy and Petrology, 48 (1993) 275-294.
[169] A. Baccouche, E. Srasra, M. El Maaoui, Preparation of Na-P1 and sodalite octahydrate zeolites from interstratified illite-smectite, Applied Clay Science, 13 (1998) 255-273.
[170] M.V. Sandoval, J.A. Henao, C.A. Ríos, C.D. Williams, D.C. Apperley, Synthesis and characterization of zeotype ANA framework by hydrothermal reaction of natural clinker, Fuel, 88 (2009) 272-281.
[171] D.B. Johnson, Chemical and Microbiological Characteristics of Mineral Spoils and Drainage Waters at Abandoned Coal and Metal Mines, Water, Air, & Soil Pollution: Focus, 3 (2003) 47-66.
[172] T. Motsi, N.A. Rowson, M.J.H. Simmons, Adsorption of heavy metals from acid mine drainage by natural zeolite, International Journal of Mineral Processing, 92 (2009) 42-48.
[173] N. Moreno, X. Querol, C. Ayora, C.F. Pereira, M. Janssen-Jurkovicová, Utilization of Zeolites Synthesized from Coal Fly Ash for the Purification of Acid Mine Waters, Environmental Science & Technology, 35 (2001) 3526-3534.
[174] B. Prasad, R.J.G. Mortimer, Treatment of acid mine drainage using fly ash zeolite, Water, Air, and Soil Pollution, 218 (2011) 667-679.
[175] B. Prasad, K. Sangita, B.K. Tewary, Reducing the Hardness of Mine Water Using Transformed Fly Ash, Mine Water and the Environment, 30 (2011) 61-66.
[176] J. Cama, C. Ayora, X. Querol, J. Ganor, Dissolution kinetics of synthetic zeolite NaP1 and its implication to zeolite treatment of contaminated waters, Environmental Science and Technology, 39 (2005) 4871-4877.
[177] U. Wingenfelder, C. Hansen, G. Furrer, R. Schulin, Removal of heavy metals from mine waters by natural zeolites, Environmental Science and Technology, 39 (2005) 4606-4613.
[178] T.E.M. De Carvalho, D.A. Fungaro, C.P. Magdalena, P. Cunico, Adsorption of indigo carmine from aqueous solution using coal fly ash and zeolite from fly ash, Journal of Radioanalytical and Nuclear Chemistry, 289 (2011) 617-626.

[179] R. Yan, F. Yang, Y. Wu, Z. Hu, B. Nath, L. Yang, Y. Fang, Cadmium and mercury removal from non-point source wastewater by a hybrid bioreactor, Bioresource Technology, 102 (2011) 9927-9932.
[180] W. Yang, P. Wang, W.L. Luo, J. Zhu, Y. Zhang, The diatomite modified by pam and applied to adsorb Pb(II) in the simulated wastewater, in: Advanced Materials Research, Changsha, 2011, pp. 382-389.
[181] N. Caliskan, A.R. Kul, S. Alkan, E.G. Sogut, T. Alacabey, Adsorption of Zinc(II) on diatomite and manganese-oxide-modified diatomite: A kinetic and equilibrium study, Journal of Hazardous Materials, 193 (2011) 27-36.
[182] P.P. Povinec, K. Hirose, M. Aoyama, Radiostrontium in the western North Pacific: Characteristics, behavior, and the Fukushima impact, Environmental Science and Technology, 46 (2012) 10356-10363.
[183] P. Froidevaux, J.J. Geering, L. Pillonel, J.O. Bosset, J.F. Valley, ^{90}Sr, ^{238}U, ^{234}U, ^{137}Cs, ^{40}K and $^{239/240}Pu$ in Emmental type cheese produced in different regions of Western Europe, Journal of Environmental Radioactivity, 72 (2004) 287-298.
[184] S. Fushiki, Radiation hazards in children - Lessons from Chernobyl, Three Mile Island and Fukushima, Brain and Development, http://dx.doi.org/10.1016/j.braindev.2012.09.004 (2012).
[185] A. Merceille, E. Weinzaepfel, Y. Barré, A. Grandjean, The sorption behaviour of synthetic sodium nonatitanate and zeolite A for removing radioactive strontium from aqueous wastes, Separation and Purification Technology, 96 (2012) 81-88.
[186] K.M. Abd El-Rahman, A.M. El-Kamash, M.R. El-Sourougy, N.M. Abdel-Moniem, Thermodynamic modeling for the removal of Cs^+, Sr^{2+}, Ca^{2+} and Mg^{2+} ions from aqueous waste solutions using zeolite A, Journal of Radioanalytical and Nuclear Chemistry, 268 (2006) 221-230.
[187] R.O. Abdel Rahman, H.A. Ibrahim, M. Hanafy, N.M.A. Monem, Assessment of synthetic zeolite Na A-X as sorbing barrier for strontium in a radioactive disposal facility, Chemical Engineering Journal, 157 (2010) 100-112.
[188] A. Sachse, A. Merceille, Y. Barré, A. Grandjean, F. Fajula, A. Galarneau, Macroporous LTA-monoliths for in-flow removal of radioactive strontium from aqueous effluents: Application to the case of Fukushima, Microporous and Mesoporous Materials, 164 (2012) 251-258.
[189] I. Sato, H. Kudo, S. Tsuda, Removal efficiency of water purifier and adsorbent for iodine, cesium, strontium, barium and zirconium in drinking water, Journal of Toxicological Sciences, 36 (2011) 829-834.
[190] Y. Kumagai, R. Nagaishi, A. Kimura, M. Taguchi, K. Nishihara, I. Yamagishi, T. Ogawa, Measurement and evaluation of hydrogen production from mixtures of seawater and zeolite in decontamination of radioactive water, Transactions of the Atomic Energy Society of Japan, 10 (2011) 235-239.
[191] V.A. Nikashina, I.B. Serova, E.M. Kats, N.A. Tikhonov, M.G. Tokmachev, P.G. Novgorodov, Mathematical modelling of the sorption dynamics of radionuclides by natural clinoptilolite in permeable reactive barriers, Clay Minerals, 46 (2011) 233-240.
[192] G. Brumfiel, D. Cyranoski, Fukushima deep in hot water, Nature, 474 (2011) 135-136.
[193] D. Petzold, Adsorption von Schwermetallen an hydrothermal synthetisierten Zeolithen (Bachelor Thesis), Graz University of Technology, 2011.
[194] G. Raab, Performance Comparison of the Ion Exchange Capacity of Hydrothermally Altered Diatomite in Wastewater Treatment (Bachelor Thesis), Graz University of Technology, 2012.
[195] E.P. Barrett, L.G. Joyner, P.P. Halenda, The Determination of Pore Volume and Area Distributions in Porous Substances. I. Computations from Nitrogen Isotherms, Journal of the American Chemical Society, 73 (1951) 373-380.

[196] B.C. Lippens, J.H. de Boer, Studies on pore systems in catalysts: V. The t method, Journal of Catalysis, 4 (1965) 319-323.
[197] D. Höllen, D. Klammer, I. Letofsky-Papst, M. Dietzel, Hydrothermal Alteration of Diatomite for Removal of Aqueous Cu^{2+}, Pb^{2+}, and Zn^{2+} Materials Science and Engineering B2, 10 (2012) 523-533.
[198] B. Konrad, Experimentelle Zeolithbildung durch Umwandlung von Blähperlit, Karl-Franzens-Universität Graz, Graz, 1989.
[199] B.H. Toby, R factors in Rietveld analysis: How good is good enough?, Powder Diffraction, 21 (2006) 67-70.
[200] S. Kabir, T.L. Panhorst, Origin of gulf coast opal-CT: A study of the Claystone-Rich Tallahatta Formation in Mississippi, Southeastern Geology, 42 (2004) 151-163.
[201] H.E. Mason, R.S. Maxwell, S.A. Carroll, The formation of metastable aluminosilicates in the Al2O3-SiO2-H2O system: Results from solution chemistry and solid-state NMR spectroscopy, Geochimica et Cosmochimica Acta, 75 (2011) 6080-6093.
[202] T. Wakihara, S. Kohara, G. Sankar, S. Saito, M. Sanchez-Sanchez, A.R. Overweg, W. Fan, M. Ogura, T. Okubo, A new approach to the determination of atomic-architecture of amorphous zeolite precursors by high-energy X-ray diffraction technique, Physical Chemistry Chemical Physics, 8 (2006) 224-227.
[203] P. Li, L. Liu, G. Xiong, Effect of zeolite precursor on the formation of MCM-41 molecular sieve containing zeolite y building units, Physical Chemistry Chemical Physics, 13 (2011) 11248-11253.
[204] P.D.G. Cradwick, V. Farmer, C. Russell, C.R. Masson, K. Wada, N. Yoshinaga, Imogolite, a Hydrated Aluminium Silicate of Tubular Structure, Nature Physical Science 240 (1972) 187-189.
[205] C. Schneider, F. Doucet, S. Strekopytov, C. Exley, The solubility of an hydroxyaluminosilicate, Polyhedron, 23 (2004) 3185-3191.
[206] K. Wada, H. Kubo, Precipitation of Amorphous Aluminosilicates from Solutions Containing Monomeric Silica and Aluminium Ions, Journal of Soil Science, 26 (1975) 100-111.
[207] P.F. Barron, M.A. Wilson, A.S. Campbell, R.L. Frost, Detection of imogolite in soils using solid state 29Si NMR, Nature, 299 (1982) 616-618.
[208] B.R. Albert, A.K. Cheetham, C.J. Adams, Investigations on P zeolites: Synthesis and structure of the gismondine analogue, highly crystalline low-silica CaP, Microporous and Mesoporous Materials, 21 (1998) 127-132.
[209] A. Bieniok, K. Bornholdt, U. Brendel, W. Baur, Synthesis and crystal structure of zeolite W, resembling the mineral merlinoite, J. Mater. Chem., 6 (1996) 271-275.
[210] K. Meyer, Physikalisch-Chemische Kristallographie, VEB Deutscher Verlag für Grundstoffindustrie, Leipzig, 1977.
[211] S. Dixit, P. Van Cappellen, A.J. van Bennekom, Processes controlling solubility of biogenic silica and pore water build-up of silicic acid in marine sediments, Marine Chemistry, 73 (2001) 333-352.
[212] K. Wu, Z. Jing, L. Pan, L. Zhou, E.H. Ishida, Hydrothermal solidification of diatomaceous earth with analcime formation, Research on Chemical Intermediates, 38 (2012) 1637-1646.
[213] R.J. Donahoe, J.G. Liou, B.S. Hemingway, Thermochemical data for merlinoite: 2. Free energies of formation at 298.15 K of six synthetic samples having various Si/Al and Na/(Na+K) ratios and application to saline, alkaline lakes, American Mineralogist, 75 (1990) 201-208.
[214] R. Fernández, M. Rodríguez, R.V.d.l. Villa, J. Cuevas, Geochemical constraints on the stability of zeolites and C-S-H in the high pH reaction of bentonite, Geochimica et Cosmochimica Acta, 74 (2010) 890-906.

[215] G. Sheng, S. Wang, J. Hu, Y. Lu, J. Li, Y. Dong, X. Wang, Adsorption of Pb(II) on diatomite as affected via aqueous solution chemistry and temperature, Colloids and Surfaces A: Physicochemical and Engineering Aspects, 339 (2009) 159-166.
[216] D.A. Fungaro, J.D.C. Izidoro, Remediation of acid mine drainage using zeolites synthesized from coal fly ash, Remediação de drenagem ácida de mina usando zeólitas sintetizadas a partir de cinzas leves de carvão, 29 (2006) 735-740.
[217] C. Amrhein, G.H. Haghnia, T.S. Kim, P.A. Mosher, R.C. Gagajena, T. Amanios, L. De La Torre, Synthesis and properties of zeolites from coal fly ash, Environmental Science and Technology, 30 (1996) 735-742.
[218] M.A.M. Khraisheh, Y.S. Al-degs, W.A.M. McMinn, Remediation of wastewater containing heavy metals using raw and modified diatomite, Chemical Engineering Journal, 99 (2004) 177-184.
[219] V.R.K. Vadapalli, W.M. Gitari, A. Ellendt, L.F. Petrik, G. Balfour, Synthesis of Zeolite-P from coal fly ash derivative and its utilisation in mine-water remediation, South African Journal of Science, 106 (2010).
[220] F.A. Cotton, G. Wilkinson, Anorganische Chemie, verlag chemie, Weilheim, Deerfield Beach/Florida, Basel, 1982.
[221] S.S. Lee, K.L. Nagy, C. Park, P. Fenter, Heavy metal sorption at the muscovite (001)-fulvic acid interface, Environmental Science and Technology, 45 (2011) 9574-9581.
[222] E. Galli, Gottardi, G., and Pongiluppi, D. , The crystal structure of the zeolite merlinoite, Neues Jahrb. Mineral. Mh., (1979) 1-9.
[223] P.J. Carl, D.E.W. Vaughan, D. Goldfarb, Interactions of Cu(II) ions with framework Al in high Si: Al zeolite Y as determined from X- and W-band pulsed EPR/ENDOR spectroscopies, Journal of Physical Chemistry B, 106 (2002) 5428-5437.
[224] C.P. Huang, T.Y. Lin, L.H. Chiao, H.B. Chen, Characterization of radioactive contaminants and water treatment trials for the Taiwan Research Reactor's spent fuel pool, Journal of Hazardous Materials, 233-234 (2012) 140-147.
[225] T. Kubota, S. Fukutani, T. Ohta, Y. Mahara, Removal of radioactive cesium, strontium, and iodine from natural waters using bentonite, zeolite, and activated carbon, Journal of Radioanalytical and Nuclear Chemistry, (2012) 1-4.
[226] M. Safa, M. Larouci, B. Meddah, P. Valemens, The sorption of lead, cadmium, copper and zinc ions from aqueous solutions on a raw diatomite from Algeria, Water Science and Technology, 65 (2012) 1729-1737.